Imperial College London
Department of Mechanical Engineering

Large Eddy Simulation of Coal Combustion

Fabrizio Cavallo Marincola

November 2013

Supervised by Prof. W. P. Jones and Prof. A. M. Kempf

Submitted in part fulfilment of the requirements for the degree of
Doctor of Philosophy in Mechanical Engineering of Imperial College London
and the Diploma of Imperial College London

Abstract

In this work an in-house code for large-eddy simulations of coal combustion is developed and tested, with a special focus on the issue of modelling radiative heat transfer effects inside a furnace. An Eulerian-Lagrangian approach is used to describe the continuous gas phase and the discrete particle phase, with a two-way coupling between the two phases (implemented by another group member). The radiative transfer equation is solved using the discrete ordinates method, testing several different angular and spatial discretisation schemes. The spectral properties of the participating media are approximated with different grey gas models of varying complexity and accuracy. The accuracy of the radiative solver is initially assessed on simple idealised static cases in both two- and three-dimensions, and validated against benchmark data found in literature. The code is then integrated, parallelised and optimised with the LES flow and combustion solver, and used to simulate a large 2.4 MW coal combustion furnace. The results of the simulations are compared quantitatively against experimental data in terms of velocity, temperature, species distribution and solid particle analysis, showing a good agreement overall. A parametric study is then also performed on the variables and parameters of the radiation solver, showing great sensitivity on the outcome of the simulations in certain cases, further highlighting the importance of accurate radiation modelling for closed coal combustion furnaces.

Copyright Declaration

Declaration of Originality

I, Fabrizio Cavallo Marincola, declare that the work presented in the thesis *Large Eddy Simulation of Coal Combustion* is my own and that anyone else's work has been appropriately referenced.

Nil Difficile Volenti

Acknowledgments

Several people have played an important role throughout the course of my PhD in helping, assisting, discussing, or simply spending time with me and sharing both the joyful and suffering moments of this experience. First and foremost I would like to sincerely thank Prof. Andreas Kempf for giving me the opportunity of pursuing the PhD and providing me with financial support from the EPSRC. His supervision has been invaluable throughout these years both before and after his move to Universität Duisburg-Essen, where he invited me to visit on several occasions, and was always efficient and reliable in communicating and discussing research matters. I would also like to thank Prof. Bill Jones, who supervised me for the remaining part of my PhD, for the very useful assistance and experience he provided. His guidance in the final stages was crucial.

A huge thanks goes to my good friend Benjamin Franchetti, with whom I shared a classroom since the age of 5. We started this joint PhD project together, and have complemented each other's research, without which we would have never achieved what has been done. I would also like to thank my current and past colleagues Yagos Pesmazoglou, Mike Pettit, Stefan Wysocki and Terence Ma for the many helpful discussions and for always patiently lending a hand when needed. I must thank all of Prof. Kempf's research group in Germany, in particular Fabian Proch, Miriam Rabacal and Andreas Rittler, for being very helpful and accommodating on my visits there, and for providing remote support when needed. A special thanks goes also to Dr. Oliver Stein who was very helpful in the beginning of my studies and has been available to give advice throughout the PhD. From other universities I must acknowledge Michele Vascellari (TU Freiberg), Sandy Black (University of Leeds) and Guido Kuenne (TU Darmstadt), for the very useful discussions and the collaborations that have stemmed from these. I would also like to thank Dr. Gaetano Burriesci from University

College London, who opened up the doors of scientific research to me as an undergraduate, and inspired me to continue doing research.

Finally, yet most importantly, I would like to thank my parents, without which any of this would not have been possible. They have given me the opportunity to pursue my studies abroad, which lead to this PhD, and all the support I could have ever asked for. A few other people deserve an acknowledgment for making these years a more than pleasurable experience, but do not need to be mentioned here: you know who you are.

Contents

List of Tables

List of Figures

Nomenclature

Latin Symbols, Uppercase

A	Area	m^2
$A_{i,char}$	Pre-exponential Arrhenius term for char	$kgm^{-2}s^{-1}$
A_j	Surface area (Sec. 4.1.2)	m^2
$A_{j,p}$	Projected surface (Sec. 4.1.2)	m^2
A'_j	Surface projected on unit hemisphere (Sec. 4.1.2)	m^2
A_p	Particle surface area	m^2
A_v	Pre-exponential factor for Arrhenius equation	s^{-1}
$A_{w,i}$	Atomic weight of element i	u
B_{char}	Char burnout fraction	$-$
$B(r)$	Flux-limiter function	$-$
C_D	Drag coefficient (Sec. 3.3)	$-$
C_{diff}	Diffusion constant	$m^3K^{-0.75}$
C_o	Dispersion constant (Sec. 3.3)	$-$
C_o	Soot model constant (Sec. 4.6.3)	$-$
C_{ox}	Concentration of oxidiser (Chapter 3)	kgm^{-3}
C_p	Specific heat capacity	$Jkmol^{-1}K^{-1}$
C_s	Smagorinsky constant	$-$
C_{vN}	Constant for von Neumann boundary condition	$-$
C_2	Soot model constant (Sec. 4.6.3)	cmK
$C1$	MWSGG model coefficient (Sec. 4.5.4)	$-$
$C2$	MWSGG model coefficient (Sec. 4.5.4)	$-$
$C3$	MWSGG model coefficient (Sec. 4.5.4)	$-$
D_e	Effective diffusivity coefficient (Chapter 3)	m^2s^{-1}
D_{kn}	Knudsen diffusion coefficient	m^2s^{-1}
D_o	Bulk diffusion coefficient	m^2s^{-1}
D_α	Diffusion coefficient of species α	m^2s^{-1}
$D_{\alpha,t}$	Turbulent diffusion coefficient of species α	m^2s^{-1}
$E_{i,char}$	Activation energy Arrhenius term for char	$MJkmol^{-1}$
E_v	Activation energy for Arrhenius equation	$MJkmol^{-1}$
$\mathbf{F}_D$	Drag force (Sec. 3.3)	N
$F_{f,C}$	Convective flux over an arbitrary surface	$-$
$F_{f,D}$	Diffusive flux over an arbitrary surface	$-$

Latin Symbols, Uppercase *(cont.)*

G	Incident radiation	Wm^{-2}
H	Total wall incident intensity	Wm^{-2}
I_b	Grey blackbody intensity	Wm^{-2}
$I_{b\eta}$	Blackbody intensity for wavenumber η	Wm^{-2}
$I_{b,t}$	Total grey blackbody intensity	Wm^{-2}
I_{pi}	Cell-centred intensity coming from direction i	Wm^{-2}
I_η	Radiative intensity for wavenumber η	Wm^{-3}
J	Number of grey gases (Sec. 4.5.2)	$-$
$J_{\Phi,j}$	Diffusion of species Φ in the j-direction	$kgm^{-2}s^{-1}$
$J_{\alpha,j}$	Diffusion of species α in the j-direction	$kgm^{-2}s^{-1}$
K	Number of temperature polynomial coefficients (Sec. 4.5.2)	$-$
$K1$	MWSGG model coefficient (Sec. 4.5.4)	$-$
$K2$	MWSGG model coefficient (Sec. 4.5.4)	$-$
$M_{w,i}$	Molecular weight of element i (Chapter 3)	$kgkmol^{-1}$
$M_{w,vg}$	Molecular weight of volatile gases (Chapter 3)	$kgkmol^{-1}$
N	Number of direction cosines (Chapter 4)	$-$
$\dot{N}$	Rate of change of particle number (Sec. 3.3)	$-$
N_i	Particle number density	$-$
N_{it}	Coupling iterations	$-$
Nu	Nusselt number	$-$
$\overline{P}$	Filtered joint-*pdf* phase space (Sec. 3.3)	$-$
P_c	CO_2 partial pressure	$-$
P_w	Water vapour partial pressure	$-$
Pr	Prandtl number	$-$
Pr_t	Turbulent Prandtl number	$-$
Q	Factor accounting for higher release of volatiles	$-$
Q_{char}	Particle heat release due to char combustion	W
R	Universal gas constant	$Jkmol^{-1}K^{-1}$
$\dot{R}$	Rate of change of particle radius (Sec. 3.3)	$-$
R_c	Chemical reaction rate	$-$
R_{ox}	Bulk molecular mass diffusion rate	m^2s^{-1}
Re	Reynolds number	$-$
S	Distance between a point and a surface (Sec. 4.1.2)	m
S	Cell surface area (Sec. 4.5.2)	m^2
$\tilde{S}$	Local strain rate (Chapter 3)	s^{-1}
S_a	Specific internal surface area	m^2g^{-1}
$S_{a,0}$	Initial specific internal surface area	$m^3K^{0.75}$
S_h	Enthalpy source term	Jkg^{-1}
S_i	Radiative source function	Wm^{-3}
$\tilde{S}_{ij}$	Strain rate (Chapter 3)	s^{-1}
$S_{p,\Phi}$	Particle source term	$-$
S_Φ	Source term of quantity Φ	$-$
$\overline{\dot{S}_\Phi}$	Filtered particle coupling source term	$-$
S_η	Source function (Chapter 4)	Wm^{-3}
Sc	Schmidt number	$-$

Latin Symbols, Uppercase *(cont.)*

Sc_t	Turbulent Schmidt number	$-$
T	Temperature	K
T	Particle temperature (Sec. 3.3)	K
$\dot{T}$	Rate of change of particle temperature (Sec. 3.3)	Ks^{-1}
T_{inf}	Cell-center gas temperature	K
T_m	Mean temperature at particle surface	K
T_{ref}	Reference temperature	K
T_s	Gas-particle surface temperature	K
T_s	Soot temperature (Sec. 4.6.3)	K
T_∞	Far field temperature	K
V	Volume	m^3
V	Volatile yield	kg
VM	Adjusted initial volatile matter in a coal particle	kg
VM_0	Initial volatile matter in a coal particle	kg
W	Wiener term (Sec. 3.3)	$-$
X_{ox}	Molar fraction of oxidiser	$-$
Y_F	Mass fraction of fuel	$-$
$Y_{FC,daf}$	Daf mass fraction of Fixed Carbon (Chapter 3)	$-$
Y_i	Mass fraction of element i	$-$
$Y_{i,U}$	Mass fraction of i from ultimate analysis (Chapter 3)	$-$
$Y_{i,vg}$	Mass fraction of element i in volatiles (Chapter 3)	$-$
Y_{ox}	Oxidiser mass fraction (Chapter 3)	$-$
Y_{pr}	Products mass fraction (Chapter 3)	$-$
Y_R	Mass fraction of reactants	$-$
$Y_{VM,daf}$	Daf mass fraction of Volatile Matter (Chapter 3)	$-$
Y_{ub}	Mass fraction of unburnt char	$-$
Y_α	Mass fraction of species α	$-$

Latin Symbols, Lowercase

a_j	Conditional particle acceleration (Sec. 3.3)	ms^{-2}
a_j	Grey gas weights (Sec. 4.5.2)	$-$
$\mathbf{a}_p$	Particle acceleration (Sec. 3.3)	ms^{-2}
$a_{w,j}$	Wall absorptivity weights (Sec. 4.5.2)	$-$
b	Char burnout fraction (Sec. 4.6.2)	$-$
$b_{j,k}$	Emissivity gas temperature coefficients (Sec. 4.5.2)	$-$
c	Model constant (Sec. 4.5.1)	$-$
c	Reaction progress variable	$-$
c_i	Model constant	$-$
$c_{p,\alpha}$	Specific heat capacity of species α	$Jkmol^{-1}K^{-1}$
c_p	Specific heat capacity of mixture	$Jkmol^{-1}K^{-1}$
$c_{w,i,j,k}$	Absorptivity polynomials (Sec. 4.5.2)	$-$
c_1	Eddy Break-Up model constant (Chapter 3)	$-$
c_2	Eddy Break-Up model constant (Chapter 3)	$-$
d_p	Particle diameter	m
$d_{p,0}$	Initial particle diameter	m
f_v	Soot volume fraction	$-$

Latin Symbols, Lowercase *(cont.)*

g_i	Gravitation vector	ms^{-2}
g_j^{sgs}	Sub-grid scalar flux	ms^{-1}
h	Enthalpy	Jkg^{-1}
h_{con}	Convective heat transfer coefficient	$Wm^{-2}K^{-1}$
h_{dev}	Heat of evaporation of volatiles	Jkg^{-1}
$h_{f,prod}$	Enthalpy of formation of products (Chapter 3)	Jkg^{-1}
$h_{f,reac}$	Enthalpy of formation of reactants (Chapter 3)	Jkg^{-1}
$h_{f,\alpha}$	Enthalpy of formation of species α	Jkg^{-1}
h_R	Enthalpy of combustion (Chapter 3)	Jkg^{-1}
h_v	Enthalpy of vaporisation	Jkg^{-1}
h_{vap}	Enthalpy of vaporisation	Jkg^{-1}
h_α	Enthalpy of species α	Jkg^{-1}
k	Kinetic energy	J
k	Absorptive index of refraction (Sec. 4.6.3)	$-$
k_i	Intrinsic reaction rate	$kgm^{-2}s^{-1}$
k_{sgs}	Unresolved (sub-grid) kinetic energy	J
l	Characteristic length	m
l_K	Kolmogorov lengthscale	m
m_p	Particle mass	kg
$\dot{m}_{p,char}$	Particle mass lost due to char combustion	kgs^{-1}
$\dot{m}_{p,dev}$	Particle mass lost due to devolatilisation	kgs^{-1}
$m_{p,0}$	Initial particle mass	kg
n	Particle number (Sec. 3.3)	$-$
n	Number of angular directions (Chapter 4)	$-$
n	Absorptive index of refraction (real part) (Sec. 4.6.3)	$-$
$\hat{\mathbf{n}}$	Unit normal vector (Chapter 4)	$-$
n_j	Unit-vector normal in the j-direction	$-$
p	Fluid pressure	Pa
p_{ox}	Partial pressure of the oxidiser	Pa
q	Heat transfer rate per particle unit area (Sec. 3.3)	Wm^{-2}
$\mathbf{q}$	Radiative heat flux	Wm^{-2}
$\dot{q}_{char}$	Heat transfer source due to char combust. (Sec. 3.3)	Wkg^{-1}
$\dot{q}_{con}$	Heat transfer source due to convection (Sec. 3.3)	Wkg^{-1}
$\dot{q}_{dev}$	Heat transfer source due to devolatilisation (Sec. 3.3)	Wkg^{-1}
q_j	Energy flux in the j-direction	Jkg^{-1}
q_j^{sgs}	Sub-grid energy (enthalpy) flux	Jkg^{-1}
q_r	Radiative heat transfer rate (Chapter 4)	Wm^{-2}
$\dot{q}_{rad}$	Heat transfer source due to radiation (Sec. 3.3)	Wm^{-2}
r	Point coordinate (Chapter 4)	$-$
r	Gradient (Sec. 2.3)	$-$
r	Particle radius (Sec. 3.3)	m
$\mathbf{r}$	Position vector (Chapter 4)	$-$
r_p	Pore radius (Chapter 3)	m
r_p	Particle radius (Sec. 3.3)	m
$\mathbf{r_w}$	Position vector at wall	$-$
s	Stoichiometric coefficient (Chapter 3)	$-$

Latin Symbols, Lowercase *(cont.)*

s	Path length (Chapter 4)	m
$\mathbf{\hat{s}}$	Unit outgoing direction vector (Chapter 4)	$-$
$\mathbf{\hat{s}}'$	Unit incoming direction vector (Chapter 4)	$-$
$\mathbf{\hat{s}_i}$	Unit direction vector (Chapter 4)	$-$
t	Time	s
t_K	Kolmogorov timescale	s
u	Velocity vector	ms^{-1}
$\overline{u}$	Bulk flow velocity	ms^{-1}
$\mathbf{u}_g$	Seen gas velocity (Sec. 3.3)	ms^{-1}
u_i	Velocity in i-direction	ms^{-1}
u_j	Velocity in j-direction	ms^{-1}
u_K	Kolmogorov velocity scale	ms^{-1}
u_k	Velocity in k-direction	ms^{-1}
$\mathbf{u}_p$	Particle velocity (Sec. 3.3)	ms^{-1}
$\mathbf{v}$	Particle velocity (Sec. 3.3)	ms^{-1}
w_i	Quadrature weights	$-$
x	Indicator for volatile gas constituents (Chapter 3)	$-$
x_i	Spatial coordinate in i direction	$-$
x_j	Spatial coordinate in j direction	$-$
x_k	Spatial coordinate in k direction	$-$
$\mathbf{x}_p$	Particle position (Sec. 3.3)	$-$
z	Mixture fraction	$-$

Greek Symbols, Uppercase

Δ	LES filter width	m
ΔA	Arbitrary control surface-area	m^2
Δt_{LES}	LES (combustion) timestep	s
Δt_{RAD}	Radiation timestep	s
ΔV	Arbitrary control-volume	m^3
Δx_{min}	Minimum characteristic cell-size	m
Φ	Generic (scalar) field quantity (Sec. 2)	$-$
Φ	Polar angle (Sec. 4.1.2)	rad
Φ_η	Scattering phase function (Chapter 4)	sr^{-1}
Ω	Total solid angle (Chapter 4)	sr

Greek Symbols, Lowercase

α	Absorptance (Chapter 4)	$-$
α	Atoms of C for postulate substance (Chapter 3)	$-$
α_η	Absorptivity for wavenumber η (Chapter 4)	$-$
β	Atoms of H for postulate substance (Chapter 3)	$-$

Greek Symbols, Lowercase *(cont.)*

β	Char combustion zone parameter (Chapter 3)	$-$
β_η	Extinction coefficient for wavenumber η	m^{-1}
γ	Atoms of O for postulate substance (Chapter 3)	$-$
γ	Particle characteristic size (Chapter 3)	m
γ	Differencing scheme constants (Sec. 4.4)	$-$
δ	Atoms of N for postulate substance (Chapter 3)	$-$
δ_{ij}	Kronecker symbol	$-$
ϵ	Dissipation rate	m^2s^{-3}
ϵ	Emittance (Sec. 4.2.4)	$-$
ϵ_p	Particle emissivity	$-$
ϵ_η	Emissivity for wavenumber η	$-$
η_i	Direction cosines in y-coordinate	$-$
θ	Particle porosity (Chapter 3)	$-$
κ	Grey absorption coefficient	m^{-1}
κ_{g,H_2O-CO_2}	Grey Absorption coefficient for H_2O and CO_2	m^{-1}
κ_t	Total grey absorption coefficient	m^{-1}
κ_η	Absorption coefficient for wavenumber η	m^{-1}
λ	Thermal conductivity	$Wm^{-1}K^{-1}$
λ	Wavelength (Chapter 4)	m
λ_t	Turbulent thermal conductivity	$Wm^{-1}K^{-1}$
μ	Dynamic viscosity	$kgs^{-1}m^{-1}$
μ_i	Direction cosines in z-coordinate	$-$
μ_e	Effectiveness factor	$-$
ξ_i	Direction cosines in x-coordinate	$-$
ρ	Mass density	kgm^{-3}
ρ	Reflectance (Chapter 4)	$-$
$\rho_{p,A}$	Particle apparent density	kgm^{-3}
$\rho_{p,T}$	Particle true density	kgm^{-3}
σ	Stefan-Boltzmann constant	$Wm^{-2}K^{-4}$
$\sigma_{s,p}$	Particle scattering factor (Chapter 4)	m^{-1}
$\sigma_{s\eta}$	Scattering factor for wavenumber η (Chapter 4)	m^{-1}
τ	Pore tortuosity (Chapter 3)	$-$
τ_{ij}	Stress tensor	Pa
τ_{ij}^{sgs}	Sub-grid scale stress tensor	Pa
τ_{kk}^{sgs}	Sub-grid scale stress tensor	Pa
τ_p	Particle relaxation time (Sec. 3.3)	s
τ_t	Sub-grid timescale (Sec. 3.3)	s
τ_η	Optical thickness	$-$
υ	Kinematic viscosity	m^2s^{-1}
υ_t	Turbulent kinematic viscosity	m^2s^{-1}
ϕ	Generic field quantity	$-$
ϕ	Thiele modulus (Chapter 3)	$-$
ψ	Azimuthal angle (Sec. 4.1.2)	rad
$\tilde{\omega}_{fu}$	Filtered EBU reaction rate term (Chapter 3)	$kgm^{-3}s^{-1}$
$\dot{\omega}_\alpha$	Chemical source term of species α	$kgm^{-3}s^{-1}$
ω_η	Single scattering albedo (Chapter 4)	$-$

Operators

$\tilde{\cdot}$	Favre filtering
$\cdot''$	Favre fluctuations
$\dot{\cdot}$	Time derivative
$\cdot'$	General fluctuation
$\cdot'$	Incoming direction (Chapter 4)
$\bar{\cdot}$	Spatial filtering
$\nabla\cdot$	Gradient
$\cdot \cdot \nabla$	Divergence
$\hat{\cdot}$	Unit vector
$\lvert \cdot \rvert$	Absolute value
MAX[$\cdot$]	Maximum value
MIN[$\cdot$]	Minimum value

Subscripts

$\cdot g$	Gas phase quantity
$\cdot p$	Particle phase quantity
$\cdot s$	Soot phase quantity
$\cdot ref$	Reference quantity
$\cdot \alpha$	Quantity related to species α
$\cdot F$	Fuel quantity
$\cdot fu$	Fuel quantity
$\cdot U$	Ultimate analysis quantity
$\cdot ox$	Oxidiser quantity
$\cdot pr$	Products quantity
$\cdot 0$	Initial state quantity
$\cdot o$	Initial state quantity
$\cdot R$	Reactant quantity
$\cdot vg$	Volatile gas quantity (gaseous state)
$\cdot daf$	dry-ash-free quantity
$\cdot VM$	Volatile matter quantity (solid state)
$\cdot FC$	Fixed carbon quantity (solid state)
$\cdot t$	Turbulent quantity
$\cdot \eta$	Spectral quantity
$\cdot \Phi$	Quantity related to a general scalar Φ
$\cdot char$	Quantity related to char combustion
$\cdot f$	Cell face quantity
$\cdot con$	Convection quantity
$\cdot dev$	Devolatilisation quantity
$\cdot sgs$	Sub-grid scale component
$\cdot prod$	Products quantity
$\cdot reac$	Reactants quantity
$\cdot rad$	Radiation quantity
$\cdot b$	Burnt quantity
$\cdot u$	Unburnt quantity

Superscripts

$\cdot^{sgs}$	Sub-grid scale component
$\cdot^{b}$	Burnt quantity
$\cdot^{u}$	Unburnt quantity
$\cdot^{t}$	Quantity at time t

Abbreviations

CCS	Carbon Capture and Storage
CDS	Central Differencing Scheme
CFL	Courant Friederichs Lewy criterion
CFD	Computational Fluid Dynamics
CPD	Chemical Percolation and Devolatilisation model
CPU	Central Processing Unit
daf	Dry-Ash-Free
DMFS	Diamond Mean Flux Scheme
DNS	Direct Numerical Simulation
DOM	Discrete Ordinates Method
EBU	Eddy Break-Up model
FG-DVC	Functional Group-Depolymerization Vaporization and Cross-linking model
FVM	Finite Volume Method
HPC	High-Performance Computing
IB	Immersed Boundary
IC	Internal Combustion engine
IEA	International Energy Agency
IFRF	International Flame Research Foundation
LBL	Line By Line
LDV	Laser Doppler Velocimetry
LES	Large Eddy Simulation
LHS	Left Hand Side
LHV	Lower Heating Value
MDOM	Modified Discrete Ordinates Method
MWSGG	Modified Weighted Sum of Grey Gases method
NMDOM	New Modified Discrete Ordinates Method
NO_x	Nitrogen oxides
OTFA	Optically Thin Fluctuation Approximation
pdf	Probability Density Function
PIV	Particle Image Velocimetry
RANS	Reynolds-Averaged Navier-Stokes
RHS	Right Hand Side
RTE	Radiative Transfer Equation
SGS	Sub-Grid Scale
SLW	Spectral Line Weighted sum of grey gases method
SNB	Statistical Narrow Band
SNBcK	Statistical Narrow Band correlated k-distribution
TRI	Turbulence Radiation Interaction
TVD	Total Variation Diminishing
UDS	Upwind Differencing Scheme
WSGG	Weighted Sum of Grey Gases method

1 Introduction

The motivation and scope of this work is described in this chapter, followed by an outline of the structure of the thesis.

1.1 Motivation

The global electricity demand is expected to grow by 75% up to almost 32,000 TWh by 2035, according to the International Energy Agency (IEA) [1]. Fossil fuels, namely oil, gas and coal, account for 81% of the global energy mix, and despite their combined share is forecasted to fall to 71% by 2035, their overall demand will increase [1]. In particular according to the IEA, energy generation by coal combustion, which today accounts for 40% of the global mix, will still remain the main source of electricity generation by 2035 [1].

With energy prices and demand set to increase, and global CO_2 emissions being at a record-high, it is evident that more efficient energy generation is the way forward to mitigate pollution and spur economic growth [1]. Furthermore, advances in oxy-fuel combustion and carbon capture and storage (CCS) present a great opportunity for more efficient and less polluting energy generation.

The ability to rapidly and accurately simulate the combustion process could greatly aid the development of new burners and lead to more efficient designs, thereby reducing fuel consumption and pollutant emission. However the physical and chemical processes occurring in the combustion process are extremely complicated and their prediction is an arduous task. A direct approach to their simulation (direct numerical simulation - DNS) is unfeasible for practical and industrial applications due to the incredibly high computational costs involved. Moreover, whereas DNS is a useful tool to research the physics of fluids, the exact solution of all the turbulent structures might not be necessary to aid new efficient burner designs.

Large Eddy Simulation (LES) instead relies on solving only the largest turbulent structures, and portrays an opportunity to achieve accurate and reliable predictions, at a moderate computational cost. The ability to simulate particle-laden flows with complex geometries has already been demonstrated [4], as well as gaseous turbulent reacting flows in simpler geometries [55].

To date, the simulation of coal combustion instead has mostly relied on Reynolds-Averaged Navier Stokes (RANS) predictions, due to the increased complexity and computational costs involved in DNS and LES. However this approach has been shown to not be sufficiently accurate, and highly dependent on the turbulence and combustion model selection.

It is therefore the author's belief that large eddy simulation presents an interesting opportunity for the development of more efficient burners for energy generation by coal combustion in the future.

This work focuses on the large eddy simulation of coal combustion, with a particular attention on the issue of radiation modelling. The effects of radiative heat transfer are often neglected in the numerical simulation of combustion due to their high level of complexity and computational efforts required. However in realistic furnaces, radiation is often the main mode of heat transfer and thus its effect cannot be neglected. In this work the discrete ordinates method is implemented as a solution method for radiation, and coupled with LES of combustion. This method is validated against several different stationary benchmark cases both in 2D and 3D, and various global spectral models are also implemented to describe the radiative properties of the media. Large eddy simulations of a large coal-fired furnace are presented, and the performance of different radiation models is compared against experimental data.

Simulations of partially premixed stratified gaseous flames were also performed as an intermediate step towards the modelling and simulation of volatiles combustion for coal fired furnaces, where highly inhomogeneous dual-air mixtures occur. The work resulted in a presentation at the 34^{th} International Symposium on Combustion in Warsaw, Poland, and successively in a publication in the Proceedings of the Combustion Institute [20], to which the interested reader is directed for further details.

1.2 Thesis Outline

In this section the structure of the thesis is presented as an outline for the reader.

In Chapter 2 the background knowledge of fluid dynamics and combustion necessary for the understanding of this work is presented. The fundamental equations and assumptions used in this work are described, and a basic introduction to turbulence and the turbulent scales is given. The three main approaches to modelling turbulent flows with computational fluid dynamics are then discussed, namely Reynolds-Averaged Navier-Stokes, direct numerical simulation, and large eddy simulation. Greater emphasis and detail is given on the latter, as this is the sole technique used in this work. The filtering procedure is described, as well as the treatment of the sub-grid scales in LES. The numerical description techniques used are then presented, showing the different discretisation schemes used to describe convection. The treatment of diffusion is also introduced, as well as the time integration technique employed, to advance a solution in time.

The background knowledge of coal combustion necessary for the understanding of this work is given in Chapter 3. The main properties of coal and its characterisation are introduced, and successively the combustion process and the modelling approach used in this work is presented. The method used to describe the volatiles composition is given, together with the models used to describe the devolatilisation, volatiles combustion and char combustion processes. A brief introduction to the description of particles is included, presenting the basics of the Euler-Lagrange approach used in this work, and the treatment of the influence of the sub-grid scales on the particles and vice-versa. Finally, the main equations describing the heat transfer to and from the particles by means of the various processes affecting them are shown, together with the two-way coupling method used in this work.

Chapter 4 introduces radiative heat transfer, a process that has often been neglected to date in the numerical simulation of combustion, but which is likely to be the dominant heat transfer mode in certain specific applications, such as coal combustion in closed furnaces. The basic concepts underlying radiative heat transfer are defined, and the radiative transfer equation for absorbing, emitting and scattering media and its main boundary conditions are presented. Solution methods to the radiative transfer equation are discussed, with a special focus on the Discrete Ordinates Method (DOM), which is the focus of this work. The various spectral models that can be used to describe the radiative properties of the medium are also introduced, with a detailed description of various grey gas models used in this work. The extension of the radiative transfer equation to deal with particle laden flows is described, together with the equations used to define the particles' radiative properties. An introduction to the treatment of soot for radiation calculations is also given. The inclusion and coupling of radiation modelling with large eddy simulations is presented, as well as the implemented parallelisation strategy.

The validation studies of the radiation models carried out by the author are presented in Chapter 5. Five different two-dimensional cases and three three-dimensional stationary cases are investigated, and the results are compared to other models or same model predictions by other authors found in literature. Different angular and spatial discretisation schemes are investigated, to provide a sensitivity analysis on the former and study the influence of the latter. Overall a good agreement is obtained with the models used, in some cases even outperforming other author's work with the same models.

In Chapter 6 the large eddy simulations carried out on the International Flame Research Foundation furnace are presented. This is a relatively large 2.4MW pulverised coal furnace which has been studied extensively, and for which a significant amount of experimental data is available in terms of mean quantities. Velocity, temperature and species concentration data as well as the incident radiative heat flux measured on the wall of the furnace are available at various locations along the furnace length. The simulations are compared to these quantities, with a special focus on the temperature and radiation data available. Several different radiation models are compared to each other, to provide a sensitivity analysis for the influence and impact of radiation modelling on the large eddy simulations of coal combustion.

Finally in Chapter 7, the main findings and conclusions of this work are summarised, and recommendations are made for future work.

2 Fluid Dynamics and Combustion

In this chapter, an overview of the theory underlying fluid dynamics is presented, including the main assumptions in the present work, and the governing equations used. The different modelling techniques commonly used to describe turbulent flows are then introduced, with an emphasis on Large Eddy Simulation, as this is the sole technique used by the author.

2.1 Theory of Fluid Dynamics

2.1.1 Fundamental Equations and Assumptions

In the present work, fluids are assumed to be *incompressible.* This assumption is valid for low Mach numbers, where the flow speed is well below the speed of sound, which is the case in the coal combustion, and gaseous combustion cases considered in this work. What *incompressibility* means is that the density of the fluid is independent of pressure (although it will still vary with heat release):

$$\frac{\partial \rho}{\partial p} = 0 \tag{2.1}$$

Conservation of Mass

A further assumption is made, that the fluid is *continuous.* Even though fluids are made up of millions of discrete microscopic particles, at the macroscopic level which is that of major interest in fluid flow for combustion applications, these can be treated as a *continuous* phase. Since atoms cannot be created or destroyed, a fluid cannot change its mass, and as such we have a conservation principle for mass. The conservation equation for mass is generally known as the *continuity equation* (Eq. 2.2), which describes the local change of density ρ with time t, and its convection in space x_j with velocity components u_j.

$$\frac{\partial \rho}{\partial t} + \frac{\partial}{\partial x_j}(\rho u_j) = 0 \tag{2.2}$$

Conservation of Momentum

A fluid will not change its velocity unless external forces act upon it. Momentum is thus conserved, and can be described by Eq. 2.3. The local change of momentum ρu_i in time t is related to the convective transport of the former by a velocity u_j in the x_j direction, and to the forces on the right-hand side which are due to deformation, pressure and gravitation. The stresses τ_{ij} that result from the local deformation of the fluid depend on its properties, the $\partial p/\partial x_i$ term describes the effect of local pressure-gradients, and the last term ρg_i represents the earth's gravitational attraction.

$$\underbrace{\frac{\partial}{\partial t}(\rho u_i)}_{\substack{\textit{rate of change}\\ \textit{of momentum}}} + \underbrace{\frac{\partial}{\partial x_j}(\rho u_i u_j)}_{\textit{convection}} = \underbrace{\frac{\partial}{\partial x_j}\tau_{ij}}_{\textit{deformation}} - \underbrace{\frac{\partial p}{\partial x_i}}_{\textit{pressure}} + \underbrace{\rho g_i}_{\textit{gravitation}} \tag{2.3}$$

All gases and most liquids, and certainly all the fluids employed in this work are Newtonian in nature. What this means is that the stress acting on a fluid is linearly related to its' strain rate, and as such the two can be related by a constant of proportionality, which is the dynamic viscosity μ. Using Stokes hypothesis, the fluids deformation can be expressed mathematically as in Eq. 2.4, where δ_{ij} is the Kronecker delta ($\delta_{ij} = 1$ for $i = j$, and $\delta_{ij} = 0$ for $i \neq j$).

$$\tau_{ij} = \mu \left(\frac{\partial u_j}{\partial x_i} + \frac{\partial u_i}{\partial x_j} - \frac{2}{3}\frac{\partial u_k}{\partial x_k}\delta_{ij} \right) \tag{2.4}$$

The Navier-Stokes equations are obtained by substituting Eq. 2.4 into Eq. 2.3, which together with the continuity equation (Eq. 2.2) fully describe the flow of an isothermal, incompressible Newtonian fluid.

$$\frac{\partial}{\partial t}(\rho u_i) + \frac{\partial}{\partial x_j}(\rho u_i u_j) = \frac{\partial}{\partial x_j}\mu \left(\frac{\partial u_j}{\partial x_i} + \frac{\partial u_i}{\partial x_j} - \frac{2}{3}\frac{\partial u_k}{\partial x_k}\delta_{ij} \right) - \frac{\partial p}{\partial x_i} + \rho g_i \tag{2.5}$$

General Transport Equation

In order to describe a turbulent reacting flow, in addition to the conservation equations for mass (Eq. 2.2) and momentum (Eq. 2.3), an equation describing the chemical state of the fluid must be employed. This is known as a scalar transport equation, and a general transport equation describing the evolution of an arbitrary quantity Φ can be expressed as in Eq. 2.6. The terms on the LHS describe the change of quantity Φ with time t, and its convective transport through x_j with velocity u_j, whereas the first term on the RHS describes the rate of diffusion of the scalar $J_{\Phi,j}$, and the last term describes production or destruction of the scalar by a source or sink, S_Φ.

$$\underbrace{\frac{\partial \Phi}{\partial t}}_{accumulation} + \underbrace{\frac{\partial}{\partial x_j}(\Phi u_j)}_{convection} = \underbrace{-\frac{\partial J_{\Phi,j}}{\partial x_j}}_{diffusion} + \underbrace{S_\Phi}_{source} \tag{2.6}$$

Such a transport equation (Eq. 2.6) can be applied to any scalar by simply substituting for Φ. For example by setting $\Phi \equiv \rho$, the continuity equation is readily recovered (Eq. 2.2), as mass cannot be created or destroyed ($S_\Phi = 0$), and density is not affected by mass diffusion ($\partial J_{\rho,j}/\partial x_j = 0$). In a similar way, the momentum equation (Eq. 2.3) can be recovered from Eq. 2.6 by setting $\Phi \equiv \rho u_i$, since the diffusion of momentum is equal to the stress tensor τ_{ij}, and the source/sink term for momentum is equal to the pressure and gravitational forces acting on the fluid.

Species Mass Fraction

The composition of a gas mixture can be described with the mass fraction Y_α of each of the chemical species α in the mixture. Individual transport equations for each of the species involved can be derived by substituting $\Phi = \rho Y_\alpha$ in Eq. 2.6, where J_α is the diffusive flux and $\dot{\omega}_\alpha$ is the source term of species α.

$$\frac{\partial(\rho Y_\alpha)}{\partial t} + \frac{\partial}{\partial x_j}(\rho Y_\alpha u_j) = -\frac{\partial J_{\alpha,j}}{\partial x_j} + \dot{\omega}_\alpha \tag{2.7}$$

Diffusion can be described using Fick's law (Eq. 2.8), where D_α is the diffusion coefficient of species α.

$$J_{\alpha,j} = -\rho D_\alpha \frac{\partial Y_\alpha}{\partial x_j} \tag{2.8}$$

Substituting Eq. 2.8 into Eq. 2.7 and using the species Schmidt number, $Sc_\alpha = \mu/\rho D_\alpha$ to substitute the diffusion coefficient, the final form of the species transport equation is obtained, Eq. 2.9. Throughout this work it is assumed that all species have an equal diffusivity, and thus a unique Schmidt number is used, $Sc_\alpha = Sc$.

$$\frac{\partial(\rho Y_\alpha)}{\partial t} + \frac{\partial}{\partial x_j}(\rho Y_\alpha u_j) = \frac{\partial}{\partial x_j}\left(\frac{\mu}{Sc_\alpha}\frac{\partial Y_\alpha}{\partial x_j}\right) + \dot{\omega}_\alpha \tag{2.9}$$

In gaseous combustion however, several chemical species are involved in the reactions, and the use of a transport equation for each species mass fraction is usually unnecessary and costly. Depending on the combustion mode, certain specific transport equations can be used to reduce the overall number of transported quantities, as outlined in the following two paragraphs.

Mixture Fraction

For a case of pure mixing of fuel and oxidiser in non-premixed combustion, a quantity known as the *mixture fraction z,* can be defined and transported as a single conservation equation, assuming equal diffusivity of all species and unity Lewis number. By substituting ρz in Eq. 2.6 and simplifying as above, the number of species transport equations is reduced from 2 to 1 as both the fuel and oxidiser are represented by the mixture fraction. The mixture fraction is generally defined as 0 in the oxidiser stream, and 1 in the fuel stream, with mass balances for intermediate values.

$$\frac{\partial(\rho z)}{\partial t} + \frac{\partial}{\partial x_j}(\rho z u_j) = \frac{\partial}{\partial x_j}\left(\frac{\mu}{Sc}\frac{\partial z}{\partial x_j}\right) \tag{2.10}$$

Progress Variable

For premixed combustion, a very useful quantity is the *reaction progress variable c.* This is generally defined as 0 in the unburnt regions (fresh gases) and 1 in the fully burnt regions (burnt products), with intermediate values at the flame front. It can be expressed in terms of the reactant mass fraction Y_R, or assuming unity Lewis numbers and low-Mach numbers in terms of temperature T, as in Eq. 2.11 and Eq. 2.12, where the subscripts u and b indicate the unburnt and burnt states respectively [24].

$$c \equiv \frac{Y_{R,b} - Y_R}{Y_{R,u} - Y_{R,b}} \tag{2.11}$$

$$c = \frac{T - T_u}{T_b - T_u} \tag{2.12}$$

In the same way as for the mixture fraction, the transport equation is obtained by substituting ρc in Eq. 2.6 and simplifying, and prevents the need to solve transport equations for each individual species.

$$\frac{\partial(\rho c)}{\partial t} + \frac{\partial}{\partial x_j}(\rho c u_j) = \frac{\partial}{\partial x_j}\left(\frac{\mu}{Sc}\frac{\partial c}{\partial x_j}\right) + \dot{\omega}_c \tag{2.13}$$

For partially-premixed combustion, where a premixed air-fuel stream coexists with a pure air stream, it is necessary to transport both the mixture fraction (Eq. 2.10) and the progress variable (Eq. 2.13) to accurately describe the chemical state and composition of the fluid flow.

Enthalpy

In reactive flows, the temperature change associated with the chemical reactions and due to radiative effects can be described by solving a transport equation for energy, which can be expressed in terms of enthalpy, sensible enthalpy, temperature and internal energy among others. In this work the static enthalpy h was used, which is a function of the local species mass fractions and temperature, defined in Eq. 2.14.

$$h = \sum Y_\alpha \left(h_{f,\alpha} + \int c_{p,\alpha} dT\right) \tag{2.14}$$

Here, $h_{f,\alpha}$ is the enthalpy of formation of species α and $c_{p,\alpha}$ is it's specific heat capacity.

Throughout this work an incompressibility assumption is made, and as such pressure is assumed to remain constant with respect to the enthalpy equation and the effects of pressure gradients are neglected, as well as those of viscous heating (dissipation), which are negligible. The transport equation for enthalpy can therefore be simplified as in Eq. 2.15 below, where

q_j is the energy flux (Eq. 2.16), dependent upon both the heat and species diffusion [125].

$$\frac{\partial(\rho h)}{\partial t} + \frac{\partial}{\partial x_j}(\rho h u_j) = \frac{\partial q_j}{\partial x_j} \tag{2.15}$$

The first term on the right-hand side of Eq. 2.16 represents the heat diffusion expressed by Fourier's law, where λ is the thermal conductivity, whereas the second term represents the summation of the diffusion of each specie α.

$$q_j = \lambda \frac{\partial T}{\partial x_j} - \sum_{\alpha=1} h_\alpha J_\alpha \tag{2.16}$$

.

Assuming a unity Lewis number (equal mass and thermal diffusion), the energy flux can be further simplified as in Eq. 2.17 [125].

$$q_j = \frac{\lambda}{c_p} \frac{\partial h}{\partial x_j} \tag{2.17}$$

Using the definition of the Prandtl number, which compares momentum and heat transport, $Pr = \mu c_p / \lambda$, and performing the relevant substitutions, the final version of the enthalpy equation is obtained, Eq. 2.18.

$$\frac{\partial(\rho h)}{\partial t} + \frac{\partial}{\partial x_j}(\rho h u_j) = \frac{\partial}{\partial x_j}\left(\frac{\mu}{Pr} \frac{\partial h}{\partial x_j}\right) \tag{2.18}$$

It is important to note that in this work the enthalpy transport equation also has a source term which originates from the heat transfer to and from the discrete particle phase (see Sec. 3.3.2) and to account for radiative heat transfer effects (see Chapter 4). This has been omitted here for consistency, but will be discussed in the relevant sections, where a complete version of the enthalpy equation used in this work will be presented.

2.1.2 Turbulence and Turbulent Scales

The term *fluid flow* has a very broad significance, and as such it is useful to classify it as being either *laminar* or *turbulent* with a transitional region. Laminar flows can be one, two and three-dimensional and often do not vary with time (steady), whereas turbulent flows are always three-dimensional and transient, and appear chaotic in nature with a range of different structure sizes.

The classification of fluid flows is attributed to Reynolds [135, 136], who by conducting a set of simple experiments determined the four factors affecting the nature of the flow, and classified these by deriving a non-dimensional number known today as the *Reynolds number* (Eq. 2.19), which remains to date one of the most useful quantities in fluid-mechanics. He concluded that the four factors affecting the nature of the flow are its density ρ, velocity u, viscosity μ and characteristic length l, which depends on the specific problem. For instance for a simple pipe flow the characteristic length would be taken as the diameter of the pipe, and the critical (transitional) Reynolds number is around $Re \approx 2000$, below which the flow is laminar.

$$Re = \frac{\rho u l}{\mu} = \frac{u l}{\upsilon} \tag{2.19}$$

Reynolds formulated another important concept known as the *Reynolds decomposition* (Eq. 2.20), which separates the mean (steady) and the fluctuating (unsteady) velocity components in a turbulent flow field. This equation can be substituted inside the continuity and momentum equations (Eq. 2.2 and Eq. 2.3) and forms the basis for *Reynolds-Averaged Navier-Stokes (RANS),* which is briefly outlined in Sec. 2.2.1.

$$u_i(x_j, t) = \bar{u}_i(x_j) + u_i'(x_j, t) \tag{2.20}$$

Turbulent flows are characterised by rotating structures having a wide range of different sizes, commonly known as *eddies.* However the two most crucial turbulent scales, of which a brief explanation is given in this paragraph, are the *integral* and *Kolmogorov* length scales, which represent the typical and minimum structure sizes respectively. Such scales are better understood with an appreciation of the *energy cascade* [137]: the large eddies carry the greatest kinetic energy k, and as they move through the flow they transfer energy to the smaller eddies. Eventually, the eddies become so small that they are completely dissipated due to viscous forces. The rate at which viscous forces convert the kinetic energy of the eddies into heat is known as the *dissipation rate* ϵ, and is defined as the ratio of kinetic energy to the eddie's time scale [125].

The integral length scale represents the size of the largest eddies, and can usually be estimated from the characteristic length of the flow problem, for instance the diameter of the pipe flow discussed above. This is defined as the integral of the auto-correlation function (of velocity) in the flow direction. In simpler terms, the velocity auto-correlation indicates how much the velocity fluctuation at a given point in the flow is correlated with the nearby fluctuations, in order to indicate a size of the rotating structures.

The range of different length scales in a flow was intensively studied by Kolmogorov [90, 91], who was the first to propose that there must be a limit to the size of the smallest eddies in the flow, beyond which only viscous forces are present, and these are known today as the *Kolmogorov scales*, expressed in terms of length, velocity and time (Eq. 2.21).

$$l_K = (\upsilon^3/\epsilon)^{1/4} \ , \ u_K = (\upsilon\epsilon)^{1/4} \ , \ t_K = (\upsilon/\epsilon)^{1/2} \tag{2.21}$$

2.2 Modelling Turbulent Flows

An overview of the fundamental governing equations describing an incompressible turbulent reactive flow has been given in the previous section. Such equations however can be directly applied and solved only for the simplest of problems due to the complexity of the possible solutions, and as such numerical methods are used to tackle more challenging and relevant problems. The three most common and widely acknowledged numerical methods for computational fluid dynamics applications in turbulent flows are *Reynolds-Averaged Navier-Stokes* (RANS), *Direct Numerical Simulations* (DNS) and *Large Eddy Simulations* (LES). The first two are only briefly introduced in the following subsections, whereas a more detailed explanation of LES is given, as this is the focus of the author's work.

2.2.1 Reynolds-Averaged Navier-Stokes (RANS)

RANS is historically one of the first numerical methods to be widely accepted and is the least computationally expensive of the three methods, making it the most popular method in solving fluid dynamics problems to date. As previously mentioned, the fundamental RANS equations are obtained by substituting the Reynolds decomposition (Eq. 2.20) in the continuity and momentum equations (Eq. 2.2 and Eq. 2.3). This yields a set of equations for the time-averages of velocity $\bar{u}_i$ and pressure $\bar{p}$, which unfortunately lead to new, unclosed terms such as $\overline{u_i' u_j'}$, known as *Reynolds stresses.* This term can be closed by deriving further transport equations, which however include other unclosed terms (this is known as the *Turbulence Closure Problem*), or it can be modelled based on known quantities [157].

2.2.2 Direct Numerical Simulation (DNS)

Whereas in RANS a lot of modelling is involved, DNS relies on solving all possible scales with no modelling at all. The continuity and momentum equations (Eq. 2.2 and Eq. 2.3) are thus discretised on a grid having a characteristic length equal to or less than the Kolmogorov lengthscale l_K, and solved with timesteps equal to or shorter than the Kolmogorov timescale t_K (generally even shorter for reactive simulations). The procedure is extremely computationally expensive, although outstanding results can be obtained. As a matter of fact DNS is currently used in research to investigate and obtain important information concerning the physics of fluids, to aid simple, more cost-effective model development [14, 42]. Whilst improvements in High Performance Computing (HPC) make the use of DNS for industrial applications a feasible prospect for the future, this may never become the preferred solution, as the huge amounts of data generated by DNS are difficult to process, and the exact solution of all turbulent structures is not necessarily of interest.

2.2.3 Large Eddy Simulation (LES)

Whereas in DNS all turbulent scales are resolved, and from RANS only time-averaged quantities are obtained, LES can be seen as an intermediate method of the two, providing potentially greater accuracy than RANS, at a lower cost than DNS. In LES in fact a low-pass filter is applied to the governing equations, and as a result only the larger scales are resolved, whereas the smaller ones require modelling. The filtering procedure (Eq. 2.22) for a quantity Φ, results in a spatial mean $\overline{\Phi}$, and it's Sub-Grid Scale (SGS) contribution Φ'.

$$\Phi = \overline{\Phi} + \Phi' \qquad \text{or} \qquad \Phi' = \Phi - \overline{\Phi} \tag{2.22}$$

To simplify the numerical method in variable-density problems, a density-weighted filter is applied (Eq. 2.23), known as *Favre filtering*, where for the same quantity Φ, its density weighted average is $\widetilde{\Phi}$, and the Favre-fluctuations are represented by Φ''.

$$\Phi = \widetilde{\Phi} + \Phi'' \quad \text{with} \quad \widetilde{\Phi} = \frac{\overline{\rho\Phi}}{\overline{\rho}} \quad \text{or} \quad \overline{\rho\Phi} = \overline{\rho}\widetilde{\Phi} \tag{2.23}$$

The benefit of such operation is that it allows to re-express the filtered correlation $\overline{\rho\Phi}$ as the product of filtered quantities $\overline{\rho}\widetilde{\Phi}$. The filtered governing equations for LES are presented in the following paragraphs.

Filtered Navier-Stokes Equations

The low-pass and Favre-filtered continuity equations are presented in Eq. 2.24, respectively.

$$\frac{\partial \overline{\rho}}{\partial t} + \frac{\partial}{\partial x_j}\overline{(\rho u_j)} = 0 \quad \text{or} \quad \frac{\partial \overline{\rho}}{\partial t} + \frac{\partial}{\partial x_j}(\overline{\rho}\tilde{u}_j) = 0 \tag{2.24}$$

Comparing the filtered continuity equation (Eq. 2.24) with its original unfiltered version (Eq. 2.2) one may notice that no additional term is introduced, and as such no SGS modelling is required.

Applying a low-pass filter to the conservation of momentum equation (Eq. 2.3), assuming that filtering and differentiation are commutative, and rewriting the dynamic viscosity μ in terms of density and kinematic viscosity υ results in Eq. 2.25.

$$\frac{\partial}{\partial t}\overline{(\rho u_i)} + \frac{\partial}{\partial x_j}\overline{(\rho u_i u_j)} = \frac{\partial}{\partial x_j}\left[\overline{\rho\upsilon\left(\frac{\partial u_j}{\partial x_i} + \frac{\partial u_i}{\partial x_j} - \frac{2}{3}\frac{\partial u_k}{\partial x_k}\delta_{ij}\right)}\right] - \frac{\partial \overline{p}}{\partial x_i} + \overline{\rho} g_i \tag{2.25}$$

Favre-filtering and approximating $\widetilde{\upsilon\frac{\partial u_j}{\partial x_i}} \approx \tilde{\upsilon}\widetilde{\frac{\partial u_j}{\partial x_i}}$, leads to Eq. 2.26.

$$\frac{\partial}{\partial t}(\overline{\rho}\tilde{u}_i) + \frac{\partial}{\partial x_j}(\overline{\rho}\widetilde{u_i u_j}) = \frac{\partial}{\partial x_j}\left[\overline{\rho}\tilde{\upsilon}\left(\frac{\partial\widetilde{u_j}}{\partial x_i} + \frac{\partial\widetilde{u_i}}{\partial x_j} - \frac{2}{3}\frac{\partial\widetilde{u_k}}{\partial x_k}\delta_{ij}\right)\right] - \frac{\partial\overline{p}}{\partial x_i} + \overline{\rho}g_i \quad (2.26)$$

LES filtering of the momentum equation thus results in an unknown non-linear convection term $\widetilde{u_i u_j}$, which is associated to the *sub-grid stress tensor* τ_{ij}^{sgs}.

$$\tau_{ij}^{sgs} \approx \widetilde{u_i u_j} - \tilde{u}_i\tilde{u}_j \quad \text{or} \quad \widetilde{u_i u_j} \approx \tilde{u}_i\tilde{u}_j + \tau_{ij}^{sgs} \quad (2.27)$$

Eq. 2.27 can be substituted in Eq. 2.26 to obtain the unclosed form of the filtered momentum equation (Eq. 2.28). The sub-grid stress tensor requires modelling to be closed, as discussed in the following paragraph.

$$\frac{\partial}{\partial t}(\overline{\rho}\tilde{u}_i) + \frac{\partial}{\partial x_j}(\overline{\rho}\widetilde{u_i}\widetilde{u_j}) = \frac{\partial}{\partial x_j}\left[\overline{\rho}\tilde{\upsilon}\left(\frac{\partial\widetilde{u_j}}{\partial x_i} + \frac{\partial\widetilde{u_i}}{\partial x_j} - \frac{2}{3}\frac{\partial\widetilde{u_k}}{\partial x_k}\delta_{ij}\right) + \overline{\rho}\tau_{ij}^{sgs}\right] - \frac{\partial\overline{p}}{\partial x_i} + \overline{\rho}g_i \quad (2.28)$$

Sub-grid Stress Modelling

In this work, closure of the sub-grid stress tensor is obtained with the *eddy viscosity approach.* In this model the sub-grid contribution to the turbulent energy balance is represented by adding a turbulent eddy viscosity term $\widetilde{\upsilon}_t$ to the molecular viscosity $\widetilde{\upsilon}$ as in Eq. 2.29.

$$\tau_{ij}^{sgs} - \frac{1}{3}\tau_{kk}^{sgs}\delta_{ij} = \widetilde{\upsilon}_t\left(\frac{\partial\widetilde{u_j}}{\partial x_i} + \frac{\partial\widetilde{u_i}}{\partial x_j} - \frac{2}{3}\frac{\partial\widetilde{u_k}}{\partial x_k}\delta_{ij}\right) \quad (2.29)$$

Substituting Eq. 2.29 into Eq. 2.28 gives the closed, filtered momentum equation (Eq. 2.30).

$$\frac{\partial}{\partial t}(\overline{\rho}\tilde{u}_i) + \frac{\partial}{\partial x_j}(\overline{\rho}\widetilde{u_i}\widetilde{u_j}) = \frac{\partial}{\partial x_j}\left[\overline{\rho}\left(\tilde{\upsilon} + \tilde{\upsilon}_t\right)\left(\frac{\partial\widetilde{u_j}}{\partial x_i} + \frac{\partial\widetilde{u_i}}{\partial x_j} - \frac{2}{3}\frac{\partial\widetilde{u_k}}{\partial x_k}\delta_{ij}\right) + \frac{1}{3}\overline{\rho}\tau_{kk}^{sgs}\right] - \frac{\partial\overline{p}}{\partial x_i} + \overline{\rho}g_i \quad (2.30)$$

The only remaining unknown term in this equation is the turbulent viscosity υ_t, which in the present work is approximated using the *Smagorinsky model* [149]. The model (Eq. 2.31) is dependant upon the LES filter width (characteristic cell size) Δ, the filtered strain tensor $\tilde{S}_{ij}$, and its model constant C_s.

$$\widetilde{\upsilon_t} = (C_s\Delta)^2\sqrt{2\tilde{S}_{ij}\tilde{S}_{ij}} \quad \text{where} \quad \tilde{S}_{ij} = \frac{1}{2}\left(\frac{\partial \widetilde{u_j}}{\partial x_i} + \frac{\partial \widetilde{u_i}}{\partial x_j}\right) \tag{2.31}$$

This model can offer good results and is of simple implementation, however results can be affected by the chosen value of the model constant, and an appropriate selection of this is not always obvious. Lilly suggested a value of $C_s = 0.173$ for channel flows [102], however in general $0.065 < C_s < 0.2$ is an acceptable range, and often sensitivity analyses must be conducted to determine the optimal value. The need for setting this parameter can be spared by using the Germano dynamic model [53], however at a higher computational cost.

Filtered Scalar Transport Equations

To perform an LES of a reacting flow at least one scalar transport equation must be solved, depending on the problem. For non-premixed combustion, the *mixture fraction* z is a common choice (Eq. 2.10), whereas for premixed combustion the *reaction progress variable* c (Eq. 2.13) is the usual scalar used. For partially premixed combustion a combination of the two is needed, whereas for coal combustion the current undertaken approach is to transport the individual species mass fractions. The filtering of a general species mass fraction is presented below, which is similar to the mixture fraction and progress variable filtering operations. Applying a low-pass filter to Eq. 2.9 yields Eq. 2.32, which by Favre-filtering and using a gradient assumption [125] gives Eq. 2.33.

$$\frac{\partial \overline{(\rho Y_\alpha)}}{\partial t} + \frac{\partial}{\partial x_j}\overline{(\rho Y_\alpha u_j)} = \frac{\partial}{\partial x_j}\overline{\left(\frac{\mu}{Sc}\frac{\partial Y_\alpha}{\partial x_j}\right)} + \overline{\dot{\omega}_\alpha} \tag{2.32}$$

$$\frac{\partial(\overline{\rho}\widetilde{Y_\alpha})}{\partial t} + \frac{\partial}{\partial x_j}(\overline{\rho}\widetilde{Y_\alpha u_j}) = \frac{\partial}{\partial x_j}\left(\frac{\tilde{\mu}}{Sc}\frac{\partial \widetilde{Y_\alpha}}{\partial x_j}\right) + \overline{\dot{\omega}_\alpha} \tag{2.33}$$

This leads to the unclosed convective term $\widetilde{Y_\alpha u_j}$, and the filtered reaction rate $\dot{\overline{\omega}}$, which both require modelling. Similar to the sub-grid stress for the momentum equation (Eq. 2.27), the species convection term is approximated as in Eq. 2.34.

$$g_j^{sgs} = \widetilde{Y_\alpha}\widetilde{u_j} - \widetilde{Y_\alpha u_j} \tag{2.34}$$

The effect of the species sub-grid scale may be understood as turbulent molecular diffusion, and this is approximated with a gradient assumption [125].

$$g_j^{sgs} = \overline{D}_{\alpha,t}\frac{\partial \widetilde{Y}_\alpha}{\partial x_j} = \frac{\widetilde{\upsilon}_t}{Sc_t}\frac{\partial \widetilde{Y}_\alpha}{\partial x_j} \tag{2.35}$$

In this work the turbulent Schmidt number Sc_t is taken as 0.7. The final closed form of the species transport equation can therefore be obtained by grouping the viscosity terms, where the filtered turbulent viscosity $\tilde{\mu}_t$ is obtained from the Smagorinsky model, as previously described.

$$\frac{\partial(\overline{\rho}\tilde{Y}_\alpha)}{\partial t} + \frac{\partial}{\partial x_j}(\overline{\rho}\tilde{Y}_\alpha\tilde{u}_j) = \frac{\partial}{\partial x_j}\left[\left(\frac{\tilde{\mu}}{Sc} + \frac{\tilde{\mu}_t}{Sc_t}\right)\frac{\partial \tilde{Y}_\alpha}{\partial x_j}\right] + \dot{\tilde{\omega}}_\alpha \tag{2.36}$$

Filtered Enthalpy Equation

The enthalpy transport equation (2.18) can be filtered in a similar way to the scalar transport equation above, yielding Eq. 2.37.

$$\frac{\partial\overline{\rho}\widetilde{h}}{\partial t} + \frac{\partial}{\partial x_j}(\overline{\rho}\widetilde{hu_j}) = \frac{\partial}{\partial x_j}\left(\frac{\lambda}{c_p}\frac{\partial \widetilde{h}}{\partial x_j}\right) \tag{2.37}$$

This gives an unclosed term: the enthalpy convection term $\widetilde{hu_j}$, which is treated with a similar approach to the species mass fraction convection term (Eq. 2.34), as in Eq. 2.38.

$$q_j^{sgs} = \widetilde{h}\widetilde{u_j} - \widetilde{hu_j} \tag{2.38}$$

The enthalpy sub-grid contribution may be seen as turbulent thermal diffusion, again approximated by a gradient assumption, where Pr_t is the turbulent Prandtl number, which given the unity Lewis number assumption is the same as the turbulent Schmidt number: $Pr_t = 0.7$.

$$q_j^{sgs} = \frac{\widetilde{\lambda}_t}{c_p}\frac{\partial \widetilde{h}}{\partial x_j} = \frac{\widetilde{\upsilon}_t}{Pr_t}\frac{\partial \widetilde{h}}{\partial x_j} \tag{2.39}$$

The final form of the closed enthalpy transport equation is given in Eq. 2.40. Note that here the source terms due to the coupling between the continuous and discrete phase, and due to radiation have been omitted for consistency. Closure models for the radiative source term are presented in Chapter 4.

$$\frac{\partial \bar{\rho}\tilde{h}}{\partial t} + \frac{\partial}{\partial x_j}(\bar{\rho}\tilde{h}\tilde{u}_j) = \frac{\partial}{\partial x_j}\left[\left(\frac{\tilde{\mu}}{Pr} + \frac{\tilde{\mu}_t}{Pr_t}\right)\frac{\partial \tilde{h}}{\partial x_j}\right] \tag{2.40}$$

2.3 Numerical Description

To solve the filtered governing equations presented in the previous sections, it is necessary to discretise the problem in space and time. By inspection of the general transport equation (Eq. 2.6) one may notice that the terms requiring spatial discretisation are the ones concerning convection and diffusion, whereas the accumulation term requires temporal discretisation. Discretisation via the Finite Volume Method (used in this work) is introduced in the following subsections, however for a more detailed explanation the reader is referred to [79, 174].

The general transport equation (Eq. 2.6) for the scalar Φ is volume-integrated over an arbitrary volume ΔV:

$$\int_{\Delta V} \frac{\partial \Phi}{\partial t} dV + \int_{\Delta V} \frac{\partial}{\partial x_j}(\Phi u_j) dV = -\int_{\Delta V} \frac{\partial J_{\Phi,j}}{\partial x_j} dV + \int_{\Delta V} S_\Phi dV \tag{2.41}$$

The Gauss-Integration formula (Eq. 2.42) is then applied to transform the convection and diffusion terms into fluxes over $\partial \Delta V$. Here the volumes are replaced by the surface elements dA, and the unit vector normal to the surface n_j.

$$\int_{\Delta V} \frac{\partial}{\partial x_j} \phi dV = \int_{\Delta A} \phi n_j dA \tag{2.42}$$

The standard integral form of the transport equation is then obtained by performing the above substitution and writing the time-derivative term outisde the integral, as in Eq. 2.43.

$$\frac{\partial}{\partial t}\left(\int_{\Delta V}\Phi dV\right)+\int_{\Delta A}(\Phi u_j)n_j dA=-\int_{\Delta A}J_{\Phi,j}n_j dA+\int_{\Delta V}S_\Phi dV \quad (2.43)$$

2.3.1 Convection

The convection term from Eq. 2.43 can be discretised for an arbitrary control volume, where $F_{f,C}$ describes the convective (subscript C) flux over an arbitrary surface (subscript $f =$ *north, east, south, west, front or back surfaces*).

$$\int_{\Delta A}(\Phi u_j)n_j dA=\sum_f F_{f,C} \quad (2.44)$$

The values of Φ are averaged at the cell-surface centres and as such one may deduce that $\int_{\Delta A_f}\Phi dA \approx \Phi_f \Delta A_f$. It is also worth noting that in this work equally sized cubic cells are used, and hence cell-surface areas can be simplified to the square of the length Δ, i.e. $\Delta A_f = \Delta^2$. With this information, it is possible to calculate the convective fluxes $F_{f,C}$ over a surface A_f as:

$$F_{f,C}=\Phi_f u_f \Delta^2 \quad (2.45)$$

Where u_f is the surface normal velocity component. All conserved scalars are stored at the cell-centres, however velocity is interpolated at the cell faces once, used for the calculation of all fluxes, and is then independently corrected in a projection step [157]. Several differencing schemes exist in literature, and the most common are described below. Adequate selection of the differencing scheme can be crucial for both accuracy and stability.

Upwind Differencing Scheme (UDS)

A very basic differencing scheme is the UDS, which consists in equating the value of the scalar at each cell-face to that of the upstream cell's centre (Eq. 2.46). Whereas this scheme is computationally efficient and stable, it can lead to false diffusion.

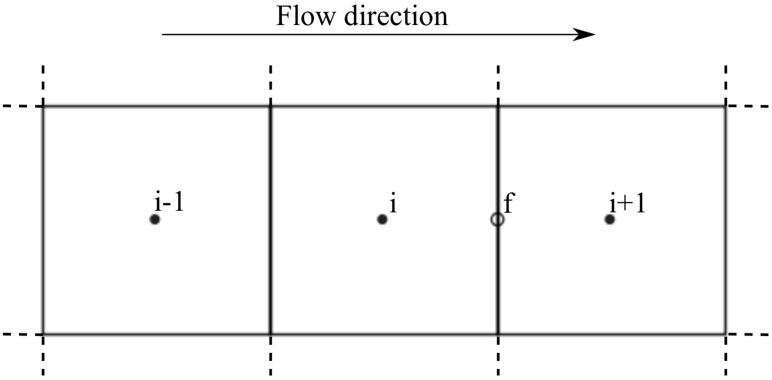

Figure 2.1: Illustration of neighbouring cells.

$$\Phi_f = \Phi_i \tag{2.46}$$

Central Differencing Scheme (CDS)

Another relatively simple and common differencing scheme is the CDS. Here an average of the cell-centred values of the adjacent cells (or a linear interpolation for non-equidistant grids) is taken to evaluate the cell-face value (Eq. 2.47). This scheme however is *non-bounded*, and can give rise to large oscillations, or unphysical quantities, for example leading to negative or greater than unity mass fractions ($Y_\alpha > 1$ or $Y_\alpha < 0$).

$$\Phi_f = \frac{\Phi_i + \Phi_{i+1}}{2} \tag{2.47}$$

Total Variation Diminishing (TVD)

A TVD scheme can be seen as a compromise between the previously discussed UDS and CDS schemes, as it includes both terms, and results in more stable (less oscillatory), conservative (less diffusive) results. It can be expressed, for example, as in Eq. 2.48.

$$\Phi_f = \Phi_i + \frac{B(r)(\Phi_i - \Phi_{i-1})}{2} \tag{2.48}$$

where the flux limiter *B(r)* depends on the gradient r:

$$r = \frac{\Phi_{i+1} - \Phi_i}{\Phi_i - \Phi_{i-1}} \tag{2.49}$$

Several flux limiter functions have been proposed in literature [139, 164, 172, 197], however the description here is limited to the CHARM limiter [197], as this is the one used in the current work:

$$B(r) = \begin{cases} r(3r+1) & : \quad r > 0 \\ 0 & : \quad r \leq 0 \end{cases} \tag{2.50}$$

2.3.2 Diffusion

As in Eq. 2.44, the diffusive term can be discretised for an arbitrary control volume (Eq. 2.51) and simplified to Eq. 2.52. In the equations below $F_{f,D}$ describes the diffusive flux (subscript D) over an arbitrary surface *f*, and $J_{\Phi,j}$ is proportional to the gradient of Φ (Eq. 2.53), where D_Φ is the diffusion coefficient.

$$\int_{\Delta A} J_{\Phi,j} n_j dA = \sum_f F_{f,D} \tag{2.51}$$

$$F_{f,D} = (J_{\Phi,j})_f n_j \Delta^2 \tag{2.52}$$

$$(J_{\Phi,j})_f = -D_\Phi \frac{\partial \Phi}{\partial x_j} \tag{2.53}$$

The diffusion gradient at the cell-surface is then obtained from the values of the neighbouring cells (Eq. 2.54).

$$(J_{\Phi,j})_f \approx -D_\Phi \frac{\Phi_i - \Phi_{i-1}}{\Delta} \tag{2.54}$$

Substituting Eq. 2.53 and Eq. 2.54 into Eq. 2.52 and simplifying, one obtains the discretised equation for the diffusive flux:

$$F_{f,D} = D_\Phi (\Phi_i - \Phi_{i-1}) \Delta \tag{2.55}$$

2.3.3 Time Integration

The scalar transport equation in terms of its time-derivative reads:

$$\frac{\partial \Phi}{\partial t} = -\frac{\partial}{\partial x_j}(\Phi u_j) - \frac{\partial J_{\Phi,j}}{\partial x_j} + S_\Phi \tag{2.56}$$

To simplify this brief introduction to time integration, the right-hand side of Eq. 2.56 is abbreviated to RHS(Φ) in this section. The simplest time integration scheme is the *Euler-explicit* scheme, which computes the value of the scalar Φ at a time $t + \delta t$ by adding its value at a time t, with the product of the new value of the RHS(Φ) and the time interval δt, as in Eq. 2.57.

$$\Phi^{t+\delta t} \approx \Phi^{t} + \mathrm{RHS}(\Phi^{t})\delta t \tag{2.57}$$

However such a scheme is only first-order accurate, and causes errors that reduce stability. In this work in fact, a third-order low storage Runge-Kutta scheme [189] is used. In simple terms, this scheme divides a single time-step into three intermediate steps that are weighted in a way that increases accuracy and stability. For further details the reader is referred to Kempf's thesis [79].

The stability and accuracy of a simulation can be greatly influenced by the time-step width. Data such as transported scalars should not be allowed to *jump* cells between time-steps so as to avoid instabilities, and this is what usually determines the maximum time-step width. A carefully chosen, static time-step width may be used, or as in the present work, a varying time-step that satisfies the CFL criterion (Courant, Friederichs and Lewy [37]) can be calculated (Eq. 2.58).

$$\mathrm{CFL} = \frac{\delta t\,|u|}{\Delta} < 1.0 \tag{2.58}$$

It is important to note that the CFL criterion only accounts for convection, and for problems with very fine grids the time step width might become controlled by diffusion, thus requiring a different stability criteria. However in the present work, relatively coarse grids and high velocities are involved, and as such the time step width is always convection-controlled, justifying the use of the CFL criterion.

2.3.4 Boundary Conditions

In this section the different boundary conditions used in this work to solve the various transport equations are presented. Three different types of boundaries are dealt with, namely inlets, outlets and walls, briefly presented in this respective order in the following subsections.

Inlet Boundaries

Throughout this work the inflow boundaries are described with *Dirichlet* conditions, which by definition set an arbitrary value for each quantity Φ, as in Eq. 2.59 below. In order to model flows, the averaged inlet conditions must always be specified, and therefore setting the inflow boundaries to known values is a non-trivial operation.

$$\Phi = \Phi_{in} \tag{2.59}$$

However when dealing with turbulent flows, as is the case in this work, the flow at the inlet will be experiencing fluctuations, and hence cannot be described by a mean quantity on it's own. In order to describe appropriately the turbulent fluctuations in a given inlet, both their magnitude and lengthscale must be represented accurately. If one were to impose random and un-correlated fluctuations in an inlet, these would rapidly dissipate as they would likely cancel each other out. It is therefore important to consider the size of the eddies passing through an inlet, and ensure that the fluctuations are accurately correlated in their spatial discretisation, to accurately represent the turbulent fluctuations.

In this work turbulent inflow conditions are generated using the artificial turbulence generator developed by Klein *et* al. [86] and later extended by Kempf *et* al. [78]. This inflow generator creates spatially-correlated artificial turbulence by satisfying the magnitude of the inflow fluctuations (by specifying the Reynolds stress tensor) and their characteristic eddy size (by specifying an inflow lengthscale). A detailed description of this method is beyond the scope of this work however, and the interested reader is referred to [79, 157, 190].

Outlet Boundaries

Outflow boundaries in this work are described using *von Neumann* boundary conditions, as is common in CFD. In this condition a constant value C_{vN} is set for the gradient of a quantity $\partial\Phi/\partial x_j$ at the interface with a given boundary, in a direction normal to the boundary $\mathbf{\hat{n}_j}$.

$$\frac{\partial \Phi}{\partial x_j} \hat{\mathbf{n}}_{\mathbf{j}} = C_{vN} \tag{2.60}$$

The value of C_{vN} is normally set to zero, and positive outflow is enforced by clipping negative outflow velocities.

Walls

Realistic turbulent reacting flow applications, such as the combustion chambers of gas-turbines or large industrial furnaces to name but a few, are normally confined by walls. Resolving the near-wall flow in LES is a computationally expensive task, and even more so when dealing with complex geometries. However the present work is restricted to simple geometries discretised on equally-sized cubic cells, and applications where the near-wall flow is of lesser interest, since the bulk of the flow is generally far from the walls. This makes the use of the *Immersed Boundary* (IB) technique an appealing one, since it is computationally very efficient, and of reasonable accuracy if the near-wall flow is not of great interest. The IB technique works by completely blocking out specific cells where walls are present. Cells neighbouring the blocked-off regions have velocities and diffusive fluxes in the direction normal to the wall re-set to zero, and their convection is recomputed using the upwind differencing scheme, which only considers the upstream cell.

3 Coal Combustion

In this section an introduction to the properties of coal, its combustion process and the modelling approach is given. The coal combustion models and the two-way coupling technique presented in this section have been implemented by Benjamin Mario Franchetti, whereas the Lagrangian particle dynamics description and parallelisation have been implemented by Yagos Pesmazoglou. For further details the reader is referred to Franchetti's PhD thesis [52].

3.1 Coal Properties and Characterisation

Unlike many fuels which have standard compositions and properties, different coal types exist, and their properties can be very different from one another [188], which can greatly influence the combustion process. In this section, a brief introduction to the different constituents of coal, and their experimental methods of characterisation is given.

3.1.1 Proximate Analysis

Coal is generally made up of *volatile matter, fixed carbon, moisture* and *ash,* however the proportions in which these are found varies from type to type.

Volatile matter consists of a mixture of gases (usually carbon dioxide, carbon monoxide and several hydrocarbons) and tar, which are retained as solids in the coal particle at room temperature. As heat is supplied however, the gases leave the particle by means of a process known as *devolatilisation* (see Sec. 3.2.1). As coal is porous in nature, it can retain considerable amounts of water, or *moisture,* which evaporates with heat and inevitably cools the combustion process. *Ash* is an inert constituent of coal, which generally consists of hydrated aluminia silicates, iron pyrites, calcium and magnesium carbonates, and alkali chlorides [188]. Once all the volatiles have been emitted from a coal particle, and all the moisture has evaporated, the remaining coke (minus the ash) is referred to as *fixed carbon.*

A *proximate analysis* is usually conducted on different coal types in order to determine the proportions of its constituents, and to rank it against other types. The coal rank generally increases with higher fixed carbon content, whereas it decreases with higher moisture and ash proportions (as these are inert), and higher volatile matter content. For a typical bituminous coal, common constituent proportions are 50-60% fixed carbon, 5-10% moisture, 10-15% ash and 20-30% volatile matter by mass [188].

3.1.2 Ultimate Analysis

A *ultimate analysis* is also performed on different coals to report the proportions of its constituent elements, usually *hydrogen, carbon, oxygen, nitrogen* and *sulfur.* This data is usually given on a dry-ash-free (daf) basis, which means that the inert species (moisture and ash) are excluded.

As an example, a proximate and ultimate analysis for a high-volatile bituminous coal of the Saar-region can be found in Table 6.2.

3.1.3 Coal Properties

The density of a coal particle can be defined in terms of its true density $\rho_{p,T}$, or the apparent density $\rho_{p,A}$. The true density assumes the coal particle has no internal pores, and can be calculated on a *daf* basis using Eq. 3.1, where Y_i represents the mass fractions of the coal's constituent elements, $A_{w,i}$ are the atomic weights of said elements, and c_i are model constants which were obtained experimentally [116, 145].

$$\frac{1}{\rho_{p,T,daf}} = \sum_{i=1} c_i \frac{Y_i}{A_{w,i}} \tag{3.1}$$

In practice however, coal is very porous in nature, and as such the apparent density is a much more useful quantity. The apparent density can be measured experimentally, and the most common approach is to immerse a particle in mercury and increase the pressure until all of the particle's pores are filled; the change in the level of mercury is measured and used to obtain the particle's apparent density [145]. Once both the true and apparent densities are known, the particle's porosity θ can be defined, Eq. 3.2.

$$\theta = 1 - \frac{\rho_{p,A}}{\rho_{p,T}} \tag{3.2}$$

Throughout the combustion process, as the particle heats up, devolatilises, and burns, it's density is constantly changing. However, modelling the particle's change in density is quite arduous, and as often done by other authors, throughout this work the density is assumed to stay constant.

Modelling the changes in the coal's specific heat capacity is another complex task, as this changes considerably throughout the whole combustion process. Several models have been proposed relating a particle's specific heat capacity to its' temperature [115], however the accuracy of such models is difficult to predict and as such in several works a constant particle specific heat capacity is retained, with typical values ranging from $1.1kJ/kgK$ to $1.6kJ/kgK$ [5, 161, 180]. Throughout this work, a fixed coal specific heat capacity is also assumed.

3.2 Combustion Process and Modelling Approach

The coal combustion process is complex compared to gaseous combustion, and involves different steps, which are outlined in this chapter. Figure 3.1 attempts to represent this process in a simple way. As pulverised coal enters a burner it heats up rapidly. The volatile matter is emitted from the particle in a process known as *devolatilisation,* and the volatiles (gases) then burn with the surrounding oxygen. The particle is then left with char and ash once all volatiles and moisture have been emitted. The char (solid) then slowly combusts with the surrounding oxidiser, and the remaining inert ash is transported, having a negligible effect on the combustion process.

3.2.1 Devolatilisation

Devolatilisation starts at around $500K$, and the typical gases emitted in this process are hydrogen, carbon dioxide, carbon monoxide, water vapour, HCN, NH_3 as well as various hydrocarbons and tar [5, 154]. This process is generally very fast as heating rates in a coal burner are of the order of $10^5 K/s$, and typically coal particles start emitting volatiles within microseconds [188].

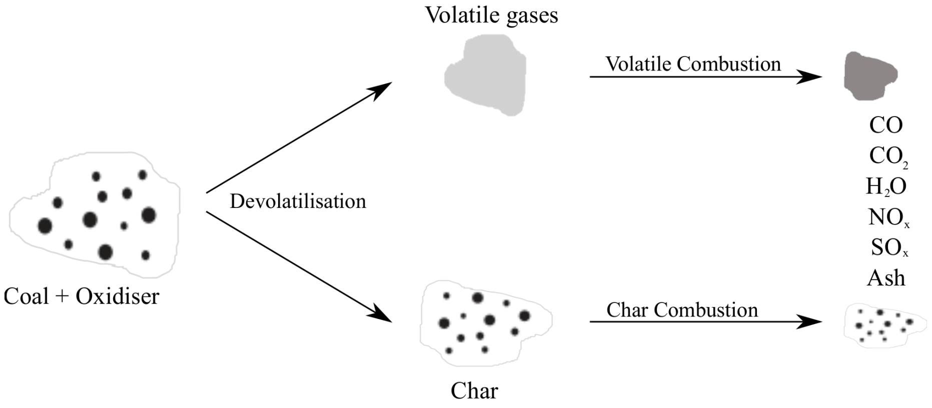

Figure 3.1: Schematic representation of the coal combustion process.

Both the devolatilisation rate and the constituents of the volatile gases require adequate modelling in order to appropriately simulate the combustion process. Various models to simulate the rate at which volatiles are emitted exist, varying in complexity and accuracy.

The simplest model is known as the *constant rate* model [182, 183], which assumes the gases begin to leave the particle above a certain temperature ($T > 500°C$), and are henceforth emitted at a linear rate until they reach a peak temperature ($T = 1000°C$) at which point they are all emitted.

A more advanced model is the *single-step* model [6], which considers the initial mass of volatile matter and calculates the rate at which volatiles are emitted with an Arrhenius expression. This requires knowledge of the Arrhenius constants, namely the pre-exponential factor and the activation energy, which can be obtained experimentally or by using sophisticated codes such as the Functional Group-Depolymerization Vaporization and Cross-Linking model (FG-DVC) [154], or the Chemical Percolation and Devolatilisation (CPD) model [49, 50]. These functional group models are very useful to obtain accurate volatile release rates as well as detailed volatile compositions. However they are far too expensive (computationally) to integrate directly in CFD, and as such they are usually used as pre-processors to obtain model constants, as is the case with the single step model described above.

In the single step model the constants are independent of the individual particle specific heating rates, whereas it has been shown that a link between temperature and devolatilisation rate exists [88]. Consequently, Kobayashi et al. [88] developed a model known as the *two competing reaction mechanism*, which splits the devolatilisation process into two *pseudo* reactions, one dominant at low temperatures, and the other one at higher temperatures.

Another approach taken by Hashimoto et *al.* [64] was to tabulate the different Arrhenius constants against temperature and heating rates, to account for the relationship between the two.

Throughout this work, the single-step reaction rate model by Badzioch and Hawksley [6] is used to describe the devolatilisation process, a brief description of which is given below. The rate at which volatiles are emitted from a coal particle is described by Eq.3.3, assuming a single reaction.

$$\frac{dV}{dt} = A_v T_p^{\beta} \exp\left(\frac{-E_v}{RT_p}\right) \times (VM - V) \tag{3.3}$$

In this equation the Arrhenius constants A_v and E_v are the pre-exponential factor and activation energy respectively, the determination of which has been briefly discussed above, and β is the temperature exponent. The volatile yield is V, and VM represents the initial volatile matter in the coal particle, whereas T_p and R represent the particle temperature and the universal gas constant respectively.

The initial volatile matter VM however, isn't the volatile matter obtained by the proximate analysis VM_0, but is in fact adjusted by a Q-factor, as in Eq.3.4.

$$VM = VM_0 \times Q \tag{3.4}$$

During pyrolysis, the thermal decomposition of a coal particle depends on the particle's heating rate and its final temperature [6]. At high heating rates, the volatile yield from a coal particle is normally higher than the actual volatile matter content found from the coals' proximate analysis, as more char decomposes to form volatile matter [6, 85]. An arbitrary factor Q is therefore introduced to account for this difference, the value of which can be either determined experimentally or using functional group models. Further, there is no unique Q-factor value for any given coal type, as this depends on the specific cases' heating rates and temperatures, however values usually lie in the range $Q = 1.0 - 2.0$ [85].

3.2.2 Volatiles Composition

Volatile gases are made up of light gases (CO, CO_2, H_2, H_2O, CH_4, C_2H_4, C_2H_2, ...) and heavy gases such as *tar*. They can either be approximated to a single or a few hydrocarbon species, or obtained either experimentally or by using functional group models, depending on the desired accuracy, and given sufficient information of the coal used. However, modelling the release and transport of each specie individually would be prohibitively expensive in LES, and as such in this work all the volatiles are treated as a single postulate substance $C_\alpha H_\beta O_\gamma N_\delta$. The volatiles then react with oxygen in a one-step reaction, as in Eq. 3.5 below.

$$C_\alpha H_\beta O_\gamma N_\delta + \left(\frac{\alpha}{2} + \frac{\beta}{4} - \frac{\gamma}{2}\right) O_2 \rightarrow \alpha CO + \frac{\beta}{2} H_2O + \frac{\delta}{2} N_2 \tag{3.5}$$

The values of the volatile composition and stoichiometric coefficients α, β, γ and δ in the equation above can be obtained with Eq. 3.6, where $x = \alpha, \beta, \gamma, \delta$, the subscript $i = C, H, O, N$ respectively, and $Y_{i,vg}$ is the mass fraction of element i in the volatiles. The molecular weight M_{W_i} of the elements i is known, whereas the molecular weight of the volatiles $M_{W_{vg}}$ is estimated.

$$x = Y_{i,vg} \frac{M_{W_{vg}}}{M_{W_i}} \tag{3.6}$$

The mass fractions of the elements C, H, O, N of the volatile gases can be found using the mass fractions resulting from the ultimate analysis of the coal $Y_{i,U}$, as in Eqs. 3.7a-3.7d.

$$Y_{C,vg} = \frac{Y_{C,U} - Y_{FC,daf}}{Y_{VM,daf}} \tag{3.7a}$$

$$Y_{H,vg} = \frac{Y_{H,U}}{Y_{VM,daf}} \tag{3.7b}$$

$$Y_{O,vg} = \frac{Y_{O,U}}{Y_{VM,daf}} \tag{3.7c}$$

$$Y_{N,vg} = \frac{Y_{N,U}}{Y_{VM,daf}} \tag{3.7d}$$

where $Y_{FC,daf}$ and $Y_{VM,daf}$ represent the dry-ash-free mass fractions of fixed carbon and volatile matter found in a coal particle, respectively. On a *daf* basis, the coal particle is only made of fixed carbon and volatile matter, and as such their mass fractions can be obtained from the proximate analysis.

Since the volatiles are described using a postulate substance, their enthalpy of formation $h_{f,vg}$ cannot be directly found in literature, but rather must be calculated. The Lower Heating Value (LHV) of coal on a *daf* basis is the summation of the LHV's of fixed carbon and the volatiles factored by their respective mass fractions, Eq. 3.8.

$$\text{LHV}_{coal,daf} = \text{LHV}_{FC,daf} Y_{FC,daf} + \text{LHV}_{VM,daf} Y_{VM,daf} \tag{3.8}$$

The lower heating value of coal $\text{LHV}_{coal,daf}$ is usually obtained by experiments, and the LHV of fixed carbon can be taken to be $\text{LHV}_{FC,daf} = 32.76 MJ/kg$ assuming that the fixed carbon content is purely C. Rearranging Eq. 3.8, $\text{LHV}_{VM,daf}$ can be readily obtained. The enthalpy of combustion of the volatiles (Eq. 3.5) can be calculated as $h_R = \text{LHV}_{VM,daf} \times M_{W_{vg}}$. Knowing the enthalpies of formation of all other species from literature, and the enthalpy of combustion of the reaction, one can use Hess's law to obtain the enthalpy of formation of the volatiles, Eqs. 3.9a-3.9b.

$$h_R = \sum h_{f,prod} - \sum h_{f,reac} \tag{3.9a}$$

$$h_{f,vg} = \alpha h_{f,CO} + \frac{\beta}{2} h_{f,H_2O} + \frac{\delta}{2} h_{f,N_2} - \left(\frac{\alpha}{2} + \frac{\beta}{4} - \frac{\gamma}{2}\right) h_{f,O_2} - h_R \tag{3.9b}$$

3.2.3 Volatiles Combustion

As volatiles are emitted from the coal particle, they combust with the surrounding oxidiser, forming mainly carbon dioxide, carbon monoxide and water vapour. The combustion mode is generally non-premixed, however this cannot be modelled easily with the common *mixture fraction* approach (see Sec.2.1.1), as the gases do not enter the domain from it's boundaries, but are generated by the devolatilisation process, and therefore the mixture fraction approach would have to be extended to include a source term. Despite this, recently Stöllinger et *al.* proposed a two-mixture fraction approach, which was applied to the RANS of coal combustion [160, 161].

Nonetheless, simpler gaseous combustion models have been more commonly adopted to model this process, involving the transport of the individual mass fractions. The simplest model is known as the *mixed-is-burnt* [16] model, which assumes infinitely fast chemistry, where the reaction rate is purely dominated by mixing, or in the case of coal combustion by devolatilisation. If stoichiometric amounts of fuel and oxidiser mix, the reactants combust instantly and are converted into products, with no excess. For a lean mixture all the fuel is assumed to burn, leaving excess air, and conversely for a rich mixture all the air and the stoichiometric proportion of fuel are converted to products, leaving some excess fuel. The temperature is then computed by performing a weighted average of the species, assuming that the products are at adiabatic flame temperature and the reactants at their unburnt temperature. This is clearly a big assumption as heat transfer and the ignition limits are completely neglected, as well as intermediate temperatures.

A more popular approach to model the volatile combustion is the eddy break-up model, originally proposed by Spalding in a RANS framework [156]. In this model the reaction rate is determined by turbulent mixing, and limited by the smallest concentration of fuel, oxidiser or products in a given control volume. The reaction rate is calculated explicitly, and the temperature is obtained by transporting enthalpy. In this way a more accurate representation is obtained, and heat transfer effects are more easily incorporated.

However both models assume infinitely fast chemistry which is physically not correct, and can cause numerical modelling stability issues due to the instantaneous formation of large amounts of products, and their consequent sudden expansion. This problem can be partially solved, or relaxed, via the use of subgrid models (see Sec.2.2.3), which also aim to increase the accuracy of the solution.

A more detailed representation of the chemistry is possible via the use of finite rate chemistry models which consider the combustion of several hydrocarbons, giving a more accurate representation of the combustion process. However for LES of gaseous combustion, let alone coal combustion, the transport of hundreds of species and the computation of thousands of reactions would be prohibitively expensive, and often unnecessary to achieve the required level of accuracy [125]. Furthermore, a reasonable simulation with detailed chemistry would require a very fine DNS like grid or the use of complex subgrid models to resolve the thinnest, smallest structures of a flame, both of which would further increase the computational cost. Simpler finite rate chemistry models exist, such as the 4-step mechanism proposed by Jones and Lindstedt [72], which can provide good accuracy whilst only considering C_nH_{2n+2} hydrocarbons up to butane $n = 4$, thereby limiting the computational resources required. However, even with this robust mechanism, a very fine resolution in space and time is necessary, leading to a very high computational cost.

Throughout this work, the volatile combustion is described using the Eddy Break-Up (EBU) model [156] adapted to LES by Hu et *al.* [67] and Zhou et *al.* [198]. A two-step chemical mechanism is considered, Eqs. 3.10a-3.10b, where the volatiles (represented by the postulate substance $C_\alpha H_\beta O_\gamma N_\delta$ detailed in Sec. 3.2.2) react with O_2 in the first step, and the CO produced then further reacts with oxygen in the second step to create CO_2.

$$C_\alpha H_\beta O_\gamma N_\delta + \left(\frac{\alpha}{2} + \frac{\beta}{4} - \frac{\gamma}{2}\right) O_2 \rightarrow \alpha CO + \frac{\beta}{2} H_2O + \frac{\delta}{2} N_2 \tag{3.10a}$$

$$CO + \frac{1}{2} O_2 \rightarrow CO_2 \tag{3.10b}$$

The rate at which the reactions occur is limited by the least abundant mass fraction of fuel $\tilde{Y}_{fu}$, oxidiser $\tilde{Y}_{ox}$ and products $\tilde{Y}_{pr}$ in a given control volume, as described in Eq. 3.11.

$$\tilde{w}_{fu} = c_1 \overline{\rho} \tilde{S} \min\left(\tilde{Y}_{fu}, \frac{\tilde{Y}_{ox}}{s}, c_2 \frac{\tilde{Y}_{pr}}{1+s}\right) \tag{3.11}$$

There are two model constants, c_1 and c_2, and their suggested values are $c_1 = 4.0$ and $c_2 = 0.5$ [67, 198]. To the best of the author's knowledge however, there is no apparent specific reason for choosing such values for LES, and a sensitivity analysis on these two parameters could be worthwhile. Finally, the local strain rate $\tilde{S}$ can be computed using the turbulent viscosity (approximated with the Smagorinsky model, Eq. 2.31), according to Eq. 3.12:

$$\tilde{S} = \sqrt{2\tilde{S}_{ij}\tilde{S}_{ij}} \approx \frac{\mu_t}{\overline{\rho}\left(C_s\Delta\right)^2} \tag{3.12}$$

Whereas this model can yield good results in terms of the description of the volatiles combustion, its simplicity does not come without limitations. Both Hu et *al.* [67] and Zhou et *al.* [198] agree that in cases where the effects of chemical kinetics become important (slower reactions, less turbulence-dominated), the model does not perform well, as is to be expected with all models which assume infinitely fast chemistry. Furthermore, the two model constants make this model very adjustable, in a sense that the parameters can be tweaked to fit experimental results, so that its usefulness in actually predicting combustion is limited. The main advantage of this model is it's simplicity and low computational cost requirements, which are significant for simulating coal combustion. However, for future research it is advised to look into models which do not include any arbitrary parameters, or where computational resources permit this, finite rate chemistry models. Nonetheless, in an LES framework the EBU is expected to perform much better than in RANS (for which it was originally developed), as the large scale mixing is already accurately resolved, whereas in RANS it is entirely modelled.

3.2.4 Char Combustion

Once the volatiles have been emitted, the remaining char combusts at a later stage and with a slower rate (generally an order of magnitude slower than the devolatilisation process), mainly forming carbon dioxide, carbon monoxide and various polluting nitrogen oxides (NO_x). However this process is relatively complex to model as the particles are constantly experiencing physical and chemical changes. For this reason char combustion is often described by defining three *zones* [98, 187].

The first zone (*zone 1*) concerns low temperatures or small particles, where oxygen diffusion is not limiting the reaction. The reaction is slow, so that the oxygen penetrates the particles, which start burning from inside. The reacting oxygen is constantly replaced, and the particle decreases in density whilst staying roughly the same size.

Zone 2 occurs at higher temperatures, where the reaction is controlled by both oxygen diffusion and the chemical reaction itself. The reaction is faster so less oxygen can diffuse through the pores of the char, and the particle burns both within the pores and at the surface, thus decreasing in both size and density.

At very high temperatures instead *zone 3* occurs: the reaction is much faster and as a result there is no oxygen diffusion and all the reaction occurs at the surface of the particle. Consequently, the density of the particle doesn't change much whilst it decreases in size.

Throughout this work it is assumed that char is made up entirely of carbon, and a single heterogeneous reaction forming carbon monoxide is assumed, Eq. 3.13.

$$C_{char} + \frac{1}{2}O_2 \rightarrow CO \tag{3.13}$$

Two of the most popular models for simulating char combustion are the *Baum and Street* model [10], and the *intrinsic reaction rate* model by Smith [151, 152], both of which can yield accurate predictions. The Baum and Street model describes the chemical reaction rate of the char with an Arrhenius expression, similar to the single step devolatilisation model (Sec 3.2.1), and thereby shares the same inconvenience of having to determine the pre-exponential factor and activation energy of the char experimentally, for each specific coal type. The intrinsic reaction rate model instead, used throughout this work and described in greater detail below, requires knowledge of certain physical information of the coal particles.

The change in mass due to char combustion of a coal particle $dm_{p,char}/dt$ is given in Eq. 3.14, where $A_p = \pi d_p^2$ is the particle's surface area, and X_{ox} is the mole fraction or partial pressure of the oxidiser.

$$\frac{dm_{p,char}}{dt} = A_p p_g X_{ox} \frac{R_{ox} R_c}{R_{ox} + R_c} \tag{3.14}$$

where R_{ox} and R_c are the bulk molecular mass diffusion rate (Eq. 3.15) and the chemical reaction rate (Eq. 3.16) respectively.

$$R_{ox} = C_{diff} \frac{T_m^{0.75}}{d_p} \tag{3.15}$$

Here, the constant C_{diff} is given the value of the bulk diffusion coefficient of oxygen into air $C_{diff} = 5 \times 10^{-12} m^3/K^{0.75}$, whereas $T_m = (T_g + T_p)/2$ represents the *mean* temperature at the particle surface [161].

According to the intrinsic reaction rate model [151, 152], the chemical reaction rate presented in Eq. 3.16 depends on the particle characteristic size γ, the apparent density $\rho_{p,A}$, the specific internal surface area S_a (m^2/g), the effectiveness factor μ_e and the intrinsic reaction rate k_i.

$$R_c = S_a \mu_e \gamma \rho_{p,A} k_i \tag{3.16}$$

All particles in this work are assumed to be spherical, so the characteristic size is taken as $\gamma = d_p/6$. The initial internal specific surface area $S_{a,0}$ can be found in literature for various chars, or alternatively can be estimated using an empirical relationship [161, 187] based on the carbon mass fraction (daf) of the specific coal type. Throughout this work the specific internal surface area of the particles is assumed to stay constant, and the values used are based on those found in literature.

The effectiveness factor μ_e relates the rate of actual carbon consumption to the maximum rate obtainable if there were no pore diffusion resistance (Eq. 3.17), where ϕ is the Thiele modulus, obtained from Eq. 3.18 [5].

$$\mu_e = \frac{3}{\phi^2}\left(\phi \coth \phi - 1\right) \tag{3.17}$$

$$\phi = \frac{d_p}{2} \times \left(\frac{s S_a \rho_{p,A} k_i p_{ox}}{D_e C_{ox}}\right)^{\frac{1}{2}} = \frac{d_p}{2} \times \left(\frac{s S_a \rho_{p,A} k_i R T_p}{D_e M_{W,ox}}\right)^{\frac{1}{2}} \tag{3.18}$$

Here, $s = 1.33$ is the stoichiometric coefficient assuming that the reaction occurring between carbon and oxygen forms carbon monoxide CO, and $C_{ox}(kg/m^3)$ and $p_{ox}(kPa)$ are the concentration and partial pressure of the oxidiser in contact with the coal particle, respectively.

$$D_e = \frac{\theta}{\tau^2}\left(\frac{1}{D_{kn}} + \frac{1}{D_o}\right)^{-1} \tag{3.19}$$

The effective diffusivity coefficient D_e (Eq. 3.19) is affected by either bulk diffusion D_o or Knudsen diffusion D_{kn} (Eq. 3.20), depending on the pore size of the char. If the pores are much larger than the mean free path of the diffusing gas molecules, bulk diffusion is predominant. If however the pores are very small (2-50 nm), Knudsen diffusion will be dominant due to the molecules colliding with the pore walls [5, 144]. The tortuosity of the pores is assumed to be constant $\tau = \sqrt{2}$, which corresponds to an intersecting angle of 45° [5], whereas the porosity is calculated according to Eq. 3.2.

$$D_{kn} = 97 r_p \sqrt{\frac{T_p}{M_{W,ox}}} \tag{3.20}$$

The Knudsen diffusion coefficient depends on the pore radius r_p, which can be assumed to have a constant size $r_p = 6.0 \times 10^{-8} m$ [5] as undertaken in this work, or calculated with a mathematical relationship [152].

Finally, the intrinsic reaction rate k_i has an Arrhenius form, Eq. 3.21, where the pre-exponential factor $A_{i,char} = 3050 kgm^{-2}s^{-1}$ and the activation energy $E_{i,char} = 161.0 MJ/kmol$ are obtained from a line of best fit of several chars, at standard pressure of 1atm [151, 152].

$$k_i = A_{i,char} \exp\left(\frac{-E_{i,char}}{RT_p}\right) \tag{3.21}$$

The particle's diameter d_p varies as coal undergoes devolatilisation and char combustion. The char burnout and the variation in particle diameter can be calculated using a simple relationship [5, 145], which takes into account the presumed char combustion zone.

Throughout this work however it is assumed that char combustion always occurs in zone 3, with the simplifying assumption that the coal particle's density remains constant and only the diameter decreases as the coal particles undergo both devolatilisation and char combustion. Assuming spherical particles at all times, the variation in particle diameter can be directly obtained from the variation in particle mass, as the density stays constant.

3.3 Particle Description

In this section the Lagrangian approach used to describe the coal particles is briefly introduced, as well as the heat transfer between the discrete and the continuous phase. The two-way coupling method used to model the influence that the gaseous phase has on the discrete phase and vice-versa is also presented.

For simplicity, and as conventionally done in numerical particles description for coal applications, throughout this work coal particles are assumed to be perfectly spherical, non-deformable, and having infinite heat conductivity, which means that a unique and uniform particle temperature is defined.

3.3.1 Euler-Lagrange Approach

Whereas the continuous gaseous phase is described by Eulerian equations (see Chapter 2), the discrete particle phase is described with Lagrangian equations. A particle's position and direction, and hence it's trajectory, can be described by two ordinary differential equations as in Eq. 3.22 and Eq. 3.23. In these equations the subscript p denotes a specific particle, $\mathbf{x}_p$ represents the position of a particle, and $\mathbf{u}_p$ and $\mathbf{a}_p$ describe the particles' velocity and acceleration.

$$\frac{d\mathbf{x}_p}{dt} = \mathbf{u}_p \tag{3.22}$$

$$\frac{d\mathbf{u}_p}{dt} = \frac{\mathbf{a}_p}{m_p} \tag{3.23}$$

A particles' motion through a turbulent flow is affected by many forces, the most common of which are momentum, gravitation, buoyancy, Brownian and thermophoretic forces. Momentum exchange occurs between the particle and the Eulerian flowfield, and is seen by the particle as drag or lift. Gravitational and buoyancy forces also act (oppositely) on particles, depending on their mass and that of the displaced fluid. At a small scale Brownian forces also act on the particles: the individual molecules of fluid displace a particle with no preferential direction. Thermophoretic forces are caused by temperature gradients in the surrounding fluid, and result in a particle being displaced towards colder fluid molecules. Modelling all these forces on each individual particle is an arduous and expensive task, which fortunately can be simplified. Since coal particles are solid and have a density which is much larger than that of air (the carrying fluid), all Brownian and thermophoretic forces can be ignored, and in some cases gravitation and buoyancy can also be disregarded, as their effect will be small. Therefore the only force to be considered is the momentum exchange between the solid and fluid phase, which takes the form of a drag force, $\mathbf{F}_D$ (Eq. 3.24).

$$\mathbf{F}_D = \frac{3}{4}\frac{\rho_g m_p}{\rho_p d_p} C_D \left(\mathbf{u}_g - \mathbf{u}_p\right) \left|\mathbf{u}_g - \mathbf{u}_p\right| \tag{3.24}$$

In Eq. 3.24 above, the subscript g indicates the gas phase, C_D is the particles' drag coefficient, and d_p is the particles' diameter. Assuming spherical particles, the drag coefficient can be related to the particles' Reynolds number Re_p using the empirical relationship proposed by Yuen-Chen, Eq. 3.25 [194, 195].

$$C_D = \begin{cases} \frac{24}{Re_p}\left(1 + \frac{Re_p^{2/3}}{6}\right) & Re_p \leq 1000 \\ 0.424 & Re_p > 1000 \end{cases} \tag{3.25}$$

Besides fluid-particle interactions, particle-particle interactions exist such as particle collisions, agglomeration and coalescence. However in this work, and in general for pulverised coal combustion, the particles can be assumed to be dilute, and hence all particle-particle interactions can be neglected.

3.3.1.1 Sub-grid Scales

As discussed in Chapter 2, in LES only the filtered quantities, $\tilde{\phi}(x_i, t)$ are known, whereas the sub-grid scales are unknown and require modelling. Since coal particles are much smaller than the LES filter width in this work, the effect of the sub-grid scales on particle motion can become significant, and is modelled using a stochastic process. A review of stochastic models and their application to sub-grid particle dynamics is outside the scope of this work, and the interested reader is referred to [11, 12, 13, 45, 101, 110]. The modelling of the sub-grid scales' influence on the particles has been implemented by Yagos Pesmazoglou, another student in our research group, and is only reported here for completeness.

In this work the *spray-pdf* (probability density function) approach proposed by Bini and Jones [12] is used, where the state of the particles is characterised only in terms of radius r, velocity $\mathbf{v}$, temperature T, and number n. The filtered joint-*pdf* $\overline{P}(\mathbf{v}, R, T, N; \mathbf{x}, t)$ can be obtained from Eq. 3.26 [101].

$$\frac{\partial \overline{P}}{\partial t} + \frac{\partial}{\partial v_j}\left(a_j \overline{P}\right) + \frac{\partial(\dot{R}\overline{P})}{\partial R} + \frac{\partial(\dot{T}\overline{P})}{\partial T} + \frac{\partial(\dot{N}\overline{P})}{\partial N} = 0 \tag{3.26}$$

In Eq. 3.26 above, a_j is the conditional mean particle acceleration (conditioned on the local continuous phase and particle quantities), $\dot{R} = dr/dt$ is the conditional rate of change of particle radius, $\dot{T} = dT/dt$ is the conditional rate of change of particle temperature, and finally $\dot{N} = dn/dt$ is the rate of change of particle number. The particle number varies with the break-up and coalescence of particles, but since particle-particle interactions are ignored in this work, this term is neglected and has only been initially presented here for completeness. The phase space can therefore be reduced to $\{\mathbf{v}, R, T\}$.

Rather than solving the spray-pdf equation (Eq. 3.26) in an Eulerian framework, a Lagrangian trajectory approach is used. Assuming a Markovian evolution for the *spray-pdf*, each path represents a particle's motion and is modelled with an Itô equivalent system of stochastic differential equations [12].

The change in velocity of a particle $d\mathbf{v}_p$ is only influenced by the resolved drag force and the unresolved fluctuations experienced by the particle (first and last term on the RHS of Eq. 3.27 respectively), following the solution of Bini and Jones [12, 13]:

$$d\mathbf{v}_p = \frac{\tilde{\mathbf{u}}_g - \mathbf{v}_p}{\tau_p} dt + \sqrt{C_o \frac{k_{sgs}}{\tau_t}} d\mathbf{W} \tag{3.27}$$

where τ_p is the particle relaxation time (Eq. 3.28), and can be substituted to recover the original formulation in Eq. 3.24.

$$\tau_p^{-1} = \frac{3}{4} \frac{\rho_g C_D}{\rho_p d_p} |\tilde{\mathbf{u}}_g - \mathbf{v}_p| \tag{3.28}$$

The terms in the *sgs* term (last term in Eq. 3.27) are the dispersion constant C_o, the unresolved kinetic energy k_{sgs} (Eq. 3.29), the sub-grid timescale τ_t (Eq. 3.30), which represents the rate of interactions between the particle and turbulence, and the increment of the Wiener process $d\mathbf{W}$. The Wiener term is calculated using $d\mathbf{W} = \mathcal{N}\sqrt{dt}$, where $\mathcal{N}$ is a random variable sampled from a normal distribution with mean 0 and standard deviation 1.

$$k_{sgs} = 2\Delta C_s^{2/3} \tilde{S}_{ij} \tilde{S}_{ij} \tag{3.29}$$

$$\tau_t = \tau_p \left(\frac{\tau_p}{\Delta / \sqrt{k_{sgs}}} \right)^{0.6} \tag{3.30}$$

Finally, the particle position is updated according to Eq. 3.22. Equation 3.26 can be reconstructed by ensemble averaging over the particle trajectories.

3.3.2 Particle Heat Transfer

Modelling the heat transfer between the coal particles and the surrounding gas is a crucial aspect. A coal particles' heat is affected by convection (subscript *con*), devolatilisation (subscript *dev*), char combustion (subscript *char*) and radiation (subscript *rad*), as shown in the particle surface energy balance, Eq. 3.31.

$$m_p C_{p,p} \frac{dT}{dt} = \dot{q}_{con} + \dot{q}_{dev} + \dot{q}_{char} + \dot{q}_{rad} \tag{3.31}$$

Here, $C_{p,p}$ is the particles' specific heat capacity, and it is assumed that the temperature within the particle is uniform. In the following subsections, the equations used to calculate the various heat sources (sinks) $\dot{q}_i$ are presented.

3.3.2.1 Heat Transfer due to Convection

The heat exchange between the particle and the surrounding gas due to convection is a function of the particles' surface area A_p, the temperature gradient across the radius r, and its thermal conductivity λ (Eq. 3.32).

$$\dot{q}_{con} = A_p \lambda \frac{dT}{dr} \tag{3.32}$$

At this point it is convenient to introduce the Nusselt number, which describes the ratio of convective to conductive heat transfer across a boundary:

$$Nu = \frac{h_{con} d_p}{\lambda} \tag{3.33}$$

The convective heat transfer coefficient h_{con} is found as $h_{con} = q/\left(T_g - T_p\right)$, where q is the rate of heat transfer per unit area of a particle, $q = \lambda \left(dT/dr\right)$. Substituting and rearranging, the heat transfer due to convection $\dot{q}_{con}$ becomes:

$$\dot{q}_{con} = \frac{A_p \lambda Nu \left(T_g - T_p\right)}{d_p} \tag{3.34}$$

The Nusselt number is calculated explicitly using the Ranz-Marshall method (Eq. 3.35) [134], where Pr is the Prandtl number, defined by Eq. 3.36.

$$Nu = 2 + 0.552 Re_p^{1/2} Pr^{1/3} \tag{3.35}$$

$$Pr = \frac{\mu C_p}{\lambda} \tag{3.36}$$

3.3.2.2 Heat Transfer due to Devolatilisation

As a particle heats up and undergoes devolatilisation, the particle experiences a change in mass and heat due to the loss of volatile matter. The heat transfer due to devolatilisation is simply dependant on the loss in particle mass due to devolatilisation $\dot{m}_{p,dev}$, and the latent heat of evaporation of the volatiles h_{dev}, as in Eq. 3.37.

$$\dot{q}_{dev} = -\dot{m}_{p,dev} h_{dev} \tag{3.37}$$

Note that since the heat is lost from the particle and given to the surrounding gas, there is a negative sign.

3.3.2.3 Heat Transfer due to Char Combustion

In a similar way to the particle heat transfer due to devolatilisation process, as the char reacts with the surrounding oxygen to form CO (Eq. 3.13), the heat exchange depends on the loss in particle mass due to char combustion $\dot{m}_{p,char}$, and the heat released or absorbed by the particle Q_{char}, as defined in Eq. 3.38.

$$\dot{q}_{char} = \dot{m}_{p,char} Q_{char} \tag{3.38}$$

Note that throughout this work the heterogeneous reaction (Eq. 3.13) is considered to only affect the particle temperature, and not that of the surrounding gas. The heat change in the gas phase is accounted for by the combustion of the newly formed CO (Eq. 3.10b). Further, the problem has been simplified to consider only the reaction of char with oxygen, but in reality, and even more significantly for the case of oxy-coal combustion, the char will also react with CO_2 and H_2O. For more details the interested reader is referred to Wall *et* al. [178], or to Franchetti's PhD thesis [52].

3.3.2.4 Heat Transfer due to Radiation

The heat exchange between a particle and the gas due to radiation is presented in Eq. 3.39, where ϵ_p is the particle emissivity, $I_{b,p}$ the particle blackbody intensity, and G is the total incident radiation in a control volume. The particle blackbody intensity is given in Eq. 3.40, where $\sigma = 5.670373 \times 10^{-8} W m^{-2} K^{-4}$ is the Stefan-Boltzmann constant. For more information on radiation modelling and the evaluation of G and ϵ_p, the reader is referred to Chapter 4.

$$\dot{q}_{rad} = \epsilon_p \frac{\pi d^2}{4} \left(4\pi I_{b,p} - G\right) \tag{3.39}$$

$$I_{b,p} = \frac{\sigma T_p^4}{\pi} \tag{3.40}$$

3.3.2.5 Particle Heat Equation

Having shown how the individual heat exchange terms occurring on a particle are calculated, it is possible to substitute them back in the particle energy balance equation, to obtain the final form. Substituting Eq. 3.34 and Eqs. 3.37-3.39 into Eq. 3.31:

$$\begin{aligned} m_p C_{p,p} \frac{dT}{dt} = \frac{A_p \lambda Nu \left(T_g - T_p\right)}{d_p} - \dot{m}_{p,dev} h_{dev} \\ + \dot{m}_{p,char} Q_{char} + \epsilon_p \frac{\pi d^2}{4} \left(4\pi I_{b,p} - G\right) \end{aligned} \tag{3.41}$$

Rearranging in terms of dT/dt to obtain the final particle heat equation, and using the substitution $m_p = \rho_p \times (4/3)\pi r^3$ and $Pr_g = \mu C_{p,g}/\lambda$ for the convection term, Eq. 3.41 becomes:

$$\begin{aligned} \frac{dT}{dt} = \frac{Nu C_{p,g}}{3 Pr_g C_{p,p}} \left(\frac{T_g - T_p}{\tau_m}\right) - \frac{\dot{m}_{p,dev} h_{dev}}{m_p C_{p,p}} \\ + \frac{\dot{m}_{p,char} Q_{char}}{m_p C_{p,p}} + \frac{\epsilon_p \pi d^2 \left(4\pi I_{b,p} - G\right)}{4 m_p C_{p,p}} \end{aligned} \tag{3.42}$$

The diffusion relaxation time τ_m is equal to $\tau_m = \rho_p 4r^2 / \left(18\mu\right)$ [101]. The gas specific heat capacity $C_{p,g}$ and viscosity μ used in Eq. 3.42 above depend on temperature, and hence require knowledge of the gas temperature surrounding the particle, which will not be the same as that computed at the cell-centre. For this reason a 1/3 rule is used [101, 195] to calculate a reference temperature T_{ref}, (Eq. 3.43), where T_s is the gas-particle surface temperature, taken as the particle temperature, and T_{inf} is the cell-center gas temperature, treated as a far-field temperature.

$$T_{ref} = T_s + \frac{1}{3}\left(T_{\text{inf}} - T_s\right) \tag{3.43}$$

3.3.3 Two-way Coupling

Throughout this chapter, the equations accounting for the effects of the gas phase on the particles have been presented. In this section, the terms describing the effect that the particles have on the gas phase are presented, to complete the two-way coupling description. The coupling terms presented here are all filtered, as they influence the gas phase on a large (resolved) scale, whereas the effects on the sub-grid scales are neglected since they are assumed to have a negligible contribution on the overall flowfield [101].

The total contribution of the particles on the gas phase in a given cell is described by the filtered source term $\overline{\dot{S}_\Phi}$ (Eq. 3.44), where $p = 1, 2, ..., P$ and $S_{p,\Phi}$ is the source term for a given particle p.

$$\overline{\dot{S}_\Phi} = \frac{1}{\Delta^3}\sum_{p=1}^{P} S_{p,\Phi} \tag{3.44}$$

The two-way coupling source terms for mass, species and enthalpy are presented in the equations below. The momentum source term, which describes the effect of the particles' momentum on the gas phase, has not been accounted for since in pulverised coal combustion applications, where the dispersed phase is very dilute, its influence will be negligible [52]. The mass and species source terms are identical, and are due to the devolatilisation and char combustion processes. Finally, the enthalpy source term accounts for the heat gained or lost by the surrounding gas phase as a particle heats up or cools down due to convection, devolatilisation, char combustion, and radiation. The first term on the RHS accounts for convection and radiation of a particle $\dot{q} = \dot{q}_{conv} + \dot{q}_{rad}$, the second term describes the change in enthalpy due to the mass released from the devolatilisation and char combustion processes, and the last term is the enthalpy of vaporisation, which describes the energy required to bring the vaporised solids to the surrounding gas temperature.

$$\dot{S}_{p,mass} = \dot{S}_{p,Y_i} = -\frac{dm_p}{dt} \tag{3.45}$$

$$\dot{S}_{p,h} = -\left(\dot{q} - \frac{dm_p}{dt}h(T_p) + \frac{dm_p}{dt}\left[h_s(T_g) - h_s(T_p)\right]\right) \tag{3.46}$$

3.4 Multiphase Flow Equations for Coal Combustion

Having previously defined the governing equations of fluid-flow and combustion for the description of a single gaseous phase in Chapter 2, and having outlined the two-way coupling approach in Sec. 3.3.3 above, it is now possible to extend the governing equations for the complete description of a multiphase flow. The equation for conservation of mass, Eq. 2.24 is extended as in Eq. 3.47 below to include the mass source terms arising from the mass lost from the particle phase, which are due to the devolatilisation and char combustion processes.

$$\frac{\partial \overline{\rho}}{\partial t} + \frac{\partial}{\partial x_j}(\overline{\rho}\tilde{u}_j) = \overline{\dot{S}}_{mass} \tag{3.47}$$

The effect of the particle's momentum on the gas phase has been neglected, as explained in the previous section, and therefore the conservation of momentum equation for the multiphase flows considered in this work remains the one presented in Chapter 2 (Eq. 2.30), without the addition of any other source term.

The species transport equation (Eq. 2.36) instead requires modification to include an additional source term arising from the particle phase, as in Eq. 3.48. For instance, the postulate substance $C_\alpha H_\beta O_\gamma N_\delta$ representing the volatile gases will have an additional source term to represent the volatile gases emitted from the coal particles undergoing devolatilisation. Similarly, the oxygen mass fraction will have a negative source to represent the amount of O_2 being consumed in the char combustion process.

$$\frac{\partial(\overline{\rho}\tilde{Y}_\alpha)}{\partial t} + \frac{\partial}{\partial x_j}(\overline{\rho}\tilde{Y}_\alpha\tilde{u}_j) = \frac{\partial}{\partial x_j}\left[\left(\frac{\tilde{\mu}}{Sc} + \frac{\tilde{\mu}_t}{Sc_t}\right)\frac{\partial \tilde{Y}_\alpha}{\partial x_j}\right] + \tilde{\dot{\omega}}_\alpha + \overline{\dot{S}}_{Y_\alpha} \tag{3.48}$$

Finally, the enthalpy equation (Eq. 2.40) for the description of multiphase combustion requires an additional source term to account for the heat exchanged between the gaseous and the particle phase, which occurs by means of convection, devolatilisation, char combustion and radiation, all grouped in one source term for convenience, as in Eq. 3.49 below.

$$\frac{\partial \bar{\rho}\tilde{h}}{\partial t} + \frac{\partial}{\partial x_j}(\bar{\rho}\tilde{h}\tilde{u}_j) = \frac{\partial}{\partial x_j}\left[\left(\frac{\tilde{\mu}}{Pr} + \frac{\tilde{\mu}_t}{Pr_t}\right)\frac{\partial \tilde{h}}{\partial x_j}\right] + \overline{\dot{S}}_h \tag{3.49}$$

4 Radiative Heat Transfer

Whereas in most applications conductive and convective heat transfer rates are *linearly* proportional to temperature differences, radiative heat transfer rates are proportional to the *fourth power* of temperature differences, or $q_r \propto \; T^4 - T_\infty^4$ [109]. This means that for high temperature applications, such as air-fired, and in particular oxy-fired combustion chambers, radiation effects not only become non-negligible, but are likely to become the dominant heat transfer mode [2]. Modelling radiation in an accurate and cost-efficient manner is a challenging task, as the *non-local, instantaneous, directional and spectral* aspects of this heat transfer mode make it a considerably complex phenomenon [2].

In this chapter, the basic concepts of radiative heat transfer are presented (Sec. 4.1), followed by the derivation of the radiative transfer equation (Sec. 4.2). Common solution methods to this equation are then presented (Sec. 4.3), with a special focus on the discrete ordinates method (Sec. 4.4), which is used in this work. Note that the basic concepts, the derivation of the radiative transfer equation, and parts of the explanation of the discrete ordinates method given here (Secs. 4.1, 4.2, and 4.4) are based on Modests' book, *Radiative Heat Transfer* [120]. The different types of spectral models available to describe the radiative properties of the medium are also introduced (Sec. 4.5), focusing on the global models used in this work. The treatment of particles and soot for radiative heat transfer solutions in particle laden flows is then presented (Sec. 4.6), and finally the coupling methodology and parallelisation of radiation with LES is discussed (Sec. 4.7).

4.1 Basic Concepts

The basic technical jargon required to understand this and the following chapters is presented here, with the essential definitions and the introduction of the concept of solid angles.

4.1.1 Definitions

Transparent media, or *non-participative media* is that through which no energy attenuation can be measured from travelling photons, an example of which may be a vacuum. On the contrary, media which interact with photons by means of absorption, emission or scattering (deflection), are known as *participative media*, or *non-transparent media.* A *blackbody* constitutes perfectly absorbing media, or in other words media that absorbs all incident radiation, without reflecting any photons.

Electromagnetic waves are characterised by their *frequency* (*Hz*, or cycles per second) and *wavelength* λ (metres), which ranges over several orders of magnitude, from nanometres to metres. However *thermal radiation* only relates to the electromagnetic waves that are emitted by a medium due to its temperature, and as such the only wavelengths in consideration range from the ultraviolet ($\lambda \approx 0.1\mu m$) to the mid-infrared spectrum ($\lambda \approx 100\mu m$) [2, 120].

A *spectral quantity* is a quantity relevant only to a narrow frequency range, whereas a *total quantity* is a spectral quantity integrated over the whole electromagnetic spectrum. For instance, *radiative intensity*, which is defined as radiative energy flux per unit area and unit solid angle (see the next section) [120], can be characterised as total intensity I, or spectral intensity I_η, where the spectral intensity is specific to a certain wavelength, and its integration over the whole electromagnetic spectrum yields the total intensity. Media which exhibits properties independent of wavelength is known as *gray media*, and although in most real-life applications *non-gray* (or spectral) behaviour is commonly observed in participating media, gray approximations are very useful for modelling purposes.

When media is said to be at *local thermodynamic equilibrium*, all its radiative properties (within a small volume) are independent from the surrounding environment.

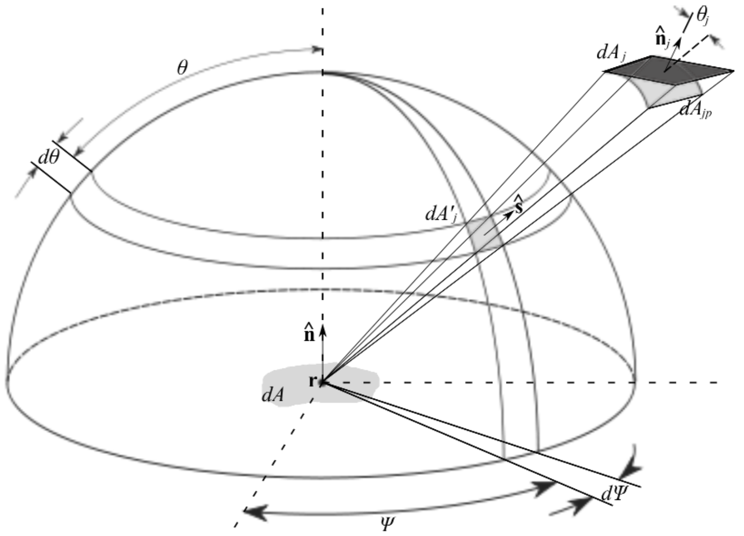

Figure 4.1: Graphic representation of a solid angle, based on [120].

4.1.2 Solid Angles

The concept of solid angles is crucial to understand radiative heat transfer problems and their solutions. An attempt to explain this concept, based on the description of Modest [120], is made here.

If we take an arbitrary point r with position vector $\boldsymbol{r}$ on an arbitrary surface dA having a unit normal vector $\hat{\boldsymbol{n}}$ as in Fig. 4.1, it can be said that from this point, energy can radiate in an infinite number of directions. However, all the rays must pass through a hemisphere of unit radius, having a total surface area of 2π, which is known as the *total solid angle*. If we then take an arbitrarily emitted photon with unit direction vector $\hat{\boldsymbol{s}}$, defined by its *polar angle* θ and the *azimuthal angle* ψ, it becomes clear that the unit hemisphere has the limits $0 \leq \theta \leq \pi/2$ and $0 \leq \psi \leq 2\pi$.

From point r, an infinitesimal surface dA_j can be defined as having a solid angle equal to the projection of its surface to a plane normal to the direction vector dA_{jp}, divided by the square of the distance S between the point and the surface (Fig. 4.1) [120]. By projecting the surface on the unit hemisphere $dA_j^{'}$, this becomes equal to the solid angle, Eq. 4.1.

$$d\Omega = \frac{dA_{jp}}{S^2} = \frac{cos\theta_j dA_j}{S^2} = dA_j^{'} \tag{4.1}$$

In other words, an infinitesimal solid angle $d\Omega$ can be seen as an infinitesimal area on a unit sphere, as in Eq. 4.2 [120]. Integration over the limits of the hemisphere yields a total solid angle of 2π, whereas for a unique point in space integration over the limits of a whole sphere would give a total solid angle of 4π.

$$d\Omega = dA_j^{'} = sin\theta d\theta d\psi \tag{4.2}$$

4.2 The Radiative Transfer Equation (RTE)

Radiative energy in a medium is transferred by means of emission, absorption and scattering, and these are all accounted for in the Radiative Transfer Equation (RTE), which is described here based on the description by Modest [120]. The RTE is conventionally expressed in terms of intensity I_η (where the subscript η indicates the wavenumber), and involves both intensity attenuation and augmentation, discussed in the following subsections. It is assumed that the media has a constant refractive index (i.e. media through which electromagnetic waves travel along straight lines), that the medium is stationary compared to the speed of light, and that it is at local thermodynamic equilibrium.

4.2.1 Intensity Attenuation

Any photon or beam travelling through participating media will be attenuated by absorption and scattering. The two phenomenons are explained separately below.

Attenuation by Absorption

The amount of energy attenuated by absorption is directly proportional to the magnitude of the incident intensity (energy) I_η and the distance a beam travels ds through the medium [120]. This can be expressed mathematically as in Eq. 4.3, where κ_η is the *absorption coefficient* $[m^{-1}]$, and the negative sign is introduced to reflect the decrease in intensity.

$$(dI_\eta)_{abs} = -\kappa_\eta I_\eta ds \tag{4.3}$$

The absorption of radiation also depends on the number of *participating* molecules per unit volume, and as such a *mass absorption coefficient* or a *pressure absorption coefficient* can also be used, Eq. 4.4 [120].

$$(dI_\eta)_{abs} = -\kappa_{\rho\eta} I_\eta \rho ds = -\kappa_{p\eta} I_\eta p ds \tag{4.4}$$

Integrating Eq. 4.3 over a geometric path $0 \rightarrow s$ gives Eq. 4.5, where $I_\eta(0)$ is the intensity entering the medium at $s = 0$, and τ_η is the optical thickness for absorption, Eq. 4.6 [120].

$$I_\eta(s) = I_\eta(0) exp\left(-\int_0^s \kappa_\eta ds\right) = I_\eta(0) e^{-\tau_\eta} \tag{4.5}$$

$$\tau_\eta = \int_0^s \kappa_\eta ds \tag{4.6}$$

It is also possible to define the *absorptivity* of the medium for the same path $0 \rightarrow s$, as in Eq. 4.7.

$$\alpha_\eta \equiv \frac{I_\eta(0) - I_\eta(s)}{I_\eta(0)} = 1 - e^{-\tau_\eta} \tag{4.7}$$

Attenuation by Out-scattering

Similar to energy attenuation by absorption, the energy attenuated by out-scattering (scattering away from the beam's direction of travel) is proportional to the magnitude of the intensity I_η and the path-length ds, and is expressed with the *scattering coefficient* $\sigma_{s\eta}$ $[m^{-1}]$, as in Eq. 4.8. However in this case the scattered energy is deflected and will appear as *in-scattering* (or augmentation due to scattering) in another direction (see Sec. 4.2.2), whereas the absorbed energy is converted into internal energy [120].

$$(dI_\eta)_{sca} = -\sigma_{s\eta} I_\eta ds \tag{4.8}$$

Similar to absorption, mass and pressure scattering coefficients can be derived, as well as the scattering optical thickness.

Total Intensity Attenuation

The *extinction coefficient* β_η can be defined as the quantity describing the total attenuation of intensity in a beam due to absorption and scattering, as in Eq. 4.9. Further, the optical thickness can also be defined in terms of the extinction coefficient (Eq. 4.10) [120].

$$\beta_\eta = \kappa_\eta + \sigma_{s\eta} \tag{4.9}$$

$$\tau_\eta = \int_0^s \beta_\eta ds \tag{4.10}$$

4.2.2 Intensity Augmentation

The energy of a pencil of rays travelling through participating media will be attenuated by absorption and scattering, as explained in the previous section. However, emission and scattering from other directions will also contribute to increasing the energy of rays through the direction in consideration, by *emission* and *in-scattering*, as explained below.

Augmentation by Emission

The intensity emitted along an infinitesimally small path ds is proportional to the local energy (intensity) of the medium, and the path's length. Since at thermodynamic equilibrium the intensity everywhere is equal to the blackbody intensity $I_{b\eta}$ [120], local energy augmentation due to emission from other directions can be expressed as in Eq. 4.11. The same constant for absorption κ_η can be used for emission, by removing the negative sign that was found in the equation describing attenuation due to absorption (Eq. 4.3).

$$(dI_\eta)_{em} = \kappa_\eta I_{b\eta} ds \tag{4.11}$$

Combining absorption and emission (Eq. 4.3 and Eq. 4.11 respectively), one obtains the radiative transfer equation for an absorbing-emitting and not scattering medium (Eq. 4.12).

$$\frac{dI_\eta}{ds} = \kappa_\eta (I_{b\eta} - I_\eta) \tag{4.12}$$

Using the optical thickness for absorption/emission (Eq. 4.6), and if the temperature field is known, the equation of transfer can be explicitly solved for absorbing-emitting media in a path $0 \rightarrow s$ (Eq. 4.13) [120].

$$I_\eta(s) = I_\eta(0)e^{-\tau_\eta} + I_{b\eta}(1 - e^{-\tau_\eta}) \tag{4.13}$$

Further, if absorption is neglected ($I_\eta(0) = 0$) and only emission is considered, the *emissivity* ϵ_η can also be defined, Eq. 4.14.

$$\epsilon_\eta = \frac{I_\eta(s)}{I_{b\eta}} = 1 - e^{-\tau_\eta} \tag{4.14}$$

Augmentation by In-scattering

As previously discussed, intensity is scattered from a point in all directions, resulting in a local energy attenuation (*out-scattering*), described by Eq. 4.8. Conversely, *in-scattering* refers to the augmentation in local energy caused by the photons scattered from other directions into the direction in consideration. In-scattering can come from all directions, and therefore an integration over the total solid angle (4π) must be performed.

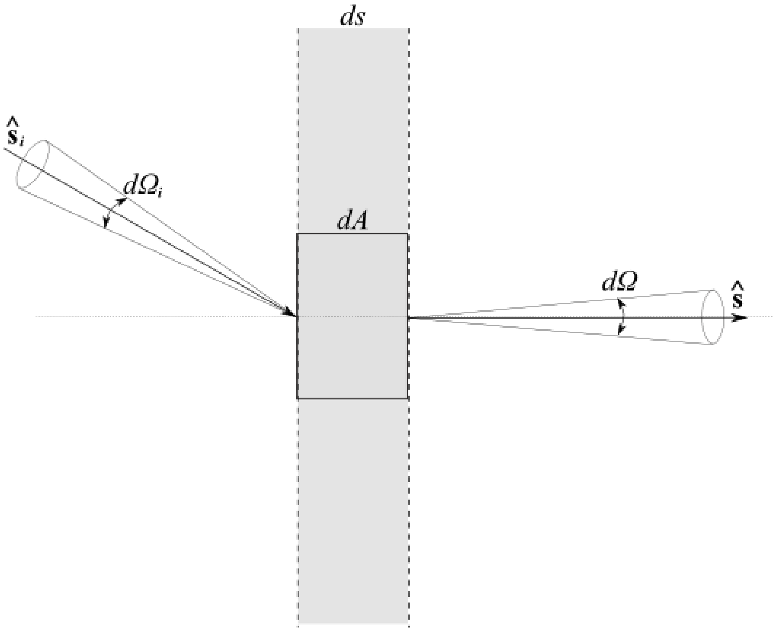

Figure 4.2: Radiative intensity due to scattering, based on [120].

The best way to illustrate this phenomenon is by means of example, as done below, based on Modest [120]. If a beam travelling with intensity I_η

and a given direction $\mathbf{\hat{s}_i}$ hits an infinitesimally small volume $dV = dAds$ as in Fig. 4.2, the heat flux incident with dA from the angle $d\Omega_i$ will be equal to $I_\eta(\boldsymbol{\hat{s}_i})(dA\boldsymbol{\hat{s}_i} \cdot \boldsymbol{\hat{s}})d\Omega_i d\eta$ [120]. The distance through which this beam will travel within the element dV will be equal to $ds/\boldsymbol{\hat{s}_i} \cdot \boldsymbol{\hat{s}}$, and recalling the out-scattering equation (Eq. 4.8), it is possible to calculate the total intensity out-scattered from $\boldsymbol{\hat{s}_i}$, as in Eq. 4.15.

$$\sigma_{s\eta}\left(I_\eta(\boldsymbol{\hat{s}_i})(dA\boldsymbol{\hat{s}_i} \cdot \boldsymbol{\hat{s}})d\Omega_i d\eta\right)\left(\frac{ds}{\boldsymbol{\hat{s}_i} \cdot \boldsymbol{\hat{s}}}\right) = \sigma_{s\eta} I_\eta(\boldsymbol{\hat{s}_i})dAd\Omega_i d\eta ds \tag{4.15}$$

At this point it is convenient to introduce the *scattering phase function* Φ_η, which represents the probability of a beam travelling in a given direction to be scattered in another specific direction. In the current example, the fraction of the beam travelling with direction $\mathbf{\hat{s}_i}$ that will be scattered in the cone $d\Omega$ with direction $\mathbf{\hat{s}}$ is given by $\Phi_\eta(\boldsymbol{\hat{s}_i}, \boldsymbol{\hat{s}})d\Omega/4\pi$, and hence the total flux coming from $d\Omega_i$ into $d\Omega$ can be expressed as $\sigma_{s\eta} I_\eta(\boldsymbol{\hat{s}_i})$ $dAd\Omega_i d\eta ds \Phi(\boldsymbol{\hat{s}_i}, \boldsymbol{\hat{s}})/4\pi d\Omega$, where the 4π has been included for convenience as will be later explained [120]. Thus, the flux scattered from *all* directions $\mathbf{\hat{s}_i}$ into the direction $\mathbf{\hat{s}}$ can be calculated by integration over the total solid angle, as in Eq. 4.16, which is further simplified to Eq. 4.17 [120].

$$\left(dI_\eta\right)_{sca}(\boldsymbol{\hat{s}})dAd\Omega d\eta = \int_{4\pi} \sigma_{s\eta} I_\eta(\boldsymbol{\hat{s}}_i)dAd\Omega_i d\eta ds \Phi_\eta(\boldsymbol{\hat{s}_i}, \boldsymbol{\hat{s}})\frac{d\Omega}{4\pi} \tag{4.16}$$

$$\left(dI_\eta\right)_{sca}(\boldsymbol{\hat{s}}) = ds\frac{\sigma_{s\eta}}{4\pi}\int_{4\pi} I_\eta(\boldsymbol{\hat{s}}_i)\Phi_\eta(\boldsymbol{\hat{s}_i}, \boldsymbol{\hat{s}})d\Omega_i \tag{4.17}$$

The energy flux scattered from $d\Omega_i$ into all directions is equal to $\sigma_{s\eta} I_\eta(\boldsymbol{\hat{s}_i})$ $dAd\Omega_i d\eta ds \frac{1}{4\pi}\int_{4\pi}\Phi(\boldsymbol{\hat{s}_i}, \boldsymbol{\hat{s}})d\Omega$ and must also be equal to the RHS of Eq. 4.15, which represents the flux scattered away from $\mathbf{\hat{s}_i}$, hence Eq. 4.18 is true [120].

$$\frac{1}{4\pi}\int_{4\pi}\Phi(\boldsymbol{\hat{s}_i}, \boldsymbol{\hat{s}})d\Omega \equiv 1 \tag{4.18}$$

Thus, for the case of *isotropic scattering*, which is when scattering is uniform across all directions, the phase function is constant, and thanks to the arbitrary 4π term previously introduced, it can be defined as $\Phi_\eta \equiv 1$ [120]. Note that whereas particles have been found to exhibit anisotropic scattering characteristics [112], throughout this work isotropic scattering is always assumed for simplicity.

4.2.3 The Complete Radiative Transfer Equation

In the previous subsections the terms contributing to the transfer of radiative energy have been derived, namely the intensity attenuation by absorption and scattering (Eq. 4.3 and Eq. 4.8 respectively), and the intensity augmentation by emission and scattering (Eq. 4.11 and Eq. 4.17 respectively). These equations can be combined with an energy balance on the radiative energy traveling in a given direction through a control volume to obtain the final form of the RTE for an absorbing-emitting and scattering medium. For a detailed description of how this is done the reader is referred to [120], as here only the final result is presented in Eq. 4.19.

$$\frac{dI_\eta}{ds} = \kappa_\eta I_{b\eta} - \kappa_\eta I_\eta - \sigma_{s\eta} I_\eta + \frac{\sigma_{s\eta}}{4\pi} \int_{4\pi} I_\eta(\hat{\boldsymbol{s}}_{\boldsymbol{i}}) \Phi_\eta(\hat{\boldsymbol{s}}_{\boldsymbol{i}}, \hat{\boldsymbol{s}}) d\Omega_i \tag{4.19}$$

The terms on the right-hand side of the above equation represent respectively augmentation due to emission, attenuation due to absorption, attenuation due to scattering, and augmentation due to scattering. Having defined the extinction coefficient, the middle two terms can be combined to simplify the RTE as in Eq. 4.20. Note that the process is assumed to be *quasi*-steady (compared to the speed of light), and as such the intensity gradient dI/ds can be expressed as a total derivative.

$$\frac{dI_\eta}{ds} = \hat{\boldsymbol{s}} \cdot \boldsymbol{\nabla} I_\eta = \kappa_\eta I_{b\eta} - \beta_\eta I_\eta + \frac{\sigma_{s\eta}}{4\pi} \int_{4\pi} I_\eta(\hat{\boldsymbol{s}}_{\boldsymbol{i}}) \Phi_\eta(\hat{\boldsymbol{s}}_{\boldsymbol{i}}, \hat{\boldsymbol{s}}) d\Omega_i \tag{4.20}$$

For the solution methods which will be discussed in the following sections, it is also convenient to express the RTE in terms of non-dimensional optical coordinates. This can be obtained by defining the *single scattering albedo* as in Eq. 4.21 below, and using the definition of the extinction coefficient (Eq. 4.9), and its optical thickness (Eq. 4.10) [120].

$$\omega_\eta \equiv \frac{\sigma_{s\eta}}{\kappa_\eta + \sigma_{s\eta}} = \frac{\sigma_{s\eta}}{\beta_\eta} \tag{4.21}$$

Substituting for τ_η and ω_η in Eq. 4.20 gives Eq. 4.22, which in turn can be further simplified by defining the *source function* for radiative intensity (Eq. 4.23), obtaining Eq. 4.24 [120].

$$\frac{dI_\eta}{d\tau_\eta} = -I_\eta + (1-\omega_\eta)I_{b\eta} + \frac{\omega_\eta}{4\pi}\int_{4\pi} I_n(\hat{\boldsymbol{s}}_{\boldsymbol{i}})\Phi_\eta(\hat{\boldsymbol{s}}_{\boldsymbol{i}}, \hat{\boldsymbol{s}})d\Omega_i \qquad (4.22)$$

$$S_\eta(\tau_\eta, \hat{\boldsymbol{s}}) = (1-\omega_\eta)I_{b\eta} + \frac{\omega_\eta}{4\pi}\int_{4\pi} I_n(\hat{\boldsymbol{s}}_{\boldsymbol{i}})\Phi_\eta(\hat{\boldsymbol{s}}_{\boldsymbol{i}}, \hat{\boldsymbol{s}})d\Omega_i \qquad (4.23)$$

$$\frac{dI_\eta}{d\tau_\eta} + I_\eta = S_\eta(\tau_\eta, \hat{\boldsymbol{s}}) \qquad (4.24)$$

4.2.4 Boundary Conditions

In order to solve the equation of radiative transfer for a given direction, the radiative intensity at (at least) a single location in the domain and in the specified direction must be known. This usually occurs at the boundaries of the domain, where the intensity can be independently specified on the surface of an enclosure surrounding the participating medium. Throughout this work, only black or grey diffusely emitting and reflecting opaque surfaces are considered, and their boundary conditions are explained in this section.

The radiation impinging on any solid surface, known as the irradiation H (or incident radiation) can be either reflected back to the medium, absorbed, or transmitted through the solid surface. In this work however only opaque surfaces are considered, and as such transmission through a solid surface is neglected. The fraction of reflected radiation from the total irradiation to a surface is specified by a quantity known as the *reflectance* ρ, and similarly a quantity describing the fraction of absorbed radiation is known as the *absorptance* α. Since energy is always conserved, and transmission through surfaces is neglected, the summation of these two quantities must be equal to unity, as in Eq. 4.25.

$$\rho + \alpha = 1 \qquad (4.25)$$

The total intensity leaving a wall is given by the difference between the total irradiation to the wall and the sum of the reflected and emitted radiation, as illustrated in Fig. 4.3.

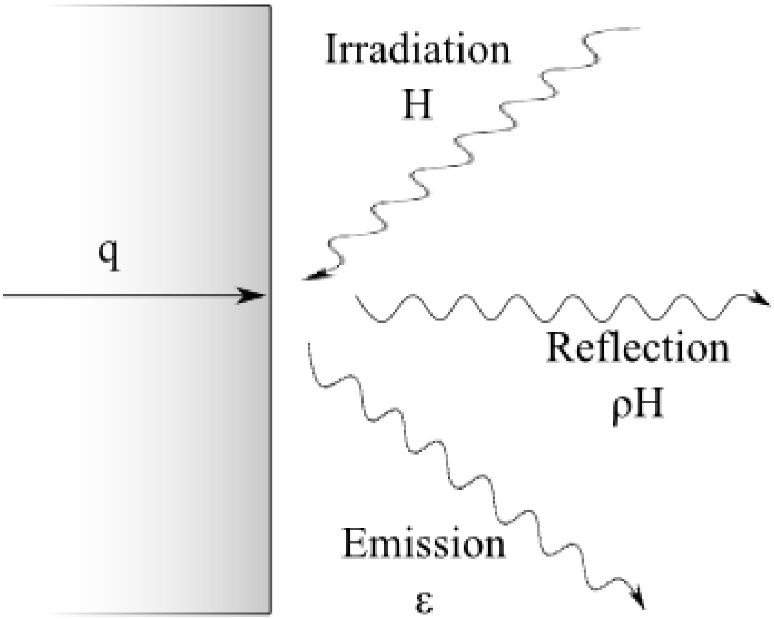

Figure 4.3: Surface energy balance, based on [120].

Unless a surface is assumed to be cold (0 K), in which case no radiation is emitted, the amount of thermal radiation emitted from a solid surface is linked to its temperature [2]. This is accounted for by the surface's equivalent blackbody radiation (how much a blackbody would have emitted at that given temperature), and its *emittance* ϵ, a non-dimensional coefficient that (like *absorptance* and *reflectance*) varies between 0 and 1. In real-surfaces, an angular dependency of emission may exist, however in this work only diffusely emitting surfaces are considered, and as such all surfaces are assumed to emit equally in all directions. The total intensity emitted by a surface can therefore be expressed as $\epsilon(\boldsymbol{r}_w)I_b(\boldsymbol{r}_w)$.

Similar to emission, the reflection from a surface can be diffuse or specular, and only diffusely reflecting surfaces are considered. This implies that a fraction ρ of the total incident intensity $H(\boldsymbol{r}_w)$ is uniformly reflected back to the medium over all directions. The reflected intensity in one direction can therefore be specified as $\rho(\boldsymbol{r}_w)H(\boldsymbol{r}_w)/\pi$, where the hemispherical irradiation of the wall is defined as in Eq. 4.26 [120]. As described in Fig. 4.4, $\hat{\boldsymbol{n}}$ is the local outward surface normal and $\hat{\boldsymbol{n}} \cdot \hat{\boldsymbol{s'}} = cos\theta'$ is the cosine of the angle between any incoming direction $\hat{\boldsymbol{s'}}$ and the surface normal.

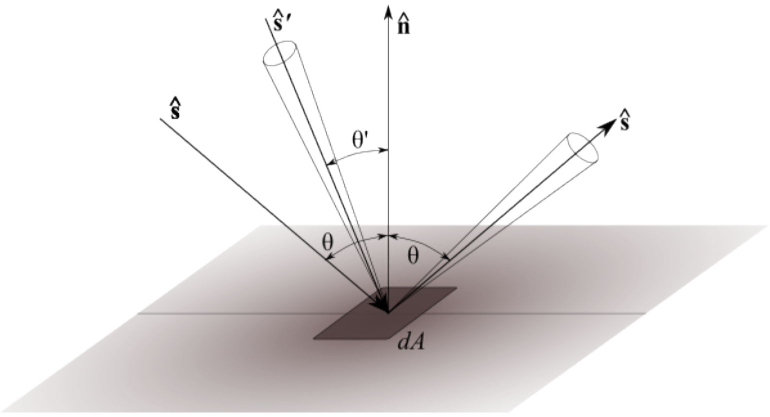

Figure 4.4: Intensity reflected on a surface, based on [120].

$$H(\boldsymbol{r_w}) = \int_{\hat{\boldsymbol{n}}\cdot\hat{\boldsymbol{s'}}<0} I(\boldsymbol{r_w}, \hat{\boldsymbol{s}}) \left|\hat{\boldsymbol{n}} \cdot \hat{\boldsymbol{s'}}\right| d\Omega' \tag{4.26}$$

The total intensity leaving a surface can thus be defined as the summation of emission and reflection, as in Eq. 4.27 below.

$$I(\boldsymbol{r_w}, \hat{\boldsymbol{s}}) = \epsilon(\boldsymbol{r_w}) I_b(\boldsymbol{r_w}) + \rho(\boldsymbol{r_w}) \frac{H(\boldsymbol{r}_w)}{\pi} \tag{4.27}$$

Since the properties of solid surfaces in this work are always assumed to be constant through the spectrum (grey), the emittance of a solid is equal to its absorptance, $\epsilon(\boldsymbol{r}_w) = \alpha(\boldsymbol{r}_w)$. The emissivity and reflectivity of a surface can therefore be expressed in terms of one another by substituting in Eq. 4.25, giving $\rho(\boldsymbol{r}_w) = 1 - \epsilon(\boldsymbol{r}_w)$.

Performing all the relevant substitutions, the final form of the equation for the total intensity leaving a grey opaque diffusely emitting and reflecting surface is presented in Eq. 4.28.

$$I(\boldsymbol{r_w}, \hat{\boldsymbol{s}}) = \epsilon(\boldsymbol{r_w}) I_b(\boldsymbol{r_w}) + \frac{1 - \epsilon(\boldsymbol{r_w})}{\pi} \int_{\hat{\boldsymbol{n}}\cdot\hat{\boldsymbol{s'}}<0} I(\boldsymbol{r_w}, \hat{\boldsymbol{s}}) \left|\hat{\boldsymbol{n}} \cdot \hat{\boldsymbol{s'}}\right| d\Omega' \tag{4.28}$$

For the simple case of a black surface, all the irradiation is emitted back to the medium without any reflection ($\epsilon = 1$ and $\rho = 0$), and consequently Eq. 4.28 is reduced to:

$$I(\boldsymbol{r_w}, \hat{\boldsymbol{s}}) = I_b(\boldsymbol{r_w}) \tag{4.29}$$

In the case of non-black walls however (where reflection is present), the outgoing intensity of a surface is not known initially, but is related to the incoming intensity and can be solved using the methods outlined in the following chapters.

4.2.5 Derived Quantities

In the previous sections the RTE and its boundary conditions have been defined, and in this section the useful quantities that can be derived from the solution of the RTE are presented. The radiative heat flux $q(\mathbf{r})$ impinging on the surface of a control volume in the medium, or on a solid surface can be obtained by Eq. 4.30.

$$q(\mathbf{r}) = \int_{4\pi} I(\mathbf{r}, \hat{\mathbf{s}})\hat{\mathbf{s}} d\Omega \tag{4.30}$$

The net radiative heat flux on a surface can be obtained by calculating the difference between the emitted and reflected radiation (see previous section) as in Eq. 4.31.

$$q \cdot \hat{\mathbf{n}}(\mathbf{r_w}) = \epsilon(\mathbf{r_w}) \left(\pi I_b(\mathbf{r_w}) - H(\mathbf{r_w})\right) \tag{4.31}$$

Another very useful quantity is the incident radiation G, which is obtained by summing the intensity impinging on a given control volume from all directions, and this is performed by integration over the total solid angle (Eq. 4.32).

$$G(\mathbf{r}) = \int_{4\pi} I(\mathbf{r}, \hat{\mathbf{s}}) d\Omega \tag{4.32}$$

Finally, the divergence of the radiative heat flux, which represents the radiative source/sink term, can be obtained from Eq. 4.33. Note that here it is only defined, and for its derivation the interested reader is referred to [120].

$$\boldsymbol{\nabla} \cdot \boldsymbol{q} = \kappa \left(4\pi I_b(\boldsymbol{r}) - \int_{4\pi} I(\boldsymbol{r}, \hat{\boldsymbol{s}}) d\Omega\right) = \kappa \left(4\pi I_b(\boldsymbol{r}) - G(\boldsymbol{r})\right) \tag{4.33}$$

4.3 Solutions for the Radiative Transfer Equation

Exact solutions to the RTE can only be obtained when dealing with very simple cases, such as ones having uniform radiative properties and homogeneous boundary conditions, or one-dimensional problems [19]. In most engineering applications however, one-dimensional assumptions are invalid, and the spectral properties of the medium are non-uniform, making exact solutions to the RTE inconvenient or impossible. For this reason several approximate solution methods to the RTE have been developed over the years, which can be broadly divided into integral or differential methods. A hybrid solution method known as the *discrete transfer radiation method* was also developed by Lockwood and Shah [108], for radiative problems in combustion applications. This method has been widely used [15, 29, 36, 38, 43, 113, 160, 161] as it offers a great amount of flexibility in terms of varying solution accuracy with cost, however the method is non-conservative, and difficult to extend to include anisotropic scattering [19]. In this section a brief introduction to the various solution methods is presented, however the interested reader is referred to [19, 120, 175] for more detailed reviews.

The most common integral methods are the *zonal method* [65, 66], *ray tracing methods* [120, 148], and the *Monte Carlo method* [121], whereas common differential solutions include *flux methods* [120], and the *spherical harmonics approximation* [120]. A brief introduction to these methods is given below, followed by a detailed explanation of the *discrete ordinates method* (Sec. 4.4), which is a type of flux method, and is the solution method used throughout this work.

Integral Methods

These methods rely on solving the integral formulation of the RTE, which can be obtained by integrating Eq. 4.24 over a path $0 \rightarrow s$.

The zonal method consists of a spatial discretization of the domain, with uniform radiative properties over volumes and surface elements. Surface/surface, surface/volume and volume/volume interactions are possible, and any element can exchange energy with another element in the domain through an interaction matrix [2]. Although this method was originally developed for the solution of engineering problems, its accuracy is limited and the computation can become very difficult with complex geometries [2].

In the ray tracing method, the solid angle at each point in the domain is discretized into several directions, and each direction is further discretized in segments of equal size, with uniform properties. Starting from the boundaries of the domain, the RTE is integrated to each evaluation point. The accuracy of this method is highly dependent on the number of beams (directions) and segments chosen for the solution. With a high number of beams and segments this becomes the most accurate method available, and is used for benchmark calculations of simple cases, but is too expensive to be used in an engineering context [2].

The Monte Carlo method instead is a statistical method that calculates a system's evolution by sampling random inputs. In other words, instead of calculating all the beams and segments, with the aid of a probability density function random samples are generated for a random beam. The response is known as a realization, and when further realizations do not alter the gathered statistics, the solution is considered converged. This method is known to be very accurate, but although the statistical approach reduces the computational time, this is still prohibitive for most engineering applications [2]. It is worth mentioning however that recently this method, with the aid of high-performance computing, is becoming increasingly feasible [140, 196], and may present a realistic alternative for the near future.

Differential Methods

Differential methods are the most widely used in combustion applications of computational fluid dynamics, as the two are somewhat similar in their numerical discretisation, and provide a better cost-to-accuracy ratio than integral methods.

Flux methods rely on separating the angular and spatial dependencies of the radiation intensity. A number of solid angle intervals is chosen, over which the intensity is assumed to be constant. The differential form of the RTE is thus reduced to a set of coupled linear differential equations, which can be solved with simple numerical methods. The number of solid angle intervals can be easily varied, altering the accuracy and cost of the solution.

In the spherical harmonics approximation, also known as the P_N approximation, the angular and spatial dependencies of the intensity are split in two terms by a generalized Fourier series for intensity [2]. This method reduces the governing equation to simple partial differential equations, the order of which can be varied for increased accuracy. For near-isotropic radiative intensity, the method works well with low-order approximations, however for more complex problems higher order approximations are required, which rapidly become computationally expensive. For more information on this method the interested reader is referred to Modest's book [120].

The discrete ordinates method (DOM), often grouped with the flux methods briefly introduced above, was originally proposed by Chandrasekhar [25] for atmospheric and stellar radiation problems as early as 1960, and later applied to neutron transport theory by Lathrop [96] and Lee [99]. It wasn't until much later though that the method was applied and optimised for general radiative heat transfer by Fiveland [47, 48] and Truelove [168, 169, 170] in 1986. To date, this is one of the most widely used solution methods for radiative heat transfer problems combined with CFD applications, due to its high flexibility in terms of spatial and angular discretisation, and high quality to cost ratio. As this is the method implemented and used in this work, a detailed explanation is given in the following section.

The finite volume method (FVM) for radiation [22, 131] is very similar to the DOM. However, whereas in the DOM the RTE is integrated over each control volume and the solid angle is discretised into small portions defined by discrete directions, in the FVM the RTE is integrated over both the control volume and over each discrete solid angle [19].

4.4 The Discrete Ordinates Method

In this section the DOM is presented based on Modest's explanation [120], as this is the chosen solution method implemented in this work. The general RTE for an absorbing, emitting and scattering medium was presented in the previous section (Eq. 4.20). Here it is proposed in a more compact form (Eq. 4.34), having dropped the wavenumber subscript η and the position vector $\mathbf{r}$, where $\hat{\mathbf{s}}$ is the direction in consideration, and $\hat{\mathbf{s}}'$ represents all the in-scattering directions. In this form, the equation is only valid for a grey medium (as total quantities are considered), or for a nongray medium if taken on a spectral basis [120].

$$\frac{dI(\mathbf{\hat{s}})}{ds} = \kappa I_b - \beta I(\mathbf{\hat{s}}) + \frac{\sigma_s}{4\pi}\int_{4\pi} I(\mathbf{\hat{s}}')\Phi(\mathbf{\hat{s}}', \mathbf{\hat{s}})d\Omega' \tag{4.34}$$

The RTE is subject to the boundary condition for opaque, diffusely emitting and reflecting walls specified earlier in Eq. 4.28 and here reproposed in the more compact form, with the same simplifications applied to the RTE above (Eq. 4.35).

$$I_w(\mathbf{\hat{s}}) = \epsilon_w I_b + \frac{1-\epsilon_w}{\pi}\int_{\mathbf{\hat{n}}\cdot\mathbf{\hat{s}}'<\mathbf{0}} I_w(\mathbf{\hat{s}}')|\mathbf{\hat{n}}\cdot\mathbf{\hat{s}}'|d\Omega' \tag{4.35}$$

Here, the subscript w indicates a wall location, $\boldsymbol{\hat{n}}$ is the local outward surface normal and $\boldsymbol{\hat{n}} \cdot \boldsymbol{\hat{s}'} = cos\theta'$ is the cosine of the angle between any incoming direction $\boldsymbol{\hat{s}'}$ and the surface normal. As previously explained, the outgoing intensity in the direction in consideration $I_w(\boldsymbol{\hat{s}})$ is not explicitly known, except for the case of a black surface, where $\epsilon_w = 1$ and the equation is reduced to $I_w(\mathbf{\hat{s}}) = I_b$, but can be related to the incoming intensity.

4.4.1 DOM Formulation

In the DOM, the radiative transfer equation is discretised into a finite number n of different directions $\mathbf{\hat{s}_i}$, where *i=1,2,...,n*. In addition, numerical quadratures with relative weights w_i are used to replace the integral over the total solid angle (4π), as in Eq. 4.36.

$$\int_{4\pi} f(\boldsymbol{\hat{s}})d\Omega \simeq \sum_{i=1}^{n} w_i f(\boldsymbol{\hat{s}_i}) \tag{4.36}$$

The RTE and its boundary conditions can therefore be replaced by Eq. 4.37 and Eq. 4.38 respectively, which will need to be solved for each direction individually.

$$\frac{dI(\mathbf{\hat{s}_i})}{ds} = \kappa I_b - \beta I(\mathbf{\hat{s}_i}) + \frac{\sigma_s}{4\pi}\sum_{j=1}^{n} w_j I(\mathbf{\hat{s}_j})\Phi(\mathbf{\hat{s}_i}, \mathbf{\hat{s}_j}), \quad i = 1, 2, ..., n \tag{4.37}$$

It is worth to point out that a ray traveling in any given direction will intersect a wall (or edge of the domain) twice, both when it is emitted from a boundary ($\boldsymbol{\hat{n}} \cdot \boldsymbol{\hat{s}_i} > 0$), and when it hits a boundary ($\boldsymbol{\hat{n}} \cdot \boldsymbol{\hat{s}_i} < 0$) and can then be reflected back or absorbed [120].

$$I_w(\mathbf{\hat{s}_i}) \;=\; \epsilon_w I_{b,w} + \frac{(1-\epsilon_w)}{\pi} \sum_{\mathbf{\hat{n}}\cdot\mathbf{\hat{s}_j}<0} w_j I_w(\mathbf{\hat{s}_j})|\mathbf{\hat{n}}\cdot\mathbf{\hat{s}_j}|, \quad \mathbf{\hat{n}}\cdot\mathbf{\hat{s}_i} \;>\; 0 \quad (4.38)$$

The RTE and its boundary condition in their DOM approximation are (first order) simultaneous linear partial differential equations that can be solved for each discrete direction n, through an iterative procedure which is outlined in the following sections. Only in a simple case with black boundaries and absorbing-emitting (non-scattering) media, can a solution be obtained without needing any iterations. However, this is generally restricted to simple test cases in *idealised* conditions, and is certainly not the case for closed furnaces or combustors, and much-less for pulverised coal combustion, where particle scattering plays an important role.

4.4.2 DOM Derived Quantities

In Sec. 4.2.5, the important derived quantities of interest in combustion applications, or for general model validation have been outlined. In the DOM, the radiative heat flux at a wall q_w, incident radiation G, radiative source term (or divergence of the heat flux) $\nabla \cdot q$ and the net wall heat flux $q_w \cdot \hat{n}$ are all approximated as in the equations below, where as previously explained integrals are discretised into a number of n directions, with associated weights w_i.

$$\mathbf{q_w} = \int_{4\pi} I_w(\mathbf{\hat{s}})\mathbf{\hat{s}} d\Omega \simeq \sum_{i=1}^{n} w_i I_{i,w} \mathbf{\hat{s}_i} \quad (4.39)$$

$$G = \int_{4\pi} I(\mathbf{\hat{s}}) d\Omega \simeq \sum_{i=1}^{n} w_i I_i \quad (4.40)$$

$$\nabla \cdot \mathbf{q} = \kappa \left(4\pi I_b - \int_{4\pi} I(\mathbf{\hat{s}}) d\Omega \right) \simeq \kappa \left(4\pi I_b - G \right) \quad (4.41)$$

$$\mathbf{q_w} \cdot \mathbf{\hat{n}} \simeq \epsilon_w \left(\pi I_b - \sum_{\mathbf{\hat{n}}\cdot\mathbf{\hat{s}_i}<0} w_i I_{i,w} |\mathbf{\hat{n}}\cdot\mathbf{\hat{s}_i}| \right) \quad (4.42)$$

4.4.3 Angular Discretisation

In literature several different angular quadrature schemes have been proposed to define the discrete ordinate directions, the most common of which are by Lathrop and Carlson [97], Fiveland [47] and Truelove [169]. Other common quadrature schemes are the T_N quadrature by Thurgood *et* al. [165], and the more recent LC_{11} quadrature by Koch and Becker [89].

Throughout this work, only the S_N approximation by Lathrop and Carlson is used, presented in Table 4.1 and illustrated in Fig. 4.5, as this allows sufficient variation in the number of directions, and extension to different quadrature schemes is relatively straightforward.

Order	Ordinates			Weights
	ξ	η	μ	w
S_4	0.2958759	0.2958759	0.9082483	0.5235987
	0.2958759	0.9082483	0.2958759	0.5235987
	0.9082483	0.2958759	0.2958759	0.5235987
S_6	0.1838670	0.1838670	0.9656013	0.1609517
	0.1838670	0.6950514	0.6950514	0.3626469
	0.1838670	0.9656013	0.1838670	0.1609517
	0.6950514	0.1838670	0.6950514	0.3626469
	0.6950514	0.6950514	0.1838670	0.3626469
	0.9656013	0.1838670	0.1838670	0.1609517
S_8	0.1422555	0.1422555	0.9795543	0.1712359
	0.1422555	0.5773503	0.8040087	0.0992284
	0.1422555	0.8040087	0.5773503	0.0992284
	0.1422555	0.9795543	0.1422555	0.1712359
	0.5773503	0.1422555	0.8040087	0.0992284
	0.5773503	0.5773503	0.5773503	0.4617179
	0.5773503	0.8040087	0.1422555	0.0992284
	0.8040087	0.1422555	0.5773503	0.0992284
	0.8040087	0.5773503	0.1422555	0.0992284
	0.9795543	0.1422555	0.1422555	0.1712359

Table 4.1: Discrete ordinates quadratures and weights for the S_N-approximation, where $N = 4, 6, 8$ [97].

The principle of the angular discretisation consists in decomposing any given direction $\mathbf{\hat{s}_i}$ into Cartesian co-ordinates (i, j, k) using specific direction cosines (ξ_i, η_i, μ_i), as in Eqs. 4.43a- 4.43c. The order of the approximation (S_N) indicates the N different direction cosines required for each different

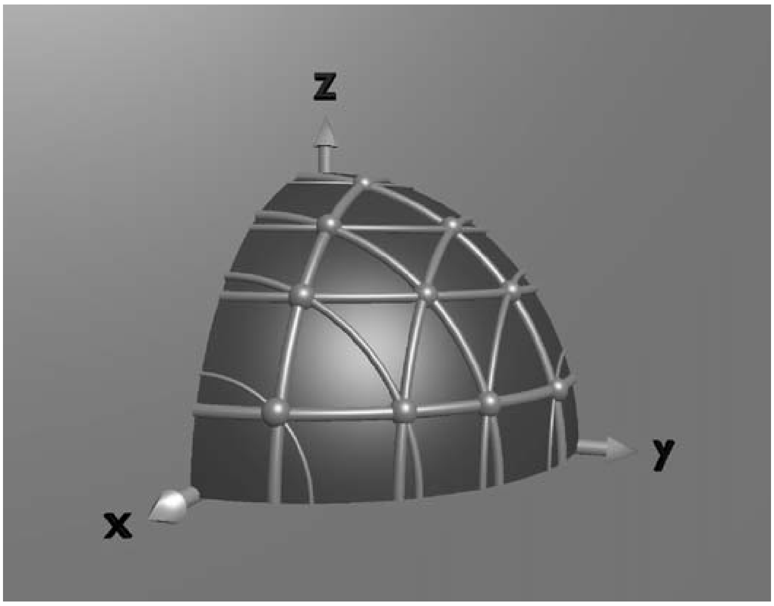

Figure 4.5: Illustration of the S_8 angular discretisation scheme by Koch and Becker [89]. One of the 8 quadrants of the total solid angle is shown, with the 10 discrete directions represented by the dots intersecting the lines on the sphere.

principal direction $\hat{\boldsymbol{s}}_{\boldsymbol{i}}$, for a total of $n = N(N+2)$ discrete directions to solve for.

$$\hat{\mathbf{s}}_{\mathbf{i}} \cdot \hat{\mathbf{i}} = \xi_i \tag{4.43a}$$

$$\hat{\mathbf{s}}_{\mathbf{i}} \cdot \hat{\mathbf{j}} = \eta_i \tag{4.43b}$$

$$\hat{\mathbf{s}}_{\mathbf{i}} \cdot \hat{\mathbf{k}} = \mu_i \tag{4.43c}$$

Using the above equations, each direction can be expressed in Cartesian co-ordinates, as in Eq. 4.44 below.

$$\hat{\boldsymbol{s}}_{\boldsymbol{i}} = \xi_i \hat{\boldsymbol{i}} + \eta_i \hat{\boldsymbol{j}} + \mu_i \hat{\boldsymbol{k}} \tag{4.44}$$

4.4.4 Implementation of the DOM

In this section the implementation of the DOM in Cartesian co-ordinates is described, followed by a step-by-step description of the numerical procedure employed.

A definition for the source function S_η was given in Sec. 4.2.3, and this becomes useful in the DOM, where it is decomposed into $i = 1, 2, ..., n$ individual directions S_i and approximated as in Eq. 4.45, again by replacing the integral with a weighted numerical quadrature.

$$S_i = (1-\omega)I_b + \frac{\omega}{4\pi}\sum_{j=1}^{n} w_j \Phi_{ij} I_j \tag{4.45}$$

Using the source function and the Cartesian-coordinate directional decomposition (Eq. 4.44), the whole RTE can be expressed in the more convenient coordinate system, as in Eq. 4.46 below [120].

$$\xi_i \frac{\partial I_i}{\partial x} + \eta_i \frac{\partial I_i}{\partial y} + \mu_i \frac{\partial I_i}{\partial z} + \beta I_i = \beta S_i \tag{4.46}$$

The boundary conditions must also be expressed in Cartesian coordinates. For a surface normal to the i direction we have $\hat{\mathbf{n}} = \hat{\mathbf{i}}$, and therefore Eq. 4.43a can be substituted into the DOM boundary condition (Eq. 4.38) to obtain Eq. 4.47. The same procedure can be applied to the different surface normals to obtain the boundary conditions for each surface orientation.

$$I_i = \epsilon_w I_{bw} + \frac{1-\epsilon_w}{\pi}\sum_{\xi_j<0} w_j I_j |\xi_j| \tag{4.47}$$

The description of the implementation of the DOM in this work is limited to equally-sized cubic cells, as this is the type of cells used in *PsiPhi*, our in-house LES code, and also in the radiation solver implemented in this work. In Fig. 4.6, a simple 2D cell is shown to illustrate the cell faces corresponding to the axes and discrete ordinates ξ_i and η_i, and this can be readily extended to the third dimension by adding the z-coordinate and the μ_i ordinates. The beauty of working with equally-sized cubic cells lies in the simplicity of the numerics: all faces have the same characteristic length $\Delta = \Delta_x, \Delta_y, \Delta_z$ and surface area $A = A_E, A_W, A_N, A_S, A_B, A_F$, and the volume is thus easily obtained, $V = \Delta^3$. To obtain the spatial discretization with the finite volume formulation, the terms in Eq. 4.46 are volume integrated as in Eq. 4.48, yielding Eq. 4.49.

$$\xi_i \int_V \frac{\partial I_i}{\partial x} dV + \eta_i \int_V \frac{\partial I_i}{\partial y} dV + \mu_i \int_V \frac{\partial I_i}{\partial z} dV + \beta \int_V I_i dV = \beta \int_V S_i \tag{4.48}$$

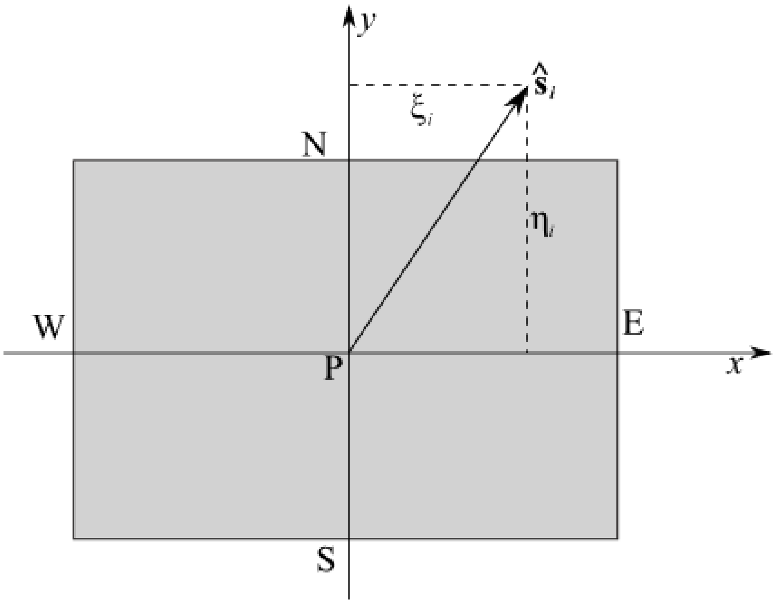

Figure 4.6: A computational cell in two-dimensions, based on [120].

$$\xi_i(I_{E,i}-I_{W,i})A+\eta_i(I_{N,i}-I_{S,i})A+\mu_i(I_{B,i}-I_{F,i})A = -\beta V I_{p,i}+\beta V S_{p,i} \quad (4.49)$$

In Eq. 4.49 above, the cell face f intensities $I_{f,i}$ are surface-averaged, whereas $I_{p,i}$ and $S_{p,i}$ are taken at the cell-centre as volume-averaged quantities.

To solve for the cell-centred intensity $I_{p,i}$, it is necessary to reduce the number of unknowns, and it is possible to do so by relating the cell-face intensities to their nodal value. This can be done in different ways, and will be dealt with in more detail in Sec. 4.4.6, in which several common spatial differencing schemes are explained. For the purpose of simplicity, in the current explanation the relationship is made as in Eqs. 4.50a-4.50c below, which is the relationship used in linear differencing schemes [19]. Here γ is a constant that takes different values depending on the choice of the differencing scheme.

$$I_{pi} = \gamma I_{E,i} + (1-\gamma) I_{W,i} \tag{4.50a}$$

$$I_{pi} = \gamma I_{N,i} + (1-\gamma) I_{S,i} \tag{4.50b}$$

$$I_{pi} = \gamma I_{B,i} + (1-\gamma) I_{F,i} \tag{4.50c}$$

A solution for $I_{p,i}$ can be obtained by rearranging Eq. 4.49, and substituting the relationships defined in Eqs. 4.50a-4.50c to reduce the number of unknowns. This gives Eq. 4.51, where the only cell-face intensities required are the ones *upstream* of the direction in which the beam is travelling, and are generally known.

$$I_{p,i} = \frac{\xi_i A I_{W,i}/\gamma + \eta_i A I_{S,i}/\gamma + \mu_i A I_{F,i}/\gamma + \beta V S_{p,i}}{\xi_i A/\gamma + \eta_i A/\gamma + \mu_i A/\gamma + \beta V} \tag{4.51}$$

This equation holds when calculating the radiation intensity for a direction i which points in the positive x, y, z directions, and therefore has the west, front and south upstream cell-faces (W, S, F), as well as positive ordinates ξ, η, μ. However, radiation propagates in every direction, and as such it is convenient to re-express the cell-face intensities in Eq. 4.51 in terms of incoming i (*upstream*) intensities, and the ordinates as absolute values, in order to make the equation applicable to any direction, as in Eq. 4.52 below.

$$I_{p,i} = \frac{|\xi_i| A I_{x_i,i}/\gamma + |\eta_i| A I_{y_i,i}/\gamma + |\mu_i| A I_{z_i,i}/\gamma + \beta V S_{p,i}}{|\xi_i| A/\gamma + |\eta_i| A/\gamma + |\mu_i| A/\gamma + \beta V} \tag{4.52}$$

Similarly, it is useful to express the nodal intensities in terms of incoming and exiting intensities, as below.

$$I_{pi} = \gamma I_{x_e,i} + (1-\gamma) I_{x_i,i} \tag{4.53a}$$

$$I_{pi} = \gamma I_{y_e,i} + (1-\gamma) I_{y_i,i} \tag{4.53b}$$

$$I_{pi} = \gamma I_{z_e,i} + (1-\gamma) I_{z_i,i} \tag{4.53c}$$

4.4.5 Computational Procedure

In this section the numerical procedure for the solution of the RTE using the DOM is explained step by step to better illustrate how such calculations are performed computationally. The computation is iterative, and always begins at a corner of the domain (or any corner-cell for non-rectangular geometries), since at this location the incoming cell-surface intensities are those of a wall or of the domain boundary, and hence they can be estimated. This is then repeated from all other corners, to solve for all directions. In the following procedure an example is given starting from the west, front and south corner of the domain, as in Fig. 4.7

1. For a given direction i pointing away from the corner cell in Fig. 4.7, the boundary condition (Eq. 4.47) is solved, considering only the emission term (first term on the RHS) at the first iteration, since the reflected intensity (which is a portion of the incident intensity coming from opposite directions) is unknown at this stage.
2. The wall/boundary intensity is matched to the incoming intensities $I_{x_i,i}, I_{y_i,i}, I_{z_i,i}$ of the first (corner) cell.
3. The nodal intensity $I_{p,i}$ of the corner cell can now be calculated with Eq. 4.51
4. Knowing the nodal intensity for the corner cell, it is possible to compute the *exiting* intensities, by rearranging the relationships defined in Eqs. 4.53a-4.53c, or similar depending on the choice of spatial differencing scheme.
5. The exiting intensities correspond to the *incoming* intensities of the relevant neighbouring cells. For adjacent cells of which the incoming intensities are known for all three coordinates, it is possible to repeat Steps 1-4 above, by recalculating the boundary conditions of their incoming faces, or matching the exiting neighbour cell intensity, where appropriate.
6. The procedure is repeated until all nodal intensities for such given direction have been computed.

7. The above procedure is then repeated for all other directions pointing away from the chosen starting corner.
8. This process is repeated from all the remaining corners, for all directions pointing away from the chosen corner, in such a way that the intensity is computed at each cell, for all directions, covering the total solid angle appropriately.
9. Having computed the incident intensity at each cell, coming from each direction, it is now possible to calculate the incident radiation (Eq. 4.40) and the source function (Eq. 4.45).
10. At this point a convergence check is performed. The convergence criteria used in this work is that the largest normalised change of the source function from the previous iteration (for any cell) should be less than 10^{-5}, as in Eq. 4.54 below. Note that for a case involving non-black walls (or boundaries) and/or scattering media, this check is redundant at the first iteration, since the source function was assigned an initial arbitrary value. Conversely, for a case involving black boundaries and non-scattering media, the source function (step 9) can be evaluated prior to the nodal intensities (since $\omega = 0$) and included directly in their calculation, making the solution non-iterative.
11. If convergence is obtained, the computation proceeds to the following step, otherwise it starts again from step 1, where this time the reflected portion of the boundary condition is included in the calculation, as is the source function obtained at the previous iteration.
12. After convergence, the useful derived quantities such as the divergence of the radiative heat flux (radiative source term) and wall heat fluxes can be explicitly computed.

$$\max \frac{|S_i^n - S_i^{n-1}|}{S_i^n} \leq 10^{-5} \tag{4.54}$$

4.4.6 Spatial Differencing Schemes

Similar to convection for CFD simulations, several spatial differencing schemes exist for the spatial discretization of the RTE using the DOM. A lot of work

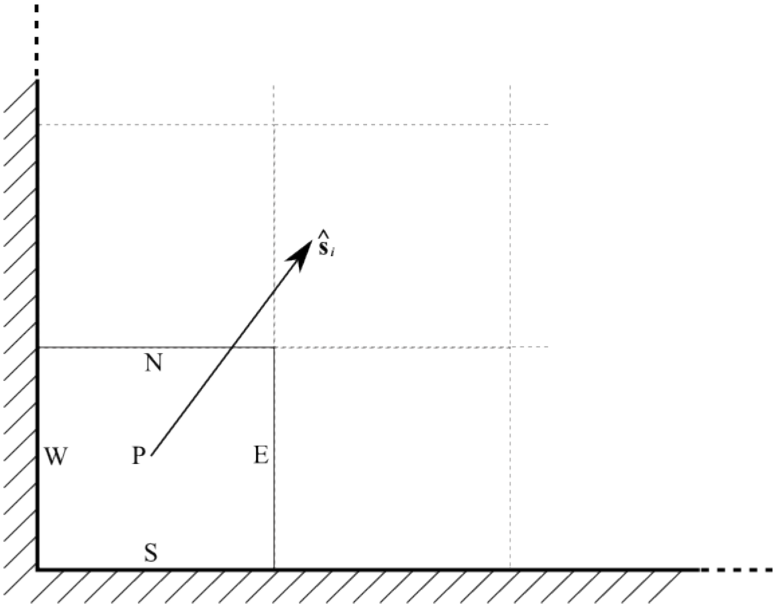

Figure 4.7: Domain corner cell, with walls at South and West ends [120].

has been done on spatial differencing schemes for radiation, in the quest to find the most accurate scheme suitable for a wide range of radiation applications [23, 27, 69, 104, 131], however no one scheme is superior to all. In this section, the most commonly used schemes are introduced, and in the following chapter they are tested and validated against each other to assess their relative performance. However for the application of radiation in coal combustion, the simple *step scheme* is used to ensure stability and avoid added computational cost.

Step Scheme

The most basic differencing scheme for the DOM is the *step scheme,* which is very similar to the upwind scheme in convection calculations for CFD (see Sec. 2.3.1). The nodal intensities are related to their surface intensities by setting $\gamma = 1$ in Eqs. 4.53a-4.53c, which leads to $I_{x_e,i} = I_{p,i}$ and similar solutions for the other directions. This is a very simple scheme which gives the largest truncation error, yet it is very stable, and the only one that will never produce unphysical results such as negative intensities.

Diamond Scheme

Another common differencing scheme is the *diamond scheme*, in which the nodal intensities are again related to their surface intensities with Eqs. 4.53a-4.53c, but in this case the coefficient γ takes the value of $\gamma = 0.5$. This scheme however can lead to unphysical (negative) intensities at the cell faces. While in literature it is advised to set these intensities to zero, or to re-compute them using a *step scheme*, and continue the computation [18], the scheme remains subject to instabilities and strong oscillations in the intensity field [120]. The negative intensities can be minimised by selecting a grid size following the conditions presented in Eq. 4.55 [48].

$$\Delta < \frac{MIN(|\xi_i|, |\eta_i|, |\mu_i|)}{\beta(1-\gamma)} \tag{4.55}$$

This condition implies that increasing the number of directions (higher order S_N approximations) to improve the angular discretisation, will require a finer grid since higher-order ordinates have smaller values. Similarly, when dealing with optically thicker media, having large values of β, the grid will need refinement. On the other hand, it has also been shown that a finer mesh could actually be the cause of unphysical intensities, not only in the form of negative values, but also as overshoots, which occur when energy conservation is violated (when the intensity leaving a cell is greater than the sum of the intensities entering and its emission) [23].

An improvement to this scheme is the Diamond Mean Flux Scheme (DMFS), originally proposed by Ströhle *et* al. [162, 163]. In this scheme the cell-face intensity is related to the nodal intensity as per Eqs. 4.56a-4.56c, where the overbars denote averaged incoming and exiting intensities, and the γ terms retain the 0.5 value. The averaged incoming/exiting cell-face intensities are defined as the weighted (by projected area) sum of all incoming/exiting intensities in a given direction [162]. This scheme has been shown to be particularly useful for solvers with unstructured grids [74]. Furthermore, it removes the oscillations that occur in the classic *diamond scheme*, is more stable than the latter, and can yield slightly improved results compared to the *step scheme* [162].

$$I_{p,i} = \gamma \overline{I_{x_e,i}} + (1-\gamma)\overline{I_{x_i,i}} \tag{4.56a}$$

$$I_{p,i} = \gamma \overline{I_{y_e,i}} + (1-\gamma)\overline{I_{y_i,i}} \tag{4.56b}$$

$$I_{p,i} = \gamma \overline{I_{z_e,i}} + (1-\gamma)\overline{I_{z_i,i}} \tag{4.56c}$$

CLAM Scheme

Higher-order bounded spatial schemes aim to produce more accurate results than the *step scheme*, whilst being free from unphysical negative intensities [29]. In these schemes the cell face intensity is calculated as a function of three neighbouring cell-centre intensities: the upstream, central and downstream cells. It is thus convenient to use the normalised variable formulation proposed by Leonard [100], Eqs. 4.57a-4.57b, where the subscripts D and U denote the downstream and upstream cell-centre intensities respectively, and $\tilde{I}$ and $\tilde{x}$ are the normalised intensity and coordinate.

$$\tilde{I} = \frac{I - I_U}{I_D - I_U} \tag{4.57a}$$

$$\tilde{x} = \frac{x - x_U}{x_D - x_U} \tag{4.57b}$$

Several bounded high-order schemes exist [17], however in this work only the CLAM scheme is implemented and tested [69, 171]. In this scheme the normalised cell face intensity is obtained by Eq. 4.58, and this can then be related to the actual cell-face intensity by rearranging the normalised variable formulation in Eq. 4.57a above.

$$\tilde{I}_f = \begin{cases} \frac{\tilde{x}_C^2 - \tilde{x}_f}{\tilde{x}_C(\tilde{x}_C - 1)}\tilde{I}_C + \frac{\tilde{x}_f - \tilde{x}_C}{\tilde{x}_C(\tilde{x}_C - 1)}\tilde{I}_C^2 & 0 < \tilde{I}_C < 1 \\ \tilde{I}_C & otherwise \end{cases} \tag{4.58}$$

This scheme satisfies the boundedness criterion since the function $\tilde{I}_f = f(\tilde{I}_C)$ is continuous, and $\tilde{I}_C \leq \tilde{I}_f \leq 1$ for values of $\tilde{I}_C$ between 0 and 1, and $\tilde{I}_f = \tilde{I}_C$ outside this range [30, 69].

For uniform grids, and inside the domain (away from boundaries) the normalised coordinates take the values of $\tilde{x}_f = 3/4$ and $\tilde{x}_C = 1/2$, and the normalised face intensity can be simplified to $\tilde{I}_f = \tilde{I}_C(2 - \tilde{I}_C)$ for values of $\tilde{I}_C$ between 0 and 1. However, for a cell whose upstream face coincides with a boundary, some modifications need to be made. The upstream cell intensity I_C becomes the neighbouring face intensity, and the coordinates take the values of $\tilde{x}_f = 2/3$ and $\tilde{x}_C = 1/3$ [30]. The normalised cell face intensity is therefore obtained by $\tilde{I}_f = \tilde{I}_C(2.5 - 1.5\tilde{I}_C)$ for values of $\tilde{I}_C$ between 0 and 1. For a cell whose downstream cell face instead coincides with a boundary, the step scheme is used.

Since in a sequential calculation the downstream cell-centre intensities are not known at the first iteration, a deferred correction procedure is used [83]. The intensity values obtained at the current iteration are used for the upstream and current cell intensities, whereas the values obtained at the previous iteration are used for the downstream intensities. The intensity at each cell-centre is calculated as in Eq. 4.59, where the γ terms have been removed, and a deferred correction term S_{dc} is introduced (Eq. 4.60).

$$I_{pi} = \frac{\beta V S_{pi} + |\xi_i|(A_x I_{x_i i}) + |\eta_i|(A_y I_{y_i i}) + |\mu_i|(A_z I_{z_i i}) + S_{dc}}{\beta V + |\xi_i| A_{x_e} + |\eta_i| A_{y_e} + |\mu_i| A_{z_e}} \tag{4.59}$$

$$S_{dc} = |\xi_i| A_x (I_{pi} - I_{x,e}) + |\eta_i| A_y (I_{pi} - I_{y,e}) + |\mu_i| A_z (I_{pi} - I_{z,e}) \tag{4.60}$$

Whilst this scheme is very accurate compared to the first-order step and diamond scheme, it is much more computationally expensive, as several iterations are required to obtain a converged solution. In fact, as also noted by Coelho [30], the deferred correction term S_{dc} must often be underrelaxed to obtain a converged solution. It is also noteworthy to mention that to apply the CLAM scheme, the incident radiation G must be used as the convergence criteria instead of the source function S_i (Eq. 4.54).

TVD Schemes

Total variation diminishing (TVD) schemes are a popular choice for convection in CFD, and have also been applied to the DOM for simple problems [7, 56]. A basic description of TVD schemes has already been given in Sec. 2.3.1, to which the reader is referred to for further details. Recently Coelho [33] produced an interesting review of different spatial differencing schemes, comparing first-order schemes, bounded high-order schemes (such as the CLAM scheme), and TVD schemes with different flux limiters, against several test cases. No single scheme appeared to be the most accurate for all test cases, however the TVD schemes performed very well, surpassing the CLAM scheme in accuracy in most circumstances. The most accurate flux limiter for the DOM was found to be the SUPERBEE [138], which is given in Eq. 4.61 below, where r is obtained with Eq. 2.49 and $B(r)$ is applied to the intensity field as in Eq. 2.48.

$$B(r) = \begin{cases} MAX[0, MIN(2r,1), MIN(r,2)] & r > 0 \\ 0 & r \leq 0 \end{cases} \tag{4.61}$$

As for the CLAM scheme, the change of incident radiation G must be used as the convergence criterion in Eq. 4.54, instead of the source function. Whereas TVD schemes can produce very accurate results, they are very computationally expensive compared to other schemes, and often prohibitive in combined CFD-Radiation calculations.

4.4.7 Shortcomings of the DOM

The DOM represents a good compromise between computational cost and accuracy of results, making it the most popular choice for applications in combustion CFD. However this solution method has some drawbacks, such as *false scattering* and the *ray effect*, which can become more evident in certain applications [120]. These problems have been assessed in detail [21], and several proposals have been made to minimise them.

False scattering or numerical smearing (as it is known in a radiation context), can be considered as the equivalent of *false diffusion* in CFD, and results from the spatial discretisation [120]. It is best understood by means of example: if one follows a single beam through a domain discretised with the DOM as it moves away from it source, it will eventually become noticeable that the beam slowly spreads out (due to the spatial error) as if it was scattering, hence the name. False diffusion errors are inherent in the DOM, and occur under any circumstance, regardless of the properties of the participating media or the boundary conditions, however they may be reduced by using a finer grid and more accurate spatial discretisation schemes.

The ray effect, the other major source of error of the DOM, instead occurs due to the angular discretisation. To understand this one must picture a large domain with a non-uniform field, having generally low emission everywhere, except for a tiny area on one side producing very strong emission. In the DOM, this emission can only travel along a finite number of discrete ordinate directions, whereas in reality the rays would be emitted uniformly. Imagine following the rays from this high-emission area along the discrete directions: as the distance from the emission point increases, so does the distance between each high-intensity ray, and eventually if they hit a wall far enough, the radiation coming from this point may not result uniform at all, whereas in reality it should be. This problem can also be reduced by refining the grid, and increasing the order of the angular discretization, at the expense of computational time.

Both false scattering and the ray effect are sources of error for the DOM which can become significant in certain applications, and as such a significant effort has been made by several authors in an attempt to minimise these as much as possible. A modified discrete ordinates method (MDOM) has been developed in an attempt to reduce ray effects by Ramankutty and Crosbie [132, 133]. This method has been shown to successfully remove ray effects originating from wall temperature discontinuities, but not those arising from sharp gradients in the medium [31]. A new modified discrete ordinates method (NMDOM) has thus been proposed by Coelho [31], which successfully mitigates all ray effects present in both the walls and the medium.

As previously mentioned, a lot of research has been carried out to try and minimise these two main shortcomings of the DOM, however often minimisation of the ray effects and false scattering have been treated individually, whereas it must be stressed that the two are correlated problems, and reducing one may increase the other [31]. For example, using a high-order spatial differencing scheme instead of the basic step scheme could reduce the spatial error or false scattering, however at the same time this could increase ray effects, thereby decreasing the solution accuracy overall. For this reason, depending on the type of application, the use of higher-order spatial differencing schemes may not always be entirely beneficial.

4.5 Spectral Models for the Radiative Properties of the Medium

Other than finding an efficient and accurate solution to the RTE, the main challenge in radiation modelling is the accurate representation of the media's spectral properties. Molecules emit and absorb photons only at specific frequencies across the entire electomagnetic spectrum, known as spectral lines. To date, the methods used to describe the spectral properties of participating media can be classified in four different categories: *line-by-line methods, narrow band models, wide-band models,* and *global models* [2]. A brief introduction to the first three is given in this section, with a more detailed explanation of different types of global models: *grey gas models* and the *weighted sum of grey gases* model, which are the ones implemented and used throughout this work.

Line-by-Line (LBL)

As the name suggests, this method takes into account hundreds of thousands, or even millions of spectral lines across the spectrum. The radiative properties of the media are then determined by mapping the lines to databases such as HITRAN and HITEMP [143], which contain the properties of millions of lines for specific molecules [2]. Needless to say this is the most accurate method available, but is also, and will probably remain for the mid-future, impossibly expensive for application to combustion simulations. Nonetheless, the LBL method is extremely useful to develop benchmark data for very simple test cases for the validation of simpler (less expensive) models.

Statistical Narrow Band (SNB)

Within a small range of spectral lines, most radiation quantities exhibit very small changes, whereas the absorption coefficient can vary considerably [2]. By grouping spectral lines in narrow bands (relatively small bins) and smoothing (averaging) the absorption coefficients within an interval, a less costly method is developed, similar to the LBL, but considerably less expensive [2, 120, 148, 175].

A popular, recent development of the classic SNB method is the correlated k-distribution of the statistical narrow band method (SNBcK). Since within a spectral interval the same absorption coefficient is found several times at slightly different frequencies, and since the frequency does not influence the mean quantities, it is possible to reorder the spectral intervals (narrow bands) to correlate the absorption coefficients. This simplifies considerably the numerics and consequently the computational effort, whilst retaining good accuracy [60]. Generally speaking, the method remains considerably expensive, but has recently been successfully implemented in massively parallel CFD codes for gaseous combustion [2].

Wide Band

Wide band methods rely on dividing the spectrum into bands in a similar fashion to the SNB method, but instead of using narrow bands, much larger spectral intervals are employed. Consequently, quantities can no longer be assumed constant within an interval, and some modelling is required [2]. This method however, despite being more computationally efficient than the SNB methods, has not been widely used.

Global Models

The principle behind global models is that the whole spectrum is integrated and reduced to a very limited amount of properties. For instance in the simplest of *grey* models, quantities such as the absorption coefficient are assumed to be globally constant. An evolution of this method is the weighted sum of grey gases (Sec.4.5.2), in which media is treated as a weighted sum of several gray gases originating from different parts of the spectrum [65, 118]. This method has been further developed by Denison and Webb into what is known as the *Spectral Line Weighted Sum of Grey Gases* (SLW), in which an LBL database is directly used to model the spectral properties of the gases [39, 40, 41].

These models are considerably less expensive than the ones introduced above, and are a good starting point for the inclusion of radiation modelling in CFD simulations. However as with most numerical models, their accuracy is related to their cost, and a good compromise between the two must be obtained.

4.5.1 Grey Gas Models

The simplest, and least computationally expensive models to treat gas radiation are grey models, where the radiative properties of the participating media are averaged over the whole spectrum. For computationally expensive simulations, such as those coupled with LES (and even more so for LES of pulverised coal-combustion), the general approach found in the literature is to use grey gas models. In this section various different approaches to grey gas modelling for radiative calculations are presented.

Constant Grey Models

In the most basic implementation, a constant value between 0 and 1 is assigned to the gas absorption coefficient κ_g, and is used throughout the domain. This approach has been undertaken in several works for coal-combustion applications [63, 64, 93, 94, 159, 160, 161]. This is obviously an over-simplistic approximation since gas absorption depends on the local gas composition as well as local temperature and concentration. Nonetheless this can work as a very basic treatment for gas radiation. Furthermore, in particle laden flows such as coal combustion, where the prevailing participating media are the particles, less importance may be given to the accuracy of the description of gaseous radiative properties, and hence arguably less accurate methods can be adopted.

Heterogeneous Grey Models

Water vapour (H_2O) and carbon dioxide (CO_2) absorb and emit much more radiation compared to other species [82], and for this reason it is a fair assumption to consider them the only participating gases in the medium. In this case κ_g is calculated based only on the partial pressures or molar concentrations of H_2O and CO_2, leading to a varying gas absorption coefficient throughout a given domain. In such cases, the gas absorption coefficient can be described by Eq. 4.62.

$$\kappa_g = \kappa_x (X_{CO_2} + X_{H_2O}) \tag{4.62}$$

Where κ_x is the constant maximum absorption coefficient given to a finite volume containing only participating gases, and X_{CO_2} and X_{H_2O} are the molar fractions of carbon dioxide and water vapour respectively.

A more accurate description of the gas absorption coefficient, similar to the one given in Eq. 4.62, includes the extension of the participating media to the fuel, or in the case of coal combustion of the gaseous volatiles. This method was originally formulated by Gosman and Lockwood [59], and used by Khalil et *al.* [81] and Yu et *al.* [192], and is expressed in Eq. 4.63, where X_{vg} represents the molar fraction of volatile gases.

$$\kappa_g = 0.2X_{vg} + 0.1(X_{CO_2} + X_{H_2O}) \tag{4.63}$$

Heterogeneous, Temperature-Dependant Grey Models

More recently, Barlow *et* al. [8] calculated curve fits for the Planck mean absorption coefficients of CO_2, CO and H_2O expressing them as temperature polynomials valid in the range $300 - 2500K$, using RADCAL [61], a code based on an SNB database. Their work however was on opposed-flow partially premixed laminar methane/air flames [8], where radiative effects within the relevant flow-field are much less prominent, and only heat losses to the surroundings need to be considered. Consequently, they did not solve the RTE using one of the methods presented in the previous sections, but simply included a heat loss term by using the absorption coefficient polynomials. This method has also been successfully adopted by Schmitt *et* al. [147]. However in pulverised coal combustion such a simple approach is not sufficient, because other than the heat losses to the surroundings or walls, in-flame and gas-particle radiative heat transfer effects must be taken into account for an accurate overall prediction of the flowfield. Nonetheless, this presents us with the interesting opportunity of using these gas temperature polynomials to obtain an overall grey gas absorption coefficient, to use for the solution of the RTE. This method should be considerably more accurate than the other grey models described above, since the coefficients are expressed as temperature polynomials, take into account the different species, and are obtained from an actual SNB database. At the same time, it should be just as expensive as the other grey models above, since only one solution of the RTE is required per radiative timestep, requiring only a few additional pre-processing calculations.

The species grey absorption coefficients can be easily obtained from their polynomial fits, Eqs. 4.64a-4.64b below, where the coefficients c_0-c_5 vary for each specie, and have been conveniently tabulated by Barlow *et* al. [8].

$$\kappa_{g,H_2O-CO_2} = c_0 + \sum_{i=1}^{5} c_i \left(\frac{1000}{T_g}\right)^i \tag{4.64a}$$

$$\kappa_{g,CO} = c_0 + T_g(c_1 + T_g(c_2 + T_g(c_3 + Tc_4))) \tag{4.64b}$$

Here, we propose to use the temperature polynomials above to obtain local absorption coefficients for each specie, and factor this by their local partial pressure to obtain an overall grey gas coefficient κ_g, as in Eq. 4.65 below, where $i = H_2O, CO_2, CO$. This can then be used as in the other methods above, for the solution of the RTE.

$$\kappa_g = \sum^{i} X_i \kappa_{g,i} \tag{4.65}$$

4.5.2 The Weighted Sum of Grey Gases (WSGG) Model

In this model, originally developed by Hottel and Sarofim [65], a real *nongray* gas is considered as a sum of *grey* gases (usually 3-5) and a clear (non-participating) gas. The RTE is solved for each gray gas *j*, having its own absorption coefficient κ_j (for the clear gas $\kappa_j = 0$), and weight a_j.

The weight of each grey gas is accounted for in solving the individual RTE's, and the resulting intensity is therefore the sum of the individual intensities of each gas (Eq. 4.66).

$$I(s) = \sum_{j=0}^{J} I_j(s) \quad j = 0, 1, 2, ..., J \tag{4.66}$$

In Eq. 4.66 J is the number of grey gases and $j = 0$ is used to represent the clear gas. The total emissivity of the WSGG model is an important quantity [153], as although it is not directly required for the solution of the model, it can be helpful in obtaining its coefficients if they are not readily available in literature (Eq. 4.67).

Table 4.2: Coefficients for the WSGG model derived by Smith *et* al. [153].

j	$\kappa_j \times 10^5 [m^{-1}]$	$b_{j,1} \times 10^1$	$b_{j,2} \times 10^4$	$b_{j,3} \times 10^7$	$b_{j,4} \times 10^11$
$X_{CO_2} \rightarrow 0$					
1	0.3914	0.4334	2.6200	-1.5600	2.5650
2	15.4355	-0.4814	2.8220	-1.7940	3.2740
3	389.1438	5.0660	0.1087	-0.3500	0.9123
$X_{H_2O} \rightarrow 0$					
1	0.4044	5.9770	-5.1190	3.0420	-5.5640
2	6.2423	0.5677	3.3330	-1.9670	2.7180
3	118.9243	1.8000	-2.3340	1.0080	-1.4540
$X_{H_2O} \rightarrow 1$					
1	0.4437	6.3240	-8.3580	6.1350	-13.0300
2	7.0200	-0.2016	7.1450	-5.2120	9.8680
3	118.1347	3.5000	-5.0400	2.4250	-3.8880
$X_{H_2O}/X_{CO_2} \rightarrow 1$					
1	0.4247	5.1500	-2.3030	0.9779	-1.4940
2	6.9627	0.7749	3.3990	-2.2970	3.7700
3	175.7710	1.9070	-1.8240	0.5608	-0.5122
$X_{H_2O}/X_{CO_2} \rightarrow 2$					
1	0.4146	6.5080	-5.5510	3.0290	-5.2530
2	6.4308	-0.2504	6.1120	-3.8820	6.5280
3	130.7152	2.7180	-3.1180	1.2210	-1.6120

$$\epsilon(T,s) = \sum_{j=0}^{J} a_j(T)[1 - e^{-\kappa_j s}] \tag{4.67}$$

The weights of each gray gas are temperature dependent (Eq. 4.68), and are in fact represented by a polynomial of order *K-1 (K* being the number of temperature polynomial coefficients), and where $b_{j,k}$ are emissivity gas temperature polynomial coefficients. Both $b_{j,k}$ and κ_j can be obtained by fitting Eq. 4.67 to a table of total emissivities [153]. In this work, the coefficients published by Smith *et* al. [153] are used, and these are reported in Table 4.2.

$$a_j(T) = \sum_{k=1}^{K} b_{j,k} T^{k-1} \tag{4.68}$$

All weights must sum up to unity, and therefore the clear gas is evaluated

Table 4.3: Coefficients for the absorptivity of mixtures with $X_{H_2O}/X_{CO_2} \rightarrow 1$ for the WSGG model, derived by Smith *et* al. [153].

		k			
j	i	1	2	3	4
1	1	0.55657 E-01	-0.62824 E-03	0.31876 E-06	-0.52922 E-10
2	1	0.16676 E-01	0.15769 E-03	-0.10937 E-06	0.19588 E-10
3	1	0.28689 E-01	0.20697 E-03	-0.17473 E-06	0.37238 E-10
1	2	0.32964 E-03	0.27744 E-06	-0.26105 E-09	0.37807 E-13
2	2	0.50910 E-03	-0.76773 E-06	0.40784 E-09	-0.69622 E-13
3	2	0.24221 E-03	-0.55686 E-06	0.34884 E-09	-0.67887 E-13
1	3	-0.53441 E-06	0.33753 E-09	-0.10348 E-12	0.26027 E-16
2	3	0.37620 E-07	0.18729 E-09	-0.15887 E-12	0.30781 E-16
3	3	-0.19492 E-06	0.36102 E-09	-0.21480 E-12	0.41305 E-16
1	4	0.12381 E-09	-0.90223 E-13	0.38675 E-16	-0.99306 E-20
2	4	-0.32510 E-10	-0.26171 E-13	0.29848 E-16	-0.58387 E-20
3	4	0.41721 E-10	-0.73000 E-13	0.43100 E-16	-0.83182 E-20

last, and is equal to the remaining weight unoccupied by the grey gases (Eq. 4.69).

$$a_0 = 1 - \sum_{j=1}^{J} a_j \tag{4.69}$$

Once all the absorption coefficients and the weights have been evaluated, the DOM can be employed to solve the RTE for each grey gas, and the resulting quantities for the nongray gas can be readily obtained. The RTE for the individual grey gases j is modified to include the weights as in Eq. 4.70, and a similar modification for the grey wall boundary conditions is performed, Eq. 4.71.

$$\frac{dI_j}{ds} = \kappa_j a_j I_b - \beta_j I_j + \frac{\sigma_{s,j}}{4\pi} \int_{4\pi} I_j(\hat{\mathbf{s}}')\Phi(\hat{\mathbf{s}}', \hat{\mathbf{s}}')d\Omega' \tag{4.70}$$

$$I_{j,w} = \epsilon_w a_{w,j} I_b + \frac{1-\epsilon_w}{\pi} \int_{\hat{\mathbf{n}}\cdot\hat{\mathbf{s}}'<0} I_{j,w}(\hat{\mathbf{s}})|\hat{\mathbf{n}} \cdot \hat{\mathbf{s}}'|d\Omega' \tag{4.71}$$

In Eq. 4.71, the wall weighting factor $a_{w,j}$ is related to the absorptivity of the wall. Assuming total absorptivity, the individual weighting factors can be calculated by Eq. 4.72, where $c_{w,i,j,k}$ are the absorptivity polynomials, T_s is the surface irradiation temperature and T is the gas temperature neighbouring the wall [153, 167]. The total absorptivity and the wall weighting factor for the clear gas can be obtained by adapting the absorptivity weighting factors to the gas emissivity and weight equations, Eq. 4.67 and Eq. 4.69 respectively. A set of absorptivity polynomials for mixtures having equal concentrations of H_2O and CO_2 used in this work, and originally derived by Smith *et* al. [153] is reported in Table 4.3.

$$a_{w,j} = \sum_{i=1}^{I} \left[\sum_{k=1}^{K} c_{w,i,j,k} T_s^{k-1} \right] T^{i-1} \tag{4.72}$$

The incident radiation and the divergence of the heat flux (the radiative source term) are also calculated for each individual gas, and then summed to obtain the total quantities, as in Eqs. 4.73-4.74.

$$G_j = \int_{4\pi} I_j \hat{\mathbf{s}} d\Omega \tag{4.73}$$

$$\nabla \cdot q_j = \kappa_j \left(4\pi a_j I_b - \int_{4\pi} I_j \hat{\mathbf{s}} d\Omega \right) \tag{4.74}$$

4.5.3 Grey WSGG Model Implementation

In the *non-grey* implementation of the WSGG model, the RTE has to be solved once for each gas, and this can become computationally expensive, especially when dealing with large, complicated problems. For this reason the WSGG model can also be implemented with a single *grey* gas approach, and in such case a single RTE needs to be solved [29, 130]. The gas coefficients and weights are obtained following the same procedure outlined in the previous section, and then the total emissivity is calculated according to Eq. 4.67. The grey absorption coefficient is then obtained from Eq. 4.75, and a single RTE is solved using this *grey* gas.

$$\kappa = -\ln[1 - \epsilon(s)]/s \tag{4.75}$$

This however raises the question of which value to select as an appropriate path length s in obtaining the total emissivity and the absorption coefficient. Some authors select s as the mean effective path length of a control volume [59], while others use the mean beam length of the whole domain [105]. For a uniform isothermal control volume the path length s can be approximated as the mean beam length of a cell [65, 77, 148], as in Eq. 4.76 below:

$$s = \frac{3.6V}{S} \tag{4.76}$$

Where V and S are the cell's volume and surface area respectively. For equally-sized cubic cells the path length can therefore be simplified to $s = 0.6\Delta$. However this method has no sound theoretical foundations [95], and has generally shown to give very poor results [29, 60].

4.5.4 Modified WSGG Model

One of the biggest shortcomings of the WSGG model is that the coefficients evaluated for any grey gas are only valid for a given mixture of H_2O and CO_2. In combustion applications however, the molar ratio of the participating gases (X_{H_2O}/X_{CO_2}) is constantly varying in time and space. This problem can be partially solved by deriving and tabulating coefficients for different molar ratios, and applying them according to the local mixture in each control volume, as done by Johansson *et* al. [71]. However this requires a lot of computational effort, and the accuracy of the weights for intermediate molar ratios depends on the number of coefficients derived. More recently, Johansson *et* al. proposed a modification to the WSGG, in order to account for the variations in molar ratios of the participating gases in the range $0.125 - 2.0$, which is valid for gas combustion, coal combustion and oxy-coal combustion with dry or wet flue recycling [70]. Throughout this work this is known as the modified WSGG (MWSGG).

The model uses a total of $J = 5$ gases (4 grey and 1 clear), which are valid for temperature ranges of $500 - 2500K$. The weights for the clear gases are obtained from Eq. 4.77, where $T_{ref} = 1200K$ is used as a reference temperature, and $c_{j,i}$ are the weight polynomial coefficients, which have a second-order dependency on the molar ratio (Eq. 4.78).

$$a_j = \sum_i c_{j,i} \left(\frac{T}{T_{ref}} \right)^{i-1} \tag{4.77}$$

$$c_{j,i} = C1_{j,i} + C2_{j,i}\left(\frac{X_{H_2O}}{X_{CO_2}}\right) + C3_{j,i}\left(\frac{X_{H_2O}}{X_{CO_2}}\right)^2 \tag{4.78}$$

Once all the grey gas weights have been obtained, the weight for the clear gas can be obtained in the usual way, using Eq. 4.69. Finally, the absorption coefficient for each grey gas j is obtained from Eq. 4.79, which has a linear relationship with the molar ratio. All the coefficients $K1_j$, $K2_j$, $C1_{j,i}$, $C2_{j,i}$, and $C3_{j,i}$ can be found in [70].

$$\kappa_j = K1_j + K2_j\left(\frac{X_{H_2O}}{X_{CO_2}}\right) \tag{4.79}$$

4.6 Radiation in Particle Laden Flows

Until this point the description of radiation modelling has been based on the assumption of a single gaseous phase, however the problem increases in complexity when dealing with multi-phase flows such as coal flames. The particle's radiative properties, which are generally dominant over the gas phase, have to be taken into account, and the radiative transfer equation has to be extended appropriately. This section covers the extension of the RTE to treat particles, and the models used to describe the particles' radiative properties.

4.6.1 Extension of the RTE to Treat Particle Laden Flows

For simplicity, the specification of the directional dependency of the RTE ($\boldsymbol{\hat{s}}_i$) is removed from all terms in the RTE except for the in-scattering term, and thus we can recall the general radiative transfer equation for absorbing, emitting and scattering media from Eq. 4.37:

$$\frac{dI}{ds} = \kappa I_b - \beta I + \frac{\sigma_s}{4\pi}\int_{4\pi} I(\boldsymbol{\hat{s}_i})\Phi(\boldsymbol{\hat{s}_i}, \boldsymbol{\hat{s}})d\Omega_i \tag{4.80}$$

In this case however κ, σ, β and the blackbody intensity I_b all relate to a single continuous phase, and cannot be used to represent multiphase flows. To accurately describe such cases one must define individual absorption, scattering and extinction coefficients for the gas, particle and soot phases. Furthermore, the blackbody intensity will be different for the three individual phases, and thus separate treatment is necessary. Eq. 4.80 is thus expanded to Eq. 4.81, where the subscripts g, p and s indicate the gas, particle and soot phases respectively.

$$\frac{dI}{ds} = \kappa_g I_{b,g} + \kappa_p I_{b,p} + \kappa_s I_{b,s} - (\kappa_g + \kappa_p + \kappa_s + \sigma_{s,p})I + \frac{\sigma_{s,p}}{4\pi}\int_{4\pi} I(\hat{\boldsymbol{s}}_{\boldsymbol{i}})\Phi(\hat{\boldsymbol{s}}_{\boldsymbol{i}}, \hat{\boldsymbol{s}})d\Omega_i \quad (4.81)$$

Following the approach of [28, 159, 192], only particle scattering is considered since this is largely dominant over gas and soot scattering.

4.6.1.1 Instantaneous Formulation for Grey Gas Properties

Following Stöllinger *et* al. [159], if the gas phase is described by grey radiating properties, the gas and soot can be assumed to be in thermal equilibrium, therefore a combined and constant gas and soot coefficient can be introduced $\kappa_{gs} = \kappa_g + \kappa_s$, and their blackbody intensities can be taken as equal to one another $I_{b,g} = I_{b,s}$. The RTE is thus simplified to:

$$\frac{dI}{ds} = \kappa_{gs} I_{b,g} + \kappa_p I_{b,p} - (\kappa_{gs} + \kappa_p + \sigma_{s,p})I + \frac{\sigma_{s,p}}{4\pi}\int_{4\pi} I(\hat{\boldsymbol{s}}_{\boldsymbol{i}})\Phi(\hat{\boldsymbol{s}}_{\boldsymbol{i}}, \hat{\boldsymbol{s}})d\Omega_i \quad (4.82)$$

This can be further simplified by defining a total absorption coefficient as $\kappa_t = \kappa_{gs} + \kappa_p$, the total extinction coefficient $\beta_t = \kappa_t + \sigma_{s,p}$, the scattering albedo as $\omega_t = \sigma_{s,p}/\beta_t$, and a total blackbody intensity as $I_{b,t} = (\kappa_{gs} I_{b,g} + \kappa_p I_{b,p})/\kappa_t$. Using these definitions in Eq. 4.82, the original formulation of the RTE can be recovered.

$$\frac{dI}{ds} = \kappa_t I_{b,t} - \beta I + \frac{\sigma_{s,p}}{4\pi}\int_{4\pi} I(\hat{\boldsymbol{s}}_{\boldsymbol{i}})\Phi(\hat{\boldsymbol{s}}_{\boldsymbol{i}}, \hat{\boldsymbol{s}})d\Omega_i \quad (4.83)$$

The boundary conditions and total incident radiation at any point in the domain are calculated as in the single-phase case previously explained, using total quantities, whereas the radiative source term can be decomposed into individual sources for the gas and particle phase (Eqs. 4.84-4.85) [28, 192].

$$\nabla \cdot q_g = \kappa_g \left(4\pi I_{b,g} - \int_{4\pi} I d\Omega\right) \quad (4.84)$$

$$\nabla \cdot q_p = \kappa_p \left(4\pi I_{b,p} - \int_{4\pi} I d\Omega \right) \tag{4.85}$$

4.6.1.2 Instantaneous Formulation for the WSGG Method

Whereas particles will always be described by grey properties, it is still possible to use more sophisticated models to describe the spectral properties of the gas, in conjunction with grey particle and soot radiation. In this section the implementation of the non-grey weighted sum of grey gases model in particle laden flows is presented, following the approaches of Yu *et* al. [192] and Kangwanpongpan et *al.* [77].

The RTE for the WSGG model is presented in Eq. 4.86, where the wavenumber subscript η has been dropped and replaced by subscript j, which represents an individual grey gas. As previously explained in fact, in this model the non-grey medium is described by j grey gases, which are weighted with the addition of grey gas weights a_j.

$$\frac{dI_j}{ds} = \kappa_j a_j I_b - \beta_j I_j + \frac{\sigma_{s,j}}{4\pi} \int_{4\pi} I_j(\hat{\boldsymbol{s}}_{\boldsymbol{i}}) \Phi_\eta(\hat{\boldsymbol{s}}_{\boldsymbol{i}}, \hat{\boldsymbol{s}}) d\Omega_i \tag{4.86}$$

To include the treatment of particles and soot, Eq. 4.86 can be extended in a similar way to that previously shown for the case of grey gases, by defining particle and soot absorption coefficients, and considering only particle scattering (Eq. 4.87).

$$\begin{aligned} \frac{dI_j}{ds} &= \kappa_{g,j} a_{g,j} I_{b,g} + \kappa_{p,j} a_{p,j} I_{b,p} + \kappa_{s,j} a_{s,j} I_{b,s} \\ -(\kappa_{g,j} + \kappa_{p,j} + \kappa_{s,j} + \sigma_{s,p,j}) I_j &+ \frac{\sigma_{s,j}}{4\pi} \int_{4\pi} I_j(\hat{\boldsymbol{s}}_{\boldsymbol{i}}) \Phi_\eta(\hat{\boldsymbol{s}}_{\boldsymbol{i}}, \hat{\boldsymbol{s}}) d\Omega_i \end{aligned} \tag{4.87}$$

Here $a_{g,j}$, $a_{p,j}$ and $a_{s,j}$ are the weighting factors for gas, particles and soot. Since the particles and soot are treated as grey these can be simplified as $\kappa_{p,j} = \kappa_p$ and $\kappa_{s,j} = \kappa_s$, and the total intensity in Eq. 4.66 can be solved by summing all the grey-gas intensities.

The weights for the individual grey gases are calculated in the same way as in Eq. 4.68, however the appropriate subscript has been included for correctness (Eq. 4.88).

$$a_{g,j}(T_g) = \sum_{k=1}^{K} b_{j,k} T_g^{k-1} \tag{4.88}$$

Again, the soot is assumed to be in thermal equilibrium with the surrounding gas, and as such is given the same weighting factor, $a_{s,j}(T_s) = a_{g,j}(T_g)$. It can also be assumed that the particles all share the same grey gases [192], and as such their weighting factors can be evaluated in the same way as for the gas, but as functions of the individual particle temperature: $a_{p,j} = a_{g,j}(T_p)$ [193]. The RTE can therefore be simplified to Eq. 4.89.

$$\begin{aligned}\frac{dI_j}{ds} &= (\kappa_{g,j} + \kappa_s) a_{g,j}(T_g) I_{b,g} + \kappa_{p,j} a_{g,j}(T_p) I_{b,p} \\ &\quad - (\kappa_{g,j} + \kappa_{p,j} + \kappa_{s,j} + \sigma_{s,p,j}) I_j + \frac{\sigma_{s,j}}{4\pi} \int_{4\pi} I_j(\boldsymbol{\hat{s}_i}) \Phi_\eta(\boldsymbol{\hat{s}_i}, \boldsymbol{\hat{s}}) d\Omega_i\end{aligned} \tag{4.89}$$

As conventional in the WSGG method, the RTE in Eq. 4.89 is solved once for each grey gas j, and the same constant grey particle and soot absorption coefficients are used throughout, with their associated weights. The total radiative source terms for the gas and particle phases are obtained as in Eqs. 4.90-4.91 below [192].

$$\nabla \cdot q_g = \sum_{j=1}^{J} \nabla \cdot q_{g,j} = \sum_{j=1}^{J} \kappa_{g,j} \left(4\pi a_{g,j} I_{b,g} - \int_{4\pi} I_j d\Omega \right) \tag{4.90}$$

$$\nabla \cdot q_p = \sum_{j=1}^{J} \nabla \cdot q_{p,j} = \sum_{j=1}^{J} \kappa_{p,j} \left(4\pi a_{p,j} I_{b,p} - \int_{4\pi} I_j d\Omega \right) \tag{4.91}$$

4.6.2 Radiative Properties of Particles

Regardless of whether the gas radiative properties are described using grey coefficients or a more sophisticated non-grey model such as the WSGG model presented in the previous section, throughout this work the particles are always described with grey radiative properties. The particles' absorption and scattering coefficients in a given cell are calculated according to Chui *et* al. [28].

$$\kappa_p = \epsilon_p \sum_i N_i \frac{\pi d_{p,i}^2}{4} \tag{4.92}$$

$$\sigma_p = (1 - \epsilon_p) \sum_i N_i \frac{\pi d_{p,i}^2}{4} \tag{4.93}$$

In Eq. 4.92 and Eq. 4.93 above, particles are grouped by their size classes i, and N_i is the particle number density defined as the number of particles pertaining to class i in a given cell, divided by the cell's volume. The particle's projected area is $\pi d_{p,i}^2/4$, whereas ϵ_p is the grey particle emissivity.

A particle's emissivity can be defined in several different methods, varying in complexity. The simplest approach is to use a constant value between 0 and 1, as done in [54, 63, 64, 93, 94]. A more sophisticated approach is to consider the variation in particle emissivity with char burnout. Chui *et* al. [28] proposed a simple equation (Eq. 4.94) to allow a particle's emissivity to vary between 1 in a fresh, unburnt particle and 0.6 in ash, or a completely burnt particle.

$$\epsilon_p = Y_{ub} + 0.6(1 - Y_{ub}) \tag{4.94}$$

More recently, Stöllinger *et* al. [161] used an approach similar to Lockwood *et* al.'s [106], allowing particle emissivity to vary between $\epsilon_{coal} = 0.9$ and $\epsilon_{ash} = 0.5$

$$\epsilon_p = \epsilon_{coal} - (\epsilon_{coal} - \epsilon_{ash})b \tag{4.95}$$

$$b = \frac{(1 - Y_{vc,0})m_{p,0} - m_p}{(1 - Y_{vc,0})m_{p,0} - (1 - Y_{vc,0} - Y_{c,0})m_{p,0}} \tag{4.96}$$

In Eqs. 4.95-4.96 above b represents the char burnout, obtained using the mass fractions of the unburnt (subscript *0*) char (subscript c) and volatile content (subscript vc), together with the mass of the particle m_p. Finally, the particle blackbody intensity $I_{b,p}$ can be obtained as in Eq. 4.97 [161].

$$\kappa_p I_{b,p} = \epsilon_p \sum_i N_i \frac{\pi d_{p,i}^2}{4} \frac{\sigma T_{p,i}^4}{\pi} \tag{4.97}$$

4.6.3 Radiative Properties of Soot

Soot formation modelling is a very complex research area of its own, and in most cases this is not accounted for when the main focus of the research is different, and such is the case in coal combustion modelling. Consequently, developing and implementing complex soot formation models and the soot's radiative properties is beyond the scope of this work. However, whereas in gaseous flames soot formation is minimal or non-occurring, and therefore ignoring this phenomenon can be considered a valid assumption in many cases, in coal combustion soot plays an important role, and as such it should be treated in some way. Three very simple approaches to incorporating the radiative effects of soot are outlined in the following paragraphs.

Constant, Grey Soot Absorption Coefficient

The simplest possible method of inclusion of soot radiative effects is to define a constant, grey and spatially independent soot absorption coefficient κ_s. This approach has been undertaken by Khalil *et* al. [81] and Yu *et* al. [192], where a value of $\kappa_s = 0.4m^{-1}$ was selected in both works. Such an approach is extremely over-simplistic as it assumes a uniform distribution of soot throughout the furnace, and radiative properties independent of local temperature and composition.

Constant, Combined Grey Gas-Soot Absorption Coefficient

Another equally simple treatment for modelling the radiative properties of soot in coal furnaces, adopted by many in literature [28, 161, 192], is to assume that the gas and soot are in thermal equilibrium, and therefore to set a constant grey, combined gas and soot absorption coefficient: $\kappa_{gs} = \kappa_g + \kappa_s$. Despite being an overly simplistic approximation, and with all the shortcomings of the previous method, this approach still allows some sort of treatment for soot radiation, and avoids the complexity of soot formation modelling, and any other computational cost that may be associated with this.

Empirical Calculation of the Soot Absorption Coefficient

A more detailed approach to treat soot radiation based on its temperature T_s, is to calculate the Planck-mean extinction coefficient for soot, as in Eq. 4.98 [119, 192].

$$\kappa_s = \frac{3.72 f_v C_o T_s}{C_2} \tag{4.98}$$

In Eq. 4.98 above, f_v is the soot volume fraction, which typically ranges from $f_v = 1 \times 10^{-8}$ to $f_v = 1 \times 10^{-6}$ [51], and $C_o = 36\pi nk/[(n^2 - k^2 + 2)^2 + 4n^2k^2]$ and $C_2 = 1.4388 cm \cdot K$ are two constants. The former, C_o, depends only on the soot index of refraction, where $k = 0.22$ is the absorptive index for bituminous coal particles [119, 192], and $n = 1.85$ is the real part of the complex index of refraction [192].

As one can see from Eq. 4.98 however, this model is largely dependant on the estimation of the soot temperature, and even more so on its volume fraction, which can span two orders of magnitude. Yu *et* al. [192] used a constant volume fraction of $f_v = 1 \times 10^{-6}$ in their work, which is an overly simplistic approximation as this is expected to vary in time and space, but in the absence of adequate soot modelling setting a constant value seems the only possibility. Moreover, the model can be easily implemented and doesn't add much computational expense, and hence it will also be considered and evaluated in this work.

4.7 Radiation Modelling in Large Eddy Simulations

In the previous sections, the radiative transfer equation has been derived, and the discrete ordinates method has been explained together with different spectral models used to describe the radiative properties of the medium. However, this was done in a *radiation-only* context, and to be able to extend this to LES, some further description is necessary, presented below.

4.7.1 Turbulence Radiation Interactions (TRI)

Turbulence and radiation are two very complex and different phenomena, of which an understanding is required in order to simulate turbulent reacting flows. However they are not independent, and the way in which they affect each other is described by so-called Turbulence Radiation Interactions (TRI). TRI is a two-way problem: on one side the flow and species concentration fields are influenced by radiation, and on the other hand the turbulent fluctuations in the flow field affect the radiation field [32]. Radiation influences the temperature field and its fluctuations [32, 155], which affects the density field, and consequently the species concentration and velocity fields are altered, as also shown in [9]. Radiation is also influenced by the turbulent fluctuations of the flow field, since the radiative properties of the medium depend on temperature and composition, and the computation of radiation emission and the divergence of the heat flux is also entirely and non-linearly dependent on these quantities.

In a RANS context, where a time-averaged solution is obtained, TRI modelling becomes a necessity to avoid large errors [32, 35, 62]. However in LES, where the instantaneous filtered governing equations are solved, TRI is only relevant at a subgrid scale level, and is much less important. Poitou et *al.* [127, 128] have shown using filtered DNS that the influence of subgrid scale fluctuations in temperature and composition on the emitted radiation is small. This was also confirmed in other studies by Coelho [34] and Roger et *al.* [141, 142], which dealt with both emission and absorption TRI at the subgrid level. The general agreeable conclusion seems to be that for non-optically thick cases (optical thickness ≤ 100), where the attenuation of radiant energy by the participating media is low, the effect of TRI at a subgrid scale can be ignored for LES [127]. However it must be noted that all the aforementioned studies on TRI were based on single-phase gaseous flames, considering absorbing emitting and non-scattering media. In the more complex case of coal combustion, which involves absorbing emitting and scattering particles, the relevance of TRI at the subgrid scale is yet to be defined. Furthermore air-coal combustion, and especially oxy-coal combustion, involves larger optical thicknesses compared to normal gas combustion, so the relevance of TRI could become significant [46]. In literature however, to the best of the author's knowledge and to date, no study of TRI involving scattering or TRI for coal combustion has been performed. In fact, in numerical work on coal combustion found in literature to date, TRI has been mostly neglected and gone unmentioned due to its complexity and associated computational cost, including work in a RANS context where the importance of TRI has been demonstrated. The recent work by Stöllinger et *al.* [160, 161], a 2D axi-symmetric RANS calculation of pulverised coal combustion is the only article which assesses the problem of TRI in coal combustion. In their work they use the optically thin fluctuation approximation (OTFA), which assumes that the correlation between fluctuations in the local absorption coefficient and intensity can be neglected [75, 76]. However, this approximation is only valid for cases where the optical thickness is smaller than the turbulent integral length scale [32, 160], and this may well not be the case in coal combustion, as the participating media is likely to have a relatively large optical thickness. Due to the seemingly low relevance, increased complexity and added computational cost of including TRI at a subgrid scale level in LES computations of coal combustion, these are not considered throughout this work. The absorption coefficient κ, the blackbody intensity I_b, and the radiative source term $\nabla \cdot q$, are therefore approximated as in Eqs. 4.99 - 4.101, giving a result similar to the OTFA.

$$\overline{\kappa(T,p)} \approx \kappa(\tilde{T},\tilde{p}) \tag{4.99}$$

$$\overline{I_b(T)} \approx I_b(\tilde{T}) \tag{4.100}$$

$$\overline{\nabla \cdot q(T,Y_i,p)} \approx \nabla \cdot q(\tilde{T},\tilde{Y}_i,\tilde{p}) \tag{4.101}$$

4.7.2 Parallelisation

Whereas with LES domain decomposition is the most logical and efficient parallelisation strategy, with radiation the calculation of the incident intensity involves the whole domain, making domain decomposition a not so straightforward option. For this reason there has been a lot of work carried out recently on the parallelization of radiative heat transfer calculations [3, 26, 44, 57, 58, 92, 126, 127, 129, 191]. This section presents a brief introduction to the possible parallelisation strategies, with special emphasis on the method developed and implemented in this work.

Generally speaking there are two main strategies to parallelise a radiative heat transfer calculation: *task decomposition*, which involves assigning different parts or tasks of a computation to different cores, and *data decom-*

position, where the calculation is split by domain decomposition. Hybrid decomposition methods involving a combination of both task and data decomposition have also recently been proposed by Poitou et *al.* [126], however in this section the two decomposition methods will be discussed separately.

4.7.2.1 Task Decomposition

In the discrete ordinates method, the intensity is divided and computed in discrete directions at each cell, via an iterative procedure. This means that the calculation for each subiteration must begin at each corner of the domain, where the boundary conditions are known, for all directions. A task decomposition known as *directional decomposition* is therefore possible, by assigning different directions to different cores, to be computed throughout the whole domain. Furthermore, in the case of non-grey participating media, where the DOM has to be solved for several frequencies, or grey gases in the case of the WSGG model, a further task decomposition known as *frequency decomposition* is possible, where cores are assigned different directions and frequencies/grey gases.

Task decomposition is ideal to parallelize radiative heat transfer calculations, since the bulk of the computation is in the iterative calculation of the intensity at each cell, and generally speaking the load of the computation is equal for each direction and frequency, thereby giving a good load balance on the processors.

However, this strategy comes with its limitations. The scalability of calculations in task decomposition is inevitably limited to the number of directions and/or frequencies or grey gases computed. For example for an S_4 DOM calculation, which involves 24 directions, the radiative solver will only scale well up to 24 cores, or integer divisions of 24. The limit is extended when considering non-grey participating media, for example an S_4 calculation with 4 grey gases means the tasks can be equally split over 96 cores (24 directions × 4 grey gases). Another limitiation of this approach for combined CFD and radiation codes is the amount of communication involved. The CFD code will be parallelised using domain decomposition with a given number of cores, whereas the radiation solver is parallelised using direction and frequency decompositions, meaning that a total mapping of the whole domain must be done for the temperature, pressure and concentration fields, and communicated to each processor for the task calculation. Furthermore, the number of cores needed for the domain decomposition might not be equal to those used for the DOM calculation, creating load imbalances. This problem is commonly circumvented by using separate CFD and radiation solvers, and assigning specific resources to each, as done by other groups [3, 44, 127]. However, the major drawback of task decomposition parallelisation, and the reason for which this has not been used in this work, is the memory requirement of this parallelisation strategy. For unstructured grids, or when using separate solvers, memory requirements are not a problem as a lower number of cells are involved, or a re-meshing pre-processing calculation can be done, reducing the number of cells by combining those involving the same relevant fields. However, when using structured, equally sized-cubic cells as in the in-house LES code used in this work, *PsiPhi*, it is not uncommon to deal with simulations having in excess of 100m cells, loading >2m cells per core. A task decomposition of such type would mean calculating a single direction per core, but over the whole domain of 100m cells, which needless to say is impossible to store on a single core, and much less on cores with shared memory architectures. Due to this unsurmountable memory constraint given by the structured grid, it was unfeasible to implement a task decomposition parallelisation for radiation.

4.7.2.2 Domain Decomposition

Having concluded that task decomposition is not a feasible approach for implementation in *PsiPhi*, an efficient domain decomposition parallelisation strategy must be implemented. Since radiative calculations with the DOM must start at the physical corners of the domain where the boundary conditions are known, for reasons previously discussed, this is not as straightforward as for LES convection calculations.

To avoid confusions, throughout this section the physical edges of the domain will be referred to as the *physical boundaries*, whereas the internal domain boundaries defined by the domain decomposition will be referred to as *virtual boundaries* [126].

In a non-scattering radiative calculation with black (absorbing but not emitting or reflecting) physical boundaries, the radiative solver need not perform any iterations, as no portion of the intensity is scattered inside the domain, or reflected/emitted at the physical boundaries, but only absorbed by the participating gases. As such, in a parallel domain decomposition calculation, at the first radiative computation the calculation is performed in a sequential order, starting at the physical boundaries, and communicating the boundary intensity sequentially at the neighbouring virtual boundaries. In all successive radiative calculations however, the boundary intensity computed at the previous timestep can be imposed at all virtual boundaries, enabling an efficient domain decomposition requiring only a small number of iterations [126]. All domains are computed at the same time using the old boundary conditions for all virtual boundaries, communication only occurs globally at the end of a subiteration, and at most a few subiterations will be necessary to obtain the correct solution.

For non-scattering calculations with emitting and diffusely reflecting boundaries, the same approach can be taken. Non-black wall boundary conditions require a certain number of subiterations to achieve a converged radiative solution, however this number can be greatly reduced by using the boundary conditions from the previous timestep at all virtual boundaries, and the load is balanced by computing all domains at the same time and communicating the new intensity at virtual boundaries only once per subiteration.

However, for calculations involving scattering participating media, as is the case with coal combustion, this approach does not speed up the calculation. The number of subiterations required for the solution to converge is in fact mostly determined by the scattering of the particles, rather than the emission and reflection of the physical boundaries. As such the virtual boundaries are constantly updated, and using the previous timestep's boundary condition will not speed up the calculation or reduce the number of subiterations required for convergence by a significant amount.

For this reason, a different domain decomposition approach was taken, similar to the one proposed by Yldiz and Bedir [191]. In this approach, an optimised sequential parallelization is used, meaning that the processes at the corner of the physical domain are computed first, after which the virtual boundaries are communicated to the neighbouring processes, which are then computed, and the boundaries are communicated to their neighbours and so on, until the opposite corner of the domain is reached, at which point the subiteration is concluded. This strategy is best described by dividing the

DOM subiteration in steps, where *N* represents the total number of steps per subiteration:

1. In *Step 1* only the corner processes of the physical domain are computed in the directions pointing away from their respective corner, while all other processes wait.
2. In *Step 2* the processes adjacent to each corner process are computed in the relevant directions.
3. For *Step 3* to *Step N-1*, all the processes in the direction of calculation adjacent to previously computed processes are computed, in the relevant directions.
4. Finally, at *Step N*, the opposite corner processes are calculated.

In between all steps the virtual boundaries are updated by communicating the neighbouring processes' virtual boundary intensity. For a given *X, Y,Z* processor allocation domain decomposition, where *X, Y,Z* represent the number of processes in the *X, Y* and *Z* directions respectively, the total number of steps per subiteration is $N = X + Y + Z - 2$. This procedure is best illustrated in Fig. 4.8, where an example of a *6,4,2* processor allocation is given. The processor loading is best illustrated in Fig. 4.9, which shows exactly at which step each processor is called for this sample arrangement, and this is also summarised in Table 4.4.

A further extension to this parallelisation strategy, would be to begin the computations at each corner at different instances for the different directions, as proposed in [191]. This can essentially lead to an optimised version of this parallelisation method, where load imbalances can be minimised by using an algorithm to calculate the optimal distribution of calculations over the different steps. Despite creating load imbalances over the processes at the different subiteration steps, to the best of the author's knowledge, this approach represents one of the most efficient ways to perform a domain decomposition parallelisation for the discrete ordinates method, when dealing with grey walls and scattering media. It is undoubted that a tasks decomposition is more suited for such cases, but this approach is rendered impossible by the memory constraint imposed by the large number of cells. This approach retains the simpler numerics involved in structured equally-sized cell grids, and still offers good performance on massively parallel simulations.

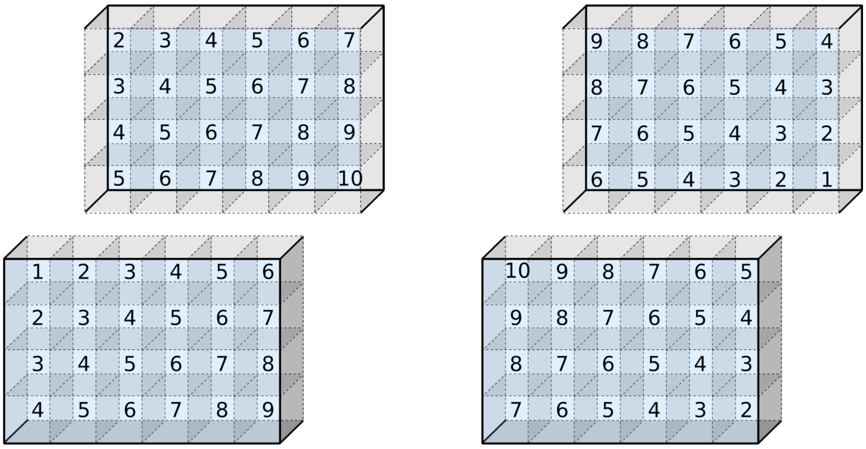

2	3	4	5	6	7
3	4	5	6	7	8
4	5	6	7	8	9
5	6	7	8	9	10

9	8	7	6	5	4
8	7	6	5	4	3
7	6	5	4	3	2
6	5	4	3	2	1

1	2	3	4	5	6
2	3	4	5	6	7
3	4	5	6	7	8
4	5	6	7	8	9

10	9	8	7	6	5
9	8	7	6	5	4
8	7	6	5	4	3
7	6	5	4	3	2

Figure 4.8: Sample domain decomposition parallelisation, processor marching operation for a 6,4,2 arrangement. Each number corresponds to the step at which the processor is called. On the left, the computation starts at the west front north corner of the domain, whereas on the right the computation begins at the east back south end of the domain. Similar operations are performed starting from all other corners.

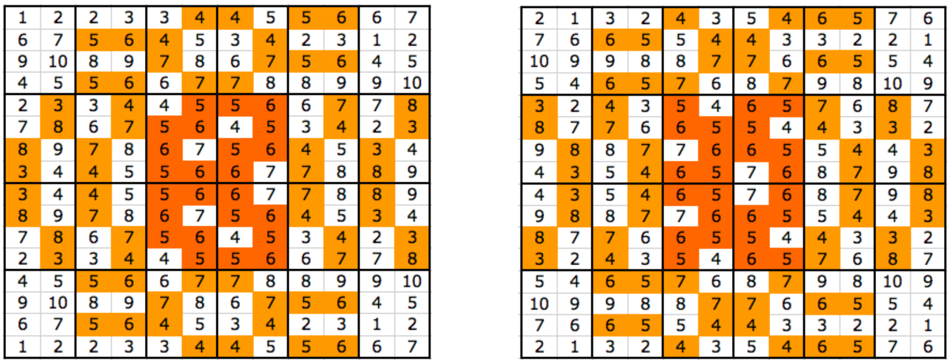

1	2	2	3	3	4	4	5	5	6	6	7
6	7	5	6	4	5	3	4	2	3	1	2
9	10	8	9	7	8	6	7	5	6	4	5
4	5	5	6	6	7	7	8	8	9	9	10
2	3	3	4	4	5	5	6	6	7	7	8
7	8	6	7	5	6	4	5	3	4	2	3
8	9	7	8	6	7	5	6	4	5	3	4
3	4	4	5	5	6	6	7	7	8	8	9
3	4	4	5	5	6	6	7	7	8	8	9
8	9	7	8	6	7	5	6	4	5	3	4
7	8	6	7	5	6	4	5	3	4	2	3
2	3	3	4	4	5	5	6	6	7	7	8
4	5	5	6	6	7	7	8	8	9	9	10
9	10	8	9	7	8	6	7	5	6	4	5
6	7	5	6	4	5	3	4	2	3	1	2
1	2	2	3	3	4	4	5	5	6	6	7

2	1	3	2	4	3	5	4	6	5	7	6
7	6	6	5	5	4	4	3	3	2	2	1
10	9	9	8	8	7	7	6	6	5	5	4
5	4	6	5	7	6	8	7	9	8	10	9
3	2	4	3	5	4	6	5	7	6	8	7
8	7	7	6	6	5	5	4	4	3	3	2
9	8	8	7	7	6	6	5	5	4	4	3
4	3	5	4	6	5	7	6	8	7	9	8
4	3	5	4	6	5	7	6	8	7	9	8
9	8	8	7	7	6	6	5	5	4	4	3
8	7	7	6	6	5	5	4	4	3	3	2
3	2	4	3	5	4	6	5	7	6	8	7
5	4	6	5	7	6	8	7	9	8	10	9
10	9	9	8	8	7	7	6	6	5	5	4
7	6	6	5	5	4	4	3	3	2	2	1
2	1	3	2	4	3	5	4	6	5	7	6

Figure 4.9: Schematic of the individual processor loading at the different steps. The two 6 by 4 arrangements are shown: front (*left*) and back (*right*). Each domain has eight numbers written inside, representing the step number at which the processor is called. Light orange shaded numbers represent Steps at which a given processor is called twice. Orange shading indicates a triple call within a Step.

Table 4.4: Processor loading at the various steps for a sample 6,4,2 processor arrangement. Active indicates the number of active ranks at a given step (out of a maximum possible of 48), Double and Triple indicates the number of ranks called twice and three times respectively, per step.

Step	Active	Double	Triple
1	24	0	0
2	32	0	0
3	40	8	0
4	40	16	0
5	40	8	8
6	40	8	8
7	40	16	0
8	32	8	0
9	24	0	0
10	8	0	0

4.7.3 Coupling LES with Radiation

Coupled combustion and radiation calculations must be synchronised in physical time to obtain an efficient calculation. Since the two have different characteristic time-steps in fact, radiation will only need to be updated every N_{it} timesteps [127]. The combustion timestep Δt_{LES} for low-Mach incompressible flows is limited by the CFL criterion (see Chapter. 2), Eq. 4.102, whereas the radiation time-step Δt_{RAD} is only defined by convection, Eq. 4.103. In fact, the radiative source term only changes as the temperature and species concentration fields change due to convection through the domain [127, 179].

$$\Delta t_{LES} = CFL \times \frac{\Delta x_{min}}{\overline{u}} \tag{4.102}$$

$$\Delta t_{RAD} = \frac{\Delta x_{min}}{\overline{u}} \tag{4.103}$$

Here Δx_{min} is the minimum characteristic cell-size, which for equally sized cubic cells $\Delta x_{min} = \Delta x$, and $\overline{u}$ represents the bulk velocity of the flow. The number of iterations at which the two calculations must be coupled, $N_{it} = \Delta t_{RAD}/\Delta t_{LES}$, and where identical grids are used, N_{it} can be simplified as in Eq. 4.104.

$$N_{it} = \frac{\Delta t_{RAD}}{\Delta t_{LES}} = \frac{1}{CFL} \tag{4.104}$$

For example for a case with a CFL number of 0.3 (typical of incompressible low-Mach flows for both gas and coal combustion), the radiative computations need only be performed every $N_{it} = 3.333 \approx 3$ combustion timesteps. Simulations have been performed by the author to verify that such simplification works, and no differences were observed in the resulting mean and fluctuating fields from two identical simulations with N_{it} of 1 and 3, and also rounding up to 4 showed no difference in the resulting fields.

5 Validation Studies for Radiation Modelling

Prior to implementing the radiation solver in the LES code, the methods presented in the previous sections have been validated against several test cases, ranging from homogeneous isothermal cases in two-dimensions to more realistic three-dimensional non-isothermal cases. These are presented and discussed in the following subsections.

5.1 2D Cases

Initially only 2 dimensions have been considered for simplicity, by selecting cases studied in literature with unit depth, which allows us to neglect the influence of the third dimension. These cases are validated against SNB data, and where possible against other authors' WSGGM results.

5.1.1 Case 1 - Homogeneous, Isothermal CO_2

This is a very simple case consisting of a rectangular enclosure ($1 \times 0.5m$), with black walls kept at 0K [60]. The participating medium is homogeneous CO_2 with 10% concentration and the remaining gas is inert nitrogen, kept at $1000K$. Data is provided by SNB calculations for the heat flux to the North and East walls. The simulation is performed using 80×40 cells in the i and j directions respectively. The RTE is solved by the DOM with S_8 quadrature [97], and the *Step* differencing scheme is used [120]. The property of the medium is described by the *non-grey* implementation of the WSGGM with 3 gray gases and one clear gas, with coefficients and weights obtained from Smith *et* al. [153].

As can be seen in Fig.5.1, the net radiative heat flux to the walls follows accurately that simulated by Goutiere *et* al. [60] with the WSGG model

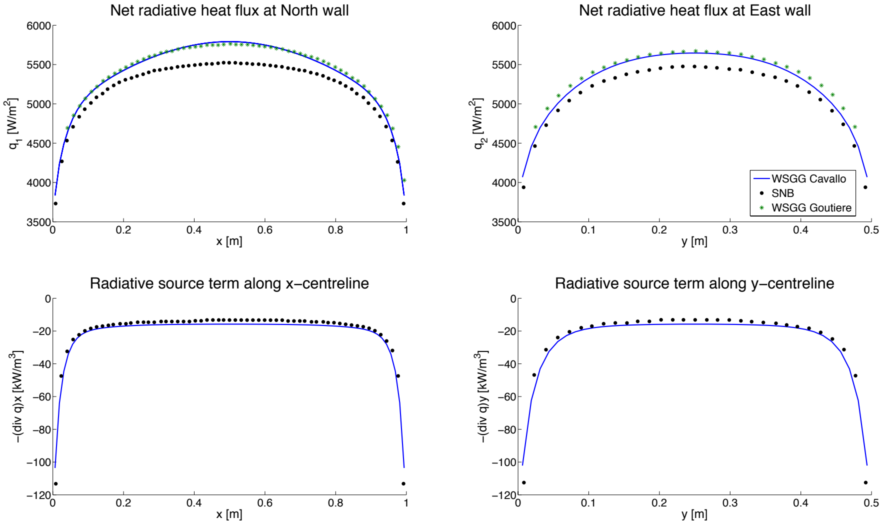

Figure 5.1: Results for test case 1. Benchmark SNB data [60] is compared to the solution obtained by Goutiere *et* al. [60] using the WSGG model with Smith *et* al.'s coefficients [153], and to the solution obtained with the code developed in this work, using the same coefficients (*WSGG Cavallo*).

(using the same parameters provided by Smith *et* al. [153]), and in both cases this overestimates the SNB data towards the centre of the walls away from the corners. The divergence of the heat flux is accurately replicated by the WSGG model throughout both x and y centrelines, and the peak variation in the centre of the domain is deemed of sufficient accuracy.

5.1.2 Case 2 - Heterogeneous, Non-isothermal CO_2

As in test case 1, the domain is described by a rectangular enclosure ($1 \times 0.5m$), with black walls kept at $0K$. The participating medium is again CO_2 and inert nitrogen, however the distribution of temperature and species is non-isothermal and non-homogeneous. The temperature T and concentration c fields are described by the equations below, and represented graphically in Fig. 5.2 and Fig. 5.3 respectively.

$$T(x,y) = T_0[0.3333(1-2|x-0.5|)(1-4|y-0.25|)+1] \tag{5.1}$$

$$c(x, y) = c_0[4(1 - 2|x - 0.5|)(1 - 4|y - 0.25|) + 1] \quad (5.2)$$

Here T_0 is 1200 K and c_0 is 0.02, and hence the temperature field varies between 1200 K and 1600 K, and the CO_2 concentration field varies between 0.02 and 0.10.

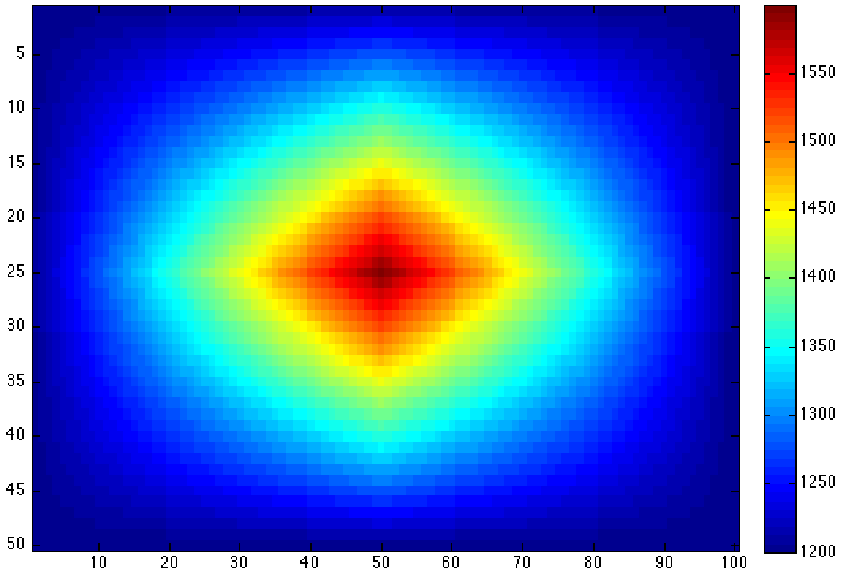

Figure 5.2: Contour plot of the temperature field (Kelvin) for test case 2, derived from Eq. 5.1

The RTE is solved with the same procedure used for test case 1, and the participating medium's properties are described with the same method as before, with the appropriate coefficients [153]. A slightly finer domain of 100 × 50 cells is used, and since the case is non-homogeneous and non-isothermal, local absorption coefficients and weights have to be computed at each cell, increasing the computational cost. The results are shown in Fig.5.4 and compared to SNB data.

The radiative heat flux at the North wall is accurately described by the WSGG model, with an increasing overestimation towards the centre of the domain, as in Case 1. The modelled flux at the East wall suffers the same problem, however this is also more noticeable closer to the edges and is of

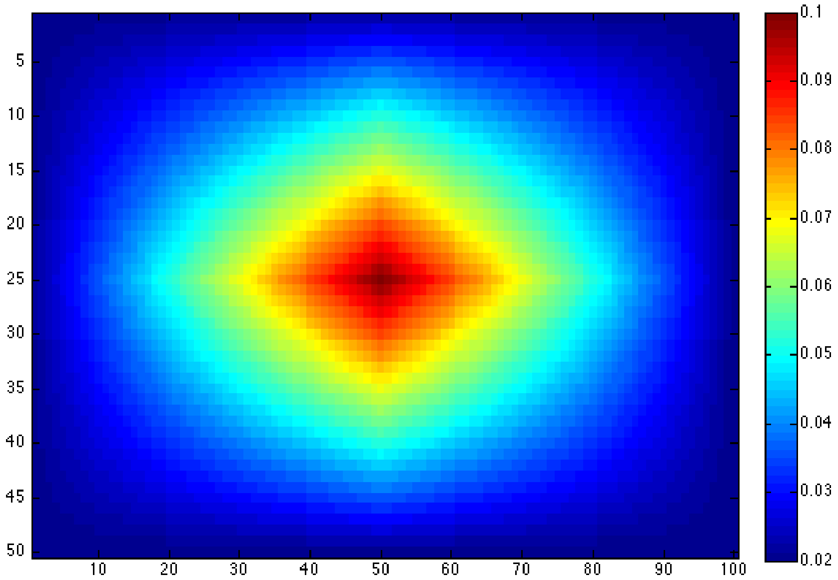

Figure 5.3: Contour plot of the CO_2 concentration field for test case 2, derived from Eq. 5.2

greater magnitude. The cause of such deviation from the SNB benchmark data could be the simple discretisation scheme employed in this simulation. The radiative source term along both centrelines matches the SNB data, with slight, acceptable discrepancies. At this point it is worth remembering that whereas the WSGG was developed for isothermal homogeneous cases, and authors refrain from presenting its non-homogeneous, non-isothermal implementation when comparing it to other models [60], its performance in such cases is promising.

5.1.3 Case 3 - Homogeneous, Isothermal H_2O

This case is very similar to Case 1, however using H_2O as the participating medium, with a concentration of 20%. The same implementation as for the first case was performed, with the respective parameters for the participating medium [153].

The wall heat fluxes calculated using the WSGG model slightly underestimate the SNB data throughout the length of the domain. However it

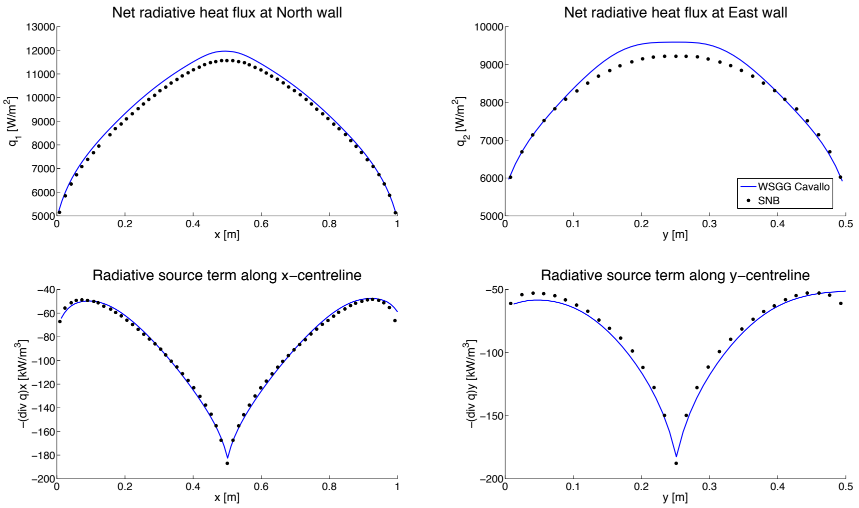

Figure 5.4: Results for test case 2. The solution obtained with the WSGG model (*WSGG Cavallo*) is compared to the benchmark SNB data [60].

must be noted that such results are considerably more accurate than those obtained by Goutiere *et* al. [60] who claim to have used the same model with the same coefficients. Two sets of coefficients are published by *Smith et al.* [153] for H_2O, namely for water partial pressures $P_w \rightarrow 0$ and for $P_w \rightarrow 1$, and the author believes that the wrong coefficients may have been employed by Goutiere *et* al. in their work. The use of standard coefficients may also be in fact the cause of the discrepancy between the SNB data and the authors' results for the heat fluxes. The coefficients used for $P_w \rightarrow 0$ can work well for a range of low concentrations or partial pressures, however a 20% concentration as in this case, may require the use of different coefficients. Despite the use of potentially inadequate coefficients, the radiative source term along the centrelines closely matches the SNB data throughout, outperforming the results published by Goutiere *et* al. [60].

5.1.4 Case 4 - Heterogeneous, Non-isothermal H_2O

This case is very similar to test case 2, in that it concerns a non-homogeneous, non-isothermal participating medium which is again described by Eqs. 5.1-5.2. In this case however the participating medium is H_2O, and whereas

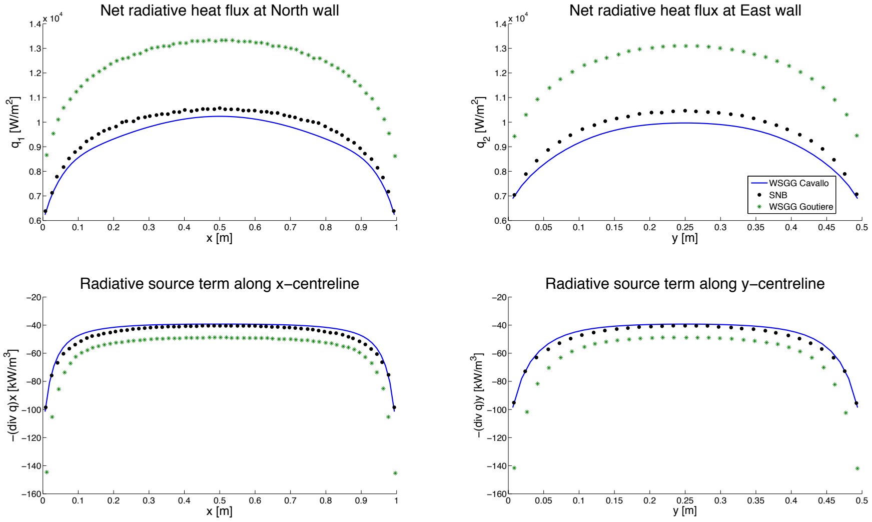

Figure 5.5: Results for test case 3. Benchmark SNB data [60] is compared to the solution obtained by Goutiere *et* al. [60] using the WSGG model with Smith *et* al.'s coefficients [153], and to the solution obtained with the code developed in this work (*WSGG Cavallo*).

T_0 in Eq. 5.1 takes the same value of 1200K, c_0 in Eq. 5.2 is now 0.04, thereby varying the concentration from 0.04 to 0.20. The same temperature and concentration distributions shown in Figs. 5.2-5.3 apply, with a different range of values as discussed. Aside from selecting the appropriate gas coefficients, the same simulation parameters of test case 2 were used.

The heat fluxes to the walls are overestimated in the WSGG model throughout the length of the walls, with an increasing error away from the corners. This coincides with the increased concentration of participating media towards the centre of the domain, and hence the loss of accuracy is due to the coefficients employed becoming progressively less suitable. The radiative source term across both centrelines instead accurately represents the SNB data.

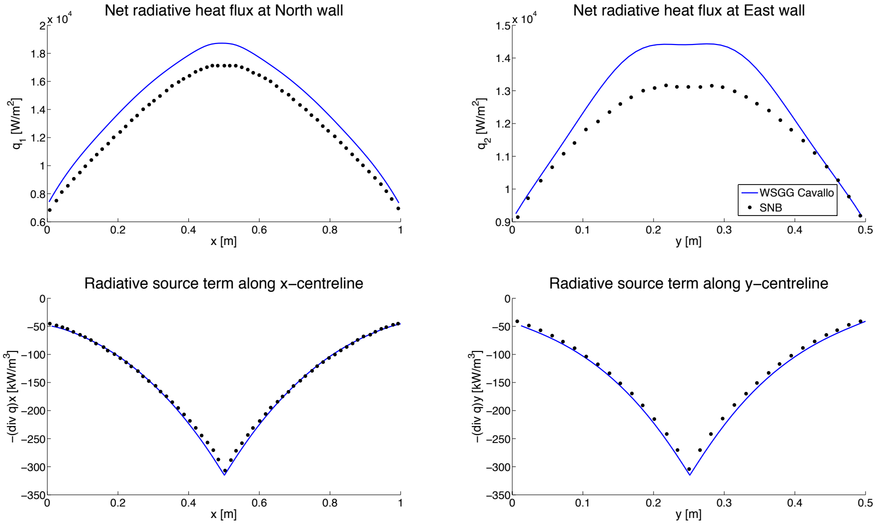

Figure 5.6: Results for test case 4. The solution obtained with the WSGG model (*WSGG Cavallo*) is compared to benchmark SNB data [60].

5.1.5 Case 5 - Homogeneous, Non-isothermal CO_2/H_2O mixture

This case is a more representative example to validate gas combustion, and has also been recently simulated by Porter *et* al. [130]. The participating medium consists of a homogeneous mixture of CO_2 and H_2O having concentrations of 10% and 20% respectively, with the remaining gas being inert Nitrogen. In instantaneous calculations of the combustion of air and methane, products are often approximated to the participating gas used in this case and with those proportions, making this a very practical test case. The temperature field is described by Eq. 5.3 below, where $y_0 = |0.25 - y|/0.25$, which results in a temperature field similar to that of a real flame, as can be seen in Fig. 5.7.

$$T(x,y) = \begin{cases} (14000x - 400)(1 - 3y_0^2 + 2y_0^3) + 800 & x \leq 0.1 \\ \frac{10000}{9}(x-1)(1 - 3y_0^2 + 2y_0^3) + 800 & x > 0.1 \end{cases} \tag{5.3}$$

For the WSGG model, the coefficients for a mixture $P_w/P_c = 2$ were

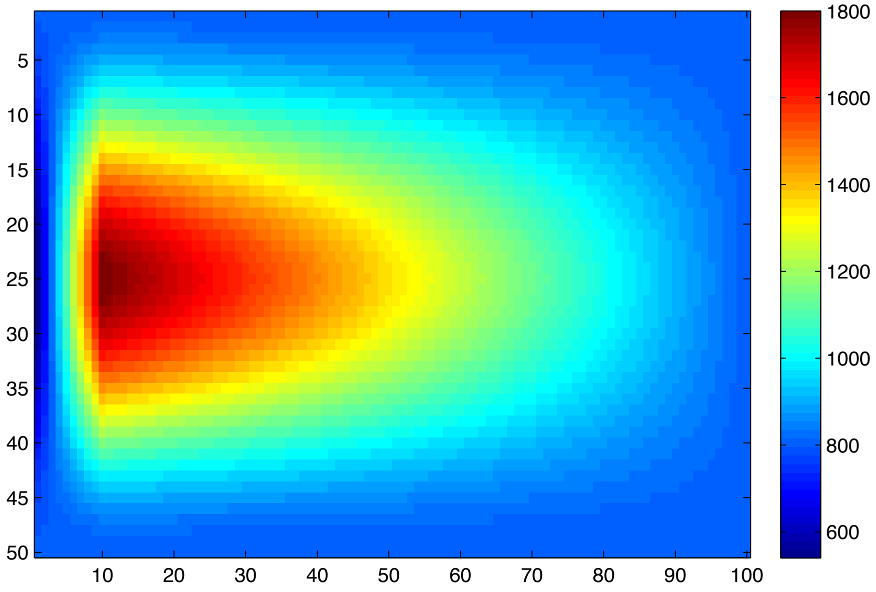

Figure 5.7: Temperature distribution for test case 5, obtained using Eq. 5.3.

used [153], and the DOM similar to test cases 2 and 4 was employed to solve the RTE. The results can be seen in Fig. 5.8.

The radiative heat flux to both the North and East walls is again overestimated throughout the domain, and the error seems to increase with increased temperature regions and not only due to the distance from the corners as was only perceptible in the other test cases. The WSGG results are of approximately the same magnitude as those obtained by Porter *et* al. [130] and Goutiere *et* al. [60], however in the present results a plateau is observed where the peaks should be. The radiative source term along the x centreline replicates quite well the SNB data, with a small error between $x = 0.1$ and $x = 0.3$. The source along the y centreline is fairly representative as well, with increasing error towards the centre, which coincides with higher source regions.

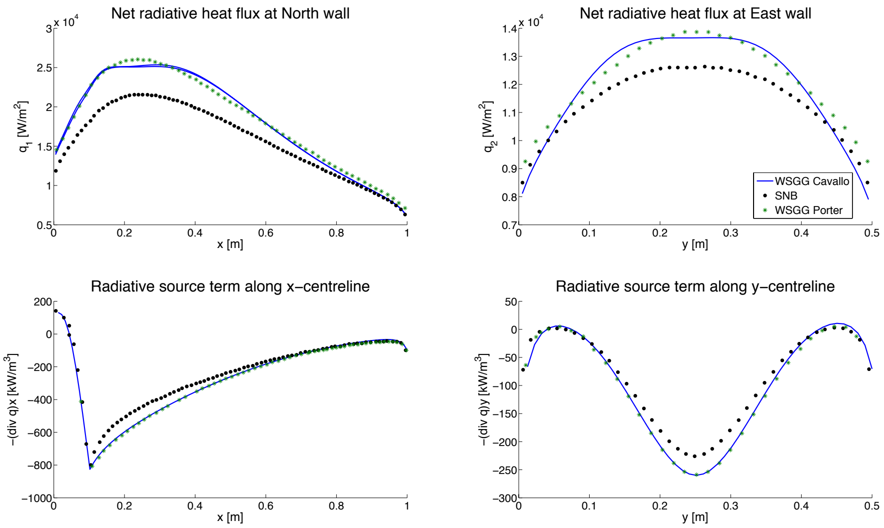

Figure 5.8: Results for test case 5, compared to benchmark SNB data [60], and to the data obtained by Porter *et* al. [130]. Note that the axis in the wall heat flux plots (top) does not start at zero to make the deviations more visible.

5.1.6 Conclusions

Test cases with different conditions in terms of species concentration and temperature distributions have been simulated in 2D, with the final one (test case 5) being slightly similar to the conditions expected in LES of gaseous combustion. The current model tends to produce some errors in calculating the heat flux to the walls, which is particularly noticeable in the more complicated cases involving non-homogeneous, non-isothermal mixtures. It is worth noting that the coefficients employed in the WSGG model [153] for these test cases are in theory only valid for temperature ranges between $600K$ and $2400K$. All cases studied involve black walls kept at $0K$, which is outside the temperature range of the coefficients, and hence may partially be the cause of the inaccurate wall fluxes. In LES calculations where walls will be employed, these will be at realistic temperatures, and better results are expected. The only case where one would use black walls at low temperatures is as boundary conditions for inlets or exits not confined by walls (where actually there is no wall), and in such cases there is less interest in accurately predicting the heat fluxes as these will have minimal influence on the source terms in the regions of interest.

The radiative source term is instead always of great significance for LES calculations, as this is the driving source term that feeds into the energy equation. The WSGG model performed remarkably well in this context, matching nearly exactly the SNB data along both the x and y centrelines in most cases. The only case where there is a more prominent deviation from the SNB data is in test case 5, where it would be ideal to have greater accuracy.

5.2 3D Cases

Prior to incorporating the radiation code in the LES solver, the code has been extended to three-dimensions and validated against three different test cases, presented in the following subsections.

5.2.1 Case 1 - Uniform, Isothermal Participating Media

The first test case [29, 103, 167] consists of a rectangular enclosure measuring $4m$ in length and having a $2m$ square cross-section ($2 \times 2 \times 4m$ in x, y, z Cartesian coordinates). The enclosure is filled with pure isothermal water vapour (H_2O), kept at $1000K$. SNB benchmark data (provided by Liu [103]) is available for the radiative source term along the z-centreline and along the x and y-centrelines at a distance *0.375 m* from the front ($z = 0.375m$). The incident heat fluxes on the wall centrelines are also obtained by *SNB* calculations, where the walls running along the length of the domain are referred to as *NSFB* and the side walls as *EW* in Figs. 5.9-5.10. The simulation is also compared to the results obtained by Coelho's WSGG implementation [29] (using the same coefficients by Smith *et* al. [153]), who employed the T_N (T_4) quadrature with 128 discrete directions and the CLAM scheme for spatial discretization, on a coarser grid.

The simulation was performed using 80 cells in the axial and 40 cells in the x and y directions, giving a characteristic cell size of 5.00 cm. The same WSGG parameters as in Case 3 in two-dimensions were used, namely $P_w = 1$.

The step discretisation scheme was used with the S_4, S_6 and S_8 angular discretizations of the DOM, to provide a sensitivity analysis on the angular

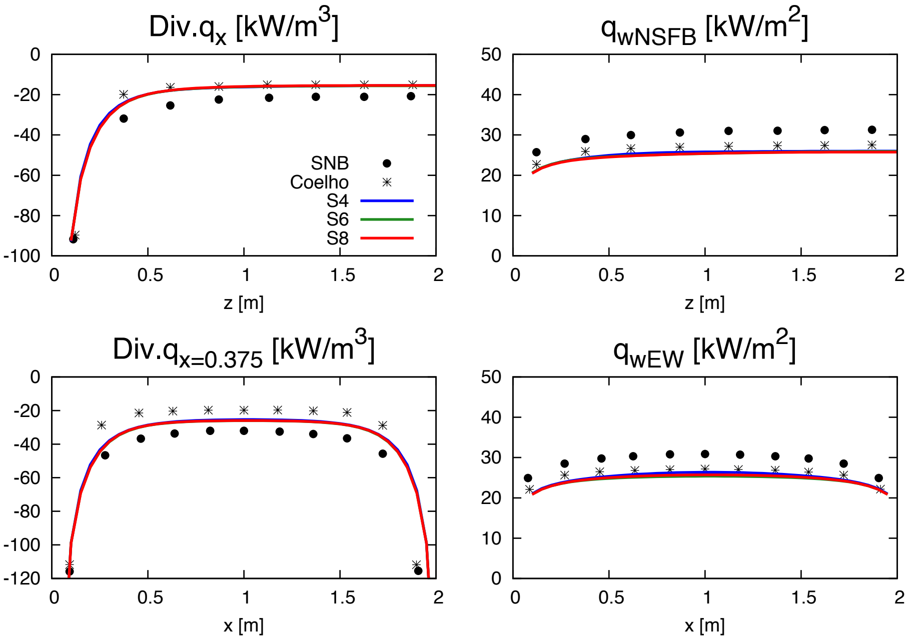

Figure 5.9: Influence of angular discretisation on simulation results. Three quadratures, S_4, S_6 and S_8 are compared, having 24, 40 and 80 directions respectively. The results are compared to SNB benchmark data by Liu [103], and WSGG data by Coelho [29].

discretization. The results are presented in Fig. 5.9, showing a negligible difference in the results obtained by varying the number of directions, which is to be expected since the participating medium is uniform and isothermal. The radiative source term is overestimated along both lines, whereas the heat flux to the walls is underestimated. The results are in agreement with Coelho's WSGG data, although the radiative source term seems to be predicted slightly better in our work, possibly due to different angular and spatial discretisations.

A study on the influence of the spatial discretisation scheme was also performed by testing the step, diamond, TVD, and CLAM schemes (presented in the previous chapter), all with the S_8 angular quadrature. The results are shown in Fig. 5.10, and it is evident that the selection of the spatial discretisation scheme can play a big role in the outcome of the simulation. Results obtained with the step scheme have been discussed above, whereas the diamond scheme yields oscillatory, unstable and unrealistic results, for the radiative source term, which can be clearly seen by the $zig-zag$ pattern

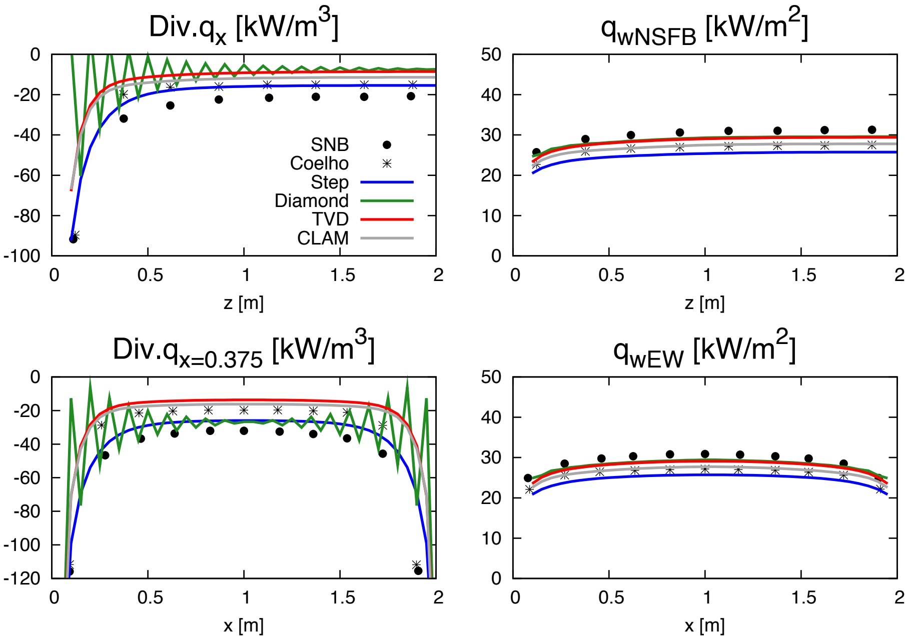

Figure 5.10: Results for 3D test case 1. The WSGG S_8 results with different spatial differencing schemes are compared to SNB benchmark data by Liu [103], and WSGG data by Coelho [29].

of the green line in Fig. 5.10. Despite this, the wall heat flux predictions with the diamond scheme yield excellent results. The TVD and CLAM scheme yield much better wall heat flux results compared to the step scheme, with the former surpassing the latter, but however give poorer predictions in terms of the radiative source term.

5.2.2 Case 2 - Uniform, Non-Isothermal Participating Media

This case is more representative of the conditions found in a gas-fired boiler [29, 103, 130, 167], and is similar to the two-dimensional Case 5. The same rectangular enclosure of the previous case is filled with 10% CO_2, 20% H_2O and the remaining 70% consists of non-participating N_2. The temperature profile varies along both the radial (x and y) direction and the axial (z) direction, as described by Eq. 5.4 and Eq. 5.5. Here T_c is the centreline temperature which increases linearly from the inlet ($z = 0m$) at 400 K to a peak of 1800 K at $z = 0.375m$, after which it decreases linearly to the end of the domain ($z = 4m$) with an exit temperature of $T_e = 800K$. The radial temperature variation is accounted for by the function $f(r/R)$ where

r is the local radius, and R is the radius of a circle *1m*, beyond which the temperature is taken to be equal to the exit temperature T_e.

$$T = (T_c(z) - T_e)\, f\left(\frac{r}{R}\right) + T_e \tag{5.4}$$

$$f\left(\frac{r}{R}\right) = \begin{cases} 1 - 3\left(\frac{r}{R}\right)^2 + 2\left(\frac{r}{R}\right)^3 & (r/R) \leq 1 \\ 0 & (r/R) > 1 \end{cases} \tag{5.5}$$

The simulation was performed using the same grid as in the previous case, again testing the different spatial and angular discretisations. The relevant WSGG coefficients for a $P_w/P_c = 2$ mixture were used [153]. The results of varying the angular quadrature with the step spatial differencing scheme are shown in Fig. 5.11, whereas different spatial differencing schemes are compared to each other in Fig. 5.12. In both figures, the data is validated against SNB results published by Liu [103] as in the previous case, however in this case the heat flux to the wall is also compared to the results obtained by Porter *et* al. [130], who used a grey implementation of the WSGG.

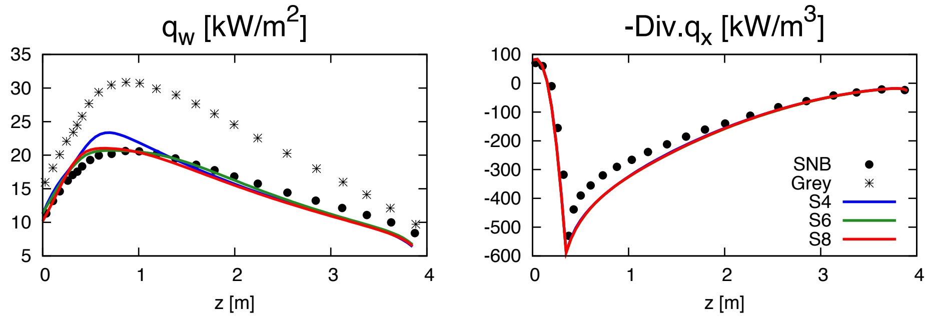

Figure 5.11: Results for 3D test case 2 using the WSGG with S_4, S_6, S_8 approximations (labelled S4, S6 and S8 respectively), compared to SNB benchmark data [103] and grey WSGG data (only for q_w, labelled Grey) [130].

Generally, the heat flux at the wall centreline obtained with the WSGG method accurately reflects the SNB benchmark data, whereas the grey implementation yields poor results due to its simplification. The radiative source term along the centreline follows the pattern of the SNB data, with some deviation, which is most noticeable in the region between *x=0.5m* and *x=1.5m*. This coincides with the high-temperature region of the domain and is similar to the error noticed in Case 5 in two-dimensions. Varying the angular discretisation seems to have little effect on the radiative source term at the centreline, however a noticeable effect is seen in the simulated wall heat flux. With 24 directions in fact (S_4), there is a relatively large overestimation of the wall heat flux in the region coinciding with the highest temperature gradients in the domain. This is highly mitigated by both the S_6 and S_8 discretisations which yield near identical results, suggesting that sufficient angular resolution is obtained with 40 directions.

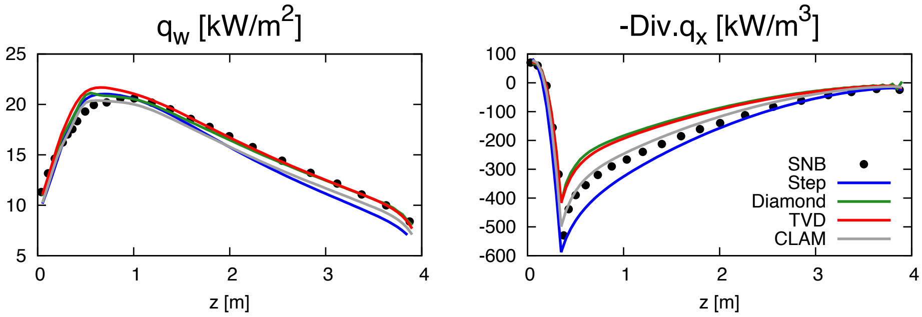

Figure 5.12: Results for 3D test case 2 obtained using the WSGG method and the S_8 angular approximation, testing different spatial differencing schemes. Results are compared to SNB benchmark data by Liu [103].

Similar to the previous case, different spatial differencing schemes are compared to each other in Fig. 5.12, all with the S_8 angular scheme. The diamond scheme in this case yields the best wall heat flux prediction, with a small instability near the top of the slope; however the radiative source term is largely underpredicted throughout. The TVD scheme also yields a good wall flux prediction, however has the largest overestimation of all schemes near the top of the slope, and the radiative source term is largely underpredicted in a similar way to the diamond scheme. Finally, the CLAM scheme gives excellent centreline predictions of the radiative heat flux, and better wall flux predictions than the step scheme.

5.2.3 Case 3 - The Ideal Furnace

The final test case is known as the ideal furnace, which was originally proposed by Menguc and Viskanta [114], and has been widely used by several authors as a validation test case [17, 22, 48, 68, 73, 84, 170].

The same domain as in the previous cases is used, a rectangular enclosure measuring $2 \times 2 \times 4m$, and discretised again using $40 \times 40 \times 80$ equally sized cubic cells, of $5cm$ characteristic size. The enclosure is filled with absorbing-emitting media having a grey absorption coefficient of $\kappa = 0.5$, and a uniform internal heat source of $\nabla \cdot q = 5kW/m^3$. However in this case the walls are defined as grey, diffusely emitting and reflecting. The east wall is hot, having a temperature of $T_E = 1200K$ and an emissivity of $\epsilon_{w,E} = 0.85$, whereas the west wall is cold, with $T_W = 400K$ and $\epsilon_{w,W} = 0.70$. The side walls have intermediate temperatures of $T_S = 900K$ and the same emissivity as the west wall, $\epsilon_{w,S} = 0.70$ [114]. No exact solution exists for this case, but the results can be compared to Hottel's zonal method solutions [114, 170], as in Fig. 5.13.

The temperature profiles are well captured by the S_6 and S_8 quadratures, whereas the S_4 quadrature gives a larger error 2m from the inlet and 0.4m from the outlet. The wall heat fluxes are also well captured, with the S_8 quadrature giving the best results at the hot wall ($z = 0m$), but the worst prediction at the cold wall ($z = 4m$). Nonetheless, a good agreement overall is obtained.

5.2.4 Conclusions

The test cases presented in this section show a sufficiently good agreement with the benchmark solutions. The net heat flux at the wall seems to be generally slightly underpredicted by the DOM throughout all test cases, and small deviations can also be observed for the radiative heat flux. Variations in the accuracy of the angular differencing scheme has shown that for non-isothermal test cases the S_4 scheme yields relatively large errors, and more accurate schemes such as the S_6 and S_8 are required. Considering the difference in computational cost between obtaining the exact (benchmark) solution and the solutions obtained with the WSGG or the grey models (for test case 3), the results are more than acceptable and the models suitable for use in the LES of coal combustion.

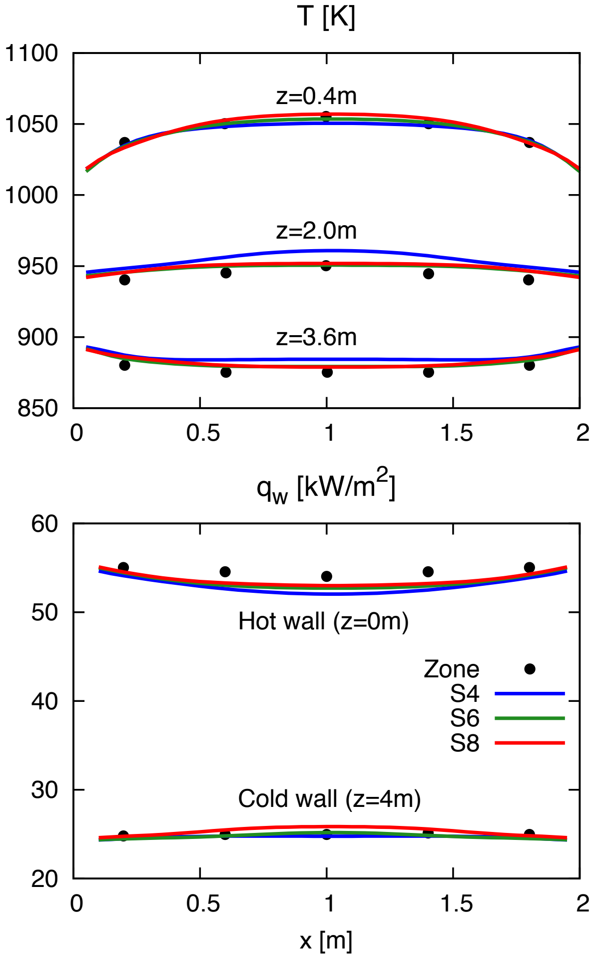

Figure 5.13: Results for 3D test case 3, the ideal furnace [114]. DOM results with different angular quadratures are compared to Zonal solutions [114, 170].

6 Large Eddy Simulation of the International Flame Research Foundation Furnace

This chapter presents the work carried out on the simulation of a near industrial-scale pulverised coal burner studied experimentally at the International Flame Research Foundation (IFRF) by Michel and Payne [117], with a particular focus on the issue of radiation modelling. The flame simulated is Flame B1 of the IFRF furnace No.1, details of which can be found in Section 6.3. The IFRF furnace has been used in the past years for experimentation with various different burners [87, 117, 122, 150, 180, 185], including both non-swirling [87, 117, 122] and swirling ones [150, 180], and also for MILD combustion studies [185]. Various numerical studies of this furnace can also be found in literature [107, 111, 123, 146, 159, 160, 161, 166, 173, 176, 177, 181, 184, 186, 192], however all of them have been performed in a RANS framework, and no LES of this furnace has been carried out to date, to the best of the author's knowledge. The burner studied by Michel and Payne [117] was chosen over others due to its simple non-swirling configuration and its coarse geometrical features, which enable a more efficient simulation on a Cartesian grid with immersed boundaries, enabling us to focus on the modelling and physics involved and to conduct the necessary sensitivity and parameter studies. Flame B1, which is the simulated configuration in this work, has already been simulated in a RANS environment by Lockwood and Salooja [107], Tian et *al.* [166] and more recently by Stöllinger *et* al. [159, 160, 161].

The aim of this work is to perform the first large-eddy simulation of a near industrial-scale pulverised coal burner, and as such a simple, computationally efficient configuration was chosen as a starting point. Extension to geometrically challenging and swirling burners should be relatively straightforward, given that the code, also used for gaseous combustion, has been found to perform well in such circumstances [124, 157, 158]. Moreover, Franchetti simulated a pulverised oxy-coal combustion swirling burner with a relatively complex geometry, using the same code, and obtained a satisfactory agreement between experiments and simulations [52].

A special focus is posed on the issue of radiation modelling for LES of coal combustion, as this is a relatively unexplored topic, due to its modelling difficulties and associated high computational cost.

6.1 Flow and Combustion Modelling

In this section the governing equations for fluid flow and combustion are referenced from previous chapters, as well as details on the numerical implementation of the coal particles, and the models used to describe coal combustion. The simulations were performed using the Euler-Lagrange version of the in-house 3D low-Mach solver, *PsiPhi* [20, 80, 124], which solves the continuous gaseous phase with Eulerian equations, and the dispersed particles phase in a Lagrangian framework.

6.1.1 Gas Phase Governing Equations

The Favre-filtered governing equations for incompressible multiphase fluid flow, mass and momentum were solved, Eq. 3.47 and Eq. 2.30 respectively. The turbulent viscosity ν_t is described using the Smagorinsky model [149] (Eq. 2.31), with a fixed constant $C_s = 0.173$ [102].

To be able to describe mixing and combustion, transport equations for enthalpy h and the main species mass fractions Y_α accounting for gas-particle heat and mass exchanges were also solved (Eq. 3.49 and Eq. 3.48 respectively). The species considered in this work were: oxygen O_2, nitrogen N_2, water vapour H_2O, carbon monoxide CO, carbon dioxide CO_2 and a postulate substance representing the volatiles $C_\alpha H_\beta O_\gamma N_\delta$ (see Section 3.2).

The enthalpy transport equation source terms arise from the heat exchange between the continuous and the dispersed phase and from radiation, and have been described in detail in Section 3.3. The source terms for the volatile gases and carbon monoxide come from the discrete phase from the devolatilisation and char combustion processes. All species except for nitrogen, which is assumed to be completely inert, have source terms arising from the gaseous combustion model, including the ones already having sources from the dispersed phase. For more details the reader is referred to Chapter 3.

The gas phase combustion is described using the Eddy Break-Up (EBU) model [156] adjusted for LES [67, 198], which has been described in detail in Sec. 3.2.3. Two reactions are considered to describe the combustion of volatile gases, the first concerning the production of carbon monoxide and water vapour (Eq. 3.10a), followed by the further reaction of carbon monoxide to carbon dioxide (Eq. 3.10b).

A Central Differencing Scheme (CDS) is used to approximate the convective fluxes for momentum, whereas a Total Variation Diminishing (TVD) scheme is used for all other scalars. Time integration was performed using an explicit low-storage third order Runge-Kutta scheme. Pseudo-turbulent inflow conditions are created using an artifical turbulence generator [78, 86].

6.1.2 Dispersed Phase

The Lagrangian coal particles' description has been already presented in Section 3.3, and only a brief overview will be given here. Particles are assumed to be composed of volatile matter, char (fixed carbon) and ash only. The change in mass of each particle is dependent on the yield of volatile gases (dm_{vg}/dt) and the char burning rate (dm_{char}/dt), whereas ash is assumed to be inert. The rate of change of temperature of each particle depends on the heat exchange with the gas phase, the particles' heat loss due to devolatilisation h_{dev} and radiation $\dot{q}_{rad}$, and the heat gain from char combustion $\dot{q}_{char}$.

The devolatilisation of the volatile gases from the coal particle is modelled using the first-order single reaction rate model by Badzioch and Hawksley [6], which has already been explained in Section 3.2.1. The emission of volatiles from a given coal particle is assumed to occur with a single reaction, the rate of which can be expressed by an Arrhenius equation. Different values for the pre-exponential factor A_v and activation energy E_v can be found in literature for high-volatile bituminous coals, which can also span several orders of magnitude. The volatile yield V, and the initial volatile matter in the coal particle $VM = VM_0 \times Q$ is adjusted by a heat release Q-factor, to account for the higher release of volatiles at high heating rates [6].

Char combustion is described using the intrinsic reaction rate model proposed by Smith [152]. The model requires several parameters to describe the physical properties of the coal particles, and has been explained in detail in Section 3.2.4, to which the reader is referred for further information.

6.2 Radiative Heat Transfer

Radiation modelling is a very important aspect for the simulation of pulverised coal combustion in closed furnaces, as this can be the main mechanism of heat transfer between the reacting particles and gas and the furnace walls. However with increasing accuracy, radiation calculations can rapidly become significantly more expensive than LES calculations, and therefore a good cost-accuracy balance must be found for an efficient simulation. This work is restricted to global spectral models of varying accuracy for the description of the radiating medium, due to the otherwise excessive computational cost of the calculations. This section briefly summarises the specific radiative heat transfer models employed in this test case, which have been covered in greater detail in Chapter 4.

6.2.1 The Radiative Transfer Equation

The Radiative Transfer Equation (RTE) for absorbing-emitting and scattering media including the effects of coal particles and soot has already been presented in Eq. 4.81, and is subject to the boundary condition for gray opaque, diffusely emitting and reflecting surfaces, Eq. 4.28. As conventional with combined gas, particles and soot radiation calculations, only particle scattering is considered as this is largely dominant over gas and soot scattering [28, 192]. Further, throughout this work only isotropic scattering is considered, and hence the scattering phase function is simplified to $\Phi(\mathbf{\hat{s}_i}, \mathbf{\hat{s}}) = 1$. The RTE is solved using the Discrete Ordinates Method (DOM) [47, 48, 169], which has been described in great detail in Chapter 4.

6.2.2 Spatial and Angular Discretisation

Since radiation propagates from a point in all directions, the DOM discretises the RTE both spatially, in discrete cells, in the same way as is done for CFD calculations, and angularly, in a set of discrete directions, with quadrature weights associated to each direction. The spatial and angular discretisations have been described in detail in Sec. 4.4.6 and Sec. 4.4.3 respectively, to which the reader is referred for further details.

For convenience, and to retain the simple numerics used in the LES, the spatial discretisation of the RTE is achieved using the same grid of the LES. Since equally-sized cubic cells are employed, a simple step scheme [120] can be used, which is similar to the upwind differencing scheme used for convection in CFD, without encountering significant errors.

Several different quadrature schemes can be found in literature for the angular discretisation of the RTE [18, 89, 165]. In this work, the S_N approximation [18], having $N(N+2)$ directions was chosen. Three different quadratures, S_4, S_6 and S_8, leading to 24, 48 and 80 radiation directions respectively have been tested, and their relative accuracy will be discussed in Section 6.5.

The selection of the angular discretisation scheme has a big impact on the cost of the DOM solver, as a higher-order discretisation implies a higher number of directions for which the RTE must be solved at each iteration of the radiative solver. Consequently, this also has a significant impact on the overall cost of the simulation, since despite the many efforts made to make the DOM solver as efficient as possible, it remains a very expensive calculation, surpassing the cost of the LES solver.

6.2.3 Gas Spectral Models

The scope of this work is to assess the influence of radiation modelling on the accuracy of the solution, and as such several different gas spectral models have been implemented and tested. The representation of the radiative properties of the gas and soot is however limited to global models, due to the high computational cost of the more sophisticated alternatives.

The most basic type of global models are *grey* models, where the gas is assumed to emit radiation in a single band, representative of the entire electromagnetic spectrum. Three different grey models, previously presented in Section 4.5.1, are covered in this work.

A more detailed model employed in this work, and still computationally affordable is the Weighted-Sum of Grey Gases (WSGG) model, originally developed by Hottel and Sarofim [65], details of which may be found in Sec. 4.5.2. Only CO_2 and H_2O are treated as participating gases in this model, as these are known to emit and absorb radiation considerably more than other species. The available grey gas coefficients determined by Smith et *al.* [153] were used, derived for mixtures having molar proportions $X_{H_2O}/X_{CO2} = 1$. Despite the molar ratio in the furnace not being constant, it was found to be the closest set of coefficients readily accessible from the literature, as discussed in detail in Sec. 6.4.

The modified WSGG (MWSGG) is also considered in this work, to overcome the problem of inadequate coefficients and varying molar ratios of the participating species. For more details on this model the reader is referred to Sec. 4.5.4.

6.2.4 Particles Radiation

The particles' absorption and scattering coefficients in a given cell are defined by Chui et *al.* [28], and described in greater detail in Sec. 4.6.2. The particle emissivity ϵ_p is defined as a function of char burnout, again following the work of Chui et *al.* [28], and its mathematical relation can be found in Eq. 4.94.

6.2.5 Soot Radiation

Modelling soot and its formation is a complex research topic, and incorporation of soot formation models is beyond the scope of this work. Nonetheless, soot plays an important role in radiation, and is always present in closed pulverised coal furnaces. For this reason, when modelling radiation for coal combustion soot radiation is often accounted for, despite the use of overly-simplistic models. Three different approaches for incorporating soot radiation effects have been already described in Sec. 4.6.3, and will be assessed in the following sections.

6.2.6 Coupling with LES

To obtain an efficient simulation, coupled combustion and radiation calculations must be synchronised in physical time. The approach for the physical time synchronisation is described in detail in Section 4.7.3. In this work a CFL number of 0.3 is used for all simulations, and as such the radiative

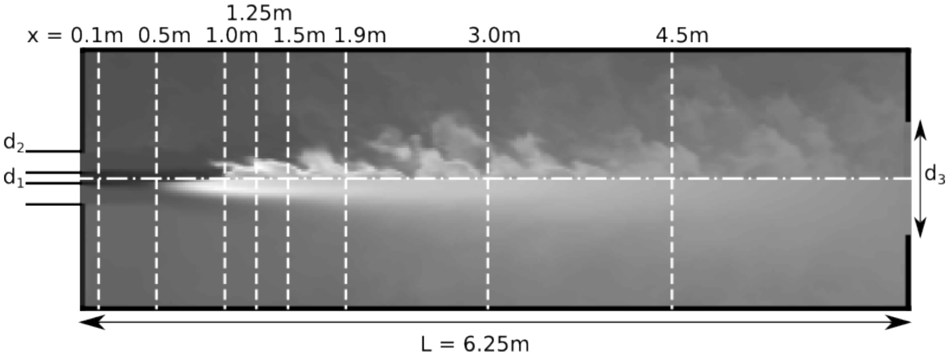

Figure 6.1: Sketch of the IFRF furnace No.1, showing contours of instantaneous (*top*) and average (*bottom*) gas temperature distribution, as well as locations where experimental data was available.

computations need only be performed every $N_{it} = 3.333 \approx 3$ LES timesteps, according to Eq. 4.104. Nonetheless, to ensure the accuracy of this simplification, a simulation with a value of $N_{it} = 1$ was also performed, showing negligible difference in the results.

6.2.7 Turbulence-Radiation Interactions (TRI)

A review of the relevance and importance of TRI for LES has already been given in Section 4.7.1. In this work TRI is neglected assuming a sufficiently well-resolved grid, therefore the absorption coefficient κ, the blackbody intensity I_b, and the radiative source term $\nabla \cdot q$, are approximated as in Eqs. 4.99 - 4.101.

6.3 Experimental Setup and Numerical Implementation

The IFRF furnace No.1 has an approximately square cross-section measuring around 1.9m × 1.9m, and a total length of 6.25 m. The burner has two streams: the primary stream from a central tube through which coal and air are fed, having a diameter $d_1 = 0.0703$ m, and a wall thickness of 0.5 cm, whereas the secondary stream is a concentric tube through which only hot air is fed, with an inner diameter of $d_2 = 0.1995$ m. The exhaust gases and particles eventually leave the furnace through a circular exhaust at the end of the furnace, having a diameter of $d_3 = 0.784$ m. The burner is illustrated

Table 6.1: Summary of the operating conditions of the IFRF furnace no.1 flame B1.

Primary stream		
Coal mass flow	212	kg/h
Bulk velocity, u_1	40.7	m/s
Temperature, T_1	463.15	K
Secondary stream		
Bulk velocity, u_2	9.6	m/s
Temperature, T_2	773.15	K

in Figure 6.1, and the operating conditions for the particular setup of flame B1 are shown in Table 6.1.

A wide range of data is available from the experiments conducted, which allows a good comparison between the simulation and experiments to be made. In-flame measurements of gas temperature and velocity were made at several locations in the furnace using a standard water-cooled suction pyrometer and a Prandtl-probe, respectively [117]. Gas-compositions were measured for the main species at various locations, the most relevant of which will be compared to the simulation results in the following sections. Local solid samples were taken using water-cooled filter probes, at several locations inside the furnace. Finally, the distribution of total radiant heat flux incident at the furnace side-wall was measured using an ellipsoidal radiometer probe; this data will be of great interest for the comparison of the different radiation models implemented.

6.3.1 Coal Representation

The coal used in this burner is a high volatile bituminous coal from the Saar region in Germany, which was chosen due to its high volatile content, characteristic of several US coals, and due to its low ash content which helps minimise deposition on the burner walls [117]. The proximate and ultimate analysis of the coal are presented in Table 6.2.

In the IFRF report [117], the particle size distribution is described as having a unity gradient in a Rosin-Rammler distribution, with 30% (by mass) of the particles being greater than $75\mu m$. However, the particle properties are said to vary considerably with size: the volatile content increases by

Table 6.2: Proximate and ultimate analysis as received and on a dry base respectively, of the high volatile bituminous coal of the Saar-region.

Proximate analysis (as recvd.)	[%wt.]
Fixed carbon	59.5
Volatiles	31.0
Ash	7.5
Moisture	2.0

Ultimate analysis (dry)	[%wt.]
C	74.65
H	4.7
O	11.08
N	1.12
S	0.85

20%, whilst the ash content decreases by 44% from the finest to the coarsest particles [117]. Modelling such composition changes in itself isn't an arduous task, but deriving appropriate coefficients and parameters for the devolatilisation and char combustion models is. For this reason, a mean and constant particle size of $d_p = 63.0 \mu m$ was used in this work, which corresponds to the mean diameter obtained following the cumulative distribution function.

Moreover, due to the large size of the furnace and long particle residence times a vast amount of particles is present, in excess of 500 million, which cannot be modelled individually due to elevated computational costs. Consequently, computational particles each representing 1000 real coal particles were used in this work to reduce the cost of the computation. This assumption has been validated by performing a sensitivity study with ratios of real to computational particles of 100:1 and 50:1, showing a negligible difference in the results.

The volatiles, represented with a postulate substance $C_\alpha H_\beta O_\gamma$ have been given the coefficients $\alpha = 2.31$, $\beta = 5.85$, $\gamma = 0.87$, which have been obtained from the proximate and ultimate analysis of the coal, using the method outlined in Sec. 3.2.2.

For the devolatilisation model, values of $A_v = 2.082 \times 10^4 s^{-1}$ and $E_v = 4.696 \times 10^4 kJ/kmol$, were used, obtained using the FG-DVC model [154], courtesy of Michele Vascellari from TU Freiberg. The initial mass fraction of volatile matter in the coal particles was adjusted to $Y_{vm} = 0.398$ to account for the higher yield of volatiles at rapid heating rates [6]. This value was also obtained using FG-DVC, and corresponds to a Q factor of approximately 1.3. All the parameters used in the char combustion model are described and summarised in Table 6.3.

Table 6.3: Parameters used in the intrinsic reaction rate char combustion model.

Parameter	Symbol	Value	[Units]
Porosity	θ	0.70	[-]
Diffusion coeff.	C_{diff}	5×10^{-12}	[$m^3/K^{0.7}$]
Int. Surf. A.	S_a	250×10^3	[m^2/kg]
Stoichiometric coeff.	s	1.33	[-]
Tortuosity	τ	$\sqrt{2}$	[-]
Pore radius	r_p	1×10^{-7}	[m]
Pre-exponential fac.	A_i	3050.0	[$kg/(m^2 s)$]
Activation Energy	E_i	-1.615×10^5	[kJ/kmol]

6.3.2 Grid and LES Boundary Conditions

To accurately simulate the flow in the furnace with LES it was necessary to discretise the full three-dimensional furnace, without reducing either the width or length, or using periodic boundary conditions and simulating only a slice of the furnace, as this approximation is not valid in LES since the instantaneous fields for which the LES equations are solved are never symmetric. The domain is discretised on a Cartesian grid using equally-sized cubic cells to achieve good numerical efficiency and avoid numerical errors, which also works well for the case of a rectangular furnace like the IFRF furnace no.1. Initially a coarse grid having $\Delta = 2$ cm characteristic cell-size was used, which is equal to the LES filter size, leading to 2.82m cells, and later a fine grid with $\Delta = 1.5$ cm, leading to 6.69m cells was also simulated to study the effects of grid refinement. The high computational effort required for particle tracking and radiation modelling made the use of finer grids unfeasible, but as will be shown in the next section the agreement with experiments implies that a sufficiently resolved grid has been used.

The inlet bulk velocities and temperatures have been defined using the values specified in Table 6.1. The Reynolds numbers for the primary and secondary stream have been estimated at 8.53×10^4 and 4.06×10^4 respectively, suggesting a fully turbulent flow in both streams. All the side walls including those at the inlet and exit of the furnace have been blocked out using immersed boundaries, however no wall modelling was deemed necessary since the interesting region of the flow is far away from the furnace boundaries. Finally, von Neumann conditions are applied at the exit of the domain, enforcing positive outflow.

6.3.3 Radiative Heat Transfer Boundary Conditions

The temperature at the side-walls of the furnace was set equal to the measured temperature profile along the wall centreline [117], following the approach of Stöllinger *et* al. [161]. Despite reports stating that the furnace walls increased in temperature after long hours of operation [117], they were cooled, and the assumption is that these measurements of wall temperature were conducted after a near-steady state wall temperature had been achieved. Different wall emissivities ϵ_w are assessed in Sec. 6.5 for the furnace side walls, using the boundary conditions for grey, diffusely emitting and reflecting walls (see Section 6.2). The inlet and outlet of the furnace are described as black surfaces, in order to neglect reflected radiation. The walls (domain boundaries) corresponding with the inlet and outlet of the furnace have been modelled using adiabatic boundary conditions, as these were not cooled [161].

6.3.4 Numerical Test Cases

One of the main objectives of this work is to determine the influence of accurate radiation modelling on an LES of coal combustion, and therefore several different simulations have been run and compared against experimental data, using the different radiation models previously described. The mean total incident radiative heat flux on the side walls of the furnace, Eq. 4.39, was used as benchmark for quality comparisons, as well as the effect on the mean axial temperature.

Three different grey gas models are considered, all of which have been described in more detail in Sec. 4.5.1. In the first approach, henceforth

Table 6.4: Summary of the different grey gas radiation models evaluated in this work. For further details on the models the reader is referred to Sec. 4.5.1

Model	Description
Grey1	$\kappa_{gs} = 0.5$
Grey2	$\kappa_g = 0.2X_{vg} + 0.1\,(X_{CO_2} + X_{H_2O})$
Grey3	$\kappa_g = \sum^i X_i \kappa_{g,i}$

named *Grey1*, a combined and constant grey-gas and soot coefficient for all gases was used and set to $\kappa_{gs} = 0.5$, following the work carried out by Stöllinger *et* al. [161]. In the second approach, *Grey2*, only the volatiles and the products CO_2 and H_2O are considered as participating (radiating) gases, following the work of Yu et *al.* and Khalil et *al.* [81, 192]. In their work the gas absorption coefficient is calculated as previously described in Eq. 4.63. Finally, a third grey case is considered, *Grey3*, where the absorption coefficients of CO_2, H_2O and CO are evaluated independently using temperature polynomials derived by Barlow *et* al. [8] (Eqs. 4.64a-4.64b), and then combined using the approach described in Sec. 4.5.1. All the grey gas models employed in this work are summarised in Table 6.4.

In addition to these grey models, the more expensive non-grey implementations of the *WSGG* and *MWSGG* methods with four and five grey gases respectively were also considered.

6.4 Flow Field Description

The contour plots in Figs. 6.2-6.6 illustrate both the instantaneous and averaged velocity, temperature, and O_2, CO_2 and H_2O species concentration fields, which are helpful to understand the overall flow field in the furnace. The contour plot in Fig. 6.7 instead shows the ratio of H_2O to CO_2 mole fractions, which was helpful for the selection of adequate coefficients for the WSGG radiation model.

The velocity field shows the high-speed central (primary) jet surrounded by the secondary lower velocity stream, as expected from the burner configuration. Closer to the side-walls in the second half of the furnace, negative velocities are visible, which indicate a slow recirculation zone. Since the

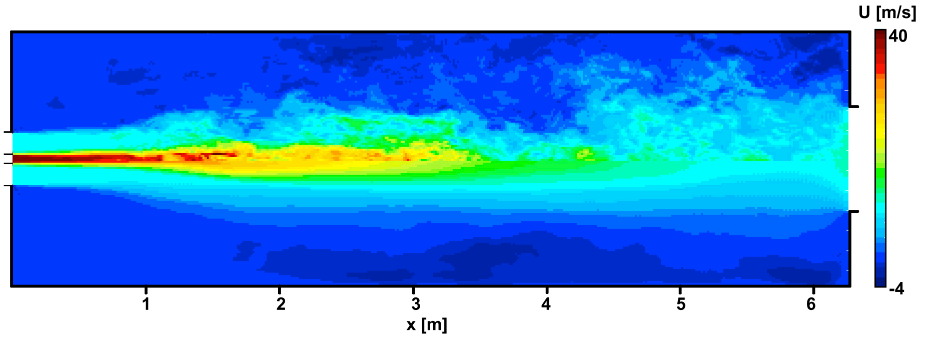

Figure 6.2: Contour plot of instantaneous (*top*) and mean (*bottom*) axial velocity distribution along the furnace centreline.

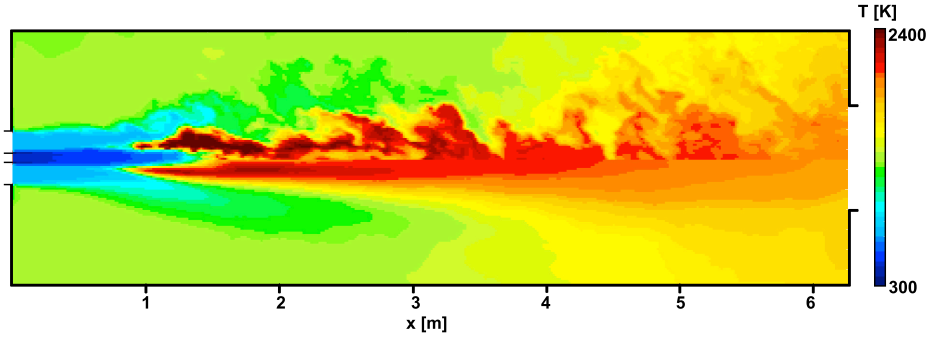

Figure 6.3: Contour plot of instantaneous (*top*) and mean (*bottom*) temperature field distribution along the furnace centreline.

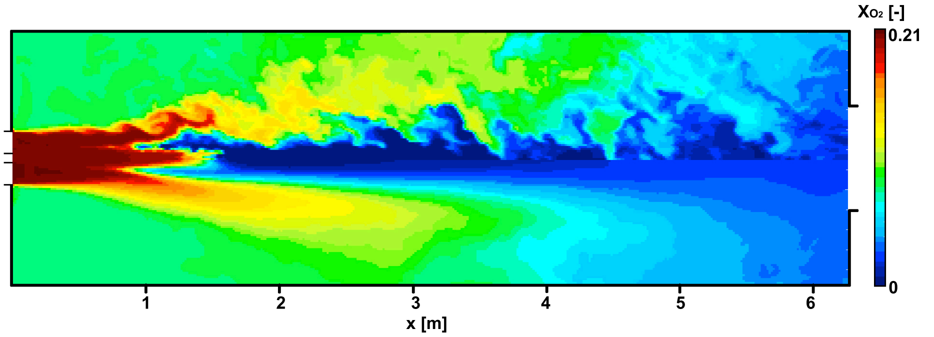

Figure 6.4: Contour plot of instantaneous (*top*) and mean (*bottom*) O_2 mole fraction along the furnace centreline.

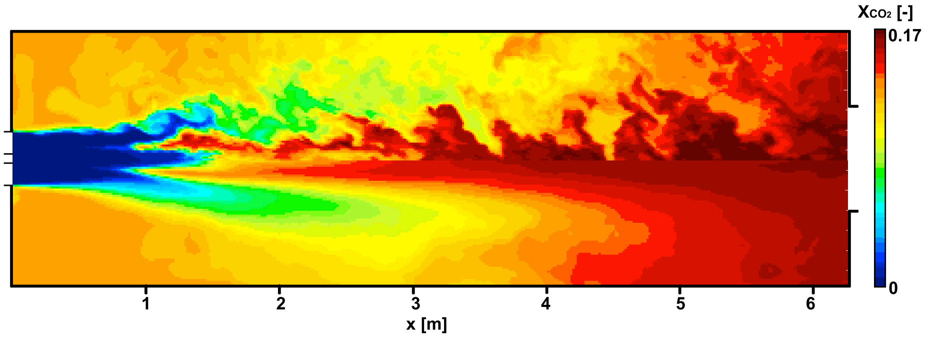

Figure 6.5: Contour plot of instantaneous (*top*) and mean (*bottom*) CO_2 mole fraction along the furnace centreline.

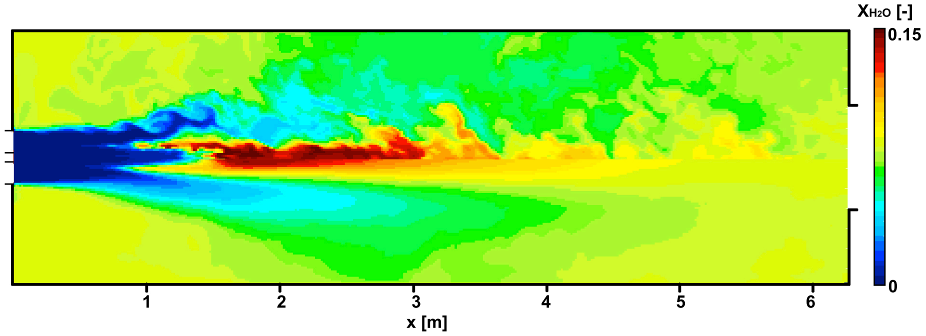

Figure 6.6: Contour plot of instantaneous (*top*) and mean (*bottom*) H_2O mole fraction along the furnace centreline.

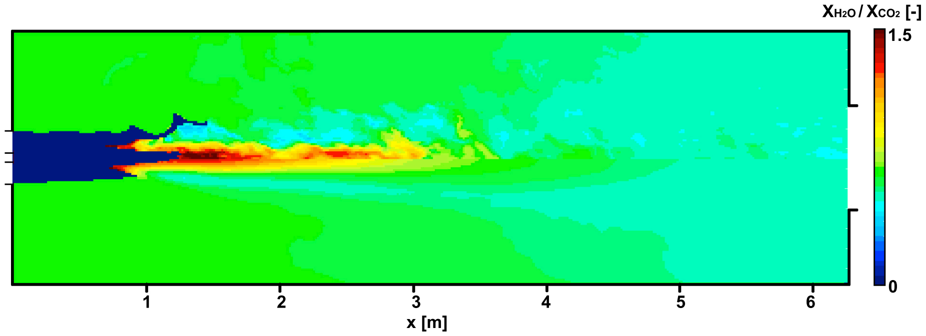

Figure 6.7: Contour plot of instantaneous (*top*) and mean (*bottom*) H_2O/CO_2 molar ratio along the furnace centreline.

circular outlet at the end of the furnace is smaller than the furnace cross-section, inevitably some of the two-phase mixture from the high-speed jet will have spread sufficiently to collide with the end-walls, and will consequently flow back against the bulk flow direction. From the temperature contour plot (Fig. 6.3) it can be clearly seen that the flame is lifted, and rather than having a unique attachment point at the centreline, the flame is attached in correspondence of the boundary between the primary and secondary stream. As the particles flow through the high-speed primary stream, they eventually spread to the secondary stream, where they heat up and undergo devolatilisation, and consequently the newly released volatiles ignite shortly after, causing the observed rise in temperature. A similar trend is observed from the O_2 mole fraction contour plot (Fig. 6.4), where the air entering the furnace from the two streams is initially consumed in correspondence of the boundary between primary and secondary stream, and further downstream also along the centreline. Towards the furnace outlet, little oxygen is present, as most of that entering the furnace is consumed by the combustion reaction with the volatile gases and the char. The opposite is true for the CO_2 and H_2O mole fractions, with the products being generated at the flame lift-off height as the volatile combustion reactions occur. Downstream, in the second half of the furnace, the CO_2 concentration further increases as a result of the char combustion process. It is also worth noting the reduced oxygen mole fraction (compared to that found in pure air), and the presence of gas products at the sides of the furnace near the inlet. This is a consequence of the slow recirculation zone at the sides of the furnace, which carries upstream some of the products that dont manage to leave the furnace through the exhaust.

The contour plot illustrating the molar ratio of the combustion products (Fig. 6.7) shows values of X_{H_2O}/X_{CO_2} ranging from 0.5 to 1.5 (note that the region where $X_{H_2O}/X_{CO_2} = 0$ indicates a location where neither of the products were found). The highest X_{H_2O}/X_{CO_2} ratio was found at the flame lift-off height, as the volatile combustion reaction generates more H_2O than CO_2. In this region, average values of around $X_{H_2O}/X_{CO_2} = 1.25$ were observed, with peak values of up to 1.5. However, further downstream as the char reacts to form additional CO_2, the ratio decreases to a minimum value of around 0.5. At the sides of the furnace towards the inlet, where the recirculated products of the volatile and char combustion reactions were found, typical values of $X_{H_2O}/X_{CO_2} = 0.7$ were observed.

As previously mentioned, the WSGG model was originally developed for simplified cases with a constant H_2O/CO_2 molar ratio throughout a given domain, and consequently different sets of coefficients for specific molar ratios were derived by the model authors. Despite observing that the simulated IFRF furnace has a non-uniform distribution of the ratio of combustion products, as previously mentioned the set of coefficients available from the literature for $X_{H_2O}/X_{CO_2} = 1$ were used, as this was the most representative set for the observed flow field.

6.5 Preliminary Sensitivity Analysis

Prior to the simulation and comparison of the different radiation models described in the previous section, it was necessary to establish a *benchmark* test case, by defining certain specific parameters. The relevant boundary conditions for the radiation solver, and the required quality of its angular discretization had to be investigated. Simulations with two different grids (for both the LES and radiation solver which share the same grid) were also performed, as described in the previous section. Further, the effect of the *crude* soot radiation models introduced in Chaper 4 was assessed. The results obtained from this sensitivity analysis are presented in the following subsections.

6.5.1 Benchmark Simulation

The benchmark simulation was performed on the coarse grid ($\Delta = 2.00cm$), using the $Grey2$ radiation model. The S_8 angular discretisation with 80 directions was used, the side wall emissivity was set to $\epsilon_w = 0.8$, and the exit temperature was taken as $1300K$. Finally, soot radiation modelling was not included in this initial simulation. The results are presented in Figs. 6.8-6.11.

Since the flame is lifted, accurately predicting the lift-off height or flame attachment point is crucial for the outcome of the simulation. The lift-off height is affected by several processes, amongst which the most significant ones are the particle and flow velocity, the devolatilisation rate of the particles, the volatile combustion, and radiative heat transfer effects. Along the centreline, the flame lift-off height is predicted remarkably well (Fig. 6.8), as the simulated location of sharp increase in temperature is very close to the experimental readings. However, by observing the radial profiles of mean gas temperature (Fig. 6.9), at around $125cm$ downstream of the inlet the simulations show two temperature peaks slightly shifted from the centreline, indicating that the flame is attached in correspondence of the hot air (secondary) stream, where the particles spread to and ignite. This differs considerably from the experimental data, which however is asymmetric in the $150cm$ and $190cm$ datasets, which is the region of interest for the purpose of comparing the flame shape and lift-off height, making accurate comparisons very difficult. Nonetheless, the predicted temperature peaks are higher than those observed in the experimental data, and this trend is also reflected further downstream. The overestimation in the burnt gas temperature could be due to a number of reasons, including all the devolatilisation, volatiles combustion and char combustion models. If the devolatilisation rate is overpredicted more fuel (volatiles) will be emitted, and more quickly, causing richer mixtures further upstream, which will lead to an overestimation in temperature by burning too rapidly. Similarly, if the char combustion model overestimates the char burning rate, higher temperatures will be observed downstream as the char burnout results in the production of CO which will then further react to form CO_2. Even more importantly, the volatiles combustion model (EBU) could have a snowball effect on both the devolatilisation and char burnout rates if the mixing rate is not well predicted. The EBU assumes infinitely fast chemistry and the reaction rate is dominated by mixing, indicating that if this is overestimated (as may well be the case), combustion will occur too rapidly. This will have an even larger effect if the devolatilisation and char burnout rates are overestimated, as more *fuel* will be burnt. Franchetti carried out a very interesting parametric study on the effects of the devolatilisation, volatiles combustion and char combustion models individually, showing that the models are in fact very sensitive to one another, as well as to their own model constants [52]. However, Franchetti's parameter study was conducted on a simpler case, that may well be more sensitive to the parameters investigated.

The consumption and production of O_2 and CO_2 respectively are well predicted overall, despite being consumed/produced slightly upstream of the position observed in the experiments, as can be seen from Fig. 6.9. However, by comparing these plots with the axial temperature measurements (top-right of Fig. 6.8), one may notice a possible inconsistency in the experiments, as the temperature seems to rise quite considerably early ($x \approx 1.25 - 1.50m$) compared to the consumption/production of O_2 and CO_2 ($x \approx 1.90m$). Unfortunately, this makes an accurate assessment of the prediction of the devolatilisation and volatile combustion rates difficult, as they may seem to be over-predicted by comparing the species data, but well-predicted by comparison with the centreline temperature data.

The release of volatiles from the solid coal particles also appears to happen slightly early in the simulation when compared to the experiments. Further, the decrease happens with a sharp slope compared to the experimental data, which is possibly due to the single particle size adopted. By considering a particle size distribution (as in the experiment), large and small particles would enter the furnace and devolatilise at different times, thereby causing the slope observed in the averaged experimental data. Nonetheless, considering the simplicity of the devolatilisation model, the simplified uniform particle size distribution, and the inconsistencies discussed above in the experimental data, the agreement is considered to be satisfactory.

The solid ash content in the particles, which can be used as a tracker for char combustion (since once the particles have devolatilised they consist only of char and ash), is well predicted until half-way through the length of the furnace, after which the simulation overestimates the ash mass fraction, indicating that the char combustion process is occurring too rapidly.

The mean axial velocity obtained by LES reflects the experimental measurements very accurately near the inlet and the exit of the furnace, however around half-way through the length of the furnace, the centreline values appear to overestimate the measurements. The radial profiles of axial velocity (Fig. 6.9) also show a very good agreement away from the centreline between the simulation and experiments.

Finally, the wall incident heat flux (Fig. 6.11) is slightly underpredicted throughout the length of the furnace whilst retaining the correct shape. Considering the simplicity of the grey gas model used for this benchmark simulation, the result is quite good.

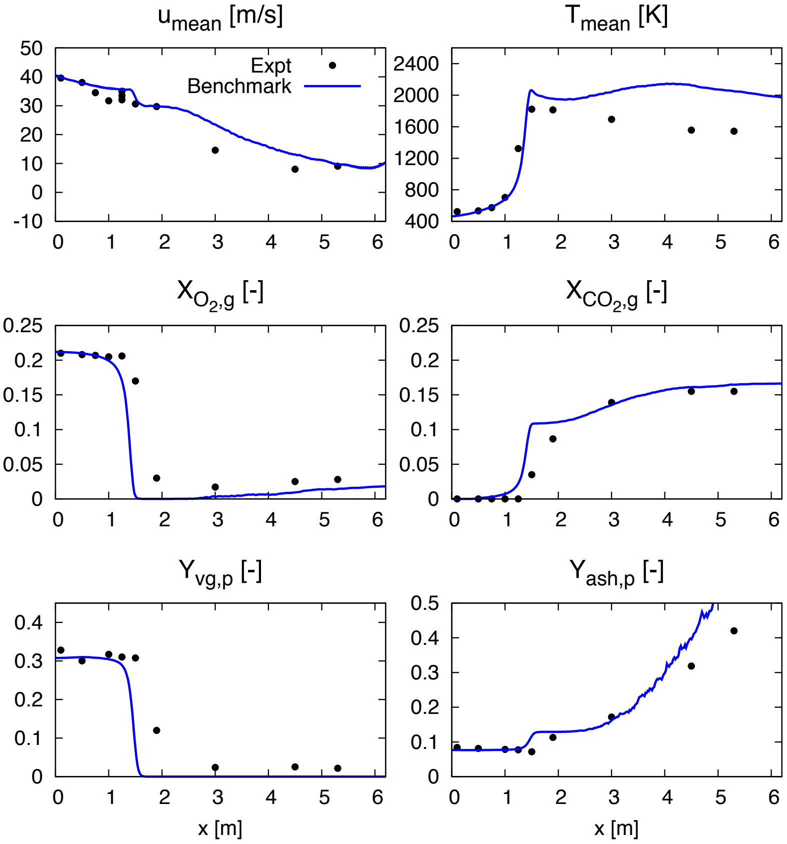

Figure 6.8: Axial mean plots along the centreline of the furnace for: gas velocity and temperature (*top*), O_2 and CO_2 gas molar fractions (*middle*), and solid volatile content and ash mass fractions (*bottom*), compared to experimental data.

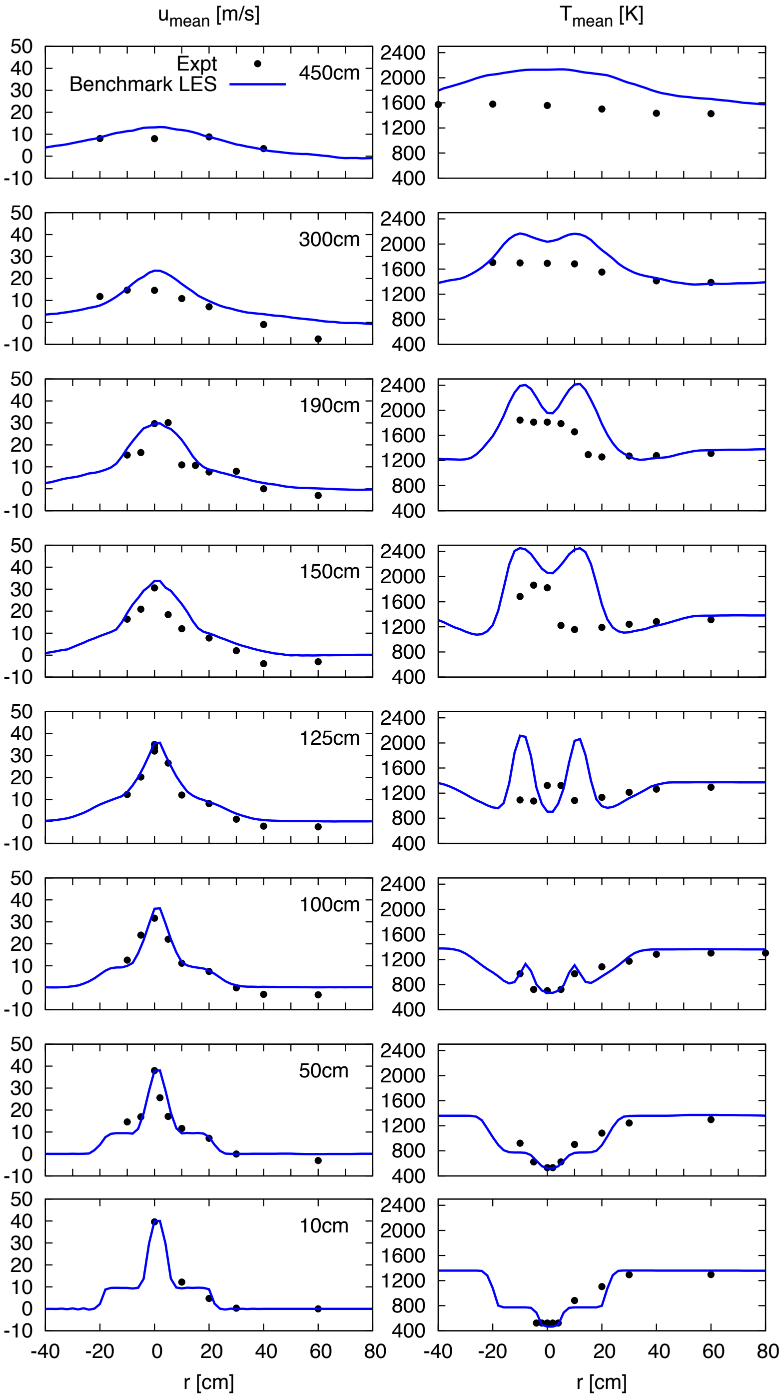

Figure 6.9: Radial profiles of mean axial velocity (*left*) and temperature (*right*) at various locations along the length of the furnace.

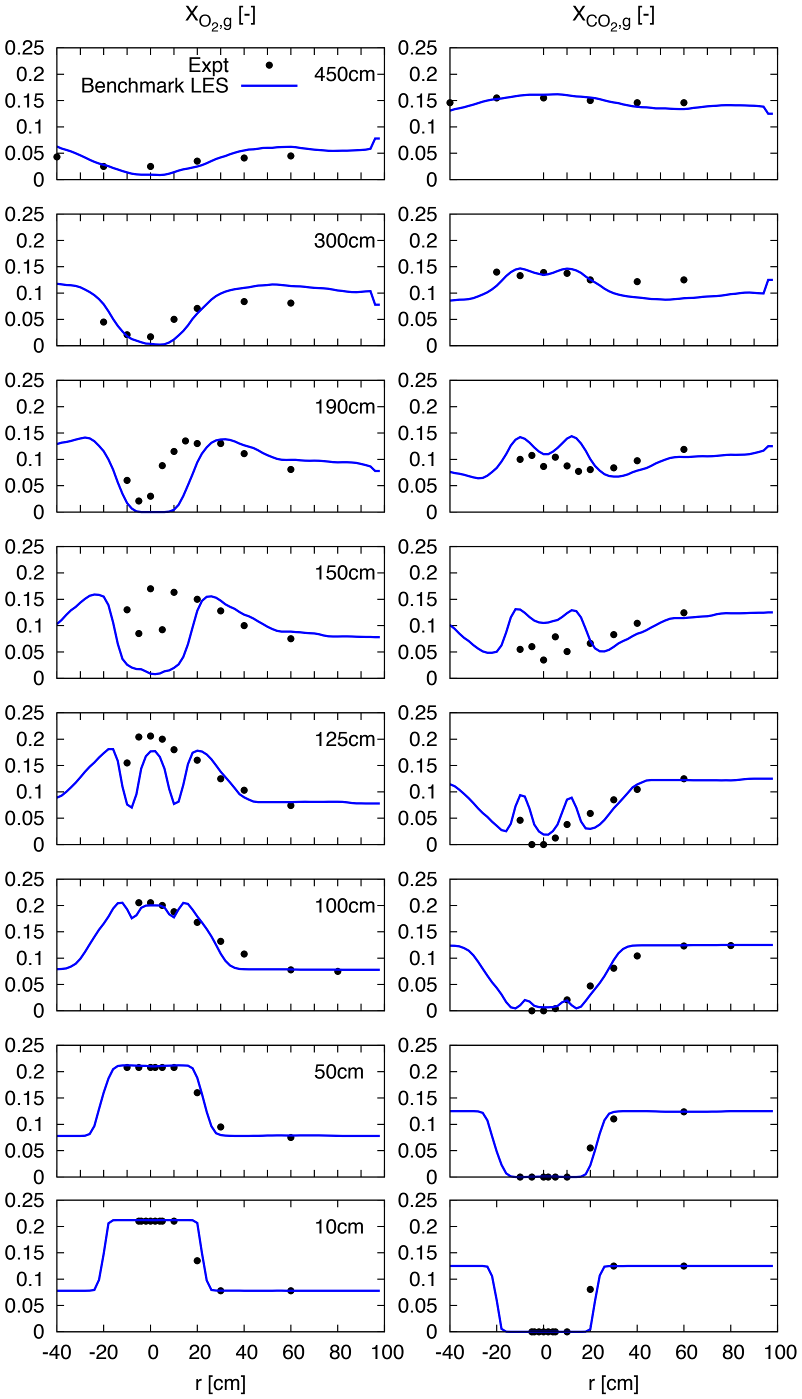

Figure 6.10: Radial profiles of mean gas molar fractions of O_2 (*left*) and CO_2 (*right*) at various locations along the length of the furnace.

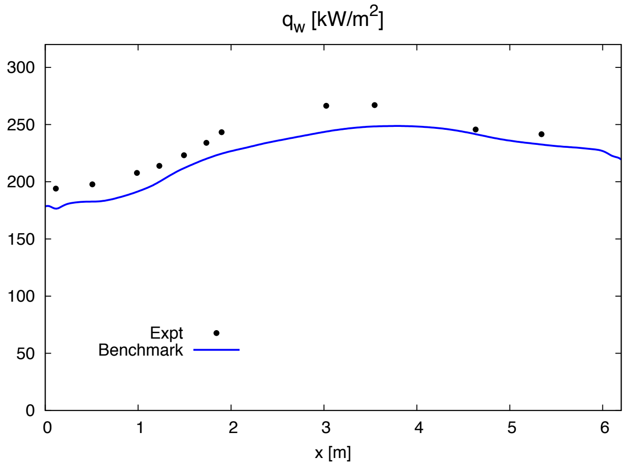

Figure 6.11: Average incident radiation along the centreline of the furnace side walls.

6.5.2 Validating the DOM Boundary Conditions

In order to define the boundary conditions for the DOM radiation solver, it is necessary to specify the wall temperatures and emissivities, and the inlet and outlet temperatures of the furnace.

Whereas the temperature of the side walls of the furnace can be approximated to the measured centreline wall temperature [117], and the inlet temperature is known from the flow boundary conditions, the exit temperature isn't explicitly known. In previous works, Stöllinger *et* al. [161] set the exit temperature to $1300K$, which yielded good predictions, and as such in this work this was chosen as the *central* value for the exit temperature. The domain boundaries (furnace walls) adjacent to the inlet and exit of the furnace instead were treated as adiabatic walls, as they are not cooled, and as such there is no need to set an explicit wall temperature.

The furnace side walls, for which a centreline temperature measurement is available, are cooled by fixed pipes, and it is assumed that their temperature stays constant for the duration of the simulation. However their wall emissivity must be specified in order to express what portion of the incident radiation is reflected back into the furnace. As is often done in coupled CFD-radiation combustion simulations involving furnaces with cooled walls, Stöllinger *et* al. [161] set a side wall emissivity of 0.8. Consequently, this value was also taken as the initial wall emissivity. The inlets and outlets were instead assigned an emissivity of 1.0, which is characteristic of a black surface, and indicates that no radiation is reflected back to the furnace, as in reality there is no surface or wall.

Outlet Temperature

As previously mentioned, the outlet temperature of the furnace was initially set to $1300K$. Two different exit temperature values were also tested, namely $1600K$ and $300K$, in order to assess the validity of the original exit temperature value, and the relative influence of this parameter on the outcome of the simulation. The simulation results were compared to all the experimental data shown in Figs. 6.8-6.11, however the differences in gas velocity, temperature, and species, as well as the solids analysis were found to be negligible. The only noticeable difference was in the heat flux to the side wall, which is shown in Fig. 6.12.

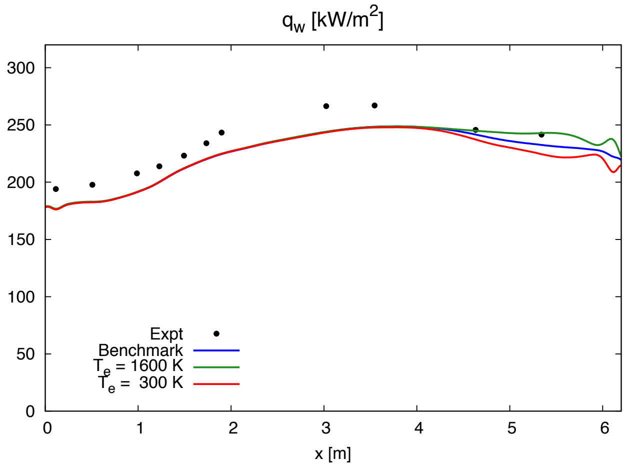

Figure 6.12: Average incident radiation along the centreline of the furnace side walls. The benchmark simulation with exit temperature of $T_e = 1300K$ is compared to runs with $T_e = 300K$ and $T_e = 1600K$.

As can be seen in Fig. 6.12, all three simulations retain the same average wall radiative flux until about $x = 4m$, after which the three diverge due to the different exit temperatures specified in the boundary conditions of the radiative solver. The higher exit temperature $T_e = 1600K$ causes an overestimation of the predicted heat flux at the side wall towards the outlet of the furnace, and an oscillation is also observed closer to the exit, suggesting that the exit temperature is too high. Conversely, the lower exit temperature $T_e = 300K$ causes an even more pronounced underprediction of the heat flux compared to the benchmark case, as expected. Similar to the high temperature simulation, an oscillation is noticeable near the corner of the furnace, again suggesting that this temperature is inappropriate. The benchmark simulation, with an exit temperature of $T_e = 1300K$, lies in between the other two in terms of wall radiative heat flux, but doesn't exhibit the unphysical oscillation in proximity of the furnace corner. Stöllinger *et* al. [161], who originally estimated $T_e = 1300K$, also found that this value provided a good agreement with the experiments, and did not cause any unphysical oscillations in the radiative heat flux along the wall centreline. Whereas this may not be the perfectly correct value of T_e, it was considered sufficiently accurate for this simulation, and therefore was retained as the exit temperature, without the need for further investigation into this parameter.

Side-Wall Emissivity

To the best of the author's knowledge there is no general scientific way of obtaining accurate wall-emissivity predictions, however for cooled walls in combustion chambers, most authors use a value of $\epsilon_w = 0.8$. The sensitivity to the side wall emissivity was assessed by testing values both larger ($\epsilon_w = 0.9$) and smaller ($\epsilon_w = 0.7$) than the original wall emissivity, $\epsilon_w = 0.8$.

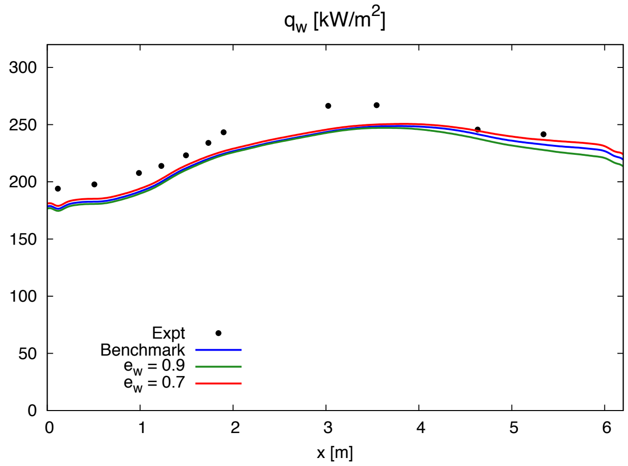

Figure 6.13: Average incident radiation along the centreline of the furnace side walls. The benchmark simulation with wall emissivity of $\epsilon_w = 0.8$ is compared to runs with $\epsilon_w = 0.9$ and $\epsilon_w = 0.7$.

Again, the only noticeable difference in the results was in the radiative heat flux to the wall, as can be seen in Fig. 6.13. The higher wall emissivity ($\epsilon_w = 0.9$) produces a lower wall radiative heat flux, and conversely the lower emissivity ($\epsilon_w = 0.7$) yields a larger mean wall radiative heat flux. The results are as expected since a lower emissivity implies a larger portion of radiation being reflected across the furnace, and therefore affecting the incident radiation on the walls more. On the other hand, a higher emissivity implies a larger portion of radiation is absorbed by the walls, and therefore not reflected to other walls as often, giving an overall lower predicted radiative heat flux on the walls. Nonetheless, the difference in the predictions obtained by varying this parameter are small, and can be considered nearly negligible. For this reason, the value of $\epsilon_w = 0.8$ was retained, in accordance with other work [161].

6.5.3 DOM Angular Discretisation

Using the S_N approximation described in Chapter 4, three different orders were simulated, namely the S_4, S_6 and S_8 (benchmark) approximations, with 24, 48 and 80 directions respectively. The only non-negligible difference in the results was observed in the radiative heat flux to the side wall (Fig. 6.14).

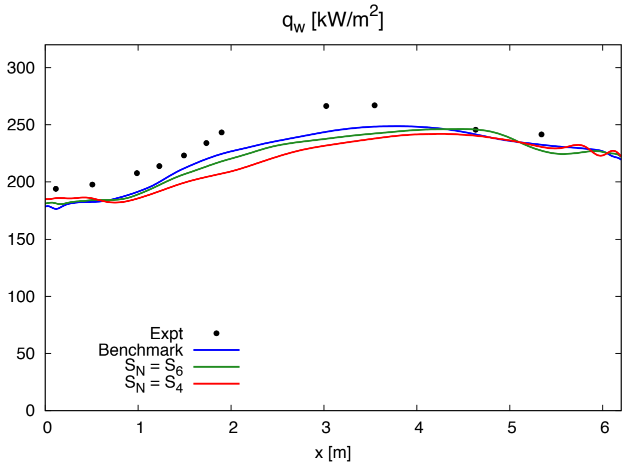

Figure 6.14: Average incident radiation along the centreline of the furnace side walls. The benchmark simulation with the S_8 approximation is compared to runs with the S_6 and S_4 approximations.

All three discretisation schemes yield different results, with the lower-order approximations producing unphysical oscillations, which are particularly noticeable towards the end of the furnace. The S_8 approximation (benchmark case) yields the most accurate prediction and is free from unphysical oscillations. This indicates that the S_8 approximation is necessary to obtain accurate wall-heat flux readings, and perhaps even more accurate angular discretisation schemes should be investigated. Nonetheless, it is worth to point out that the lower order approximations did not produce any differences in terms of the predictions of other flame quantities such as velocity and temperature, indicating that for simulations where the investigation of radiative heat transfer effects is not the main concern, these considerably less expensive schemes can be employed.

6.5.4 Soot Modelling

In Sec. 4.6.3, a brief introduction to soot radiation modelling was given, and Eq. 4.98 for the soot absorption coefficient was presented. However, as discussed this equation is strongly dependant on the soot volume fraction f_v, which as a further approximation in this work is not described by a transport equation, but is estimated and assumed to be uniformly dispersed. Since the soot volume fraction in coal furnaces typically varies within the range $10^{-6} - 10^{-8}$ [51], three different runs were performed with the benchmark simulation combined with the soot absorption coefficient calculation according to Eq. 4.98, using $f_v = 1 \times 10^{-6}$, $f_v = 1 \times 10^{-7}$ and $f_v = 1 \times 10^{-8}$. Despite some minor differences in the radial profiles of temperature and species, the most significant differences in the results are observed in the axial profiles and the wall radiative heat flux, shown in Fig. 6.15 and Fig. 6.16 respectively. As can be seen from this data, the inclusion of the soot absorption coefficient in the calculations has a significant effect on the outcome of the simulations. The two larger volume fractions, $f_v = 1 \times 10^{-6}$ and $f_v = 1 \times 10^{-7}$ yield near identical predictions, giving a better representation of centreline species mole fraction and coal particle pyrolisis and char burnout. Conversely, the flame lift-off height increases significantly and consequently deteriorates the temperature representation, however it is worth noting once again that the species and temperature predictions are subject to an inconsistency in the experimental measure-

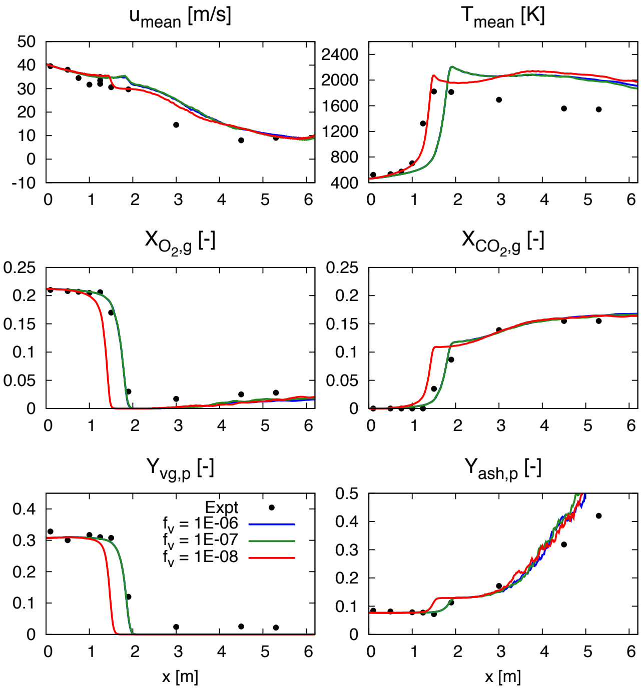

Figure 6.15: A comparison of the effect of the soot radiation modelling with different soot volume fractions - the larger volume fractions yield near identical results. Axial mean plots along the centreline of the furnace for: gas velocity and temperature (*top*), O_2 and CO_2 gas molar fractions (*middle*), and solid volatile content and ash mass fractions (*bottom*).

ments, which has been previously explained (different lift-off heights are measured for species and temperature). Furthermore, for these larger soot volume fractions the prediction of the wall radiative heat flux is worsened significantly, largely underestimating the experiments throughout, and not retaining the correct shape either.

On the other hand, the smaller soot volume fraction, $f_v = 1 \times 10^{-8}$ retains a better axial velocity and temperature prediction, whilst still predicting a too rapid consumption/production of gaseous species and pyrolisis and char burnout for the solids. However, the wall radiative heat flux retains a reasonable agreement with the experiments, and as such it is considered the most appropriate solution out of the three, if soot radiation is to be included via this method.

In their work, Yu *et* al. [192] also considered a model with a fixed soot

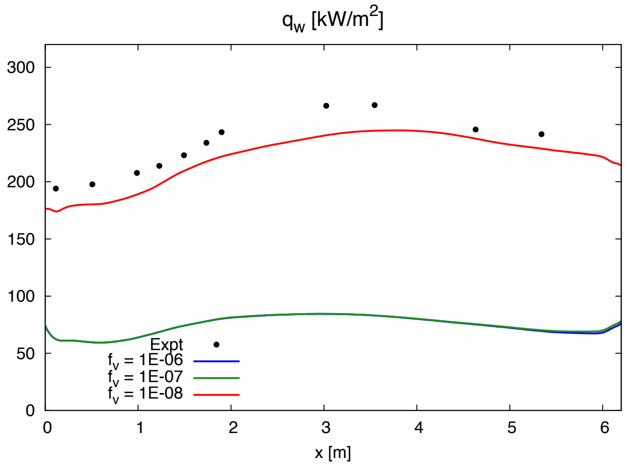

Figure 6.16: Average incident radiation along the centreline of the furnace side walls. The soot radiation model is validated with three different volume fractions. Note that the larger volume fractions (blue and green lines) yield near-identical results.

absorption coefficient of $\kappa_s = 0.4 m^{-1}$, in combination with the same gas absorption coefficient calculation used for the benchmark solution, *Grey2*. This combination has also been evaluated in this work, and is compared to the benchmark solution, as well as with the solution obtained with κ_s calculated from Eq. 4.98 with a soot volume fraction of $f_v = 1 \times 10^{-8}$, which was the best result obtained from the soot volume fraction sensitivity analysis. Similar to the soot volume fraction study, the most significant differences in results were found in the axial plots and in the wall radiative flux plot, shown in Fig. 6.17 and Fig. 6.18 respectively.

The results obtained with the constant soot absorption coefficient of $\kappa_s = 0.4 m^{-1}$ appear to be similar to those previously assessed and obtained with the larger volume fractions, using Eq. 4.98. The flame lift-off height is increased, whilst the gaseous species and the solid pyrolisis and burnout are very well predicted. However, the radiative flux to the wall is severely underpredicted, in a similar way to the previous model's with the larger soot volume fractions.

The results obtained with the soot radiation modelled by Eq. 4.98 and the small soot volume fraction are now also compared to the benchmark solution, and show that such a small volume fraction has a nearly negligible effect on the simulation results, if only giving slightly worse radiative wall flux predictions.

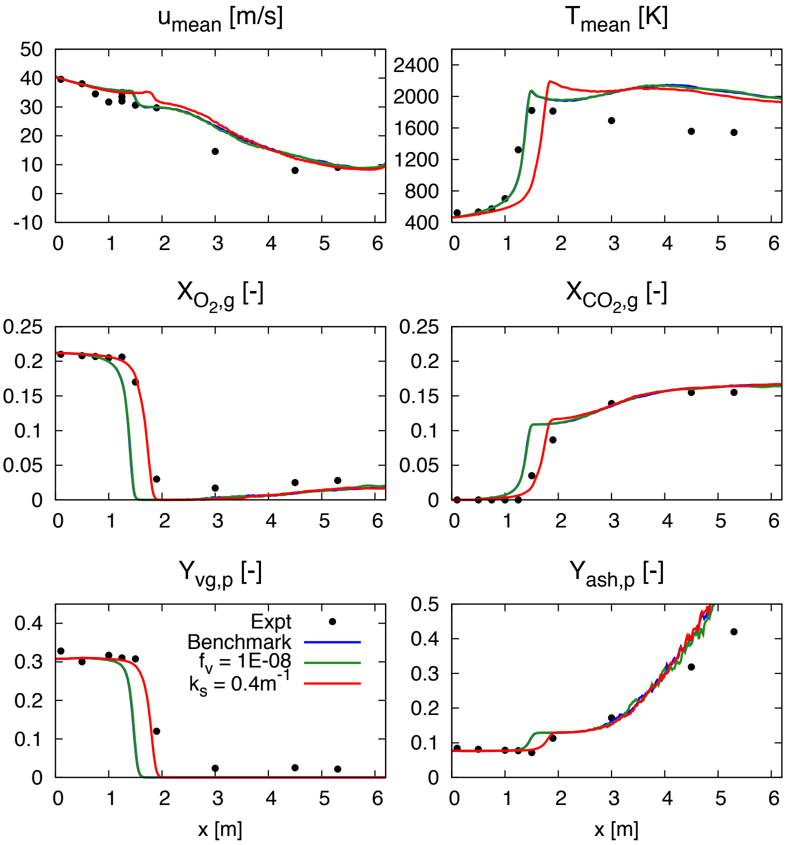

Figure 6.17: The benchmark solution (no soot radiation) is compared to the same solution with the inclusion of soot radiation obtained using Eq. 4.98 and $f_v = 1 \times 10^{-8}$, and another model with a constant soot absorption coefficient of $\kappa_s = 0.4m^{-1}$. Axial mean plots along the centreline of the furnace for: gas velocity and temperature (*top*), O_2 and CO_2 gas molar fractions (*middle*), and solid volatile content and ash mass fractions (*bottom*).

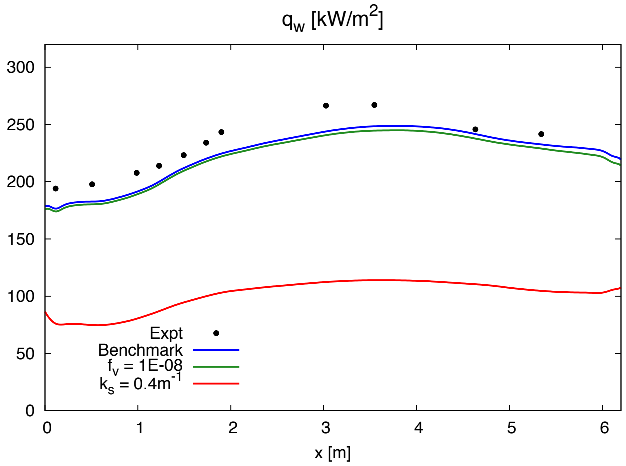

Figure 6.18: Average incident radiation along the centreline of the furnace side walls. The benchmark solution (no soot radiation) is compared to the same solution with the inclusion of soot radiation obtained using Eq. 4.98 and $f_v = 1 \times 10^{-8}$, and another model with a constant soot absorption coefficient of $\kappa_s = 0.4m^{-1}$.

This study has shown that the simple approaches taken to include soot radiation, an important contributor to the overall radiative heat transfer solution and such a complex phenomenon, are not suitable. The constant soot absorption coefficient gives poor predictions of the wall heat flux, whereas the accuracy of the mean soot absorption coefficient calculation method (Eq. 4.98) is dependant on the value assigned to the soot volume fraction. The parameter studies have shown that correct predictions are only obtained with very low soot concentrations, so it can be assumed that soot only has a small effect. In this light, and given the uncertainty and difficulty in modelling soot, soot radiative heat transfer effects were ignored in all further calculations, except for the case of *Grey1*, where a combined and constant gas-soot absorption coefficient was employed.

6.5.5 Grid Independency Tests

The furnace being simulated in this work is very large compared to most of the combustion LES test cases analysed to date, however its coarse geometrical features make it possible to obtain good accuracy on a relatively coarse grid of equally-sized cubic cells measuring $2.0cm$ per side. Nonetheless, it is appropriate to simulate a different grid resolution in order to assess the

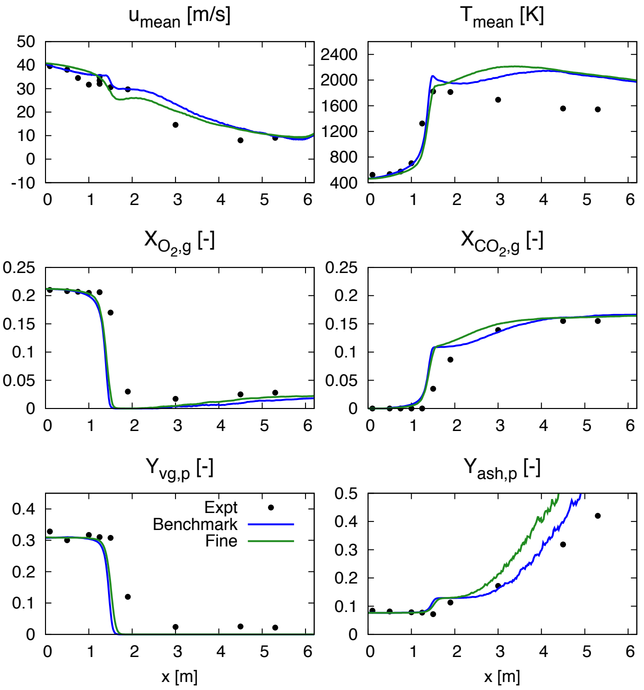

Figure 6.19: Grid resolution study: the benchmark run is compared to the results obtained with a finer grid. Axial mean plots along the centreline of the furnace for: gas velocity and temperature (*top*), O_2 and CO_2 gas molar fractions (*middle*), and solid volatile content and ash mass fractions (*bottom*).

relative grid independency of the simulations. For this reason, the benchmark configuration with a finer $1.5cm$ cell-size grid was also simulated, and the results are shown in Figs. 6.19-6.22.

The finer grid gives improved axial velocity predictions overall, and better burnt gas temperature predictions at the flame stabilisation point on the centreline, which remains unaltered, but evolves in a different manner compared to the coarse grid. The gas species concentration profiles along the centreline obtained with the two grids are very similar to each other, with the fine grid yielding slightly improved predictions. Finally, whereas the pyrolisis occurs at the same axial distance, the char burnout seems to be considerably more rapid on the fine grid, diverging from the experimental measurements. This could possibly be explained by the fact that along the centreline the temperature at this point increases more rapidly, however requires further investigation to make better conclusions. The radial

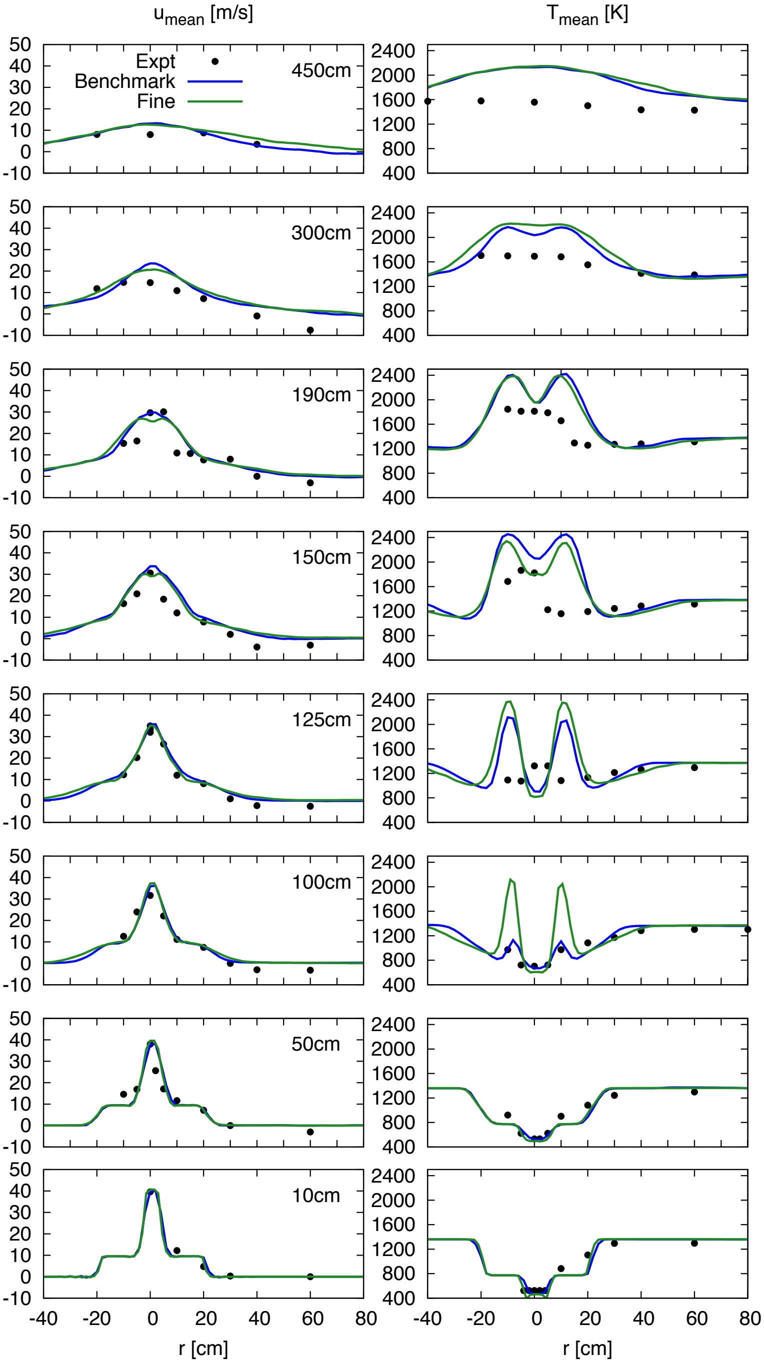

Figure 6.20: Grid resolution study: the benchmark run is compared to the results obtained with a finer grid. Radial profiles of mean axial velocity (*left*) and temperature (*right*) at various locations along the length of the furnace.

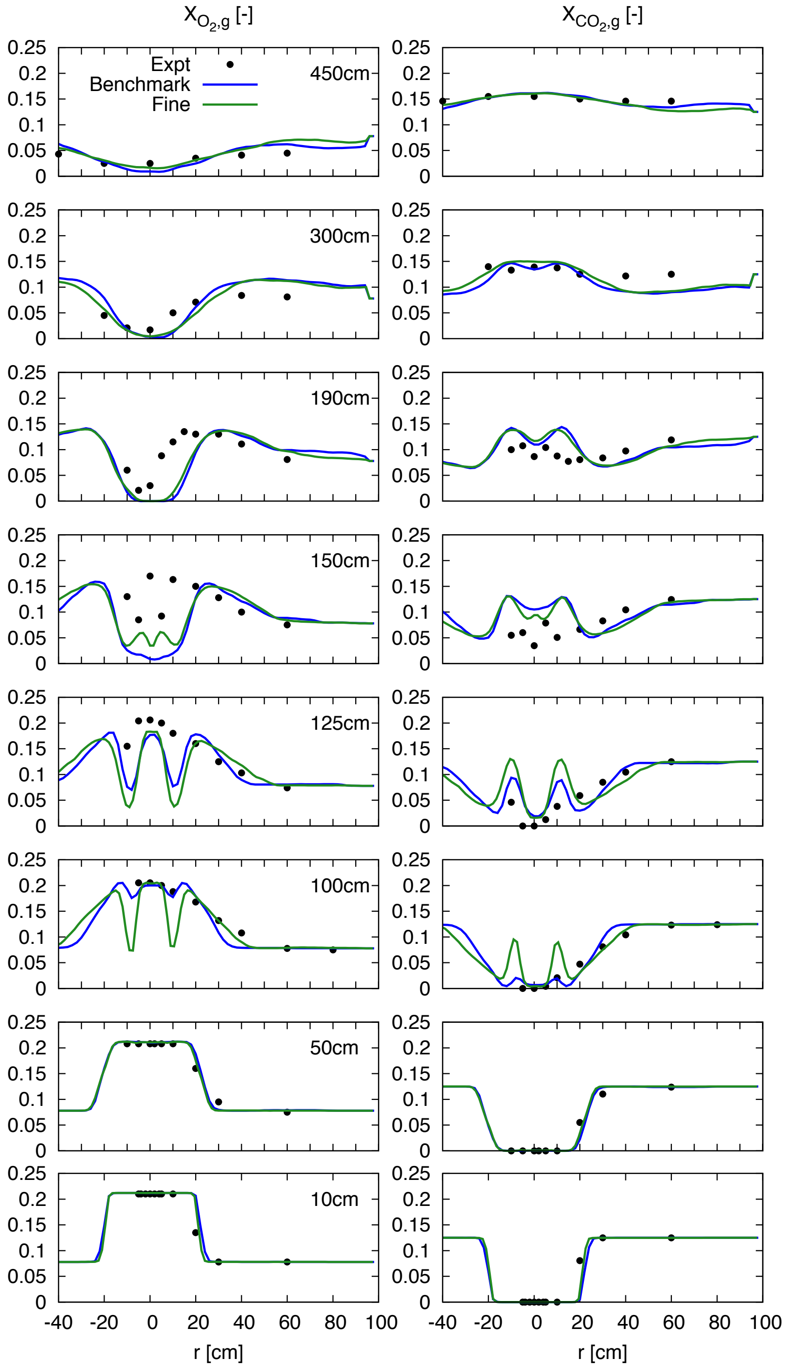

Figure 6.21: Grid resolution study: the benchmark run is compared to the results obtained with a finer grid. Radial profiles of mean gas molar fractions of O_2 (*left*) and CO_2 (*right*) at various locations along the length of the furnace.

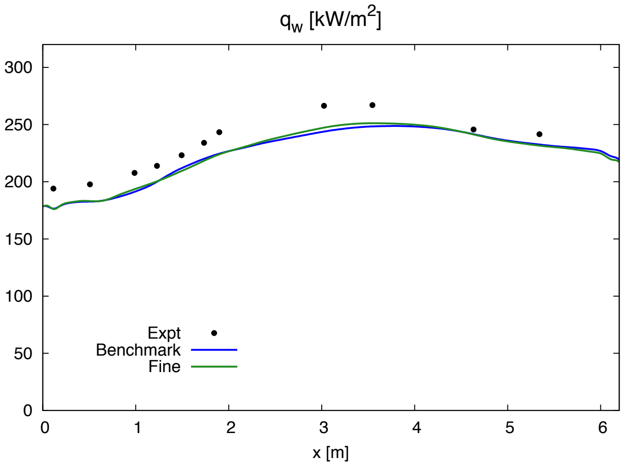

Figure 6.22: Grid resolution study: the benchmark run is compared to the results obtained with a finer grid. Average incident radiation along the centreline of the furnace side walls.

profiles (Figs. 6.20-6.21) also generally show similar results between the two grids. The only significant differences are observed in the region between $100cm - 150cm$ downstream of the furnace, which coincides roughly with the flame lift-off height. The coal particles in the fine-grid simulation spread more rapidly to the secondary stream, and consequently heat up and ignite too early, as can be seen from the temperature profiles and the early consumption and production of O_2 and CO_2 molar fractions respectively, away from the centreline. Finally, the prediction of the radiative heat flux to the wall gives near identical results, with the fine grid producing a somewhat smoother profile.

Overall, some differences are observed by comparing the results obtained with the two grids to the experimental data, and it is difficult to establish which gives better results. Theoretically speaking the fine grid should give more realistic results, and as such it is retained for the calculations performed in the following section, where the various gas radiation models are evaluated. The impact of the resolution on the results is relatively small, providing evidence that the current grid resolution is sufficient to obtain realistic results, as corroborated by the good prediction of the experimental data.

6.5.6 Summary

In this section a parametric study has been performed in order to determine the influence of certain parameters on the outcome of the simulation, and to establish good values that will enable an accurate and fair assessment of the different radiation models that will be tested in the following section. It was concluded that the wall radiative heat flux is sensitive to the furnace exit temperature, and that $T_e = 1300K$ is a good estimate. Conversely, the simulation results were found to be very insensitive to the selection of side wall emissivity, and therefore following other works a value of $\epsilon_w = 0.8$ was used.

A high-order angular discretisation is required to obtain accurate wall radiative heat flux predictions, and as such the S_8 approximation with 80 directions is used in the following simulations. However it can also be concluded that where the wall prediction is not important, a much lower order approximation can be used, such as the S_4, saving considerable computational time.

Different soot radiation modelling approaches were investigated, however all of them proved to be over-simplistic and very sensitive to specific user-defined parameters. With the simple models used, the comparison of simulation and experiment lead to the observation that the effect of soot radiation in the furnace is small. Given the large uncertainty in the models used, it was decided to not include soot radiation modelling in the following calculations.

Finally a grid independency test was performed, showing small differences in the results, mainly near the very sensitive flame lift-off height. Despite not producing significantly improved results, the finer grid was retained in all future calculations.

6.6 Results and Discussion

In this section the optimised benchmark configuration is simulated using the three different grey models, as well as the WSGG model and the MWSGG model. The grey models are initially compared against each other, and once the best performing grey model is established, this is also compared to the more sophisticated WSGG and MWSGG models.

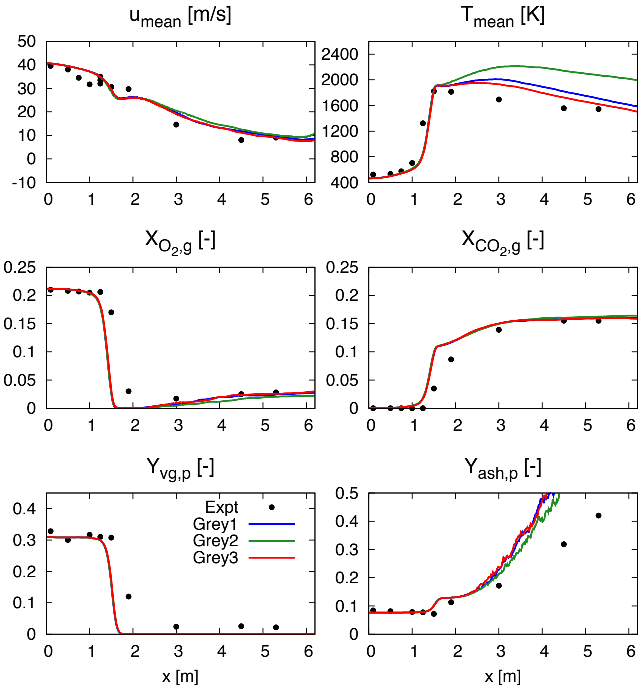

Figure 6.23: The three different grey gas radiation models are compared to each other and validated against experimental data. Axial mean plots along the centreline of the furnace for: gas velocity and temperature (*top*), O_2 and CO_2 gas molar fractions (*middle*), and solid volatile content and ash mass fractions (*bottom*).

6.6.1 Grey Gas Models

The performance of the three different grey gas models (summarised in Table 6.4) is assessed by comparing them against experimental data in Figs. 6.23-6.25. The radial profiles of the gaseous species molar fractions have been omitted as they showed a negligible difference between the three models.

As expected, the most evident differences are observed in the mean gas temperature, and in the mean radiative heat flux to the wall centreline. Conversely, in all three simulations the evolution of the species molar fractions and the coal particle pyrolisis and burnout are very similar to each other, as the different radiation models have little effect on them (figures omitted).

The axial temperature shows a significant difference between the three

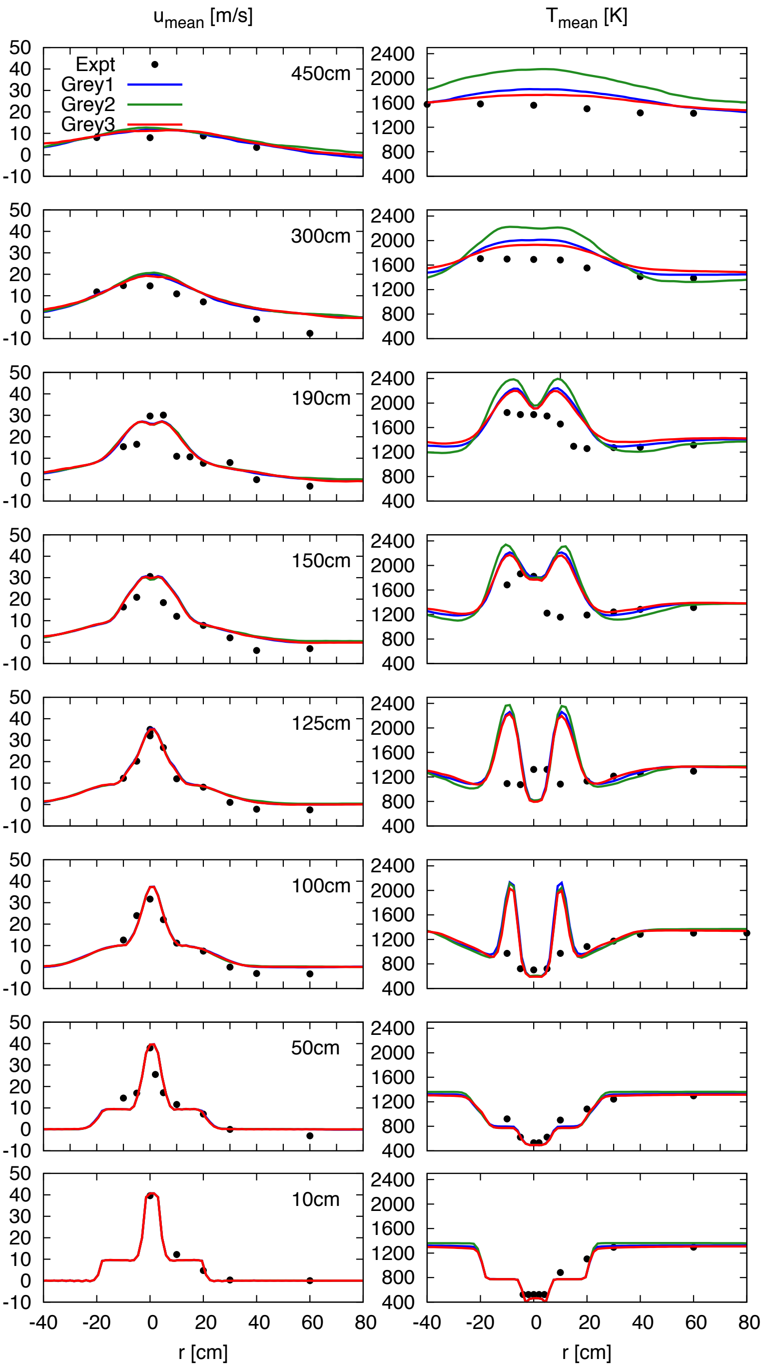

Figure 6.24: The three different grey gas radiation models are compared to each other and validated against experimental data. Radial profiles of mean axial velocity (*left*) and temperature (*right*) at various locations along the length of the furnace.

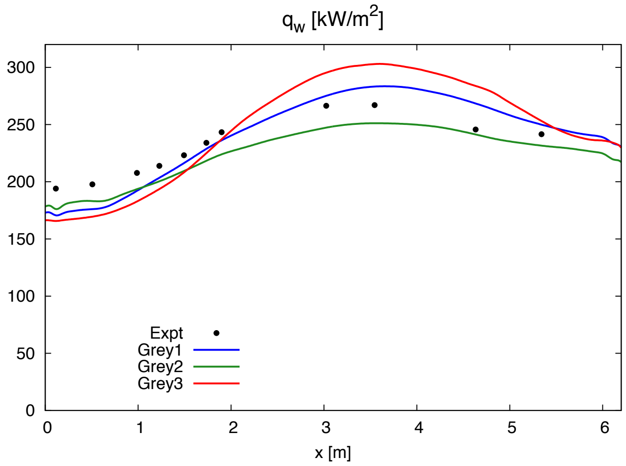

Figure 6.25: The three different grey gas radiation models are compared to each other and validated against experimental data. Average incident radiation along the centreline of the furnace side walls.

models, with both the *Grey1* and *Grey3* simulations giving considerably and progressively lower temperatures across the length of the furnace after the flame stabilisation point, as opposed to the *Grey2* simulation, which was also used as the benchmark simulation in the previous section. In this respect, and as is also confirmed from the radial profiles in Fig. 6.24, the *Grey1* and even more so the *Grey3* model considerably outperform the *Grey2* model, matching much more closely the experimental data.

From the predictions of the incident wall heat flux in Fig. 6.25 however, it is somewhat more difficult to draw conclusions. The model used to produce the benchmark solution, *Grey2*, slightly underpredicts q_w along the length of the furnace, whilst retaining a very similar shape to the experimental profile. *Grey1* instead underpredicts the radiative flux in the first half of the furnace by a larger amount compared to *Grey2*, but in the second half of the furnace the wall flux is overpredicted. A similar, yet even more exaggerated trend is observed in the case of *Grey3*, which largely underpredicts q_w in the first third of the furnace, and subsequently largely overpredicts the radiative heat flux to the wall.

From this comparison it is impossible to determine a single overall best model out of the three, as it is evident from the results that the model producing the most accurate temperature predictions, yields the worst radiative heat fluxes to the walls, and viceversa. Nonetheless, it can be concluded that

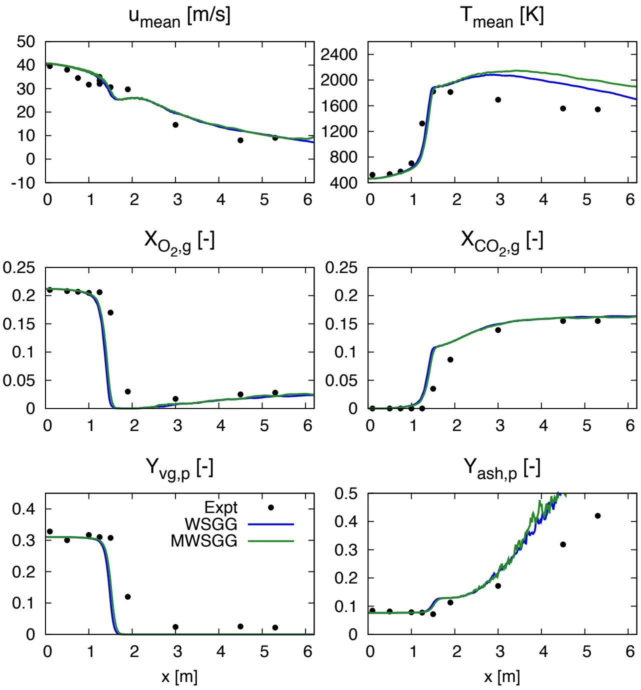

Figure 6.26: The simulations with the WSGG and MWSGG methods are compared to each other and experimental data. Axial mean plots along the centreline of the furnace for: gas velocity and temperature (*top*), O_2 and CO_2 gas molar fractions (*middle*), and solid volatile content and ash mass fractions (*bottom*).

for applications where an accurate prediction of the wall radiative heat flux is of secondary importance, or for open flames, the *Grey3* model performs remarkably well.

6.6.2 The WSGG and MWSGG Model

Both the WSGG model and the MWSGG model have been run on the fine grid, and the results are compared to each other and to experimental data in Figs. 6.26- 6.29.

Once again, the most significant differences between the performance of the two models can be observed in the temperature and incident wall heat flux data. The centreline flame lift-off height is again well predicted, however downstream of this point the centreline temperature is overestimated, in a similar way to that observed for the grey cases discussed in the previous

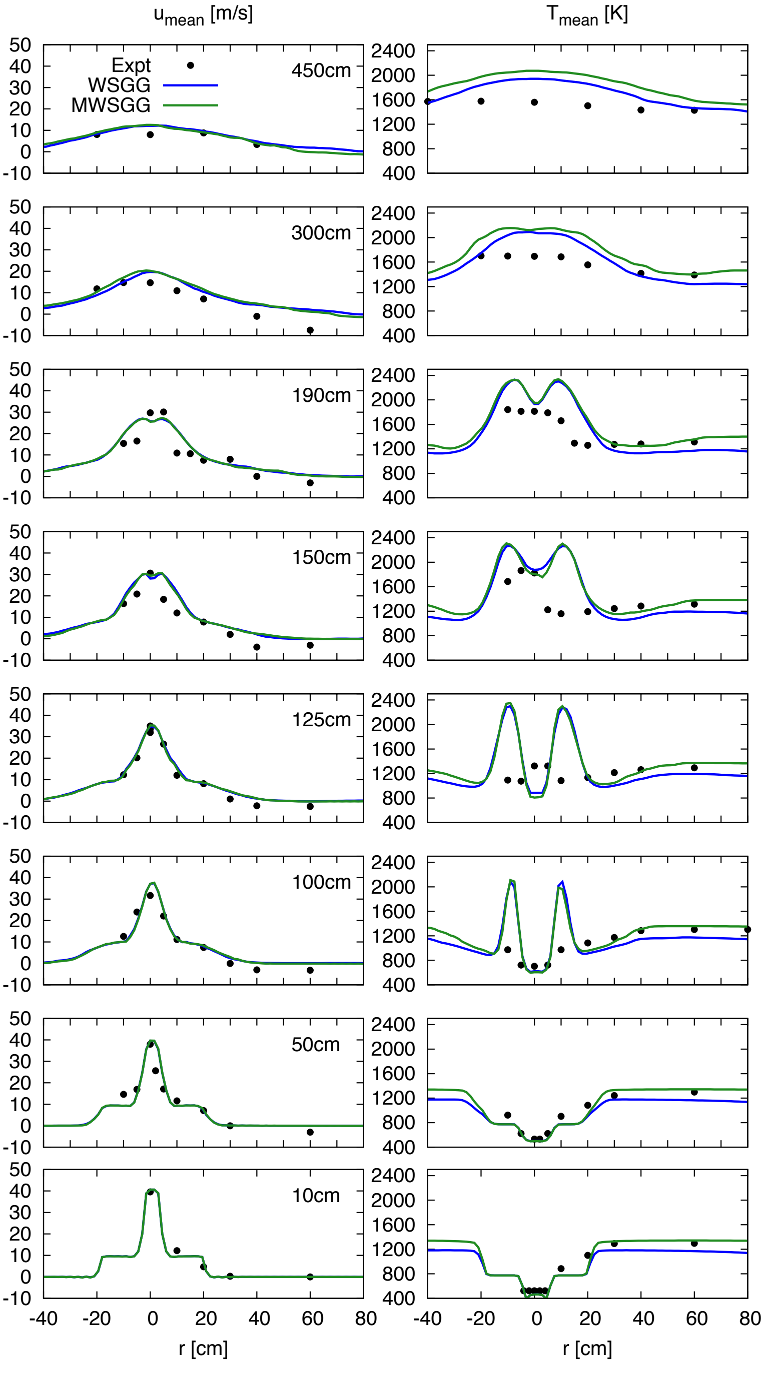

Figure 6.27: Comparison of the WSGG and MWSGG models, showing radial profiles of mean axial velocity (*left*) and temperature (*right*) at various locations along the length of the furnace.

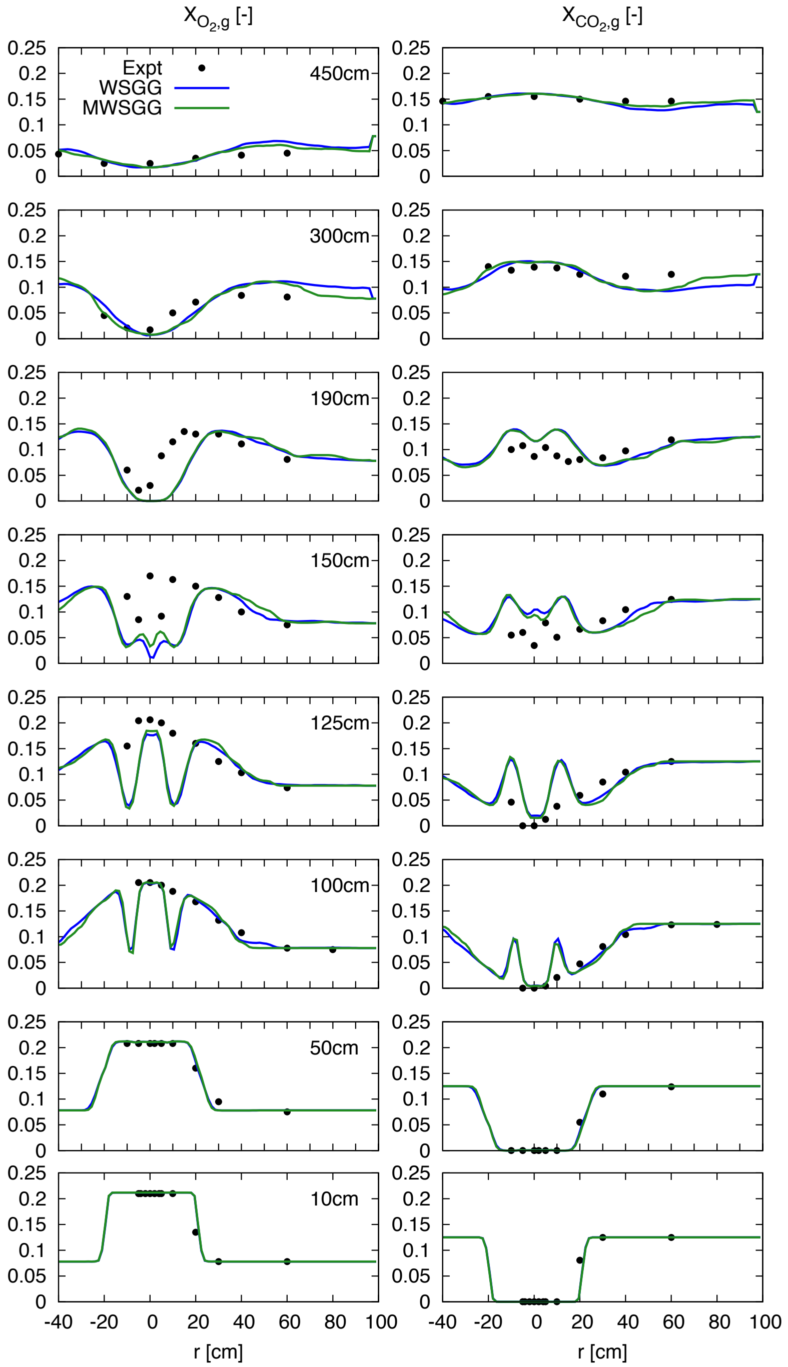

Figure 6.28: Comparison of the WSGG and MWSGG models, showing radial profiles of mean gas molar fractions of O_2 (*left*) and CO_2 (*right*) at various locations along the length of the furnace.

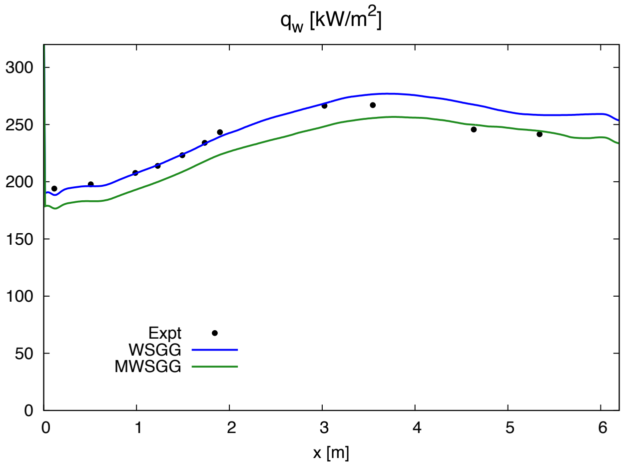

Figure 6.29: Comparison of the WSGG and MWSGG models, showing the mean incident radiation along the centreline of the furnace side walls.

section. The WSGG method predicts slightly better (lower) centreline temperatures with respect to the MWSGG, however by looking at the radial profiles of temperature (Fig. 6.27) one may notice that along the furnace length, the temperature in proximity of the side walls is slightly underestimated by the WSGG model. It is worth remembering here that the grey gas coefficients used in conjunction with the WSGG model were developed for uniform mixtures having molar ratios of $X_{H_2O}/X_{CO_2} = 1$, which is certainly not the case in this furnace, as preiously discussed in Sec. 6.4. Consequently, the inadequate coefficients used with the WSGG model may well be the reason why the side wall temperatures are underpredicted, which is not the case for the MWSGG model since this method was developed with the main intent of producing a set of coefficients valid for a wide range of molar ratios, such as those found in this furnace.

The incident heat flux to the wall is predicted quite well by both the WSGG and the MWSGG model, but with opposite trends. The WSGG model predictions are almost perfect in the first half of the furnace, after which they slightly overestimate the experimental data. The end of the furnace is the region with the highest concentration of participating gases (products), and hence the cause of the discrepancy between the simulation and the experiment in this highly participating zone (from a radiative perspective) may well be the inadequate coefficients. The MWSGG instead underpredicts the incident wall heat flux in the first half of the furnace, despite retaining a similar gradient to the experimental data, and in the second half of the furnace produces accurate predictions. It is difficult to justify the underprediction in the first half of the furnace, especially since the standard WSGG model is able to produce such accurate data. In the WSGG model wall-absorptivity coefficients have been derived to accurately define wall-weights for each grey gas, whereas for the MWSGG no such wall-absorptivity coefficients exist, and it is simply recommended to calculate the wall weights based on the wall temperature and the molar ratio in proximity of the wall (personal communication with *R. Johansson*, model author) [70, 71]. Consequently, this arguably less-accurate method of identifying the wall-weights could be the cause of the difference observed in the first half of the furnace in terms of the incident wall heat flux. Near the exit instead, accurate predictions are obtained and this could be due to the fact that in this area the media is more participating, and therefore an accurate specification of the wall-weights will have a smaller influence on the predicted incident wall flux.

6.6.3 Final Comparisons

Having assessed the results obtained with three different grey models, and the WSGG and MWSGG models, it is useful to conclude this work by comparing them all against each other in terms of axial temperature and incident wall heat flux predictions (Fig. 6.30 and Fig. 6.31 respectively), since these were the fields most affected by the different radiation models.

With regards to the axial temperature predictions, if one were to look blindly at the plot in Fig. 6.30, it would appear that the most accurate results are obtained with the *Grey3* model followed by the *Grey1* model, and then the *WSGG* and *MWSGG* models, with the *Grey2* model giving the worst predictions. However, it is the modellers' duty to go into further depth and understand what causes such differences in temperature predictions.

The WSGG and MWSGG models are formally considerably more accurate than any of the grey models employed in this work, in particular than the *Grey2* model, which is the most basic, having a constant gas-soot absorption coefficient. Consequently, there is no apparent reason why the *Grey3* and *Grey1* models should yield better temperature predictions than

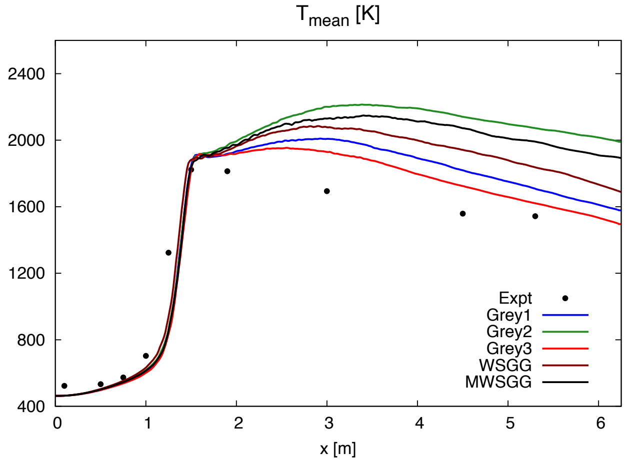

Figure 6.30: All radiation models are compared to each other and against experimental data. Axial mean plots along the centreline of the furnace for: gas velocity and temperature (top), O_2 and CO_2 gas molar fractions (middle), and solid volatile content and ash mass fractions (bottom).

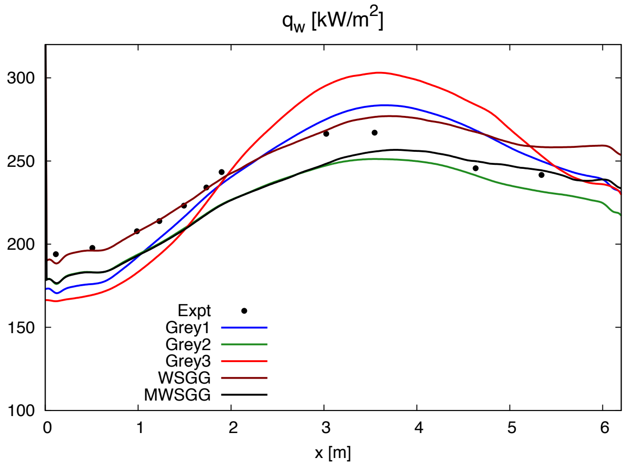

Figure 6.31: All radiation models are compared to each other and against experimental data. Average incident radiation along the centreline of the furnace side walls.

the WSGG and MWSGG models, unless the error in temperature prediction is caused by some phenomenon other than radiation. In coal combustion several processes occur at the same time and it is difficult to assess the accuracy of the individual models. It may well be the case that the downstream temperature in the furnace is generally over-predicted due to inadequate char combustion modelling, which causes this unphysical rise in temperature, rather than due to the radiation model. From the solids analysis (bottom-right of Fig. 6.26 for example), it can be seen that whereas the volatile content in the coal particles is released only slightly early, the ash mass fraction increases much more rapidly than what is shown by the experiments. This indicates that the char combustion process occurs too rapidly, which may be the major cause of the inaccurate temperature predictions in the second half of the furnace.

It is difficult to judge the accuracy of the different radiation models in terms of gas temperature predictions, as the discrepancies observed between simulation and experiment may not be caused directly from the radiation model. Nonetheless, the relative temperature differences between the models used in this work are remarkable, and highlight the importance of accurate radiation modelling in coal combustion furnaces, as different models can cause very large differences in temperature predictions.

In terms of incident wall heat flux predictions (Fig. 6.31), large differences are also observed with the different models. Evaluating the performance of the radiation models against this criterion is more legitimate, as this is less directly influenced by other models such as char combustion, as discussed above. The *WSGG* and the *MWSGG* models clearly yield the best predictions, as was expected since they are more sophisticated than the grey models. Nonetheless, the *Grey2* model yields very similar wall flux predictions to those obtained with the *MWSGG* model, which is remarkable considering the fact that the model only considers one grey gas whose participative properties are solely determined by the local concentration of H_2O and CO_2 and the volatile gases. The other two grey models, *Grey1* and *Grey3* yield worse predictions, which shift from an underestimation of the wall heat flux in the first third of the furnace, to an overestimation for the remaining part. A poor prediction was to be expected from *Grey1* since the radiative properties are defined by a constant gas-soot absorption coefficient, however it is quite surprising to see even worse predictions for the *Grey3* case, which theoretically is the most sophisticated of the three grey models, having its radiative properties defined by temperature polynomials for the individual participating species. Nonetheless, this model was not originally developed for use in conjunction with the DOM, but only to incorporate radiative heat losses in a simple cost-effective manner in gaseous combustion simulations. Consequently, it may well be that the coefficients are not suited for more complex cases or advanced predictions, such as those carried out in this work.

6.7 Conclusions

In this work LES coupled with radiation calculations by means of the DOM have been performed on a semi-industrial scale pulverised coal furnace. An initial parametric study was carried out to study the sensitivity of the simulation to specific parameters and to ensure that a good benchmark test simulation was obtained in order to *fairly* test the different radiation models implemented against each other. Several conclusions can be drawn from this study, however the complex nature of pulverised coal combustion, with its many processes occurring simultaneously, makes it difficult to go into as much detail as one would like to. The main conclusions and findings of this chapter are listed below:

- The parametric study showed that for cooled walls, the solution is not very sensitive to the wall emissivity ϵ_w parameter, as long as a relatively high value is chosen, such as the ones tested in this work.

- The outlet temperature can affect the incident radiation at the walls if its value is not selected adequately, however this can be easily recognised as instabilities (oscillations) can be noticed in the averaged incident radiation to the wall in proximity of the outlet.

- For cases where accurate prediction of the incident radiation on a wall is of primary interest, a high-order angular discretisation scheme is necessary, such as the S_8 scheme used in this work, or possibly an even higher order scheme.

- For cases in which temperature and species predictions are the main focus of interest, a very low angular discretisation such as the S_4

scheme can be used on equally-sized cubic cell grids, without a significant loss of accuracy, saving precious and considerable computational time.

- An attempt at modelling the radiative effects of soot was made, using simple models proposed and employed by other authors. However these methods were unsuccessful due to their over-simplicity, and it is recommended that these are not used except when combined with accurate soot formation models.

- The *Grey1* model involving a combined gas and soot absorption coefficient of $\kappa_{gs} = 0.5m^{-1}$, originally used by Stöllinger *et* al. [161] for the same flame, yields both an acceptable temperature and incident wall heat flux prediction.

- The *Grey2* model, which considers the heterogeneity of species (used in [81, 192]), gives a very good wall incident radiation prediction, but causes a large overestimation of the gas temperature.

- The *Grey3* model adapted in this work using the coefficients originally calculated by Barlow *et* al. [8], yields very good temperature predictions, whilst giving inaccurate wall heat flux measurements.

- The WSGG model was employed with knowingly inadequate coefficients which were developed for homogeneous and equal molar ratios of $X_{H_2O}/X_{CO_2} = 1$, but it was still found to be more accurate than other grey methods. Despite slightly underpredicting the gas temperatures at the sides of the furnace, the incident heat flux to the wall was predicted remarkably well, particularly in the first half of the furnace, where the prediction matches the experiment.

- The MWSGG model was also tested as an improvement of the WSGG, to account for mixture inhomogeneities in the furnace. The gas temperature predictions near the sides of the furnace improved as a result of the more adequate coefficients, however the incident wall heat flux predictions were not as good as those obtained with the WSGG model, possibly due to the lack of wall absorptivity weights for the MWSGG boundary condition specifications.

- Despite the coal particles being the strongest source of absorption, emission and scattering, accurate gas radiation modelling remains of paramount importance in the simulation of pulverised coal furnaces, as the different models have a significant impact on the temperature and heat flux predictions.

Finally, it is worth noting that the WSGG and the MWSGG models are formally more accurate than any of the grey models used, which is confirmed by the improved predictions of the incident radiation to the wall. However, the temperature predictions do not appear to always outperform the grey models, and this could be due to several reasons. In pulverised coal combustion systems several processes occur simultaneously within the furnace, and it is difficult to assess the relative accuracy of each one individually. It may well be the case that the temperature overestimation is due to another process occurring too rapidly, other than radiation (char combustion for example, as indicated by the results), and with a correct representation of said process the downstream temperatures would be lower, possibly giving the WSGG and MWSGG the most accurate predictions. Further, the complexity of taking experimental measurements in such furnaces, and the evident inconsistency in the experimental data between gas temperature measurements, gas species measurements and the solids analysis, shows that the experimental data against which the accuracy of the models is compared, could also involve considerable errors that are not easy to quantify. It is hence very difficult to draw reliable conclusions as to the accuracy of the temperature predictions downstream of the flame stabilisation point, and further investigations are required to assess the ability of coupled LES-radiation coal combustion simulations in obtaining accurate temperature predictions. Nonetheless, the present work has shown that LES of pulverised coal combustion with suitable radiation modelling is generally able to provide accurate results for both the flame and the radiative load on the walls.

7 Conclusions

This research project considered the large eddy simulation of coal combustion, with a special focus on the modelling of radiative heat transfer for such applications. Both coal combustion and radiation for combustion applications are two relatively unexplored topics in the field of computational fluid dynamics, and even more so in an LES framework.

As a part of the present work, a standalone DOM radiation solver has been developed using an equally-sized cubic-cell Cartesian grid. Several different angular and spatial discretisation schemes, as well as various spectral models, have been implemented to assess and investigate their relative performance and cost. The code has been successfully validated against simple static two-dimensional and three-dimensional benchmark cases, and has served as an optimal precursor to develop and assess the different discretisation schemes. This study has shown that whereas the step spatial discretisation scheme is formally less accurate than others, when combined with equally-sized cubic cells the results obtained are not necessarily worse, and if so only by small amounts. Further, the elevated difference in computational cost observed when using other schemes such as the TVD and CLAM schemes, did not justify the small increase in accuracy. For uniform grids and isothermal conditions, it was found that a low angular discretisation (S_4) is sufficient to accurately describe the radiative field, whereas for non-isothermal cases a slightly higher order discretisation was required (S_6), which hinted at the fact that for strongly non-isothermal and non-uniform computations such as those required in coal combustion, a high-order angular discretisation scheme should be preferred.

The code has also been extended to treat particles and soot radiation in addition to gas-phase radiation, and a coupling between the discrete and continuous phases was implemented. The radiative solver was integrated within *PsiPhi*, the in-house LES code used in this work. This required developing and implementing an optimal and efficient domain decomposition parallelisation strategy for the radiative solver, and synchronising the LES and radiative heat transfer calculations in physical time.

Large eddy simulations of the non-piloted, non-swirled IFRF pulverised coal combustion furnace no.1 have also been carried out. This semi-industrial scale furnace has a $2.4MW$ thermal output, and possibly represents the largest coal combustion furnace simulated by LES to date. The results of the simulations showed a satisfactory agreement with the experimental data, despite some inconsistencies in the latter. The flame lift-off height was predicted remarkably well, and the velocities and species concentration data showed good agreement overall.

A parametric analysis was performed to assess the sensitivity of the simulation on various factors such as the angular discretisation scheme and model parameters. It can be concluded that when using equally-sized cubic cells, and if an accurate prediction of the radiative heat flux to a wall is not required, a very low order angular discretisation can be used, saving considerable amounts of CPU-hours, and conversely to obtain accurate wall predictions a high-order angular discretisation is required. On the other hand, a very low sensitivity to the wall emissivity setting was found, provided that it is known whether the wall is cooled or not.

Three different approaches to modelling soot radiative effects without solving transport equations for soot or modelling soot formation were undertaken, following the work by other authors. Despite several attempts, unsatisfactory results were obtained, indicating that more work is required in this area. The models used are very sensitive to specific arbitrary parameters, and with some effort could be tweaked to obtain good results, however it is the author's belief that this is against the purpose of modelling in general, and as such this has been left aside. Including the effects of soot radiation without knowing the local soot temperature, distribution and concentration is a dangerous task, and it is recommended to not include soot effects unless accurate soot modelling is in place. Our testing has shown that soot radiation has a relatively small effect in the flame considered, thereby justifying the exclusion of such models, however this may not hold true for other pulverised coal combustion cases.

Three different grey radiation models, as well as the non-grey WSGG and MWSGG models were implemented and tested on the IFRF furnace. The results showed that the simulation is very sensitive to the radiation model in terms of average gas temperature and incident wall heat flux predictions. It is known that the WSGG and MWSGG models are formally more accurate than any of the grey models used in this work, as was reflected by the comparison with experimental data in terms of wall radiative heat flux. However the best mean gas centreline temperature predictions were obtained with the grey models, and as was discussed in the relevant chapter, it is likely that this difference is actually caused by the char combustion model over-predicting the char burnout rate, and the EBU model consuming the carbon monoxide too quickly. Nonetheless, it is remarkable how much influence the radiation model has on the temperature predictions, highlighting the importance of accurate radiative heat transfer modelling in these furnaces.

7.1 Recommendations for Future Work

A considerable amount of work has been carried out over the past few decades in the context of LES of combustion and radiation, although in most cases the two have been considered separately. Much less work has been done on the LES of pulverised coal combustion, let alone coupled flow-radiation simulations of this nature. The elevated computational costs and the added complexity of modelling and coupling multiphase flows which undergo several different processes has inhibited the spur of research publications in this field. This is combined with the difficulties of obtaining accurate experimental measurements in pulverised coal flames, which translates to a lack of sound experimental benchmark test cases, as opposed to the situation found for gaseous flames. Nonetheless, the rapid increase in computational power and availability, and the improvements in experimental techniques, give both the experimental and numerical study of pulverised coal flames a positive outlook. Endless recommendations for future work could be made due to the relatively early stage in this specific research field, however in this section only the most pressing recommendations, which are closely tied with the present work are made.

In terms of radiation modelling for coal combustion, there are several aspects that can be improved upon. The DOM has been implemented in an efficient way using a domain based parallelisation strategy and making the code as efficient as possible, but due to the complex nature of radiative heat transfer calculations, this remains a very expensive computation. During the course of the research project, a brief attempt has been made at using a coarser grid for the DOM solver by grouping eight LES cells into one DOM cell and mapping the fields between the two solvers by averaging and splitting. Despite the results showing very small differences in accuracy when using the coarser grid, the method is not entirely correct since at locations where the relevant LES fields are not uniform they are smoothed out for the radiative calculation, and conversely the radiative sources are distributed inaccurately back into the LES code. Further, this increases the relevance of turbulence radiation interactions which have been neglected in this work, and subgrid modelling for radiation may become a necessity with such coarser grids. A correct and valid approach would be to use an adaptive mesh coarsening system to identify and group only the neighbouring cells with identical scalar quantities relevant for the radiative calculation. In this way the higher definition of the LES would be retained in the near-flame region where high species and temperature gradients exist, whilst reducing the computational requirement in areas far from the region of interest, where there are little or no species and temperature gradients. This would require a pre-processing step to adapt the mesh, and would also entail slightly more complex numerics as different sized cells would be employed. However this could significantly reduce the number of cells required to compute the radiative solution, thereby making the computation considerably less expensive. At the same time, provided that the grid coarsening is significant, the quantity of cells for the DOM computation could be reduced to a number which would make task decomposition parallelisation feasible, which could improve the efficiency of the computation even further, as this is currently rendered impossible by the equally-sized cubic cell grid used, which requires several millions of cells and causes computational memory constraints.

Different gas spectral models have been implemented and used in this work, and despite more sophisticated models being present in literature, a high-level of accuracy can already be obtained with the WSGG and MWSGG models. Also considering the already very elevated computational cost of the calculations, it is not recommended as a high priority objective to employ more sophisticated gas spectral models.

A few approaches to the inclusion of soot radiation effects have been evaluated, yielding unsatisfactory results. Nonetheless, the model used for the calculation of the soot Planck mean extinction coefficient should be accurate, provided that accurate soot volume fractions and temperatures are obtained. Whereas the soot can be assumed to be in thermal equilibrium with the gas due to its small volume, and therefore share the same local temperature, its distribution and concentration within a furnace cannot be assumed homogeneous as in the current work, as this is highly unrepresentative of the experimental conditions. Soot formation is no doubt a complex phenomenon and a research area of its own, however it is very relevant and significant in coal furnaces as it is strongly radiative. It is therefore believed to be of paramount importance that some form of soot modelling is to be put in place in order to incorporate with an acceptable degree of accuracy the effects of soot radiation.

Finally, in coal flames several processes occur at the same time, and several different models are required to describe each process individually. However it is very difficult to be the judge of the individual models' performance when their effect cannot be easily and directly related to experimental data. For this reason it is the authors' belief that there is a necessity to perform more specific experiments or DNS calculations in an attempt to isolate the various phenomena occurring to a coal particle, which would enable modellers to perform more accurate model development and validation studies.

Bibliography

[1] International Energy Agency. World energy outlook 2012 fact sheet. http://www.worldenergyoutlook.org/media/weowebsite/2012/factsheets.pdf. Access date: 01/05/2013.

[2] J. Amaya. *Unsteady coupled convection, conduction and radiation simulations on parallel architectures for combustion applications.* PhD thesis, Universite de Toulouse, 2010.

[3] J. Amaya, O. Cabrit, D. Poitou, B. Cuenot, and M. El Hafi. Unsteady coupling of Navier-Stokes and radiative heat transfer solvers applied to anisothermal multicomponent turbulent channel flow. *Journal of Quantitative Spectroscopy and Radiative Transfer*, 111:295–301, 2010.

[4] S.V. Apte, K. Mahesh, P. Moin, and J.C. Oefelein. Large-eddy simulation of swirling particle-laden flows in a coaxial-jet combustor. *International Journal of Multiphase Flow*, 29:1311–1331, 2003.

[5] R.I. Backreedy, L.M. Fletcher, L. Ma, M. Pourkashanian, and A. Williams. Modelling pulverised coal combustion using a detailed combustion model. *Combustion Science and Technology*, 178:763–787, 2006.

[6] S. Badzioch and P. Hawksley. Kinetics of thermal decomposition of pulverized coal combustion. *Industrial Engineering and chemistry*, 9:521–530, 1970.

[7] D. Balsara. Fast and accurate discrete ordinates methods for multidimensional radiative transfer. part i, basic methods. *Journal of Quantitative Spectroscopy and Radiative Transfer*, 69:671–707, 2001.

[8] R. Barlow, A.N. Karpetis, J.H. Frank, and J.Y. Chen. Scalar profiles and NO formation in laminar opposed-flow partially premixed methane/air flames. *Combustion and Flame*, 127:2102–2118, 2001.

[9] H. R. Baum and W. E. Mell. Radiation and velocity fields induced by localized temperature fluctuations. *Proceedings of the Combustion Institute*, 28:473–479, 2000.

[10] M.M. Baum and P.J. Street. Predicting the combustion behaviour of coal particles. *Combust. Sci. Technol.*, 3:231–243, 1971.

[11] M. Bini. *Large eddy simulation of particle and droplet laden flows with stochastic modelling of subfilter scale.* PhD thesis, Imperial College London, 2007.

[12] M. Bini and W. P. Jones. Large-eddy simulation of particle-laden turbulent flows. *Journal of Fluid Mechanics*, 614.1:207–252, 2008.

[13] M. Bini and W.P. Jones. Particle acceleration in turbulent flows: A class of nonlinear stochastic models for intermittency. *Physics of Fluids*, 19:035104, 2007.

[14] M. Boger, D. Veynante, H. Boughanem, and A. Trouve. Direct numerical simulation anaylsis of flame surface density concept for large eddy simulation of turbulent premixed combustion. *Twenty-Seventh Symposium (International) on Combustion/The Combustion Institute*, 27:917–925, 1998.

[15] N.W. Bressloff, J.B. Moss, and P.A. Rubini. CFD prediction of coupled radiation heat transfer and soot production in turbulent flames. *Proceedings of the 26th International Symposium on Combustion, The Combustion Institute*, pages 2379–2386, 1996.

[16] S.P. Burke and T.E.W. Schumann. Diffusion flames. *Industrial and Engineering Chemistry*, 20:998–1004, 1928.

[17] R. Capdevila, C.D. Perez-Segarra, and A. Oliva. Development and comparison of different spatial numerical schemes for the radiative transfer equation resolution using three-dimensional unstructured meshes. *Journal of Quantitative Spectroscopy and Radiative Transfer*, 111(2):264–273, January 2010.

[18] B.G. Carlson and K.D. Lathrop. Transport theory - the method of discrete ordinates. *Computing Methods in Reactor Physics*, 1968.

[19] M.G. Carvalho and T.L. Farias. Modelling of heat transfer in radiating and combusting systems. *Chemical Engineering Research and Design*, 76:175–184, 1998.

[20] F. Cavallo Marincola, T. Ma, and A.M. Kempf. Large eddy simulations of the Darmstadt turbulent stratified flame series. *Proceedings of the Combustion Institute*, 34(1)(0):1307–1315, 2013.

[21] J. C. Chai, H.S. Lee, and S. V. Patankar. Ray effect and false scattering in the discrete ordinates method. *Numerical Heat Transfer, Part B: Fundamentals*, 24:373–389, 1993.

[22] J. C. Chai, H.S. Lee, and S. V. Patankar. Finite volume method for radiation heat transfer. *Journal of Thermophysics and Heat Transfer*, 8:419–425, 1994.

[23] J. C. Chai, S. V. Patankar, and H. S. Lee. Evaluation of spatial differencing practices for the discrete-ordinates method. *Journal of Thermophysics and Heat Transfer*, 8, no. 1:140–144, 1994.

[24] N. Chakraborty and N. Swaminathan. Modelling of non-unity Lewis number effects on scalar dissipation rate transport in turbulent premixed flames. In *Proceedings of the European Combustion Meeting*, 2009.

[25] S. Chandrasekhar. *Radiative Transfer*. Dover Publications, 1960.

[26] A. J. Chandy, D. J. Glaze, and S. H. Frankel. Parallelizing the discrete ordinates method (DOM) for three-dimensional radiative heat transfer calculations using a priority queuing technique. *Numerical Heat Transfer, Part B: Fundamentals*, 52:33–49, 2007.

[27] K.B. Cheong and T.H. Song. An alternative discrete ordinates method with interpolation and source differencing for two-dimensional radiative transfer problems. *Numerical Heat Transfer, Part B: Fundamentals*, 32:107–125, 1997.

[28] E. H. Chui, P. M. J. Hughes, and G. D. Raithby. Implementation of the finite volume method for calculating radiative transfer in a pulverized fuel flame. *Combustion Science and Technology*, 92:225–242, 1993.

[29] P. J. Coelho. Numerical simulation of radiative heat transfer from non-gray gases in three-dimensional enclosures. *Journal of Quantitative Spectroscopy and Radiative Transfer*, 74(3):307–328, August 2002.

[30] P.J. Coelho. Bounded skew high-order resolution schemes for the discrete ordinates method. *Journal of Computational Physics*, 175:412–437, 2002.

[31] P.J. Coelho. The role of ray effects and false scattering on the accuracy of the standard and modified discrete ordinates methods. *Journal of Quantitative Spectroscopy and Radiative Transfer*, 73:231–238, 2002.

[32] P.J. Coelho. Numerical simulation of the interaction between turbulence and radiation in reactive flows. *Progress in Energy and Combustion Science*, 33(4):311–383, August 2007.

[33] P.J. Coelho. A comparison of spatial discretization schemes for differential solution methods of the radiative transfer equation. *Journal of Quantitative Spectroscopy and Radiative Transfer*, 109:189–200, 2008.

[34] P.J. Coelho. Approximate solutions of the filtered radiative transfer equation in large eddy simulations of turbulent reactive flows. *Combustion and Flame*, 156(5):1099–1110, May 2009.

[35] P.J. Coelho. A theoretical analysis of the influence of turbulence on radiative emission in turbulent diffusion flames of methane. *Combustion and Flame*, 160:610–617, 2013.

[36] P.J. Coelho, J. M. Gonçalves, M.G. Carvalho, and D. N. Trivic. Modelling of radiative heat transfer in enclosures with obstacles. *International Journal of Heat and Mass Transfer*, 41:745–756, 1998.

[37] R. Courant, K. Friedrichs, and H. Lewy. On the partial difference equations of mathematical physics. *IBM Journal*, pages 215–234, 1967.

[38] P.S. Cumber, M. Fairweather, and H.S. Ledin. Application of wide band radiation models to non-homogenous combustion systems. *International Journal of Heat and Mass Transfer*, 41:1573–1584, 1988.

[39] M. K. Denison and B. W. Webb. A spectral line-based weighted-sum-of-gray-gases model for arbitrary RTE solvers. *Journal of Heat Transfer*, 115:1004–12, 1993.

[40] M. K. Denison and B. W. Webb. The spectral line-based weighted-sum-of-gray-gases model in non-isothermal non-homogeneous media. *Journal of Heat Transfer*, 117:359–65, 1995.

[41] M. K. Denison and B.W. Webb. The spectral-line weighted sum-of-gray-gases model for H_2O/CO_2 mixtures. *Journal of Heat Transfer*, 117:788–92, 1995.

[42] K.V. Deshmukh, D.C. Haworth, and M.F. Modest. Direct numerical simulation of turbulence-radiation interactions in homogeneous non-premixed combustion systems. *Proceedings of the Combustion Institute*, 31(1):1641–1648, January 2007.

[43] L.I. Díez, C. Cortés, and J. Pallarés. Numerical investigation of NO_x emissions from a tangentially-fired utility boiler under conventional and overfire air operation. *Fuel*, 87:1259–1269, 2008.

[44] F. Duchaine, A. Corpron, Pons L., V. Moureau, F. Nicoud, and Poinsot T. Development and assessment of a coupled strategy for conjugate heat transfer with large eddy simulation: Application to a cooled turbine blade. *International Journal of Heat and Fluid Flow*, 30:1129–1141, 2009.

[45] P.A. Durbin. Stochastic differential equations and turbulent dispersion. Technical report, NASA Reference Publications, 1103, 1983.

[46] P. Edge, M. Gharebaghi, R. Irons, R. Porter, R.T.J. Porter, M. Pourkashanian, D. Smith, P. Stephenson, and A. Williams. Combustion modelling opportunities and challenges for oxy-coal carbon capture technology. *Chemical Engineering Research and Design*, 89:1470–1493, 2011.

[47] W. A. Fiveland. Discrete ordinate methods for radiative heat transfer in isotropically and anisotropically scattering media. *ASME Journal of Heat Transfer*, 109:809–812, 1987.

[48] W.A. Fiveland. Three-dimensional radiative heat-transfer solutions by the discrete-ordinates method. *Journal of Thermophysics and Heat Transfer*, 2, no. 4:309–316, 1988.

[49] T.H. Fletcher, A. Kerstein, R. Pugmuire, M.S. Solum, and D.M. Grant. Chemical percolation model for devolatilization. 2. temperature and heating rate effects on product yields. *Energy & Fuels*, 3:54–60, 1990.

[50] T.H. Fletcher, A.R. Kerstein, R.J. Pugmuire, M. Solum, M.S., and D.M. Grant. A chemical percolation model for devolatilization: Summary. Technical report, Sandia Technical Report, SAND92-8207, 1992.

[51] T.H. Fletcher, J. Ma, J.R. Rigby, A.L. Brown, and B.W. Webb. Soot in coal combustion systems. *Progress in Energy and Combustion Science*, 23:283–301, 1997.

[52] B. M. Franchetti. *Large Eddy Simulations of Oxy-Coal Combustion.* PhD thesis, Imperial College London, 2013.

[53] M. Germano, U. Piomelli, P. Moin, and W.H. Cabot. A dynamic subgrid-scale eddy viscosity model. *Physics of Fluids A*, 3(7):1760–1765, 1991.

[54] M. Gharebaghi, R.M.A. Irons, L. Ma, M. Pourkashanian, and A. Pranzitelli. Large eddy simulation of oxy-coal combustion in an industrial combustion test facility. *International Journal of Greenhouse Gas Control*, 5S:S100–S110, 2011.

[55] L.Y.M. Gicquel, G. Staffelbach, and Poinsot T. Large eddy simulations of gaseous flames in gas turbine combustion chambers. *Progress in Energy and Combustion Science*, 38:782–817, 2012.

[56] W.F. Godoy and P. E. DesJardin. On the use of flux limiters in the discrete ordinates method for 3D radiation calculations in absorbing and scattering media. *Journal of Computational Physics*, 229:3189–3213, 2010.

[57] J. Gonçalves and P.J. Coelho. Parallelization of the discrete ordinates method. *Numerical Heat Transfer, Part B: Fundamentals*, 32:151–173, 1997.

[58] R. Gonçalves dos Santos, M. Lecanu, S. Ducruix, O. Gicquel, E. Iacona, and D. Veynante. Coupled large eddy simulations of turbulent combustion and radiative heat transfer. *Combustion and Flame*, 152(3):387–400, February 2008.

[59] A. D. Gosman and F. C. Lockwood. Incorporation of a flux model for radiation into a finite-difference procedure for furnace calculations. *Symposium (International) on Combustion*, 14(1):661–671, 1973.

[60] V. Goutiere, F. Liu, and Charette A. An assessment of real-gas modelling in 2D enclosures. *Journal of Quantitative Spectroscopy and Radiative Transfer*, 64:299–326, 2000.

[61] W. L. Grosshandler. Radcal. A narrow-band model for radiation calculations in a combustion environment. Technical report, NIST Technical Note 1402, 1993.

[62] A. Habibi, B. Merci, and D. Roekaerts. Turbulence radiation interaction in Reynolds-averaged Navier-Stokes simulations of nonpremixed piloted turbulent laboratory-scale flames. *Combustion and Flame*, 151:303–320, 2007.

[63] N. Hashimoto, R. Kurose, and H. Shirai. Numerical simulation of pulverized coal jet flame employing the TDP model. *Fuel*, 97:277–287, 2012.

[64] Nozomu Hashimoto, Ryoichi Kurose, Seung-Min Hwang, Hirofumi Tsuji, and Hiromi Shirai. A numerical simulation of pulverized coal combustion employing a tabulated-devolatilization-process model (TDP model). *Combustion and Flame*, 159(1):353–366, January 2012.

[65] H. C. Hottel and A. F. Sarofim. *Radiative Transfer*. McGraw-Hill, 1967.

[66] Cohen E. S. Hottel H. C. Radiant heat exchange in a gas-filled enclosure: Allowance for nonuniformity of gas temperature. *AiChE Journal*, 3-14:1958, 4(1).

[67] L. Y. Hu, L. X. Zhou, and J. Zhang. Large-eddy simulation of a swirling diffusion flame using a SOM SGS combustion model. *Numerical Heat Transfer, Part B: Fundamentals*, 50(1):41–58, March 2006.

[68] A.S. Jamaluddin and P.J. Smith. Predicting radiative transfer in rectangular enclosures using the discrete ordinates method. *Combustion Science and Technology*, 59:321–340, 1988.

[69] J.P. Jessee and W.A. Fiveland. Bounded high-resolution differencing schemes applied to the discrete ordinates method. *Journal of Thermophysics and Heat Transfer*, 11:540–8, 1997.

[70] R. Johansson, B. Leckner, K. Andersson, and F. Johnsson. Account for variations in the H_2O to CO_2 molar ratio when modelling gaseous radiative heat transfer with the weighted-sum-of-grey-gases models. *Combustion and Flame*, 158:893–901, 2011.

[71] Robert Johansson, Klas Andersson, Bo Leckner, and Henrik Thunman. Models for gaseous radiative heat transfer applied to oxy-fuel conditions in boilers. *International Journal of Heat and Mass Transfer*, 53(1-3):220–230, January 2010.

[72] W.P. Jones and R.P. Lindstedt. Global reaction schemes for hydrocarbon combustion. *Combustion and Flame*, 73:233–249, 1988.

[73] W.P. Jones and M.C. Paul. Combination of DOM with LES in a gas turbine combustor. *International Journal of Engineering Science*, 43:379–397, 2005.

[74] D. Joseph, M. El Hafi, R. Fournier, and B. Cuenot. Comparison of three spatial differencing schemes in discrete ordinates method using three-dimensional unstructured meshes. *International Journal of Thermal Sciences*, 44:851–864, 2005.

[75] V.P. Kabashnikov. Thermal radiation of turbulent flows in case of large fluctuations of the absorption coefficient and the Planck function. *Journal of Engineering Physics*, 49:778–784, 1985.

[76] V.P. Kabashnikov and Kmit G.I. Influence of turbulent fluctuations on thermal radiation. *Journal of Applied Spectroscopy*, 31:963–967, 1979.

[77] T. Kangwanpongpan, R. Correa da Silva, and H. J. Krautz. Prediction of oxy-coal combustion through an optimized weighted sum of gray gases model. *Energy*, 41:244–251, 2012.

[78] A. Kempf, M. Klein, and J. Janicka. Efficient generation of initial- and inflow-conditions for transient turbulent flows in arbitrary geometries. *Flow Turbulence Combustion*, 74:67–84, 2005.

[79] A.M. Kempf. *Large-Eddy Simulation of Non-Premixed Turbulent Flames.* PhD thesis, TU Darmstadt, Germany, 2003.

[80] A.M. Kempf, B.J. Geurts, and J.C. Oefelein. Error analysis of large-eddy simulation of the turbulent non-premixed sydney bluff-body flame. *Combustion and Flame*, 158:2408–2419, 2011.

[81] E. E. Khalil, D.B. Spalding, and J.H. Whitelaw. The calculation of local flow properties in two-dimensional furnaces. *International Journal of Heat and Mass Transfer*, 18:775–791, 1975.

[82] Y.U. Khan, D.A. Lawson, and R.J. Tucker. Simple models of spectral radiative properties of carbon dioxide. *International Journal of Heat and Mass Transfer*, 40(15):3581–3593, 1997.

[83] Rubin SG Khosla PK. A diagonally dominant second order accurate implicit scheme. *Comput Fluids*, 2:207–9, 1974.

[84] Seung Hyun Kim and Kang Y. Huh. A new angular discretization scheme of the finite volume method for 3-D radiative heat transfer in absorbing, emitting and anisotropically scattering media. *International Journal of Heat and Mass Transfer*, 43(7):1233–1242, April 2000.

[85] G.M. Kimber and M.D. Gray. Rapid devolatilization of small coal particles. *Combustion and Flame*, 11:360–362, 1965.

[86] M. Klein, A. Sadiki, and J. Janicka. A digital filter based generation of inflow data for spatially developing direct numerical of large eddy simulation. *J. Comput. Phys.*, 186:652–665, 2003.

[87] K. J. Knill, T. Nakamura, and M. E. Morgan. The effect of mixing on NO_x reduction by coal fuel staging. Technical report, International Flame Research Foundation, 1990.

[88] H. Kobayashi, J.B. Howard, and A.F. Sarofim. Coal devolatilisation at higher temperatures. *Proc. Combust. Inst*, 16:411–424, 1976.

[89] R. Koch and R. Becker. Evaluation of quadrature schemes for the discrete ordinates method. *Journal of Quantitative Spectroscopy and Radiative Transfer*, 84(4):423–435, 2004.

[90] A. Kolmogorov. Dissipation of energy in local isotropic turbulence. *Doklady Akademii Nauk SSSR*, 32:19–21, 1941.

[91] A.N. Kolmogorov. The local structure of turbulence in incompressible viscous fluid for very large Reynolds numbers. *Proceedings of the Royal Society*, 434:9–13, 1991.

[92] G. Krishnamoorthy, R. Rawat, and P.J. Smith. Parallel computations of radiative heat transfer using the discrete ordinates method. *Numerical Heat Transfer, Part B: Fundamentals*, 47:19–38, 2005.

[93] R. Kurose, H. Makino, and A. Suzuki. Numerical analysis of pulverized coal combustion characteristics using advanced low-NO_x burner. *Fuel*, 83:693–703, 2004.

[94] R. Kurose, H. Tsuji, and H. Makino. Effects of moisture in coal on pulverized coal characteristics. *Fuel*, 80:1457–1465, 2001.

[95] Weber R Lallemant N, Sayre A. Evaluation of emissivity correlations for $H_2O - CO_2 - N_2/air$ mixtures and couplingwith solution methods of the radiative transfer equation. *Progress in Energy and Combustion Science*, 22:543–74, 1996.

[96] K.D. Lathrop. Use of discrete-ordinates methods for solution of photon transport problems. *Nuclear Science and Engineering*, 24:381–388, 1966.

[97] K.D. Lathrop and B.G. Carlson. Discrete-ordinates angular quadrature of the neutron transport equation. Technical report, Technical

Information Series Report LASL-3186, Los Alamos Scientific Laboratory, 1965.

[98] N.M. Laurendeau. Heterogeneous kinetics of coal char gasification and combustion. *Progress in Energy and Combustion Science*, 4:221–270, 1978.

[99] C.E. Lee. The discrete S_n approximation to transport theory. Technical report, Technical Information Series Report LA2595, Lawrence Livermore Laboratory, 1962.

[100] B.P. Leonard. A survey of finite differences with upwinding for numerical modelling of the incompressible convective diffusion equation. *Computational Techniques in Transient and Turbulent Flow*, 2:1–35, 1981.

[101] Claudio Lettieri. *Large Eddy Simulation of Two-Phase Reacting Flows.* PhD thesis, Imperial College London, 2010.

[102] D. Lilly. The representation of small-scale turbulence in numerical simulation experiments. *Proceedings of the IBM Scientific Computing Symp. on Environmental Sciences*, pages 195–210, 1967.

[103] F Liu. Numerical solutions of three-dimensional non-gray gas radiative transfer using the statistical narrow-band model. *Transactions of the ASME*, 121:200–203, 1999.

[104] F. Liu, H.A. Becker, and A. Pollard. Spatial differencing schemes of the discrete-ordinates method. *Numerical Heat Transfer, Part B: Fundamentals*, 30:23–46, 1996.

[105] Bindar Y. Liu F, Becker HA. A comparative study of radiative heat transfer modelling in gas-fired furnaces using the simple gray gas and the weighted-sum-of-gray-gases models. *International Journal of Heat and Mass Transfer*, 41:3357–71, 1998.

[106] F.C. Lockwood, T. Mahmud, and M. A. Yehia. Simulation of pulverised coal test furnace performance. *Fuel*, 77(12):1329–1337, 1997.

[107] F.C. Lockwood and A. P. Salooja. The prediction of some pulverized bituminous coal flames in a furnace. *Combustion and Flame*, 54:23–32, 1983.

[108] F.C. Lockwood and N.G. Shah. A new radiation solution method for incorporation in general combustion prediction procedures. *Symposium (International) on Combustion*, 18(1):1405–1414, 1981.

[109] T. J. Love. *Radiative Heat Transfer*. Merrill, 1968.

[110] S. Lyra. *Large Eddy Simulation of Isothermal and Reacting Sprays*. PhD thesis, Imperial College London, 2010.

[111] M. Mancini, R. Weber, and U. Bollettini. Predicting NO_x emissions of a burner operated in flameless oxidation mode. *Proceedings of the Combustion Institute*, 29:1155–1163, 2002.

[112] J.G. Marakis, C. Papapavlou, and E. Kakaras. A parametric study of radiative heat transfer in pulverised coal furnaces. *International Journal of Heat and Mass Transfer*, 43:2961–2971, 2000.

[113] B. Marracino and D. Lentini. Radiation modelling in non-luminous nonpremixed turbulent flames. *Combustion Science and Technology*, 128:23–48, 1997.

[114] M. Menguc and R. Viskanta. Radiative transfer in three-dimensional rectangular enclosures containing inhomogeneous anisotropically scattering media. *Journal of Quantitative Spectroscopy and Radiative Transfer*, 33:533–549, 1985.

[115] David Merrick. Mathematical models of the thermal decomposition of coal part 2. *Fuel*, 62:540–546, 1983.

[116] David Merrick. Mathematical models of the thermal decomposition of coal part 3. *Fuel*, 62:546–552, 1983.

[117] J. B. Michel and R. Payne. Detailed measurements of long pulverized coal flames for the characterization of pollutant formation. Technical report, International Flame Research Foundation, 1980.

[118] M. Modest. The weighted-sum-of-gray-gases model for arbitrary solution methods in radiative transfer. *ASME Journal of Heat Transfer*, 113:650–656, 1991.

[119] M. F. Modest. *Radiative Heat Transfer*. Mc-Graw-Hill, Inc., 1993.

[120] M. F. Modest. *Radiative Heat Transfer, Second edition*. Academic Press, 2003.

[121] Metropolis N. The beginning of the Monte Carlo method. *Los Alamos Science*, pages 125–130, 1987.

[122] S. Orsino, M. Tamura, P. Stabat, S. Constantini, O. Prado, and R. Weber. Excess enthalpy combustion of coal (results of high temperature air combustion trials). Technical report, International Flame Research Foundation, 2000.

[123] A. A. F. Peters and R. Weber. Mathematical modeling of a 2.4 MW swirling pulverized coal flame. *Combustion Science and Technology*, 122:131–182, 1997.

[124] M.W.A. Pettit, B. Coriton, A. Gomez, and A.M. Kempf. Large-eddy simulation and experiments on non-premixed highly turbulent 'opposed jet' flows. *Proceedings of the Combustion Institute*, doi: 10.1016/j.proci.2010.06.140, 2010.

[125] T. Poinsot and D. Veynante. *Theoretical and Numerical Combustion*. R.T. Edwards, Philadelphia, PA, USA, 2nd edition, 2005.

[126] D. Poitou, J. Amaya, and F. Duchaine. Parallel computation for radiative heat transfer using the dom in combustion applications: Direction, frequency, subdomain decompositions, and hybrid methods. *Numerical Heat Transfer, Part B: Fundamentals: An International Journal of Computation and Methodology*, 62:28–49, 2012.

[127] D. Poitou, J. Amaya, M. El Hafi, and B. Cuenot. Analysis of the interaction between turbulent combustion and thermal radiation using unsteady coupled LES/DOM simulations. *Combustion and Flame*, 159:1605–1618, 2012.

[128] D. Poitou, M. El Hafi, and B. Cuenot. Diagnosis of turbulence radiation interaction in turbulent flames and implications for modeling in large eddy simulations. *Turkish Journal of Engineering and Environmental Sciences*, 31:371–381, 2007.

[129] D. Poitou, M. El Hafi, and B. Cuenot. Analysis of radiation modeling for turbulent combustion: Development of a methodology to couple turbulent combustion and radiative heat transfer in LES. *Journal of Heat Transfer*, 133:062701–1, 2011.

[130] R. Porter, F. Liu, M. Pourkashanian, A. Williams, and D. Smith. Evaluation of solution methods for radiative heat transfer in gaseous oxy-fuel combustion environments. *Journal of Quantitative Spectroscopy and Radiative Transfer*, 111:2084–2094, 2010.

[131] G. D. Raithby and E. H. Chui. A finite-volume method for predicting a radiant heat transfer in enclosures with participating media. *Journal of Heat Transfer*, 112:415–423, 1990.

[132] M.A. Ramankutty and A.L. Crosbie. Modified discrete ordinates solution of radiative transfer in two-dimensional rectangular enclosures. *Journal of Quantitative Spectroscopy and Radiative Transfer*, 57:107–140, 1997.

[133] M.A. Ramankutty and A.L. Crosbie. Modified discrete ordinates solution of radiative transfer in three-dimensional rectangular enclosures. *Journal of Quantitative Spectroscopy and Radiative Transfer*, 60:103–134, 1998.

[134] W. E. Ranz and W. R. Marshall. Evaporation from drops. *Chem. Eng. Prog*, 48.3:141–146, 1952.

[135] O. Reynolds. An experimental investigation of the circumstances which determine whether the motion of water shall be direct or sinuous, and the law of resistance in parallel channels. *Philosphy Transactions of the Royal Society*, Ser. A 174:935–982, 1883.

[136] O. Reynolds. On the dynamical theory of incompressible viscous flows and the determination of the criterion. *Philosphical Transactions of the Royal Society of London Series A*, 186:123–161, 1894.

[137] L.F. Richardson. *Weather Prediction by Numerical Process.* Cambridge University Press, 1922.

[138] P. L. Roe. Some contributions to the modeling of discontinuous flows. In *Large scale computations in fluid mechanics, lectures in applied mathematics, vol. 22.* Editors: Engquist BE, Osher S, Somerville RCJ. Providence, RI: American Mathematical Society, 1985.

[139] P. L. Roe. Characteristic-based schemes for the Euler equations. *Annual Review Fluid Mechanics*, 18:337, 1986.

[140] M. Roger, S. Blanco, M. El Hafi, and R. Fournier. Monte Carlo estimates of domain-deformation sensitivities. *Physical Review Letters*, 95(18), 2005.

[141] M. Roger, P.J. Coelho, and C.B. da Silva. The influence of the non-resolved scales of thermal radiation in large eddy simulation of turbulent flows: A fundamental study. *International Journal of Heat and Mass Transfer*, 53:2897–2907, 2010.

[142] Maxime Roger, Carlos B. Da Silva, and Pedro J. Coelho. Analysis of the turbulence-radiation interactions for large eddy simulations of turbulent flows. *International Journal of Heat and Mass Transfer*, 52(9-10):2243–2254, April 2009.

[143] L.S. Rothman et al. The Hitran 2004 molecular spectroscopic database. *Journal of Quantitative Spectroscopy and Radiative Transfer*, 96(2):139–204, 2005.

[144] C N Satterfield. *Mass Transfer in Heterogeneous Catalyst.* MIT press, Cambridge, 1970.

[145] A. N. Sayre, K. J. Knill, and J.P. Smart. Coal characterization requirements for modelling coal flames. *International Flame Research Foundation Repor*, 88/y/13, 1991.

[146] N. Schaffel, M. Mancini, A. Szlek, and R. Weber. Mathematical modeling of mild combustion of pulverized coal. *Combustion and Flame*, 156:1771–1784, 2009.

[147] P. Schmitt, T. Poinsot, B. Schuermans, and K. P. Geigle. Large-eddy simulation and experimental study of heat transfer, nitric oxide emissions and combustion instability in a swirled turbulent high-pressure burner. *Journal of Fluid Mechanics*, 570:17–46, 2007.

[148] R. Siegel and J. R. Howell. *Thermal radiation heat transfer.* Taylor & Francis, 2002.

[149] J. Smagorinsky. General circulation experiments with the primitive equations i. the basic experiment. *Monthly Weather Review*, 91(3):99–164, 1963.

[150] J. P. Smart, G. J. Nathan, N. L. Smith, G. J. R. Newbold, D. S. Nobes, and D. J. Morgan. On the development of a coal fired precessing jet burner. Technical report, International Flame Research Foundation, 1999.

[151] I.W. Smith. The intrinsic reactivity of carbons to oxygen. *Fuel*, 58:409–414, 1978.

[152] I.W. Smith. The combustion rates of coal chars: A review. *Proc. Combust. Inst.*, 19:1045–1065, 1982.

[153] T. F. Smith, Z. F. Shen, and J. N. Friedman. Evaluation of coefficients for the weighted sum of gray gases model. *Transactions of the ASME*, 104:602–608, 1982.

[154] P.R. Solomon, M.A. Serio, Y. Zhao, and R. Bassilakis. Impact of coal pyrolisis on combustion. *Proc. Combust. Inst.*, 25:463–474, 1994.

[155] A. Soufiani. Temperature turbulence spectrum for high-temperature radiating gases. *Journal of Thermophysics and Heat Transfer*, 5:489–494, 1991.

[156] D.B. Spalding. Development of the eddy-break-up model of turbulent combustion. *Symposium (International) on Combustion*, 16(1):1657–1663, 1977.

[157] O. Stein. *Large Eddy Simulation of Combustion in Swirling and Opposed Jet Flows.* PhD thesis, Imperial College London, 2009.

[158] O. Stein, A. Kempf, and J. Janicka. LES of the Sydney swirl flame series: An initial investigation of the fluid dynamics. *Combustion Science and Technology*, 179:173–189, 2007.

[159] M. Stöllinger. *Probability density function modeling of turbulent premixed combustion and pulverised coal combustion.* PhD thesis, University of Wyoming, Department of Mathematics, 2010.

[160] Michael Stöllinger, Bertrand Naud, Dirk Roekaerts, Nijso Beishuizen, and Stefan Heinz. Pdf modeling and simulations of pulverized coal combustion part 1: Theory and modeling. *Combustion and Flame*, 160(2)(0):384–395, 2013.

[161] Michael Stöllinger, Bertrand Naud, Dirk Roekaerts, Nijso Beishuizen, and Stefan Heinz. Pdf modeling and simulations of pulverized coal combustion part 2: Application. *Combustion and Flame*, 160(2)(0):396–410, 2013.

[162] J. Ströhle. Assessment of the re-ordered wide band model for non-grey radiative transfer calculations in 3D enclosures. *Journal of Quantitative Spectroscopy and Radiative Transfer*, 109:1622–1640, 2008.

[163] J. Ströhle, U. Schnell, and K.R.G. Hein. A mean flux discrete ordinates interpolation scheme for general co-ordinates. In *Proceedings of the third international symposium on radiative transfer*, 2001.

[164] P.K. Sweby. High resolution schemes using flux-limiters for hyperbolic conservation laws. *Society for Industrial and Applied Mathematics Journal of Numerical Analysis*, 21:995–1011, 1984.

[165] C.P. Thurgood, A. Pollard, and H. A. Becker. The T_n quadrature set for the discrete ordinates method. *Journal of Heat Transfer*, 117(4):1068–1070, 1995.

[166] Z. F. Tian, P. J. Witt, M. P. Schwarz, and W. Yang. Comparison of two-equation turbulence models in simulaton of a non-swirl coal flame in a pilot-scale furnace. *Combustion Science and Technology*, 181:954–983, 2009.

[167] D. N. Trivic. Modeling of 3-D non-gray gases radiation by coupling the finite volume method with weighted sum of grey gases model. *International Journal of Heat and Mass Transfer*, 47:1367–1382, 2004.

[168] J.S. Truelove. Prediction of the near-burner flow and combustion in swirling pulverised coal flames. *Proc. Comb. Inst.*, 21:275–284, 1986.

[169] J.S. Truelove. Discrete-ordinate solutions of the radiation transport equation. *ASME Journal of Heat Transfer*, 109:1048–1051, 1987.

[170] J.S. Truelove. Three-dimensional radiation in absorbing-emitting-scattering media using the discrete ordinates approximation. *Journal of Quantitative Spectroscopy and Radiative Transfer*, 39:27–31, 1988.

[171] B. Van Leer. Towards the ultimate conservation difference scheme. ii monotonicity and conservation combined in a second-order scheme. *Journal of Computational Physics*, 14:361–70, 1974.

[172] B. Van Leer. Towards the ultimate conservative difference scheme iii. upstream-centred finite-difference schemes for ideal compressible flow. *Journal of Computational Physics*, 23:263–275, 1977.

[173] M. Vascellari and G. Cau. Influence of turbulence-chemical interaction on CFD pulverized coal mild combustion modeling. *Fuel*, 101:90–101, 2012.

[174] H. Versteeg and W. Malalasekra. *An Introduction to Computational Fluid Dynamics: The Finite Volume Method.* Prentice Hall, 2007.

[175] R. Viskanta and M. P. Menguc. Radiation heat transfer in combustion systems. *Progress in Energy and Combustion Science*, 13(2):97–160, 1987.

[176] B. M. Visser, J. P. Smart, W. L. Van De Kamp, and R. Weber. Measurements and predictions of quarl zone properties of swirling pulverised coal flames. *Twenty-Third Symposium (International) on Combustion/The Combustion Institute*, pages 949–955, 1990.

[177] B. M. Visser and R. Weber. Computations of near burner zone properties of swirling pulverised coal flames. Technical report, International Flame Research Foundation, 1989.

[178] T.F. Wall, G. Liu, H. Wu, D. G. Roberts, K.E. Benfell, S. Gupta, J.A. Lucas, and D.J. Harris. The effects of pressure on coal reactions during pulverised coal combustion and gasification. *Progress in Energy and Combustion Science*, 28:405–433, 2002.

[179] Y. Wang. *Direct Numerical Simulation of Non-Premixed Combustion with Soot and Thermal Radiation*. PhD thesis, University of Maryland, 2005.

[180] R. Weber, J Dugue, A. Sayre, A. A. F. Peters, and B. M. Visser. Measurements and computations of quarl zone flow field and chemistry in a swirling pulverized coal flame. Technical report, International Flame Research Foundation, 1992.

[181] R. Weber, J Dugue, A. Sayre, and B. M. Visser. Quarl zone flow field and chemistry of swirling pulverized coal flames: measurements and computations. *Twenty-Fourth Symposium (International) on Combustion/The Combustion Institute*, pages 1373–1380, 1992.

[182] R. Weber, J. Dugue, A. Sayre, and B.M. Visser. Flow field and chemistry of swirling pulverised coal flames: measurements and computations. *IFRF report*, F 36/y/20, 1992.

[183] R. Weber, J. Dugue, A. Sayre, and B.M. Visser. Quarl zone flow field and chemistry of swirling pulverized coal flames: measurements and computations. *Symposium (International) on Combustion*, 24(1):1373–1380, 1992.

[184] R. Weber, A. A. F. Peters, P. P. Breithaupt, and B. M. Visser. Mathematical modeling of swirling flames of pulverized coal: What can combustion engineers expect from modeling? *Transactions of the ASME Journal of Fluids Engineering*, 117:289–297, 1995.

[185] R. Weber, J. P. Smart, and W. vd Kamp. On the (mild) combustion of gaseous, liquid, and solid fuels in high temperature preheated air. *Proceedings of the Combustion Institute*, 30:2623–2629, 2005.

[186] R. Weber, B. M. Visser, and F. Boysan. Assessment of turbulence modeling for engineering prediction of swirling vortices in the near burner zone. *Int. J. Heat and Fluid Flow*, 11:225–235, 1990.

[187] A. Williams, M. Pourkashanian, and J.M. Jones. Combustion of pulverised coal and biomass. *Progress in energy and combustion science*, 27:587–610, 2001.

[188] A. WIlliams, M. Pourkashanian, J.M. Jones, and N. Skorupska. *Combustion and Gasification of Coal.* Taylor and Francis, New York, 2000.

[189] J. Williamson. Low-storage Runge-Kutta schemes. *Journal of Computational Physics*, 35:48–56, 1980.

[190] S. Wysocki. *Joint Euler-Lagrange Method for Moving Surfaces in Large-Eddy Simulation.* PhD thesis, Imperial College London, 2012.

[191] O. Yldiz and H. Bedir. A parallel solution to the radiative transport in three-dimensional participating media. *Numerical Heat Transfer, Part B: Fundamentals*, 50:79–95, 2006.

[192] M. J. Yu, S. W. Baek, and S. J. Kang. Modeling of pulverized coal combustion with non-gray gas radiation effects. *Combustion Science and Technology*, 166:151–174, 2001.

[193] M. J. Yu, S. W. Baek, and J.H. Park. An extension of the weighted sum of gray gases non-gray gas radiation model to a two phase mixture of non-gray gas with particles. *International Journal of Heat and Mass Transfer*, 43:1699–1713, 2000.

[194] M. C. Yuen and L. W. Chen. On drag of evaporating liquid droplets. *Combustion Science and Technology*, 14:147–154, 1976.

[195] M.C. Yuen and L.W. Chen. Heat transfer measurements of evaporating liquid droplets. *International Journal of Heat and Mass Transfer*, 21:537–542, 1978.

[196] J. Zhang, O. Gicquel, D. Veynante, and J. Taine. Monte Carlo method of radiative transfer applied to a turbulent flame modelling with LES. *Comptes Rendus Mecanique*, 337(6-7):539–549, 2009.

[197] G. Zhou. *Numerical simulations of physical discontinuities in single and multi-fluid flows for arbitrary Mach numbers.* PhD thesis, Chalmers University of Technology, Goteborg, Sweden, 1995.

[198] L.X. Zhou, L.Y. Hu, and F. Wang. Large-eddy simulation of turbulent combustion using different combustion models. *Fuel*, 87(1314):3123–3131, October 2008.